

THÈSE

pour l'obtention du titre de

Docteur de l'Université de LILLE

Spécialité : Mécanique des solides, des matériaux, des structures et des surfaces

École doctorale : SPI

présentée par :

ARFA Essosnam

**Wear and contact modelling of heterogeneous
material using multi-scale method**

**Modélisation de l'usure et contact matériaux
hétérogènes par une méthode multi-échelle**

Thèse soutenue publiquement, jeudi le 17 septembre 2020 à 14h00,

devant le jury composé de :

Mathieu RENOUF

Zhi-Qiang FENG

Hélène DUMONTET

Vincent MAGNIER

Philippe DUFRÉNOY

Géry de SAXCE

Rapporteur

Rapporteur

Présidente du jury

Examineur

Co-directeur de thèse

Directeur de thèse

Chargé de recherche - HDR, Université de Montpellier

Professeur, Université d'Évry-Val-d'Essonne

Professeur, Université Pierre et Marie Curie

Maître de Conférences - HDR, Université de Lille

Professeur, Université de Lille

Professeur, Université de Lille

À la mémoire de mon très cher père Massimla,
à mon adorable mère Sarmata.

Remerciements

Ce travail de thèse a été réalisé au sein de l'équipe μ Frein du Laboratoire de Mécanique Multiphysique et Multiéchelle (LaMcube) de l'Université de Lille.

Mes sincères remerciements vont à la Région Hauts-de-France pour avoir financé cette thèse et ainsi permis indéniablement son aboutissement.

Je tiens à remercier mon directeur de thèse Géry de SAXCE pour toute la confiance qu'il m'a témoignée tout au long de ma thèse. Sa disponibilité, sa gentillesse, ses pertinents conseils et ses précieuses remarques ont rendu possible l'achèvement de ses travaux de thèse dans de bonnes conditions. Ce fut un honneur de travailler sous ta direction.

Mes remerciements vont à Philippe DUFRENOY, qui a co-dirigé cette thèse. Sa rigueur, son implication personnelle, ses commentaires enrichissants et surtout ses qualités humaines m'ont permis de m'améliorer et d'approfondir mes connaissances scientifiques. Je te suis reconnaissant pour ces années de travail.

Je ne saurais remercier assez Vincent MAGNIER qui a encadré mes travaux de recherche avec un grand intérêt. Sa présence hebdomadaire, ses compétences scientifiques, ses idées précises et ses encouragements continus ont contribué à l'aboutissement de ce travail. Ce fut un privilège d'apprendre et de travailler avec toi.

Mes sincères remerciements vont à Hélène DUMONTET de m'avoir fait l'honneur de présider mon jury de thèse, à Mathieu RENOUF et Zhi-Qiang FENG pour avoir accepté la lourde tâche de rapporteur. Je vous suis reconnaissant pour avoir accepté de faire partie de mon jury de thèse et pour l'intérêt porté à mes travaux.

Je tiens à remercier tout le personnel administratif du LaMcube pour leur gentillesse et accueil très chaleureux. J'adresse également mes remerciements à tous les membres de l'équipe μ Frein pour tous ces moments passés ensemble. Je remercie particulièrement Yassine Waddad pour ses conseils et pour ses routines python, Igor mon partenaire de sport pour sa joie de vivre, Amine, Van, Sanaa, Sylvain, Dimitri, Baptiste, Hoan, Muzzamal, Nada, Christian, Ncami, Qi, Nikzad, Florent, Jean-François, pour vos bonnes humeurs et les moments de qualité passés en vos compagnies.

Un grand merci à tous mes amis pour leurs gentillesse, les moments de divertissement, leurs aides (un clin d'œil à Vanessa, Julien, Catherine, Gloria, Antoine et Believe). Merci à Emmanuel, Kékéli, Maliki pour vos encouragements, conseils et soutiens. Un merci à Oncle Paul et sa femme Brigitte pour votre présence.

Je termine avec mes chers parents pour votre confiance inébranlable depuis toujours. Je vous en suis éternellement reconnaissant. Merci à mes frères et sœurs pour vos encouragements malgré la distance.

Abstract

Mobility has become a societal, environmental and economic issue. This translates into the development of means of transport that must be safer, faster for public transport and cleaner. Brake components are therefore an integral part of these new developments. Indeed, braking devices ensure that the vehicle stops (for example, the brake linings of a high-speed train can take up to twenty Megajoules) and are known to be a source of pollution (debris, noise). Moreover, for the railway sector, this is the first item of expenditure for consumables. In an attempt to have a high-performance brake system, brake linings are composite materials whose composition makes the issue of increased competition between different manufacturers. Nevertheless, the approach remains empirical and the understanding of the phenomenon remains relatively poor.

The difficulties lie in a better understanding of what happens within the contact interface, which is an area where different interactions occur: mechanical interactions, thermal exchanges, heat dissipation, etc. These interactions in return, lead to wear of contacting bodies which may impact material integrity and involves particles generation and emission. Subsequently, this affects the whole performance of the braking system and some environmental issues.

The current approach used by manufacturers to resolve these issues is the empirical feedback test. This approach is not only expensive but also do not respect technical and environmental requirements. Due to the complexity of contact interface which is multi-physics and multi-scale, in spite of the progress made in instrumentation and measuring techniques, it is still difficult, from an experimental point of view, to obtain precise measures of contact interface data. Clearly there is a need of theoretical modelling and numerical simulations to supply experimentations. Therefore, the objective of this work is to propose a numerical strategy of modelling contact of friction material taking into account the material and surface heterogeneity as well as surface evolution aspects due to wear. The challenge here is to consider at the same time the system and the material scales. A new multi-scale homogenization-based method is adopted. Unlike the classical homogenization methods, the proposed homogenization method has the advantage of considering contact constraints at the micro-scale and thus offers a macro to micro contact stresses relocation. The homogenization is done numerically by finite element method and only mechanical aspects are considered.

At micro-scale, homogenized parameters traducing material heterogeneity and surface effects have been computed and enriched at macro-scale. After macro-scale calculation is performed, mechanical fields obtained are reinjected at the micro-scale via the numerical homogenization technique. As a consequence, local mechanical parameters induced by material and surface heterogeneity are obtained. Furthermore, wear source flow modelling has been carried out at micro-scale through the multi-scale strategy implemented. Archard's law has been used for this purpose. Thanks to the numerical homogenization, material properties' evolution with wear was obtained. These new developments have been validated by comparison with reference models. The advantage of these new developments lies in the reduction of CPU time, which makes it possible to enrich the models in the future.

Key words: Contact homogenization, multi-scale finite element method, material heterogeneities, surface heterogeneities, wear source flow.

Résumé

La mobilité est devenue un enjeu sociétal, environnemental et économique. Cela implique le développement des moyens de transport qui doivent être plus sûrs, rapides et propres. Les composants de frein font donc partie intégrante de ces nouveaux développements. En effet, les dispositifs de freinage assurent l'arrêt d'un véhicule (par exemple, les garnitures de frein d'un train à grande vitesse peuvent supporter jusqu'à vingt mégajoules) et sont connus pour être source de pollution (débris, bruit). De plus, dans le secteur ferroviaire, il s'agit du premier poste de dépenses pour les consommables. Dans l'optique d'avoir un système de freinage de haute performance, la composition des garnitures de frein, qui sont des matériaux composites, est l'un des facteurs concurrentiels entre les différents fabricants. Néanmoins, l'approche reste empirique et la compréhension des phénomènes demeure relativement médiocre.

Les difficultés résident dans une meilleure compréhension des phénomènes qui se déroulent à l'interface de contact, qui est le lieu de différentes interactions : les interactions mécaniques, les échanges thermiques, la dissipation de la chaleur, etc. Ces interactions en retour, entraînent l'usure des corps en contact, ce qui peut avoir une incidence sur l'intégrité des matériaux et entraîner la production et l'émission de particules. Cela affectera l'ensemble des performances du système de freinage et posera certaines questions environnementales.

Les essais expérimentaux empiriques sur les matériaux de friction demeurent l'approche actuelle utilisée par les fabricants pour résoudre ces problèmes. Cette approche est non seulement coûteuse, mais ne respecte pas non plus les exigences techniques et environnementales. En raison de la complexité de l'interface de contact qui est multi-physique et multi-échelle et malgré les progrès réalisés dans l'instrumentation et les techniques de mesure, il est encore difficile d'un point de vue expérimental, d'obtenir des mesures précises des données de l'interface de contact. Il est clair qu'il faut une modélisation théorique et des simulations numériques pour supporter l'expérimental.

Par conséquent, l'objectif de ce travail est de proposer une stratégie numérique de modélisation du contact du matériau de friction, en tenant compte de l'hétérogénéité matériau et de surface ainsi que des aspects évolutifs de la surface dus à l'usure. Le défi majeur est de considérer à la fois les échelles du système, de l'hétérogénéité matériau et de surface. Une nouvelle méthode multi-échelle basée sur un schéma d'homogénéisation numérique est adoptée. Contrairement aux méthodes classiques d'homogénéisation, celle proposée a l'avantage de prendre en compte les contraintes de contact à l'échelle micro offrant ainsi une relocalisation des contraintes du modèle macro au micro. L'homogénéisation se fait numériquement par la méthode des éléments finis et seuls les aspects mécaniques sont pris en compte.

A l'échelle micro, des paramètres homogénéisés tenant en compte de l'hétérogénéité matériau et de surface ont été calculés et enrichis à l'échelle macro. Après ce calcul effectué, les champs mécaniques obtenus sont réinjectés à l'échelle micro via la technique d'homogénéisation numérique. En conséquence, les paramètres mécaniques locaux, induits par l'hétérogénéité des matériaux et des surfaces sont obtenus. En outre, une modélisation du débit source d'usure a été réalisée à l'échelle micro grâce à la stratégie multi-échelle mise en œuvre. La loi d'Archard a été utilisée à cette fin. Grâce à l'homogénéisation numérique, une évolution des propriétés matériaux avec l'usure a été obtenue. Ces nouveaux développements ont été validés par comparaison avec des modèles de référence. L'avantage de ces nouveaux modèles réside dans la réduction du temps de calcul, ce qui permet d'enrichir les modèles futurs.

Mots-clés: Homogénéisation avec contact, Méthode des éléments finis, Hétérogénéités matériau, Hétérogénéités surface, débit source d'usure.

Table of contents

| | |
|--|------------|
| GENERAL INTRODUCTION | 13 |
| CHAPTERS | 17 |
| I State of the art | 17 |
| I.1 Contact: a multi-physics problem | 19 |
| I.2 Contact: a multi-scale problem | 28 |
| I.3 Scope of the present work | 45 |
| II Multi-scale approach with friction: application to material heterogeneity | 49 |
| II.1 Multi-scale approach for contact modelling considering material heterogeneity | 51 |
| II.2 Extension of the proposed strategy to other cases | 80 |
| II.3 Extension to complex material behaviour laws | 91 |
| II.4 Application considering complex microstructure | 98 |
| II.5 Conclusions | 104 |
| III Modelling of non-smooth surface and evolution through wear by multi-scale approach with contact | 107 |
| III.1 Surface defects | 109 |
| III.2 Wear source flow modelling strategies | 122 |
| III.3 Numerical example illustrating different wear strategies modelling | 128 |
| III.4 Wear modelling considering a large scale model: homogeneous material | 134 |
| III.5 Multi-scale strategy for wear modelling of the heterogeneous material | 138 |
| III.6 Application of the multi-scale strategy into a complete brake system considering real microstructure | 151 |
| III.7 Chapter synthesis | 161 |
| BIBLIOGRAPHICAL REFERENCES | 163 |

General introduction

Context of the study

Contact mechanics is omnipresent in mechanical engineering and in everyday life. It has many and varied domains of applications such as the interaction of wheel and rail, bearings, tyres, clutches, electrical systems, brakes, walking, human being and animals' joint behaviour, etc. Generally, contact is very difficult to master since the interaction of the bodies depends strongly on different aspects related to on one hand, physics, and on the other hand, to the scales involved. Therefore, the objective of tribology is to try to understand these different interactions. Thus, it is necessary to consider the dimension of the third body (an intermediate film composed of particles detached from contacted bodies) where wear, source flows, different interface mechanisms etc. play an essential role. Nevertheless, contact may be necessary and indispensable to master in different industrial sectors such as braking systems, where the search for better performance is an objective for companies.

In the last decade, many contributions have been done in the transport domain. The vehicle and the TGV have reached new levels in terms of speed, inducing new challenges which have to be overcome such as the maintenance and operating costs of transport and the environmental requirements (noise, pollution, particle emissions, etc). These challenges go hand in hand with the redesign of new braking systems and new friction materials that will make it possible to reduce maintenance costs and comply with environmental requirements.

A major problem in transport is the durability of components subjected to rubbing contacts, mainly wear and its consequences in terms of generation and emission of particles. Whether it is rail, aeronautical or automotive, the ejection and emission of particles remains a common problem. These particles, by their very fine sizes, represent a potential danger for the population. Several industrial systems are responsible for this problem. The main systems are therefore, engines and disc brakes. In recent years, the use of particle filters in engines has led to a very significant reduction of particles emission in nature. Moreover, braking systems are also a very important source of particles emission and represent a major environmental challenge. Another common problem related in general to transport domain and in particular to braking system is friction-induced vibrations and waves between solids in contact. These vibrations frequently lead to radiation of sounds which are sources of disturbance of the surrounding media. Among many existing sounds, brake noise is the extreme in automotive domain particularly. Therefore, it seems relevant to study the braking system particularly the brake pads which are mostly responsible for the particles generation, emission, due to its constitution and the noise pollution.

From an industrial point of view, to improve the design of contact materials so that they meet environmental requirements, empirical tests and trial-and-error methods are

used. Another difficulty hindering the design of contact materials is at the experimental level. Indeed, even though there have been improvements in instrumentation in recent years, it is still very difficult to have accurate information within a contact interface. Another difficulty in understanding the phenomena for highly dissipative contacts lies in the use of highly heterogeneous materials. This heterogeneity is essential to combine different objectives. Nevertheless the role of these heterogeneities on contact is a still open question today.

Therefore, it is not only the contact interface but also the friction material contributes largely in the braking systems performance, as well as on the whole performances of transport systems.

Manufacturers invest a lot of money to overcome these issues by doing experimentations on the friction materials. However, these are not an easy task and most of the time do not respect the environmental requirements.

Due to the multi-physical aspect of contact, from an experimental point of view, it is very complicated to access all the useful information needed (contact pressure, area, temperature, etc) despite the progress made in instrumentation and measuring techniques. Another strategy to better understand the phenomena would be the use of numerical tools. Then, there will be a need for theoretical and numerical simulations which is of great interest to supply experimentation.

Many numerical models covering various aspects of physics have been widely widespread in literature for braking systems simulation. Usually these models separately consider either multi-physical, specifically thermo-mechanical, or multi-scales aspects. The coupling between the different scales is also ignored in most of the case.

Few models, in the recent year, propose the coupling between system scale, thermal and roughness aspects but still neglect the heterogeneities scale and the damage mechanisms associated. Subsequently this leads to a lack of efficient models allowing understanding of tribological phenomena. The major difficulty is to consider at the same time the contact and the system scale.

Objectives of the study

This thesis topic aims at the development of a strategy leading to contact modelling of heterogeneous material especially for large scale models. The material and surface heterogeneities have been considered into in a complete braking system for the application purpose. In addition, a fine-scale wear management is proposed. This approach is based on a proposition of a new multi-scale method: heterogeneities are considered at the system scale and wear is taken into account at both the system and heterogeneity scales. The proposed strategy is a first step that will allow the development of more realistic models while reducing CPU time. This approach is therefore of great industrial interest in the choice of material design processes.

Reading guide

This manuscript is divided into three chapters:

Chapter [I](#) presents a literature review quite large in the contact mechanics field. However, this is non-exhaustive. A special interest is dedicated to the multi-physical and multi-scales aspect of contact.

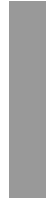
At the end of this chapter, the present work is positioned, in regard of the bibliography review, by specifying the objectives and the methodology used.

Chapter [II](#) is dedicated for the proposed multi-scale strategy for contact modelling considering the scale of heterogeneity. The numerical strategy is a multi-scale homogenization based on a micro to macro embedding and a macro to micro relocalization, where the effects of heterogeneities are highlighted. A large variety of heterogeneities cases have been presented and validated to the reference solutions.

Chapter [III](#) deals, firstly, with a strategy leading to contact modelling considering simultaneously material heterogeneity and surface defects and which is based on gap introduction in the contact law. This strategy is an extension of the numerical strategy established in chapter [I](#). Secondly, based on the proposed multi-scale strategy where gap is introduced in the contact law, wear source flow modelling has been proposed.

In conclusion, a synthesis of the results obtained has been presented illustrating the originality of this work. Thereafter, some prospects have been proposed for improving the present work.

CHAPTERS



State of the art

Mini-Contents

| | | |
|---------|--|-----------|
| I.1 | Contact: a multi-physics problem | 19 |
| I.1.1 | Thermo-mechanical | 20 |
| I.1.2 | Friction-induced vibrations | 21 |
| I.1.2.1 | Different types of brake noises | 21 |
| I.1.2.2 | Squeal noise generation mechanisms | 22 |
| I.2 | Contact: a multi-scale problem | 28 |
| I.2.1 | System scale | 29 |
| I.2.1.1 | Braking system | 29 |
| I.2.1.2 | Numerical aspects associated | 30 |
| I.2.2 | Materials heterogeneity scale | 32 |
| I.2.2.1 | Physical aspects | 32 |
| I.2.2.2 | Numerical aspects associated | 35 |
| I.2.3 | Surface scale | 38 |
| I.2.3.1 | Physical aspects | 38 |
| I.2.3.2 | Numerical aspects associated | 39 |
| I.2.4 | Third body scale | 41 |
| I.2.4.1 | Physical aspects | 41 |
| I.2.4.2 | Numerical aspects associated | 42 |
| I.3 | Scope of the present work | 45 |

I.1 Contact: a multi-physics problem

Contact interface phenomena are determined by the atomics interactions within and between contacted solids and those between atoms of the particles which are present at the interface [Vakis et al., 2018]. These interactions give birth to a multitude of physics described by different theories and models, making contact a multi-physical problem synthesized in the Figure I.1.

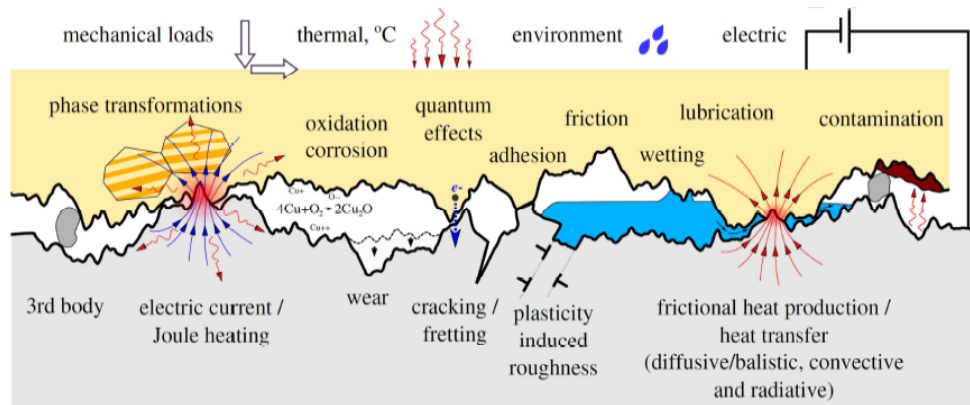


Figure I.1 – multi-physics problem associated to contact [Vakis et al., 2018].

Among the different physics near contact interface, we can distinguish: mechanical, thermal, physico-chemical, electro-magnetic, metallurgical, quantum and others types of physics.

Mechanical phenomena refer to solids mechanical deformations and their contact interactions. Surface degradation (micro-cracking, plastic deformations, abrasion and adhesion) or material removal process is associated to mechanical phenomena types.

Thermal phenomena are related to heat transfer from one solid to another, heat generation due to friction at contact interface and dissipation in the material volume. Thermo-mechanical aspects of contact are discussed in detail later.

Metallurgical phenomena generally occur at near interface layers and induce various microstructural transformations due to changes in temperature (for instance caused by joule effect or frictional heating) or by severe deformations. These microstructural changes include dynamic recrystallization and various phase transformations; an example is the formation of a fine-grained and rather brittle martensitic layer called "white layer" [Ramesh and Melkote, 2008]. Local rise in temperature can be critical for mechanical performance of materials experiencing glass transition [Ward and Hine, 2004]: in most cases, mechanical properties are strongly linked to the temperature the making thermo-mechanical aspect a strongly and natural coupled multiphysical problems in tribology.

Chemical phenomena can occur between materials in contact subjected, or not, to environmental influences. Atoms and molecules can then react between themselves to exhibit chemical decomposition. For example, corrosion which is the result of chemical reaction with an oxidant. Furthermore, there is a coupling between chemical, thermal and mechanical phenomenon's arising during contact; especially for composite materials.

Thermal investigation of a friction composite material degradation was carried out by combining thermo-gravimetry and mass spectroscopic analysis. The results show that H₂O and CO₂ emissions can be indicators of the degradation process [Cristol-Bulthé et al., 2008].

Besides chemical reactions, more complicated physics emerge especially from composite and porous materials. For example rocks experiencing chemical decomposition, pressurization, water evaporation etc. (refer to [Dieterich, 1972; Colletini et al., 2013]).

The interplay between these different physics makes contact a multi-physics problem and exhibits generally **instabilities phenomena** in the contact. A special subsection is dedicated for studying instabilities mechanisms later.

In the following, thermo-mechanical aspects of contact are discussed in more detail.

I.1.1 Thermo-mechanical

Solids in contact, submitted to mechanical loads, experience deformations due to their contact interaction. In sliding contact, friction forces are considered as a resistance to the sliding motion and typically most of the frictional energy is transformed into thermal energy through atomic and molecular interactions, plastic deformations, etc. Therefore, through contact surfaces, there is not only heat exchange from one solid to another but also heat generation due to interfacial friction. Thermal phenomena can be also related to the dissipation in the material volume through several mechanisms (damage accumulation, micro-crack, viscoelasticity, and viscoplasticity, etc): heat exchange can be either ballistic or diffusive according to the size of the contact spots [Chen, 2002; Anciaux and Molinari, 2013] whereas radiative and convective heat exchange contribute considerably to the overall heat conductance [Madhusudana and Madhusudana, 1996]. Generally, real surfaces are non-smooth. Therefore, the real area of contact is smaller than the apparent one. Then contact is performed through this non-smooth surface and mechanical and thermal loads are transmitted through these micro zones which can be represented by surface asperities. As a consequence, and since these micro zones are very small, high elevation of contact stresses and temperature occur around and within contact micro zones. The stresses and temperature around these micro zones could be extremely severe and could damage the materials, accelerate wear process and alter materials properties by overheating [Archard, 1959; Furey, 1964; Kennedy Jr, 1984]. Moreover, the contact pressure distribution and the heat generation through the surface will be non-uniform and the solids will be distorted by thermal expansion known as thermoelastic instability [Barber, 1969]. On the other hand, the local heating of contacting asperities up to the point of local melting [Bowden et al., 2001] and generally known as flash-heating, has important implications for friction especially in dry contact [Goldsby and Tullis, 2011]. Melting in return can lead to wear with sliding.

This brief and non-exhaustive above discussion does not consider all the thermo-mechanical aspects of contact. The aim being to show the complexity of multi-physics aspects of contact in order to propose an efficient strategy of modelling later.

Furthermore, there are instabilities phenomena which occur during contact and certainly do not influence the mechanical integrity of the rubbing systems but generates an important discomfort for the surrounding population. Therefore, it seems relevant to give some insights about this source of instabilities known as friction-induced vibrations in the following.

I.1.2 Friction-induced vibrations

Friction, resulting from the sliding contact, often gives birth to diverse forms of waves and oscillations within solids which frequently lead to radiation of sound to the surrounding media. Among diverse examples of friction sounds, violin music and brake noise are the most significant in terms of the sounds produced and the mechanisms by which they are generated [Akay, 2002]. Basically, these instabilities generated by friction are called friction-induced vibrations.

Friction induced vibrations in brakes are a major topic of interest principally for the automotive industry. Due to friction, structural vibrations may occur as well as the audible noise that can be related to these vibrations. Diverse consequences may occur, for example safety issues, driver discomfort and maintenance requirements. In fact, brakes are one of the most important components in terms of performances and safety in transport domain. Therefore, it is of great importance for automotive manufacturers to seek improvements in the braking system design in order to increase its power, efficiency and durability. [Kinkaid et al., 2003] noticed, in their bibliography review, that the refinement of vehicle acoustics and comfort through improvement in other aspects of vehicle design has enormously increased brake noise relative contribution to these aesthetic and environmental concerns. Consumers are very irritated because of brake noise and many of them believe that the brake system has functioning problems.

In this subsection we shall focus principally on brake noise because of the above reasons mentioned. A lot of information about brake noises in the literature exist. Here a quick summary of different types of brake noises is given, then followed by the predominant mechanisms responsible for them.

I.1.2.1 Different types of brake noises

In the literature, a wide array of brake noises and vibrations phenomena are described by a wide range of terminology: squeal, groan, chatter, judder, moan, hum, and squeak. According to the papers of [Rhee et al., 1989; Akay, 2002], they are classified in two types of brake noises according to their distribution in the frequency spectrum (Figure I.2).

In the following, some of the noises often dealt in the brake industry are presented:

Low frequency rigid body vibration

About 100 to 1000 Hz, they are summarized in Figure I.2 and some of them are described in the following:

The judder

The brake roughness or judder is a low frequency oscillation around 100 Hz which can

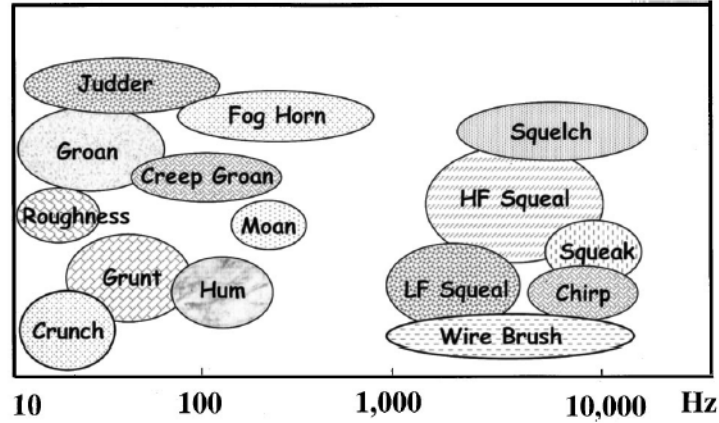


Figure I.2 – Different brake noises and their approximate spectral contents [Akay, 2002].

be detected by the driver’s foot, during braking manipulation, or hands. The main cause is the geometrical defects of brake components. For example, thickness variation of the disc(rotor) due to thermal effects or massive friction material transfer.

The moan

It is also a low frequency phenomenon occurring at around 150 to 400 Hz. It is caused by rigid body oscillation of the caliper and its mount.

The groan

Groan (100 - 400 Hz) is an audible vibration which generally occurs at a speed of 20 km/h. This type of brake noise is the result of the stick-slip, described later, phenomena happening in the contact.

Medium and high frequency vibrations

About 1000 to 18000 Hz up to the limit of human hearing. They are self-excited vibrations mostly due to the contact interface. They are described in the following:

Squeak

It is a short-lived squeal, a high-pitched sound and is similar to a clean window rubbing.

Squeal

It is a kind of sharp noise from 1 to 10 kHz and is generally observed at the end of a stop.

Wire brush

It describes a randomly modulated squeal and it appears when there are some irregularities on one of the parts in contact. From 10 to 11 kHz or 10 to 14 kHz.

From there, brake noise is referenced as squeal noise, because it is the most widespread and covers the largest bandwidth. Therefore, mechanisms responsible for squeal generation will be discussed in the following.

I.1.2.2 Squeal noise generation mechanisms

In this subsection, principal mechanisms developed in the literature concerning friction-induced noise and vibration are presented. Most of these mechanisms are inspired from experimental investigations like in [Wells, 1929], where stick-slip phenomena is observed during measurements of the kinetic friction coefficient. [Fieldhouse and Newcomb, 1993]

using holographic interferometry prove that the disc present purely diametral modes and the pad, a variety of modes such as bending, torsion and sometimes a combination of both. At noise start, disc deformation is closed to its own modes. A reconstructed hologram of a squealing disc brake system is shown in the Figure I.3.

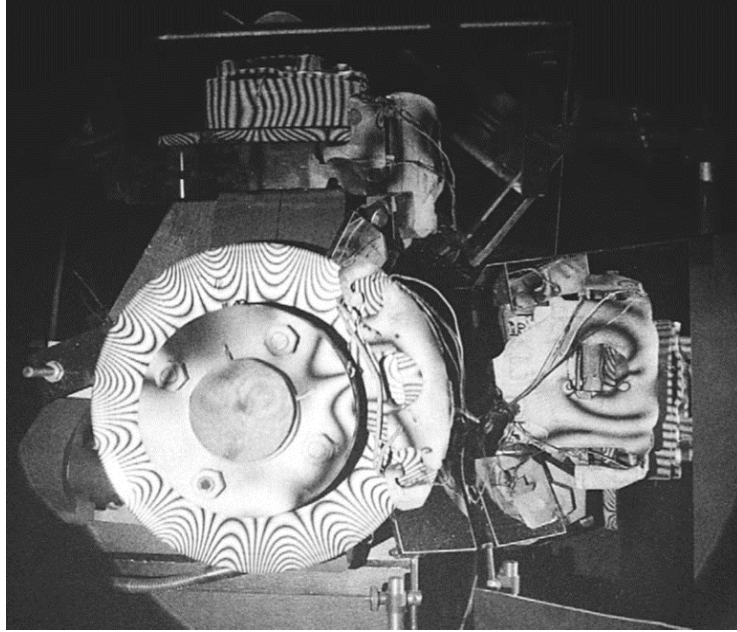


Figure I.3 – Fieldhouse and Newcomb’s reconstructed hologram of a squealing disc brake system [Fieldhouse and Newcomb, 1993].

Several mechanisms can explain self-excited vibrations in frictional systems [Popp and Stelzer, 1990; Ibrahim, 1994; Kinkaid et al., 2003]. Among them, four possible mechanisms have been proposed to be responsible of friction-induced vibration:

Surface phenomena origin

Below, the occurrence of friction-induced vibrations is related to surface phenomena. Two mechanisms are therefore presented in the following:

Stick-slip phenomena

There exist a lot of information about stick-slip mechanism in the literature. A synthesis inspired from [Popp and Stelzer, 1990; Ibrahim, 1994; Kinkaid et al., 2003] is proposed here. Usually, one degree of freedom (DOF) model, presented in Figure I.4, is used for this purpose.

The system is composed of a mass (m), a conveyor belt, a linear spring of stiffness k and a damper with damping coefficient c . A constant vertical force N is applied against the mass m and the conveyor belt which is in rotation with constant velocity v . $R_n = -N$ stands for the normal reaction force of the conveyor belt on m and T_f is the friction force. Let u_x denote the displacement of the mass. $\Delta v_x = \dot{u}_x - V$ represents the relative tangential velocity between conveyor belt and the mass. Where \dot{u}_x is the time partial derivative.

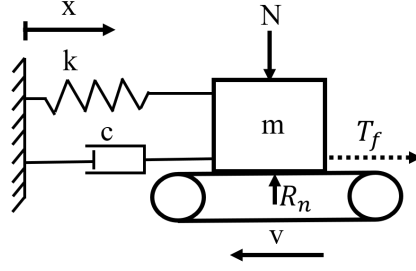


Figure I.4 – 1 DOF model.

The equation of motion is written as in (I.1):

$$m\ddot{u}_x + c\dot{u}_x + ku_x = T_f(\Delta v_x). \quad (\text{I.1})$$

Friction conditions can be described by Coulomb's friction law in (I.2):

$$T_f \leq \mu_s R_n, \quad (\text{I.2})$$

where μ_s stands for the static friction coefficient which depends on materials in contact. According to equation (I.2), friction forces cannot exceed a certain limit (stick state). If the limit is reached, the mass will start to slide with a relative velocity. This interference between stick and sliding state of the mechanical system can be the possible friction-induced vibrations known as stick-slip mechanisms. When the relative velocity equals to zero, the system is in adhesion state. Otherwise, the mass slides over the conveyor with frictional force $T_f = -\mu_d R_n \text{sign}(\Delta v_x)$, where μ_d is the dynamic friction coefficient which is considered here to be constant whenever the relative velocity and $\text{sign}(\Delta v_x)$ is the sign of Δv_x .

Negative friction-velocity slope

Here, the system presented in Figure I.4 is still used for our purpose. Let consider a friction coefficient decreasing with relative velocity. Friction force is then described by equation (I.3):

$$\mu_d = -\mu_s(1 - aV)R_n \text{sign}(\Delta v_x), \quad (\text{I.3})$$

where a is positive. Then, the equation of motion (I.1) linearized around quasi-static equilibrium state of the 1 DOF system is given by equation (I.4):

$$m\ddot{u}_x + (c - a\mu_s R_n)\dot{u}_x + ku_x = 0. \quad (\text{I.4})$$

According to equation (I.4), if $a\mu_s R_n > c$, the system damping is negative and leads to exponentially increasing of vibrations. Therefore, this negative damping coefficient can be associated to self-sustained vibrations. In conclusion, the decrease of friction coefficient in respect to the relative tangential velocity can introduce instabilities in frictional system. As noticed on [Murakami et al., 1984], the squeal occurrence is higher when the friction coefficient was a decreasing function of the relative velocity than a constant function. The

stick-slip itself and the negative damping theory are not sufficient to explain squeal noise. Other theories of geometrical origin can be one of the possible brake squeal mechanism. These theories are going to be explained in the following.

Geometrical origin of squeal noise

Below, geometrical phenomena in the occurrence of friction-induced vibrations of mechanical systems is studied:

Sprag-slip phenomenon

[Spurr, 1961] announced a theory of brake squeal named sprag-slip which applies even when the friction coefficient is not a function of the relative tangential velocity. Sprag-slip theory is introduced through the mechanical system, illustrated in Figure I.5:

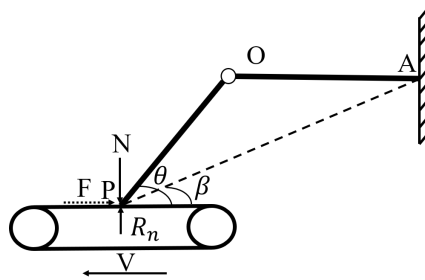


Figure I.5 – Spragging model.

The system is composed of two rigid struts AO and OP, pivoted at point O. The first rigid AO strut is clamped at point A. The rigid strut OP is loaded against a moving surface, with a constant velocity V, by a vertical force N and at angle θ . Friction coefficient was supposed to be constant. Taking moments about the pivot point O, one can show easily that the friction force is obtained from equation (I.5):

$$F = \frac{\mu N}{1 - \mu \tan \theta}. \quad (\text{I.5})$$

In equation (I.5), when θ reaches $\arctan(1/\mu)$, the friction force tend through high values and the strut can sprag leading to impossible motion. This theory demonstrate that the system unstable oscillation can occur even with constant friction coefficient. Moreover, the geometrical orientation of the contacted geometries leads to normal contact force variation playing then a key role in self friction-induced vibrations. However, the interaction between normal and tangential force is not highlighted in the mechanism exciting the squeal. Squeal theory based on modal coupling is described next.

Mode coupling

Modal coupling results in friction force changing necessary to induce self-excited vibration. There is a lot of works dealing about mode coupling theory known also as binary flutter and non-conservative displacement dependent forces (refer to [North, 1972; Kinkaid et al., 2003]). [Oden and Martins, 1985] first introduced mode coupling theory observing that a coupling exists between normal and tangential forces. Many models tried to elucidate these mechanisms in the literature. Among these works, the two DOF model, in Figure I.6, of [Hoffmann et al., 2002] is very demonstrative.

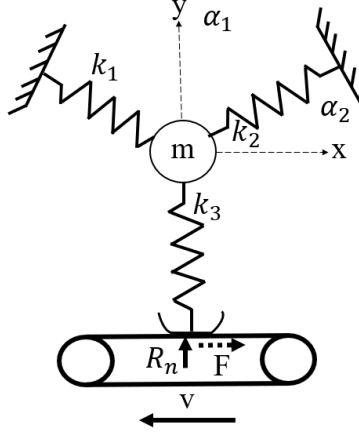


Figure I.6 – Two DOF model of [Hoffmann et al., 2002].

The model is composed of a conveyor belt in rotation with constant velocity V and pushed against a block, modelled with a point mass m , with a constant normal force R_n . The block is maintained in position by two linear springs of rigidity k_1 and k_2 . The normal contact stiffness, between the block and the moving conveyor belt, is represented by a linear spring k_3 . Sliding friction force F is considered through a Coulomb friction law assuming a constant friction coefficient μ . This model is a generalization of the one DOF model used to describe the precedent squeal theories. The only difference between stick-slip model comes from the fact that this model allows displacements normal to the sliding surface. The equations of the motion are obtained from (I.6):

$$\begin{bmatrix} m & 0 \\ 0 & m \end{bmatrix} \begin{bmatrix} \ddot{x} \\ \ddot{y} \end{bmatrix} + \begin{bmatrix} k_{11} & k_{12} \\ k_{21} & k_{22} \end{bmatrix} \begin{bmatrix} x \\ y \end{bmatrix} = \begin{bmatrix} F \\ R_n \end{bmatrix}, \quad (\text{I.6})$$

where the coefficients of the stiffness matrix are obtained from elementary considerations as:

$$\begin{cases} k_{11} = k_1 \cos^2 \alpha_1 + k_2 \cos^2 \alpha_2, \\ k_{12} = k_{21} = k_1 \sin \alpha_1 \cos \alpha_1 + k_2 \sin \alpha_2 \cos \alpha_2, \\ k_{22} = k_1 \sin^2 \alpha_1 + k_2 \sin^2 \alpha_2 + k_3. \end{cases} \quad (\text{I.7})$$

Considering small perturbations around the steady sliding state and assuming that the friction force equals $F = \mu k_3 y$, the resulting system of equations leads to a non-symmetric eigenvalues problem.

Equation (I.6) gives birth to (I.8):

$$\begin{bmatrix} m & 0 \\ 0 & m \end{bmatrix} \begin{bmatrix} \ddot{x} \\ \ddot{y} \end{bmatrix} + \begin{bmatrix} k_{11} & k_{12} - \mu k_3 \\ k_{21} & k_{22} \end{bmatrix} \begin{bmatrix} x \\ y \end{bmatrix} = \begin{bmatrix} 0 \\ 0 \end{bmatrix}. \quad (\text{I.8})$$

Because of the non-linearities induced by the friction force, the stiffness matrix becomes non-symmetric. Therefore, an eigenvalue analysis can be performed to find complex eigenvalues defined as: $\lambda = D + iw$, where D and w are the real and imaginary part of λ . D and w

stand for damping and pulsation of the perturbation respectively. It is important to notice that if the real part D is positive, the system becomes unstable. Considering a system with a mass $m = 1$, $\alpha_1 = 150$ deg, $\alpha_2 = 30$ deg, $k_1 = \frac{2}{3}(2 - \sqrt{3})$, $k_2 = \frac{2}{3}(2 + \sqrt{3})$ and $k_3 = \frac{4}{3}$, the evolution of w and D in function of the friction coefficient is shown in Figure I.4.

Figure I.7 presents two normal undamped modes with different frequencies which tend to coalesce when the friction coefficient reaches 0.5. When friction coefficient is above 0.5, the real part becomes positive leading to unstable mode in the system.

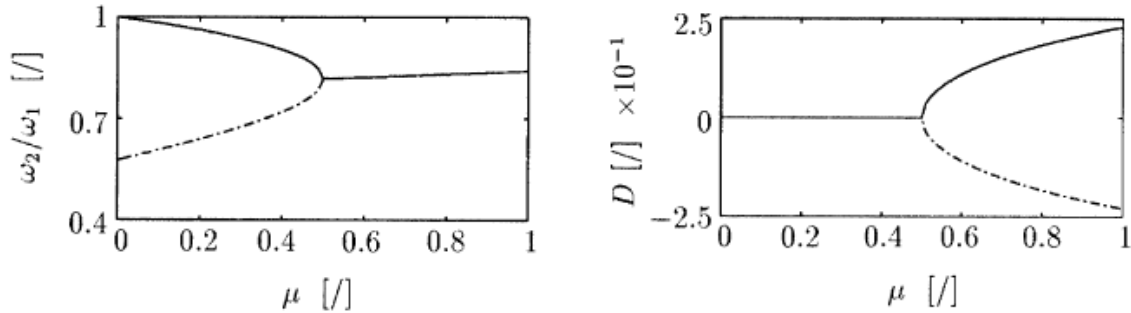


Figure I.7 – Evolution of the pulsation and the damping, in function of the friction coefficient, of the minimal mode coupling model of [Hoffmann et al., 2002].

Modal coupling is nowadays one of the most accepted theories as a necessary condition for squeal generation and therefore is considered in this work. Sprag-slip theory is a particular case for low frequency squeal and results from system components dynamic. Squeal can appear even for constant friction coefficient.

Squeal prediction based on modal coupling has been investigated for multi DOF model by the mean of Finite element analysis. Two methods exist for squeal prediction using Finite Element Method (FEM): **Complex Eigenvalue Analysis** and **Transient analysis**.

Complex Eigenvalue Analysis (CEA)

Here, the stability analysis consists in computing the eigenvalues of the whole system, after its linearization around the equilibrium. After a quasi-static equilibrium of the system is performed, an extraction of complex eigen-frequencies of the system state is followed. These complex eigen-frequencies allow system stability analysis. The system is unstable if the real part of the eigenvalue is positive and the associated eigen-frequency is considered as squeal noise frequency. Stability study by the means of FEM through **CEA** has been performed in the work of [Liles, 1989]. For instance authors like [Nagy et al., 1994; Bae and Wickert, 2000; Baba et al., 2001; Massi et al., 2007] can be cited also, but this list is not exhaustive.

Transient analysis (TA)

TA results in the computation of the dynamic response in time domain. Squeal is supposed to occur if the system responses diverge in time [Des Roches, 2011]. The system is then said

to be unstable. The major advantage of **TA** results in the consideration of non-linearities induced by contact and the ability to simulate the real behaviour of the system. However, this approach is computationally expensive and time consuming.

The **CEA** is the most suitable for this work: working on the whole brake structure, considering material and surfaces heterogeneity and also surface evolution is a lot of time consuming with **TA**.

In this subsection, four instabilities mechanisms have been presented and can be categorized in two groups. The first one is from tribological origin where it has been demonstrated that friction forces play a key role in squeal noise generation even with constant or decreasing friction coefficient with tangential velocity. The second class of mechanisms is from geometrical origin and mode coupling between normal and tangential directions. Nowadays, mode coupling theory is unanimously accepted by most of the scientific community as predominant condition for squeal generation. However, it is important to know that mode can coalesce without generated squeal noise as noticed by [Murakami et al., 1984].

Conclusion of the section

In definitive, in this section, multi-physics aspects of contact have been emphasized through several notions and examples. Since these physics are mostly coupled, it is necessary to understand that a detailed description of contact pass through the consideration of its multi-physics aspects. Then the strategy proposed later for contact modelling has been built in a way that several physics may be considered. Moreover, contact is a not only a matter of physics but also has a multi-scale nature. Recent works such as [Wang et al., 2018], show that surface roughness and wear of asperities played a key role in squeal evolution. In fact contact is multi-scale by nature. It is then necessary to consider multi-scale behaviours in the contact modelling in order to understand its effects on squeal generation which is a special issue in the transport domain. Therefore, in the next section, multi-scale aspects of contact are discussed in details.

I.2 Contact: a multi-scale problem

Previously, multi-physical aspects of contact have been highlighted. Here the multi-scale aspects of contact are discussed.

[Vakis et al., 2018] identified five different scales involving in contact problem which are illustrated in Figure I.8. Contact is multi-scale by nature since it involves the atomic scale up to the system scale. The highest scale is related to macro-scale models where the physical quantities are influenced by small scales.

The smallest scale is associated to the different components of the global system and their

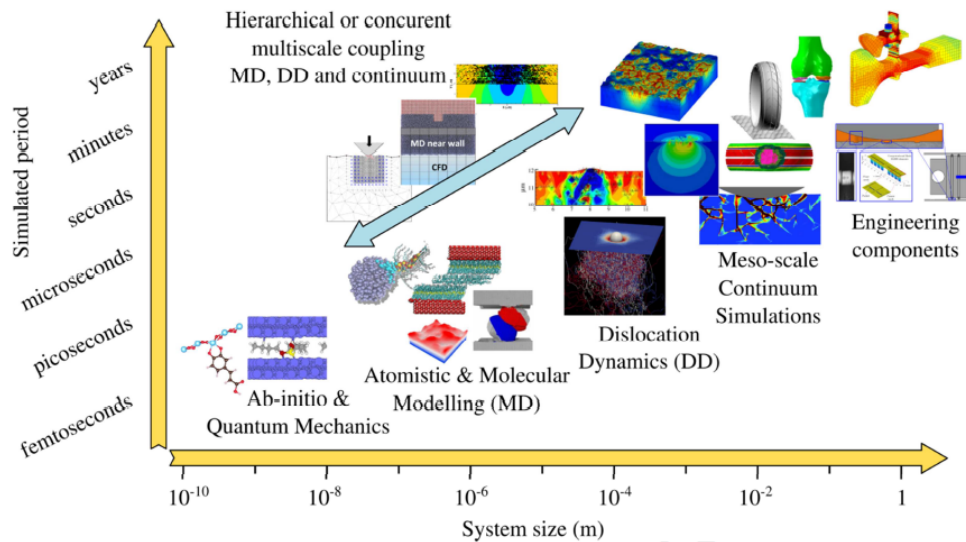


Figure I.8 – Time versus length scales associated to contact problem [Vakis et al., 2018].

surfaces topography (roughness, plateaus, etc). Another scale is related to the wear debris present between contacted first bodies which is the third body scale.

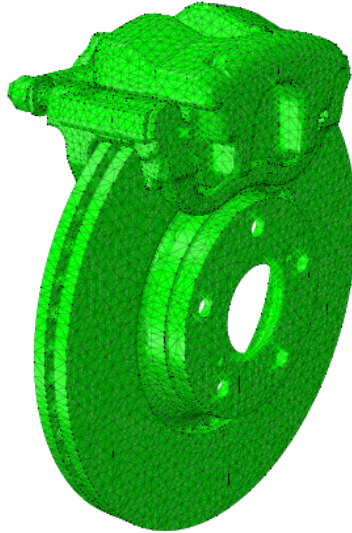
First, in the following subsection, the system scale is illustrated before going down the scales.

I.2.1 System scale

I.2.1.1 Braking system

Many braking systems exist and have different performances. However, two types of friction brakes: drum brakes and disc brakes, are commonly used especially disc brakes because of its efficiency compared to drum brakes. Disc brake system involves several components such as rotor (disc), brake pads, caliper, piston, brake fluid, and chassis. The disc can withstand temperatures from $600\text{ }^{\circ}\text{C}$ to $800\text{ }^{\circ}\text{C}$.

Usually, in the numerical simulation, a braking model consists of a pair of pads in contact with a rotating disc using specific boundaries conditions. In reality, these types of models are very simplified; the geometry of each component and the way they are assembled will influence the dynamical response of the system. In fact, each component has several exchanges between themselves (mechanical, vibratory and thermal exchange). Therefore, for a realistic braking modelling, reduce the whole braking model into brake rotor and brake pads only is not enough. The whole braking model should be considered because of the dynamical aspects of the other components. The whole braking system has influence on the performances and should be considered in numerical simulations. Thus, robust numerical systems are required in order to consider entirely braking system. That is the aim of the next subsection.



(a)

Figure I.10 – Complete FEM disc brake model [Renaud et al., 2012].

For instance, complex eigenvalue analysis method has been used in [Bajer et al., 2004; Bakar et al., 2005] for wear modelling and squeal prediction. The authors developed a three-dimensional FEM brake pads model and simulated the wear displacement process, using adaptive meshing and a wear subroutine file to adjust automatically the nodes at the disc and pads interface. These authors reported that wear could affect the appearance and disappearance of unstable frequencies. Otherwise the predicted unstable frequencies were close to the experimental values. However, they did not consider material and surface heterogeneities in the braking modelling. The real surface topography of brake pads is later considered, in the FE model, in [Abu Bakar et al., 2008]. Furthermore, in [Sinou, 2010], a non-linear model of a disc brake system was developed to study transient and stationary non-linear self-excited vibrations. The authors conclude that non-linear transient and stationary self-excited vibrations can become very complex and more unstable modes, than those predicted by a linearized stability analysis around a non-linear equilibrium point (complex eigenvalue analysis), appear. Many contributions have been done in the context of large-scale braking models. These works, even though not exhaustive, can be cited in the context of large scales braking modelling [Naidoo Ramasami, 2014; AbuBakar and Ouyang, 2008; Chung and Donley, 2003; Bajer et al., 2003; Blaschke et al., 2000]. However, there is a lack of multi-physics and multi-scale aspects consideration in these works. For example, although friction materials are heterogeneous, homogeneous hypotheses have been considered in most of the previous cited works. The scale of material heterogeneity must be incorporated for better predictions. Therefore, the scale of material heterogeneity is investigated in the next subsection.

I.2.2 Materials heterogeneity scale

I.2.2.1 Physical aspects

At a lower scale than the system one previously studied, there is friction material scale. Friction material plays a key role in the braking by dissipating the mechanical energy into heat in order to inhibit the motion of the system. Friction pads are submitted to high pressures and temperatures due to sliding with the disc (up to 800 °C). Therefore, they must have good thermo-mechanical properties, a high friction coefficient with the brake rotor and provide a relatively stable and consistent friction coefficient whatever the temperature, wear, corrosion, etc. Moreover, friction pads must have certain technical qualities: low wear rate of the disc and friction material itself, long life cycle, smooth braking without vibrations and noises, respect environmental process and finally the cost must be low. Thus, friction material selection process is not an easy task. To fulfil the performances required, friction materials are made from multi components (up to 25 components). For this reason, the term composites is attributed to them. However, in order to obtain a good friction material, which fulfil the required performances, the friction materials components must be selected carefully. Moreover, a knowledge of the fabrication process must be mastered. Then, a particular attention is dedicated to the selection of their components. The main difficulties lie in the multi-scale's aspects of the final composition of the friction material. In the following, a brief description of the friction materials is given: their different types, their composition and their mechanical behaviour which participate the most in the system vibration and set up the tribology mechanisms.

Different types of friction materials and their composition

[[Chan and Stachowiak, 2004](#)], in their bibliographic review, summarize the currents components used in automotive brake friction material for wet and dry braking. In general, 3 types of brake pads are used in the dry braking industry:

- metallic matrix,
- semi-metallic matrix,
- organic matrix.

Many components are required in part of friction material fabrication process because of exigences related to the performances of braking system. Typically brake pads contain the following components: reinforcing fibers, binders, fillers, and frictional additives. All these components have their specificities which have to be kept in the final composition. In the following, the specificities of all these components are illustrated.

The reinforcing fibers

The reinforcing fibers provide good mechanical strength to the friction material and can be categorized in 3 families: mineral, organic or metallic fibers. As an example we have glass

fibers, metallic fibers, Aramid fibers, potassium titanite fibers, sepiolite fibers, ceramic fibers. For details about the composition of the examples given above, the reader must refer to the paper of [Chan and Stachowiak, 2004].

The binders

They are generally called matrix and they allow keeping the brake pads components integrity under mechanical and thermal load; so, the choice of binders is of great importance. Different binders exist like: phenolic resin, condensed polynuclear aromatic (COPNA) resin, cyanate ester resin, epoxy modified resin, thermoplastic polyimide resin [Chan and Stachowiak, 2004].

The fillers

They have no impact on the mechanical behaviour of the frictional material and help in reducing the overall cost of the brake pad. They are in large proportion in the brake friction material. [Chan and Stachowiak, 2004] distinguished two main classes of fillers: organic and inorganic fillers. Barium, sulphate, mica, vermiculite and calcium carbonate are examples of inorganic fillers. Organic fillers commonly used are cashew dust and rubber.

The frictional additives

These types of components contribute in the modification of wear rate and the friction coefficient. They are typically categorized into two groups: solid lubricants and abrasives. Solid lubricants decrease the friction coefficient and the wear rate while the abrasives increase them. As examples of solid lubricants, we have graphite and metal sulphides. Zirconium oxide, zirconium silicate, aluminium and chromium oxides are commonly used as abrasives. The above talk mentioned different components of brake pad used in the friction material process where the frictional contact surfaces are used to be dry most of the time. In fact for wet environment only, wet friction materials are typically used. [Chan and Stachowiak, 2004] classed the wet friction material in three different types:

- paper type,
- sintered materials,
- fabric type.

The most important property of the wet friction material is its high porosity allowing great fluid permeation capacity. It must be able to not crumble under large compressive forces and to be able to withstand high thermal energy. The material should provide consistent and stable friction coefficient.

Ruddy Mann, during his phd thesis, worked on an industrial formulation of a sintered material for railway applications. This material is obtained by compacting powders of components, before being sintered at high temperature [Mann, 2017]. As shown in the Figure I.11 this material is multi components of large range of type and size. Furthermore, the presence of porosities was confirmed within the graphite particles. Through a series of

compression tests under different loads levels, the sintered material exhibited a complex behaviour because of its complex microstructure. That raises the question about the mechanical behaviour of friction material, knowing their complexity in terms of microstructure. The next subsection is dedicated to this purpose.

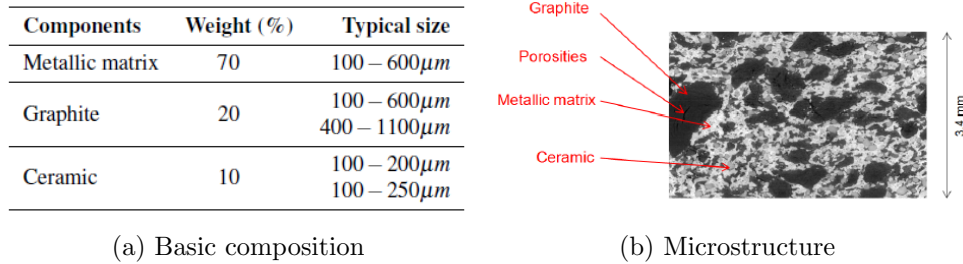


Figure I.11 – Microstructure of the sintered material [Mann, 2017].

Other works attempt to introduce new component in part of the friction material fabrication process in order to study its influences on friction and wear rate [Gurunath and Bijwe, 2007].

Mechanical behaviour of friction materials

The mechanical behaviour of friction material is not obvious since it is a mixture of many components. It has been shown earlier that the frictional material components have influences on the final composition. For example, shape, quantity and size of reinforcing fibers affect the material properties. However, in a macroscopic point of view what will be the overall behaviour of the frictional material?

[Kamat et al., 1989] evaluated Al₂O₃/ Al₂O₃ composite mechanical properties and observed that yield and ultimate tensile strength of the composite increased with Al₂O₃ particles volume fraction. [Kok, 2005] studied the mechanical properties of Al₂O₃/ Al₂O₃p composite and revealed that the hardness and tensile strength of the composite increased with the percentage of the reinforcing fibers. In [Mann et al., 2017; Serrano-Munoz et al., 2019], through compression tests on different samples, extracted from sintered friction material obtained from a realistic braking test (before and after), it has been shown that non-linear behaviour like plasticity and damage occur. The authors attribute plasticity phenomenon to a localization of strains in bands which are associated to graphite particles. Moreover, damage effects were related to the decrease in elastic modulus when increasing loading. Therefore, the material exhibits a loading history effect. This damage behaviour is related to some initial porosities inside components and porosities at components interface. Furthermore, in [Bousselham et al., 2020], it has been shown that the overall behaviour of the sintered friction material is isotropic transversal.

In conclusion, friction material has a complex mechanical behaviour which is directly related to its microstructure.

I.2.2.2 Numerical aspects associated

The mechanical description of heterogeneous material is very complex to take into consideration in numerical modelling. The complexity is much higher when we consider large scale model. At small scale, usually micro-mechanical homogenization methods are used to compute the overall behaviour of heterogeneous material. However, for large scale model there is a need of multi-scale methods in order to overcome the time consuming of direct computation. It is very important to consider material heterogeneities in complete models such as braking modelling because it plays a key role for example in the squeal generation mechanisms [Magnier et al., 2017].

In literature, there are few multi-scale methods considering material heterogeneities at the system scale. Also, tribological phenomena associated at the heterogeneity scale are most of the time ignored in numerical simulations. [Magnier et al., 2014] developed a complex eigenvalue analysis of a pin-on-disc system including frictional contact. They took into account heterogeneous distribution of material properties to analyse the effects of contact distribution on mode coupling theory. In numerical point of view most of the work dealing with friction material use homogenization techniques which gives good results when there is no contact in the models. Each components of the friction material play an important role in the local behaviour when contact is considered. These localisations can have more impact on the tribological behaviour of the brake pad system, for example wear computation. Therefore, the use of classical homogenization theory without taking into consideration contact constraints in the homogenization procedure is not sufficient; at least when it is about the wear modelling process.

For example, some works like the ones develop by [Peillex et al., 2008; Mbodj et al., 2010], studied the mechanical behaviour of a composite material, under non linear dynamical loading, whose equivalent properties have been determined through a classical homogenization technique. Using a relocalization process, results obtained from the homogeneous model are very close to those obtained by a classical dynamical analysis of a heterogeneous model through the direct computation. However, because there is no contact law in the relocalization process, stresses are overestimated especially at the contact surface [Peillex et al., 2008]. Since the classical homogenization is made under the assumption of a representative volume element, the relocalization of contact stresses will not be well estimated because the contact stresses distribution depend strongly to the location of heterogeneities in the structure.

In general, through the classical homogenization procedure, the relocalization of contact pressure at the scale of the heterogeneity is not possible. In fact, it is well known that heterogeneities disrupt contact pressure distribution which in turn influences tribological phenomena. It is then important to propose a strategy allowing material heterogeneities consideration in high scale models.

In the following lines, we will give some existing techniques used to account for material heterogeneities in a numerical modelling.

Homogenization methods

Homogenization aims to compute the overall behaviour of a complete heterogeneous media. A relation between the macro strain and stress imposed to the overall structure has to be calculated using the classical homogenization theory [Hill, 1963]. The computation becomes more harder according to the type of material behaviour (linear elasticity, elastoplasticity, viscoplasticity, elastoviscoplasticity, etc). Many approaches exist to deal with homogenization:

Mean fields theory

Many authors made hypothesis allowing to obtain upper and lower bounds of real behaviour of heterogeneous material. The upper bound corresponds to Voigt bound and the lower is for Reuss [Paul, 1959]. Other bounds which are more precise exist in the literature, one of the most used is based on the stress polarization tensor [Hashin and Shtrikman, 1963]. Other methods also exist: Mori-Tanaka method, based on the Eshelby solution [Eshelby, 1957, 1959], and the self-consistency homogenization model. For more details about mean fields theory, see the work of [Bornert et al., 2001]. Mean fields methods are very restricted. They do not give any local information and any spatial repartition. Other particular methods exist which overcome these limitations.

Transformation Field Analysis (TFA) and Non-uniform Transformation Field Analysis (NTFA)

Let consider a representative volume V of a composite material. The volume V is subdivided into several local volumes. The idea of the transformation field analysis is to approximate internal local variables fields by piecewise uniform distribution within a given subdomain ([Dvorak, 1992]). These internal variables describe irreversible phenomena (plasticity, viscoplasticity, damage...). Then, using the equilibrium and state equations, it is possible to compute the average strain in each subdomain. The average stress is therefore deduced using the appropriate material constitutive laws.

In order to obtain good results, the numbers of subdomain must be large enough. Even in this condition, the overall behaviour of the composite material using TFA is too stiff. To solve this issue, [Michel et al., 2000] propose NTFA based on the TFA idea but the internal variables are no longer piecewise uniform within each subdomain. They are supposed to follow a non-uniform distribution using plastic modes which corresponds to the slip system in the terminology of crystal plasticity (reader must refer to [Michel et al., 2000] for details).

In the context of contact modelling, NTFA method, even interesting, remains very complicated to use because of non-linearities induced by contact and will not be adopted in this work.

Direct computation

Here, the complexity of the overall heterogeneous structure is considered. All the heterogeneities are explicitly meshed and the problem is solved using FEM. All the stresses and strain distribution induced by heterogeneities are computed directly. However, direct computation is time consuming and cannot fit industrial requirements. Therefore,

multi-scale methods are required. They give good results and save a lot of computation time.

Multi-scale methods

Subdomain decomposition Method

In this method: the whole heterogeneous material is decomposed in a set of subdomains linked by interface laws. This method aims principally to the parallel computing. It is an intelligent utilization of direct computation. Therefore, this method is less time consuming than the direction computation thanks to the parallel computing.

However, The non-linearities induced firstly by contact interface and secondly by material heterogeneities may cause technical problems for domain decomposition methods. All the details about subdomain decomposition method can be found here ([Farhat and Roux, 1991],[Mandel, 1993]).

Arlequin Method

Arlequin method is a multi-scale based method which allows the superposition of different mechanical models using coupling operators. Also, the energy distribution between the coupling zones must be consistent. As an example, 1D and 2D mechanical problems can be coupled together using the Arlequin method. This method can be very interesting for a mechanical problem where there is a localized zone within the structure. For example: cracking, impact problem, etc. For details, one may refer to the paper of [Dhia, 1998].

In the context of friction materials which are highly heterogeneous and submitted to tribological loadings, the Arlequin method would be very complicated to set up with computation time which may be more important than the direct computation.

Method FE^2

FE^2 method is type of multi-scale method where two FEM problems are solved simultaneously. The macroscopic structure is discretized in finite elements and at each Gauss point a microscopic problem is associated to a corresponding Representative Volume Element (RVE) of the whole macroscopic heterogeneous structure. At a microscopic level, a numerical homogenization is performed which bypass the classical homogenization described above. In fact, there is any restriction on the material behaviour law. This method has been used in [Feyel and Chaboche, 2000; Mbodj et al., 2010; Nhu, 2013] (Figure I.12).

In this work, for contact modelling of heterogeneous material, ***a multi-scale strategy inspired from the work of [Feyel and Chaboche, 2000; Mbodj et al., 2010; Nhu, 2013] will be used.*** This kind of strategy is adopted because of its flexibility. It allows coupling between many scales and is based on numerical homogenization allowing then computation time reduction. The parallel computation is also possible.

In this subsection, material heterogeneity has been investigated: physical and numerical aspects. However, there is another finer scale related to the surface irregularities, which is the aim of the next subsection.

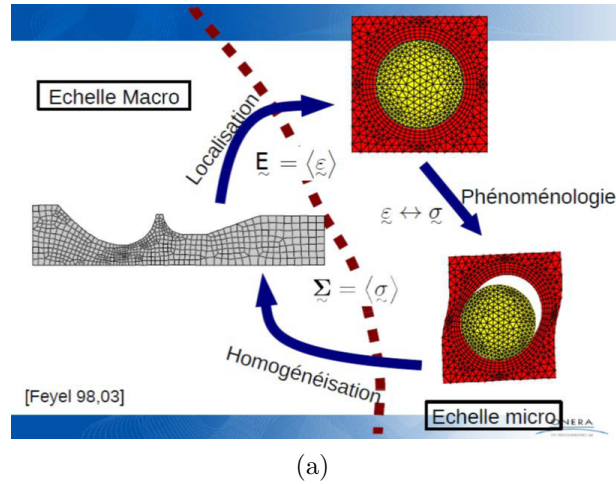


Figure I.12 – FE² strategy description [Feyel and Chaboche, 2000].

I.2.3 Surface scale

I.2.3.1 Physical aspects

As previously mentioned, surface influences contact systems performances. Therefore, knowledge about contact surfaces is of great interest in numerical modelling. [Akay, 2002] summarized the contributions to friction at different scales in Figure I.13. The first one is the engineering scale where the geometry of the first bodies are supposed to be parallel and their contact surfaces are smooth. At continuum scale, due to manufacturing defects, the heat generation and wear, contact surfaces are no longer flat. Going down the scales, there is roughness scale which is represented by a set of asperities in the contact surfaces. True contact arises on the surface of asperities and some particles trapped between them. Computational resources are very expensive in order to reproduce phenomena happening at this scale. Another subsection is dedicated to talk about the numerical strategies available to solve contact at this scale (roughness).

It is well known that the true contact area is much smaller than the one computed in the case of perfectly smooth surfaces. In fact, two mechanical surfaces brought into contact touch only over some zones known as surfaces asperities. Surface roughness affects not only many mechanical quantities (the stress state near the contact interface, the friction, wear, etc) but also heat and electrical conductivity [Cooper et al., 1969; Barber, 2003]. Since the beginning of contact modelling of rough surfaces, the realistic representation of roughness remains a key problem. This problem is due to the multi-scale aspect associated with roughness. In fact, the latter go down to the nanoscale [Solhjo and Vakis, 2017]. Then, surfaces characterization whether experimentally or created via numerical methods, using statistical approaches or fractal techniques, remains a universal problem [Suh et al., 2003; Sayles and Thomas, 1978; Deltombe et al., 2014]. Even numerical surfaces generated using the spectral density or the auto-correlation function has some lacks in roughness representation [Persson et al., 2004] (Figure I.14).

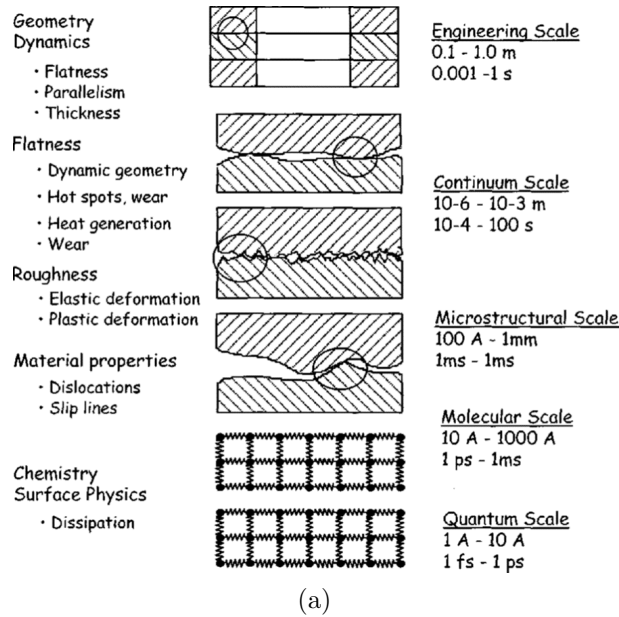


Figure I.13 – Length and time scales associated with contact surfaces [Akay, 2002].

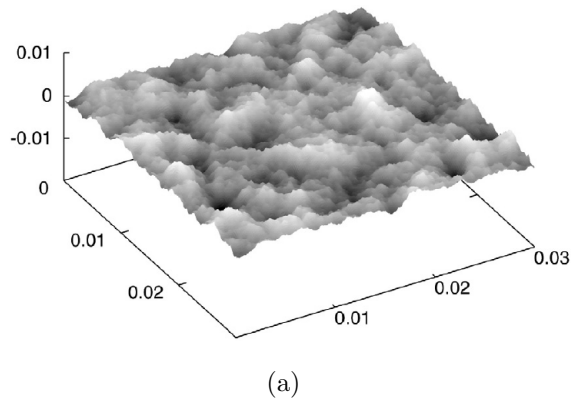


Figure I.14 – Rough fractal surface generated numerically by the power spectral density [Persson et al., 2004].

Finally, it is important to know that brake discs and pads surfaces contain wear debris (third body scale [Godet, 1984] described later) growing within time and become plateaus as noticed in the work of [Eriksson and Jacobson, 2000] (Figure I.15). In this work, surface defects modelling is included in our multi-scale strategy, which is the topic of the second chapter, in the way of plateaus.

I.2.3.2 Numerical aspects associated

Here, the numerical models associated with roughness scale are presented. On surface heterogeneities, a contact model between rough surfaces was first proposed by [Greenwood and Williamson, 1966]. This model is based on the pioneering Hertzian theory, which solves the problem of two non-conformal elastic bodies under frictionless contact [Hertz, 1882].

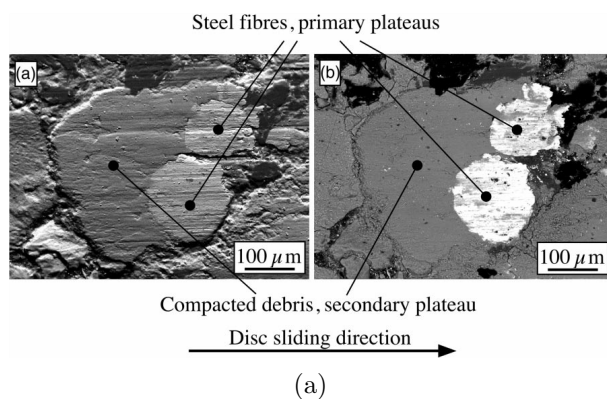


Figure I.15 – The contact situation between an organic brake pad and a brake disc, involving wear debris and contact plateaus [Eriksson and Jacobson, 2000].

Greenwood and Williamson predict a link between contact force and true contact area when considering rough surfaces. Another interesting theory after Greenwood and Williamson model is the one of [Majumdar and Bhushan, 1991] where Korcak's law was used to define a power law distribution of contact spots. These models consider surfaces roughness as a set of spherical or parabolic asperities and are ranged within statistical rough surfaces models. In the same vein, subsequent improvements have been made in the work of [Nayak, 1971; Bush et al., 1975]; where the authors presented more generalized models. Many authors like one's cited here studied also the effects of roughness in mechanical quantities but neglect all the dependence of statistical roughness parameters on the sampling length, the interaction effect between asperities and their geometrical approximation. Authors like [Ciavarella et al., 2006] improve these models by incorporating interaction between asperities.

Furthermore, rough surfaces can be generated numerically from surface parameters obtained from experimental measurements using the spectral density

All the methods listed above are analytical ones and are not designed for large scale models which are more complex. To account for roughness in a large-scale model, FEM based methods are used. Using the direct FEM computation requires a lot of computation like in [Pei et al., 2005]. Rough contact requires a highly refined mesh in order to capture precisely the contact evolution.

However, there are several methods allowing to account for roughness into large scale models. These approaches are based on homogenization or analytical methods, at the microlevel, allowing to get some contact laws or some homogenized coefficients traducing the heterogeneities (surface ones principally) and introduced into the large system model studied [De Lorenzis and Wriggers, 2013; Bandeira et al., 2004; Zavarise et al., 1992]. Basically, the contact surface is discretized in a set of patches and each patch are enriched with the contact evolution laws or the homogenized coefficient. The good thing here is that, the surface is still flat and does not require a refined mesh, allowing then reduction of computation time.

Recently, some authors proposed an analytical solution to take into account the interactions

between the different roughness's [Waddad et al., 2016]. In the latter, Waddad also proposed a thermomechanical multi-scale method to incorporate not only these surface defects into a large-scale problem but also wear evolution associated. This strategy was used to highlight the size effect of roughness on vibration instabilities in a complete brake system [Dufrenoy et al., 2016].

In the majority of these works, the material is considered to be homogeneous, which is not true for friction material. They did not consider the effects of material heterogeneities and tribological mechanisms such as wear at the macro-scale.

The material and surface scales lead to a finer scale called third body [Godet, 1984] which is located between contacted surfaces. Therefore, the third body scale is investigated in the next subsection.

I.2.4 Third body scale

I.2.4.1 Physical aspects

In addition to the different scales presented above, there is the third body scale. One must ask what is the third body concept? The benchmark work [Godet, 1984] was the first to introduce the third body concept and developed by [Berthier, 1996]. The third body concept is a qualitative description of wear and is related to the mode and mechanism of speed accommodation. It helps understanding better the wear phenomenon. According to Berthier, third body has three principal's functions: load carrying, speed accommodation and first bodies separation. These functions are summarized in Figure I.16.

During braking, there are particle detachment which grow within time, compact to form plates and present load carrying properties. These particles represent third body scale. The particle detachment is from the first bodies scale. The mechanism, the first bodies and the third body are summarised under the name of the tribological triplet [Berthier, 1996].

Basically, there is five possible speed accommodation sites induced by third body (refer to the Figure I.16) between the first bodies. S_1 and S_5 represent the skin of the first bodies, S_2 and S_4 represent screens. Screen is the zone between first and third bodies. Finally, S_3 represents the volumetric zone of third body. Each site can contain 4 modes of accommodation. The elastic mode M_1 , the normal breaking M_2 , the shearing mode M_3 during sliding of first bodies and the rolling mode M_4 . During contact, first bodies, under mechanical and thermal loading conditions, undergo damage and as consequence lead to particle detachment which is trapped into the contact (internal source flow). Due to speed accommodation, these particles circulate (internal flow). A certain amount of third body can be ejected from contact (wear flow) and another part can be recycled in the contact (recirculation flow). The sum of the wear flow and the recirculation flow constitute the external flow. This group of flows represent the tribological circuit [Berthier, 1996] (refer to Figure I.16). It is possible for external particles, which are not from the first bodies, to be trapped into the contact (external source flow). In the next section, the modelling solutions associated to the physics detailed in this section will be presented.

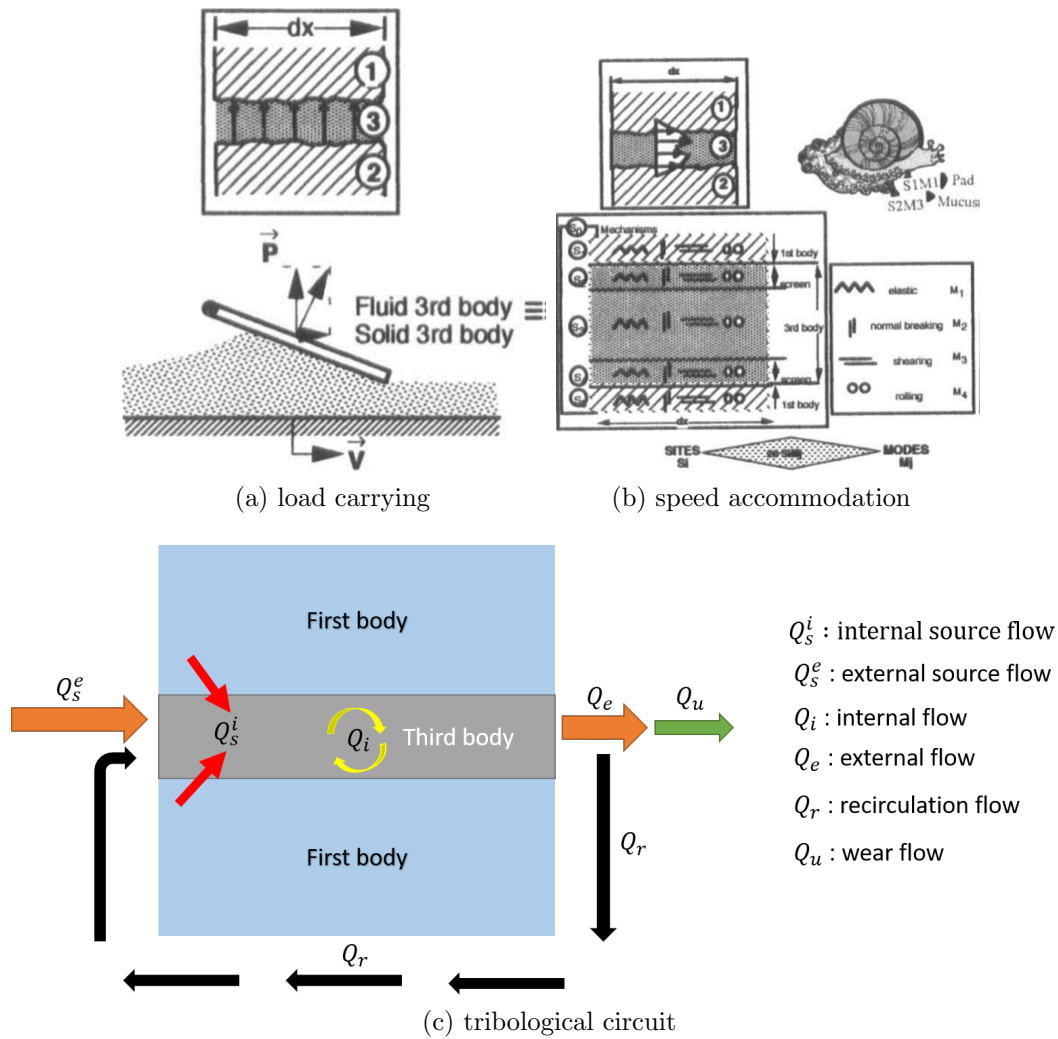


Figure I.16 – Third body functions and the tribological circuit [Berthier, 1996].

I.2.4.2 Numerical aspects associated

Wear source flow modelling

The idea for this modelling is that all the particles detached from the first bodies are completely ejected from contact. In fact, the consideration of all the flows present in the tribological circuit is very difficult. To overcome these difficulties, the modelling process of material removal is done by the use of some specific wear laws.

There are many wear models in the literature. [Meng and Ludema, 1995] after reading many articles make a conclusion that there are more than 300 equations which describe wear kinetic and some of them are specific to experimental measurements. Nowadays there is not a universal wear law. The benchmark work [Archard, 1953] considered that worn volume depends on two structural parameters (the normal load F and the sliding distance s) and is inversely proportional to material Hardness H . Mathematically, this law is written as:

$$V = \frac{k}{H} * F * s, \quad (I.9)$$

where k is the dimensionless wear coefficient, which depends on experimental measurement, relating to the probability of two asperities in contact to create a wear particle. It is important to know that this law was initially related to adhesive wear and cannot describe all degradations phenomena induced by contact. Other laws taking into account more physics exist but is difficult to set up numerically because of the lack of experimental parameters to feed them; for details the reader must refer to the works of [Quinn, 1971; Suh, 1973; Sarkar, 1980].

In the litterature, most of analytical and FEM models are based on Archard's law for wear source flow modelling. In the context of FEM, wear height at each node is calculated by dividing equation 1.9 by the contact area. This technique is used by authors like [Chmiel, 2008]. However, this kind of model suffers from the fact that there are no re-meshing techniques during the process of wear removal and the wear computation is not included during the finite element analysis. Therefore, to avoid these limitations, [Hegadekatte et al., 2004] using Archard's wear law creates two dimensional and three-dimensional models to simulate wear between steel and brass contact. After every wear cycle, the geometry is re-meshed to correct the deformed mesh due to wear. Even though, the latter approach is better than the first one, for large wear cycles, convergence is not guaranteed due to excessive mesh distortion.

Continuum approach of third body modelling

As describe before, the third body concept is a physical based approach of wear description. It remains very difficult for numerical modelling. The difficulty arises from the different scale between tribological triplet. Some researchers did many efforts to take into account wear particles in their numerical modelling in a continuum way: [Yue and Abdel Wahab, 2016], using a FEM studied the effects of wear particles in their simulations. After a certain wear cycle, they import in their simulation a debris layer which has the profile of the wear scar caused by the previous simulation. They found that wear debris can protect first bodies in contact and they can also be harmful. [Basseville et al., 2011] studied the effects of wear particles included in a fretting wear model. The third body is explicitly modelled by several rectangular particles with sizes $5 \mu\text{m} * 1 \mu\text{m}$, spaced by $2.5 \mu\text{m}$. They also studied the coupling between wear and crack in gross sliding conditions.

Recently, [Ghosh et al., 2016] investigated the effects of material properties, elastic plastic deformation and number of wear debris in fretting wear simulation. As conclusion of their work, wear particles are found to carry out an amount of the load applied in contact and these particles deform plastically. However, material heterogeneities are still neglected.

Discrete approach of third body modelling

Appropriate and robust approaches are required in order to simulate the rheology of the third body, which is a dynamic problem. Discrete approaches, for example Discrete Element Method (DEM), which is naturally designed for discontinuous medium [Cundall, 1971] can be a useful tool for the third body flows modelling. In [Cundall, 1971], DEM was used to simulate rock systems and was later extended to the simulation of granular media [Cundall and Strack, 1979]. Furthermore, DEM has been used in [Fortin, 2000], for

the dynamic modelling of granular media under contact loadings, using the bipotential method of [De Saxcé and Feng, 1998].

Then, DEM was initially used in [Elrod and Brewe, 1992] for third body flows modelling followed by several authors, for instance [Ghaouti et al., 1996; Fillot et al., 2004]. Moreover, another concurrent DEM approach, based on a different formalism, the Non-Smooth Contact Dynamics (NSCD) [Jean, 1999] which is an extension of Contact Dynamics approach [Moreau, 1988], was also used in the modelling of third body flows [Renouf et al., 2011; Champagne et al., 2014]. However, the NSCD approach allows not only the consideration of rigid particles but also deformable ones. Another class of discrete methods used for third body flows studies are the cellular automaton and the movable cellular automaton methods in [Müller and Ostermeyer, 2007; Dmitriev et al., 2010]. A cellular automaton is composed of a set of cells, with different states in function of neighbouring cells, linked to each other by some laws of evolution allowing description of phenomenon's arising at contact interface.

The majority of the discrete approaches available for third body modelling are computationally expensive and most of the time are restricted to bi-dimensional problems. Therefore, the discrete approach is not considered in this work.

In this subsection three modelling strategies have been presented in the purpose of third body scale modelling. The first one concerns wear source flow modelling. This model considers that all wear particles are ejected from contact and do not consider the tribological circuit. The second one tries to incorporate third body particles in the contact in continuum way. In other words, third body particles are assumed to form a compacted layer with known dimensions. However, hypotheses about third body geometry are too strong. The third numerical model is a discrete approach of third body and can give a good description of third body (source flow, recirculation flow). As mentioned earlier, large scale model is our interest. This model is too complex to set up for large scale model. In the purpose of this work, for surface evolution consideration, the first numerical model based (wear source flow modelling) is considered. Even Archard's wear law (I.9) is very simple, it will be used later as a physical model to describe wear source flow (adhesive wear). The main objective being to set up a multi-scale strategy capable to consider more wear mechanisms, the use of Archard's law is only for validation purpose.

Conclusion of the section

In this section, multi-scale aspects of contact have been investigated: from system scale to third body scale. Not only system scale influences performances but also the lowest scales, especially material heterogeneity, impact seriously performances. Due to the lack of experimental studies to understand mechanisms happening at fine scales, it is therefore important to build strong numerical models considering the coupling between scales in order to supply experimentations. In this work, a special interest is dedicated to the friction material heterogeneity and surface scales. Numerical models must be able to consider also multi-physics aspects.

I.3 Scope of the present work

The present literature review has displayed the multi-scale and multi-physics aspects of contact problem and the existing numerical methods available in the literature for consideration of such complexity. In regard of literature, it has been shown that there is a lack of multi-scale models for contact modelling, especially for large scale models. This is important in the research of performances (durability, squeal, etc), for instance in braking applications. Brake components, especially brake pad, play a key role on the system performances. As mentioned in the bibliographic review, friction material is highly heterogeneous. Two majors' heterogeneities have been distinguished: material and surface heterogeneities. Besides, the applied solicitations can lead to the formation of a third body layer at the contact interface. Developments exist for large scale model modelling considering surface heterogeneity but at least only few models deal with material heterogeneity and surface evolution through wear, in the large-scale models. In regard of this complexity, a better strategy of modelling is still needed for braking system in particular. ***Therefore this PhD aims to a strategy leading to contact modelling with friction considering material heterogeneity, surface heterogeneity and surface evolution through a multi-scale approach.***

On material heterogeneity, the strategy must be able to consider all the heterogeneity and can deal with complex material behaviour laws.

On surface heterogeneity, the strategy must be able to consider surface roughness and plateaux (meso and micro-scale).

On surface evolution, an application of wear source flow modelling is considered in this work. Archard's wear model is used to compute the wear source flow from contacted bodies. However, the strategy can incorporate other types of damage mechanisms at the micro-scale.

On physical aspects, mechanical loadings are considered. The key contribution here lies in the development of modelling strategy taking into account material heterogeneities in a large-scale model with gain of computation time.

The strategy proposed in this work is a multi-scale strategy based on a new homogenization method. The proposed multi-scale method allows taking into consideration, for instance adhesive wear at local scale, and later complex damage mechanisms at the micro-scale and their embedding at the macro-scale via the new homogenization method. The main aspects of the multi-scale strategy is illustrated in the following:

1. The development of a new homogenization method considering contact interface at micro-scale
2. An embedding strategy at macro-scale
3. A macro to micro strategy taking into account effects of heterogeneities on macro contact pressure distribution
4. A strategy leading to modelling of surface defects and surface evolution through wear for heterogeneous material based on contact normal gap technique described later

The strategy implemented here is useful for introducing material damage mechanisms at the micro-scale and can save a lot of computation time. Therefore, it can be very useful for industrial process.

Two main parts compose this manuscript which is organized as follow:

The first part is devoted for **contact modelling considering heterogeneous material for large scale models**. A new numerical homogenization method considering *contact interface* is developed and used in multi-scale strategy process. This development has been carried out considering linear elasticity. Thereafter, the multi-scale strategy developed is extended for transversely isotropic material behaviour. Simple numerical examples are proposed to validate the strategy.

Finally, a real microstructure example is considered to consolidate the multi-scale strategy developed.

The second part concern **surface defects**, for instance plateaux, and **surface evolution** modelling based on the homogenization model build in the first part.

Firstly, a strategy incorporating surface defects, into the material heterogeneity multi-scale strategy is proposed and validated with simple academic examples. Secondly, in the same spirit, surface evolution at the level of heterogeneities is introduced and validated through a simple case. Thereafter a real microstructure is considered. A link between surface evolution and material mechanical parameters, therefore, can be obtained.

The developments realized in this work are new and therefore results are compared with a reference example.

Finally, wear modelling is carried out at the level of a complete brake model where squeal is performed through the complex eigenvalue analysis.

The whole strategy is summarized in Figure [I.17](#)

The multi-scale strategy described in [I.17](#) is composed on three main steps:

The **first step** proposes to evaluate the overall behaviour of a heterogeneous material by the mean of homogenization method. This is possible after a numerical discretization of

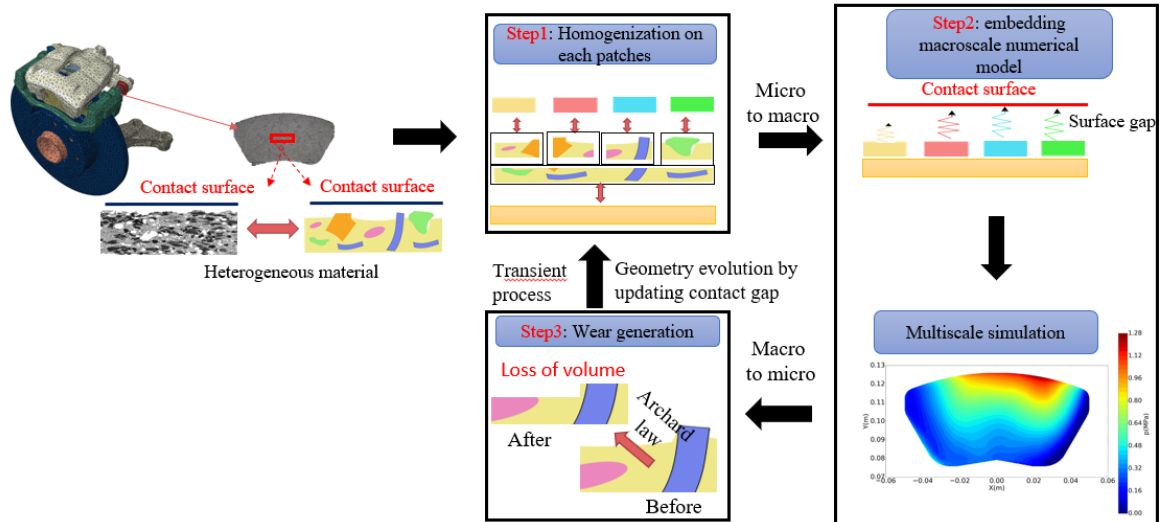


Figure I.17 – Global strategy.

the whole heterogeneous material into a set of cubical patches.

The **second step** is where the computation is done at a large scale using the previously homogenized computed in Step 1.

Finally, at **step three**, surface evolution is considered and injected in the homogenization box to account for material degradation due to wear. However, it is possible to consider other degradations mechanisms.



Multi-scale approach with friction: application to material heterogeneity

This chapter will describe the multi-scale strategy developed in the case of a complete system considering a friction material which is highly heterogeneous. The studied structures will be braking applications with either simplified systems (pin-on-disc configurations) or real automotive brake system configurations. A strategy including the complexity of the material in a multi-scale modelling is proposed. This is based on a numerical homogenization in which the boundary conditions with contact are considered. This method is quite general and allows working on any type of material.

The strategy is therefore established at two different scales (system and microscopic) that communicate in a one-to-one manner. The interest is to relocate the macro mechanical state to the scale of the components allowing the possibility of introducing new mechanisms into the contact.

An example is proposed comparing the new model with a reference one allowing the verification of the hypotheses formulated in the strategy.

Mini-Contents

| | | |
|----------|---|-----|
| II.1 | Multi-scale approach for contact modelling considering material heterogeneity | 51 |
| II.1.1 | Classical homogenization theories | 52 |
| II.1.2 | Equivalent quantities computation using KUBC | 54 |
| II.1.3 | Numerical example: Multi-scale problem | 55 |
| II.1.3.1 | Explicit method results | 57 |
| II.1.3.2 | KUBC versus explicit method | 59 |
| II.1.4 | New approach, the homogenization with contact: KUBC-Contact | 63 |
| II.1.4.1 | Contact homogenization: KUBC-Contact | 64 |
| II.1.4.2 | KUBC-Contact versus KUBC | 65 |
| II.1.4.3 | KUBC-contact versus explicit method | 70 |
| II.1.5 | Parametric study on the friction coefficient | 78 |
| II.2 | Extension of the proposed strategy to other cases | 80 |
| II.2.1 | Homogenization results | 80 |
| II.2.2 | KUBC-contact versus explicit method results | 82 |
| II.2.3 | Parametric study on Young's modulus evolution | 84 |
| II.2.4 | Mesh dependence from embedding to relocalization | 86 |
| II.3 | Extension to complex material behaviour laws | 91 |
| II.3.1 | Transversely isotropic material | 91 |
| II.3.2 | Transversely elastic isotropic: strategy and effective quantities computation | 92 |
| II.3.3 | Numerical example: | 95 |
| II.3.3.1 | Model description | 95 |
| II.3.3.2 | Results | 96 |
| II.4 | Application considering complex microstructure | 98 |
| II.4.1 | Numerical model | 98 |
| II.4.2 | Results: isotropic elasticity assumption | 101 |
| II.4.3 | Results: transversely isotropic elasticity assumption | 103 |
| II.5 | Conclusions | 104 |

II.1 Multi-scale approach for contact modelling considering material heterogeneity

As mentioned earlier, heterogeneous friction material modelling is the aim of this work. As shown in the previous chapter, material heterogeneity scale is very relevant and affects braking performances. Therefore, a consistent modelling is proposed in order to consider all the material complexity. A homogenization multi-scale-based method is chosen for this purpose, like in [Feyel and Chaboche, 2000; Peillex et al., 2008; Mbodj et al., 2010; Nhu, 2013].

The strategy adopted for material heterogeneity modelling is illustrated in Figure II.1. Thus, the multi-scale approach, which is described on the Figure II.1, is based on 3 steps:

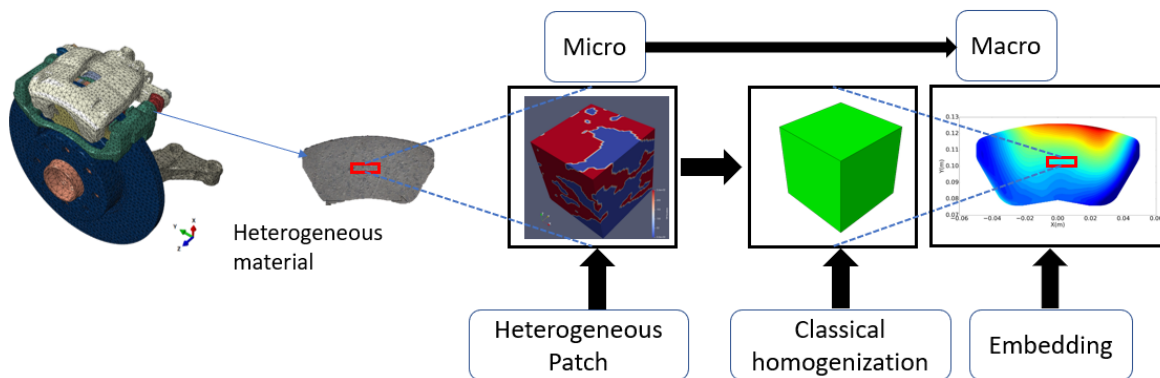


Figure II.1 – Multiscale strategy for contact modelling based on classical homogenization: macro to micro embedding.

Firstly, a discretization of the whole heterogeneous material into a set of cubical heterogeneous patches is done. By discretizing the whole heterogeneous structure, the choice of a Representative Volume Element (RVE) is no longer a necessity. Therefore, the notion of RVE is not discussed in this work.

Secondly, an overall behaviour of each heterogeneous patch is obtained by the means of the classical homogenization method described later.

Thirdly, the effective property, of each heterogeneous patch, obtained by the classical homogenization is enriched at the macroscale level in terms of behaviour. Then a computation is performed to determine the macroscopic mechanical fields.

The enrichment homogenization method is based on the numerical homogenization used in the work of [Lejeunes and Bourgeois, 2011; Peillex et al., 2008; Mbodj et al., 2010; Nhu, 2013], which consists in modelling RVE and extracting its effective properties. However, in this work, instead of RVE, the equivalent properties of each discretized patch is extracted. There are many boundary conditions: the Kinematic Uniform Boundary Conditions (**KUBC**), the Stress Uniform Boundary Conditions (**SUBC**) and the Periodic Boundary Conditions (**PBC**), etc. The classical homogenization theories are presented in the following section.

II.1.1 Classical homogenization theories

After choosing a Representative Volume Element (RVE) which is representative of the whole heterogeneous material, the effective behaviour is determined. We denote V the domain, ∂V the boundary and $|V|$ the volume of the RVE. Once the exact micro fields in the patch, σ_{ij} and ϵ_{ij} , under the applied boundary conditions, are obtained, the averaged stresses and strains are computed from (II.1) and (II.2):

$$\bar{\sigma}_{ij} = \frac{1}{|V|} \int_V \sigma_{ij} dV, \quad (\text{II.1})$$

$$\bar{\epsilon}_{ij} = \frac{1}{|V|} \int_V \epsilon_{ij} dV. \quad (\text{II.2})$$

Considering linear elasticity, using the generalized Hooke's law, the effective stiffness (C_{ijkl}) and the effective compliance (S_{ijkl}) for the homogenized heterogeneous material are determined from (II.3) and (II.4):

$$\bar{\sigma}_{ij} = C_{ijkl} \bar{\epsilon}_{kl}, \quad (\text{II.3})$$

$$\bar{\epsilon}_{ij} = S_{ijkl} \bar{\sigma}_{kl}. \quad (\text{II.4})$$

With regard to the equations (II.3) and (II.4), computation of the effective behaviour of the heterogeneous material seems simple. However, the boundary conditions and the model geometry are important factors, when using analytical methods, in order to obtain good approximations of the stress and strain fields σ_{ij} and ϵ_{ij} respectively. Nevertheless, the use of numerical methods such as FEM bypass these restrictions. In the following, three boundary conditions are presented.

1. Kinematic Uniform Boundary Conditions

The Kinematic Uniform Boundary Conditions (**KUBC**) is a numerical technique which ensures in the boundary of a RVE a uniform strain, and the solutions of the stress and strain fields in the RVE are computed by the means of finite element method. No restriction is imposed on the material behaviour law. The **KUBC** problem is presented in (II.5):

$$\begin{cases} \operatorname{div} \sigma(x) = 0 \text{ in } V, \\ u(x) - \bar{\epsilon} \cdot x = 0 \text{ in } \partial V, \\ \bar{\epsilon} = \bar{\epsilon}^d \end{cases} \quad (\text{II.5})$$

where $\bar{\epsilon}^d$ is the imposed mean strain.

The total strain energy U stored in the volume V of the effective heterogeneous material is computed from (II.6):

$$U = \frac{1}{2} \bar{\sigma} \bar{\epsilon} |V|. \quad (\text{II.6})$$

The total strain energy U' stored in the volume V of the heterogeneous material is shown in (II.7):

$$U' = \frac{1}{2} \int_V \sigma \epsilon dV. \quad (\text{II.7})$$

Using the equilibrium equation, we show that the strain energy $U = U'$. Therefore, the KUBC problem is computed from (II.8):

$$\forall u, \forall \bar{\epsilon} \mid u(x) - \bar{\epsilon} \cdot x = 0 \text{ in } \partial V, \int_V \sigma \epsilon(u) dV = \bar{\sigma} \bar{\epsilon} \mid V \mid. \quad (\text{II.8})$$

2. Stress Uniform Boundary Conditions

The Stress Uniform Boundary Conditions (**SUBC**) ensures a uniform stress in the boundary of RVE. The SUBC problem is solved from (II.9):

$$\begin{cases} \text{div} \sigma(x) = 0 \text{ in } V, \\ \sigma(x) - \bar{\sigma} = 0 \text{ in } \partial V, \\ \bar{\sigma} = \bar{\sigma}^d, \end{cases} \quad (\text{II.9})$$

where $\bar{\sigma}^d$ is the imposed mean stress.

Using the same principle described for the KUBC, we show that the equation (II.9) can be described as in (II.10):

$$\forall u, \forall \bar{\epsilon} \mid \sigma(x) - \bar{\sigma} = 0 \text{ in } \partial V, \int_V \sigma \epsilon dV = \bar{\sigma} \bar{\epsilon} \mid V \mid. \quad (\text{II.10})$$

3. Periodic Boundary Conditions

The Periodic Boundary Conditions (**PBC**) is devoted for periodic microstructure. PBC enforces in REV boundary a periodic displacement field illustrated in (II.11):

$$u^+ - u^- = \bar{\epsilon}(x^+ - x^-) \quad (\text{II.11})$$

where u is the micro-scale displacement field, the exponents $+$ and $-$ are associated with node indices on opposite sides of the REV. The PBC problem is summarized in (II.12):

$$\forall u, \forall \bar{\epsilon} \mid u^+ - u^- = \bar{\epsilon}(x^+ - x^-) \text{ in } \partial V, \int_V \sigma \epsilon(u) dV = \bar{\sigma} \bar{\epsilon} \mid V \mid. \quad (\text{II.12})$$

The use of periodic boundary conditions requires the same mesh between two opposite sides of the REV.

In the following, our enrichment method proposed in this work, is illustrated. The proposed strategy is based on the **KUBC** boundary conditions because of its easiness and convergence facility.

II.1.2 Equivalent quantities computation using KUBC

The **KUBC** problem was presented in (II.5). Isotropic linear elastic material is considered for this purpose. FEM is used for numerical resolution. Two types of boundary conditions can be distinguished for effective properties computation: the traction (in the three directions) and the shear (in the three dimensions) boundary conditions referenced respectively as **bulk** and **shear** boundary conditions.

Therefore, macro strain (E_{XX}, E_{YY}, E_{ZZ}) are applied as boundary conditions of the patch for bulk computation. Then, the displacements (U_X, U_Y, U_Z) field of the heterogeneous patch is computed from (II.13):

$$\begin{bmatrix} U_X \\ U_Y \\ U_Z \end{bmatrix} = \begin{bmatrix} E_{XX} & 0 & 0 \\ 0 & E_{YY} & 0 \\ 0 & 0 & E_{ZZ} \end{bmatrix} \begin{bmatrix} X \\ Y \\ Z \end{bmatrix}, \quad (\text{II.13})$$

with $\begin{bmatrix} X \\ Y \\ Z \end{bmatrix}$ a vector of nodal coordinates.

Subsequently, macro shear strain (E_{XY}, E_{XZ}, E_{YZ}) are applied as boundary conditions of the heterogeneous patch. The displacements (U_X, U_Y, U_Z) field are computed from (II.14):

$$\begin{bmatrix} U_X \\ U_Y \\ U_Z \end{bmatrix} = \begin{bmatrix} 0 & E_{XY} & E_{XZ} \\ E_{XY} & 0 & E_{YZ} \\ E_{XZ} & E_{YZ} & 0 \end{bmatrix} \begin{bmatrix} X \\ Y \\ Z \end{bmatrix}. \quad (\text{II.14})$$

Once the exact micro fields in the patch, σ_{ij} and ϵ_{ij} , under the applied boundary conditions, are obtained, the averaged stresses and strains are computed over the patch from (II.15) and (II.16):

$$\bar{\sigma}_{ij} = \frac{1}{|V|} \int_V \sigma_{ij} dV, \quad (\text{II.15})$$

$$\bar{\epsilon}_{ij} = \frac{1}{|V|} \int_V \epsilon_{ij} dV. \quad (\text{II.16})$$

In order to determine the effective modulus, equations (II.15) and (II.16) are used for the bulk and shear modulus computation.

The bulk modulus K is described in equation (II.17):

$$K = (\bar{\sigma}_{11} + \bar{\sigma}_{22} + \bar{\sigma}_{33})/3(\bar{\epsilon}_{11} + \bar{\epsilon}_{22} + \bar{\epsilon}_{33}), \quad (\text{II.17})$$

The shear modulus G is obtained from equation (II.18):

$$G = (\bar{\sigma}_{12} + \bar{\sigma}_{13} + \bar{\sigma}_{23})/(\bar{\epsilon}_{12} + \bar{\epsilon}_{13} + \bar{\epsilon}_{23}). \quad (\text{II.18})$$

Using equations (II.17) and (II.18), Young's modulus (\bar{E}) and Poisson's ratio ($\bar{\nu}$) are deduced from (II.19) and (II.20) respectively:

$$\bar{E} = (9KG)/(3K + G), \quad (\text{II.19})$$

$$\bar{\nu} = (3K - 2G)/(6K + 2G). \quad (\text{II.20})$$

In the following subsection, multi-scale approach based on KUBC is implemented and compared to explicit results, considering a complete brake model.

II.1.3 Numerical example: Multi-scale problem

In this subsection, a multi-scale problem is investigated considering a numerical approach. A 3D FEM model is inspired by the experimental pin-on-disc system developed in [Duboc, 2013]. The numerical model, shown in Figure II.2, is composed of a steel disc, a friction pin, two steel pin-housing and a steel thin plate. The outer and inner radius of the disc are 107.5 mm and 12.5 mm respectively.

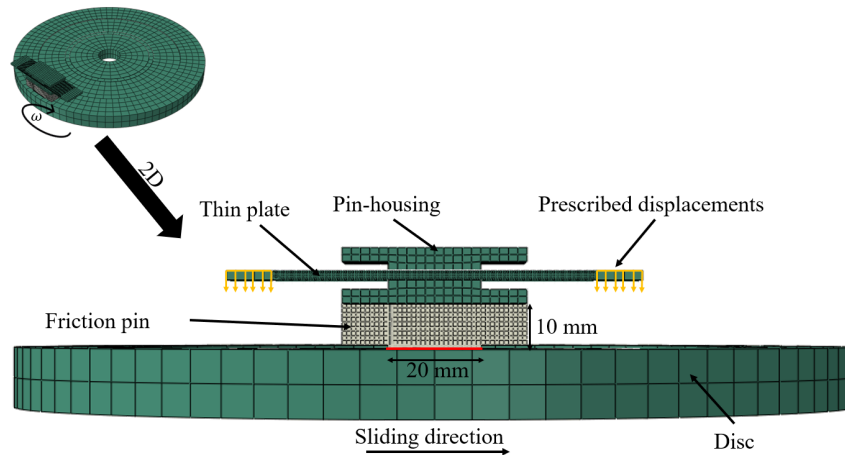


Figure II.2 – Pin-on-disc numerical model representation and its boundary conditions.

A prescribed displacement of 0.2 mm is applied at the extremities of the thin plate which enforces contact between the pin and the disc at a time period of $t = 1 \text{ s}$. The lateral displacements of the plateau's extremities are fixed. Moreover, the disc is rotating with a constant velocity of 0.1 rad/s . The contact surface of the pin is flat with $20 * 20 \text{ mm}^2$ of dimensions. In this work, the friction pin contains one inclusion near the inner side of the leading edge of the contact surface. The model is illustrated in the Figure II.3.

Figure II.3 shows a heterogeneous patch, containing a spherical inclusion located at the leading edge of the friction pad. In fact, the leading edge is generally submitted to high stresses and therefore heterogeneity effects will be more highlighted there. This justify the location of the inclusion.

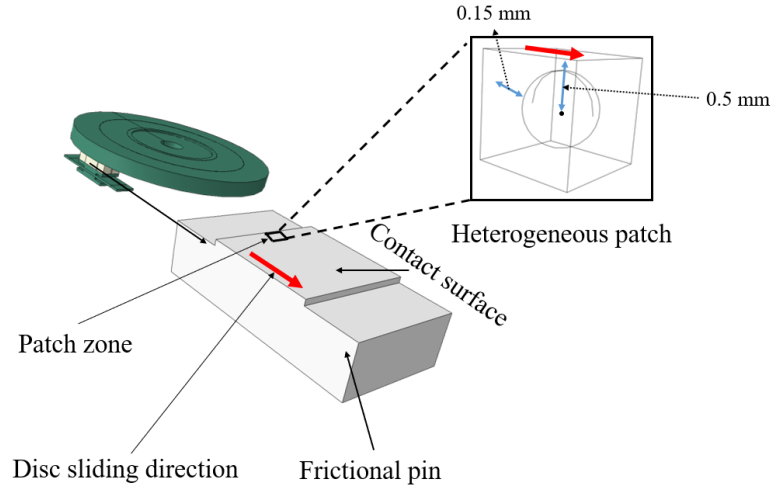


Figure II.3 – Heterogeneous pin including a spherical inclusion at the inner side of the leading edge: the inclusion is shown in cubical patch which is a part of the pin.

Furthermore, a spherical inclusion is chosen for simplicity. In first approach, it is better to choose a simple case in order to test the proposed multi-scale strategy. The spherical inclusion, of radius 0.35 mm is positioned at 0.5 mm from its centre to the contact surface and is made of steel.

Tie elements are used between inclusion and the pin, the pin and the plate, and the pin-housing and the plate in order to ensure continuity between all these components. Material properties of all the components are reported in Table III.13. Inclusion is chosen to be stiffer (200000 MPa) because some friction material particles are very stiff like fibers or ceramics. Moreover, Young modulus of the matrix is obtained from [Magnier et al., 2014].

Table II.1 – Elastic properties for the materials: large scale model.

| | Young's modulus (MPa) | Poisson's ratio |
|---------------------------|-----------------------|-----------------|
| Friction pin | 3000 | 0.3 |
| Inclusion | 200000 | 0.3 |
| Disc and other components | 220000 | 0.3 |

All simulations are performed by the commercial Finite element code ABAQUS with 10 CPU cores. Two types of models are proposed here:

- The first, called later "explicit method", is based on the conventional method where the inclusion is explicitly meshed. This will be the reference solution in this work. For contact constraints resolution, in this work, we shall focus on regularization methods currently utilized in Finite element codes. Three methods are often used: penalty method [Kikuchi and Song, 1981], Lagrange multipliers [Chaudhary and Bathe, 1986] and augmented Lagrangian method [Hestenes, 1969; Powell, 1978;

[Simo and Laursen, 1992]. Even if the penalty method allows a penetration between contacted bodies, it is chosen in this work because of its multi-scale embedded nature [Waddad et al., 2016]. Indeed, it will allow to enrich large scale numerical model with some contact laws traducing micro contact evolution as roughness or surface plateaux [Waddad et al., 2016]. Therefore, in this work, frictional contact is solved by the penalty method. Friction coefficient is set to 0.3. The complete model is meshed with 155447 hexahedrons elements and 175859 nodes. The inclusion is meshed with 13440 hexahedrons elements with 0.033 mm of mesh size. The heterogeneous patch is meshed with 48120 hexahedrons elements with a mesh size of 0.033 mm .

- The second model is based on the KUBC homogenization method presented in the previous section. The heterogeneous problem, where spherical inclusion is centred within the square of 1 mm^3 volume, is replaced by a homogeneous problem. In other words, the heterogeneous patch is replaced by a homogeneous cube enriched by an effective module obtained from KUBC homogenization method (see Figure II.4). The homogeneous enriched patch is meshed with 27000 hexahedrons elements with 0.033 mm of mesh size.

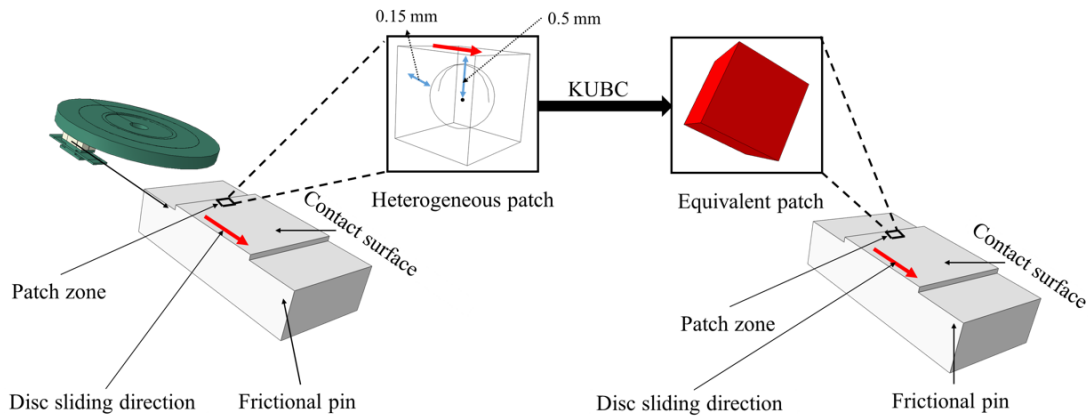


Figure II.4 – Macroscale embedding strategy based on KUBC homogenization method: heterogeneous patch is replaced by homogeneous one in the embedded model.

II.1.3.1 Explicit method results

Explicit model results are illustrated in this subsection. Contact between the disc and the pin is our main interest. Therefore in this work, the contact pressure distribution over the contact surface of the pin is presented. Two cases are distinguished and discussed: Heterogeneous compared to homogeneous cases where the inclusion material property is the same as the matrix, making then the whole frictionnal material homogeneous. Results are shown, for time period $t = 1 \text{ s}$, in Figure II.5.

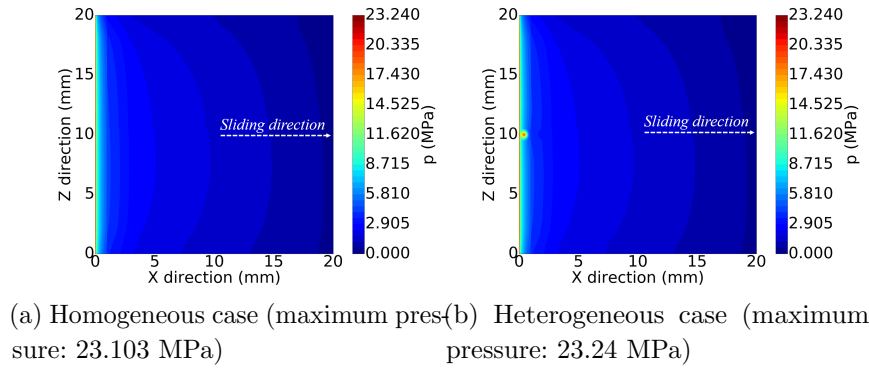


Figure II.5 – Contact pressure distribution at the contact surface of the frictional pin for two cases: homogeneous and heterogeneous explicit models.

Figure II.6 shows a zoom of the contact pressure distribution in the heterogeneous patch area.

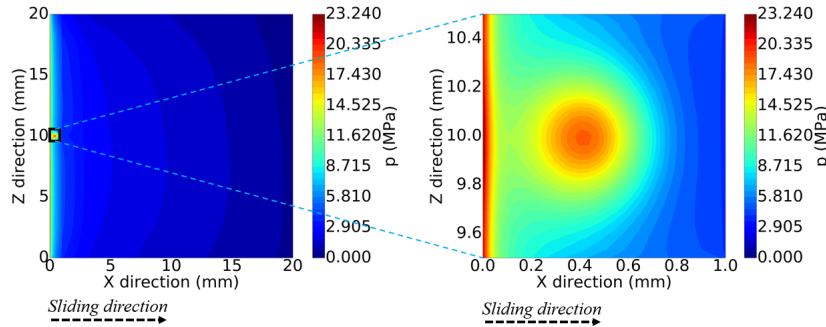


Figure II.6 – Zoom of the contact pressure distribution in the patch area: explicit model

X and Z represent respectively the sliding and the transverse directions. Contact pressure distribution, for all contact surface, in the presence of the inclusion is represented in Figure II.5 (b). Facing each other on the Figure II.5 (a) is presented a case where the patch inclusion has a property of 3000 MPa , thus making the friction material completely homogeneous. Figure II.5 (a) shows a conventional pressure distribution where the maximum value is reached on the leading edge of the pin and decreases with the sliding direction. At the back of the pin, contact separation is observed. The maximum contact pressure between the two models is almost the same and is reached at the leading edge. In Figure II.5 (a), in the patch area, the contact pressure evolution is uniform. However, Figure II.5 (b) shows a contact pressure localization at the centre of the patch due to the spherical rigid inclusion. The introduction of an inclusion disrupts the pressure distribution which is concentrated on the area where the spherical inclusion is placed. Logically, there is a spherical pressure distribution which is related to the inclusion geometry. Next, the explicit method and the multi-scale strategy, based on KUBC, results are confronted.

II.1.3.2 KUBC versus explicit method

Two results are compared here: the explicit method, presented in the previous subsection, and the multi-scale strategy described in Figure II.1. As mentioned earlier, the core of this strategy is the homogenization method based on KUBC. In the following, the numerical complete brake model of the Figure II.2, is implemented through multi-scale homogenization approach:

1. KUBC homogenization results

Figure II.7 shows the actual step which is implemented here.

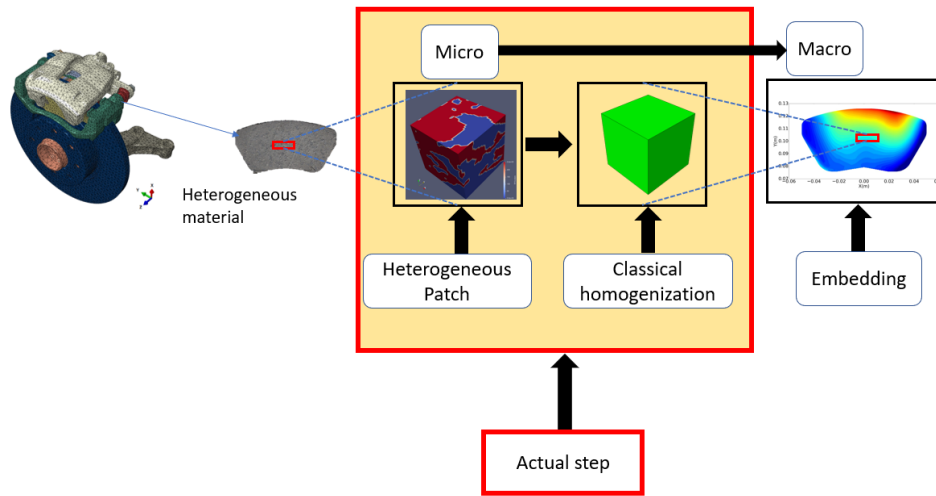


Figure II.7 – Multiscale strategy: homogenization step.

The heterogeneous frictional pin considered in Figure II.2, is composed of a heterogeneous patch which is used in part of the homogenization process.

As mentioned earlier, the heterogeneous patch is composed of an elastic isotropic cubic patch, of 1 mm^3 of size, with a centred inclusion of radius 0.35 mm at 0.15 mm from the contact surface. The constitutive law of the inclusion material is elastic isotropic. The material properties of the heterogeneous two phases patch are summarized in Table III.12:

Table II.2 – Elastic properties for the materials

| | Matrix | Inclusion |
|-----------------------|--------|-----------|
| Young's modulus (MPa) | 3000 | 200000 |
| Poisson's ratio | 0.3 | 0.3 |

The matrix and the inclusion are meshed with 8-node linear brick elements. Moreover, the complete model is meshed with 49528 hexahedrons elements and 53761 nodes. The KUBC model is illustrated in Figure II.8.

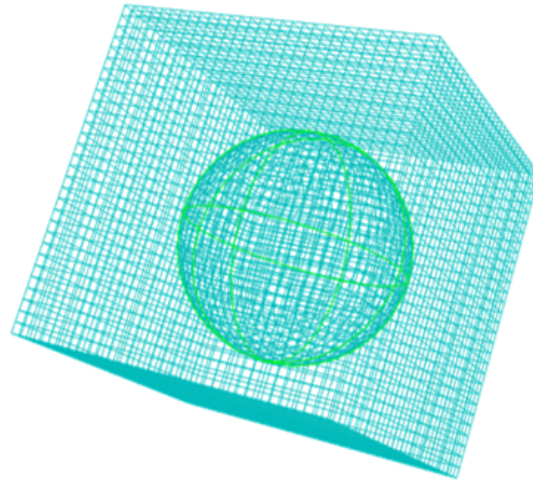


Figure II.8 – KUBC model: spherical inclusion centred in the cubical part.

Macro hydrostatic strains (0.01, 0.01, 0.01) are applied as boundary conditions of the patch for bulk computation. The applied displacement field (U_X, U_Y, U_Z) in the boundaries of the heterogeneous patch is computed from equation (II.13).

Macro shear strains (0.005, 0.005, 0.005) are applied as boundary conditions of the heterogeneous patch. In the latter case, the displacement field (U_X, U_Y, U_Z) in the boundaries of the patch is computed from (II.14).

KUBC boundary conditions have been applied, at each node of the boundary of the heterogeneous patch, through a set of python routines.

From equation (II.15) to (II.20), bulk modulus, shear modulus, Young's modulus and Poisson's ratio are computed.

Before presenting the equivalent quantities, stresses resulting from bulk and shear computation are shown in Figure II.9.

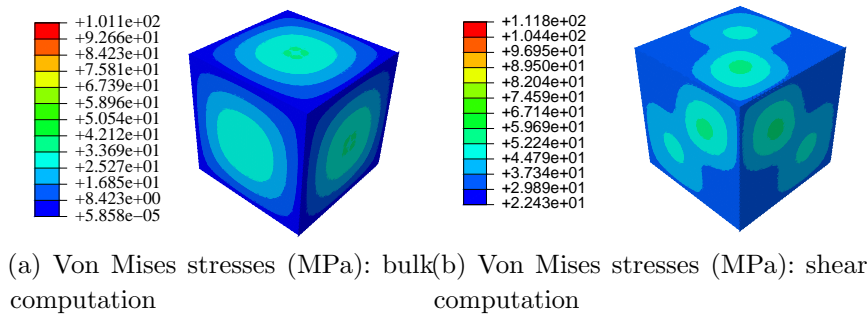


Figure II.9 – Stresses distribution for bulk and shear computation : KUBC homogenization method

In Figure II.9 (a), the linear distribution of equation (II.13) implies symmetrical stress distribution over the entire patch. Stress distribution of Figure II.9 (b) is the result of simple shear apply, in equation (II.14), as boundary conditions. Once

bulk and shear stresses are obtained, effective quantities are deduced from equations (II.15) to (II.20).

Mesh convergence study has been carried out. Different mesh size has been used from coarse to fine mesh. Young's modulus evolution is plotted against total number of elements of the heterogeneous patch. Results are illustrated in Figure II.10:

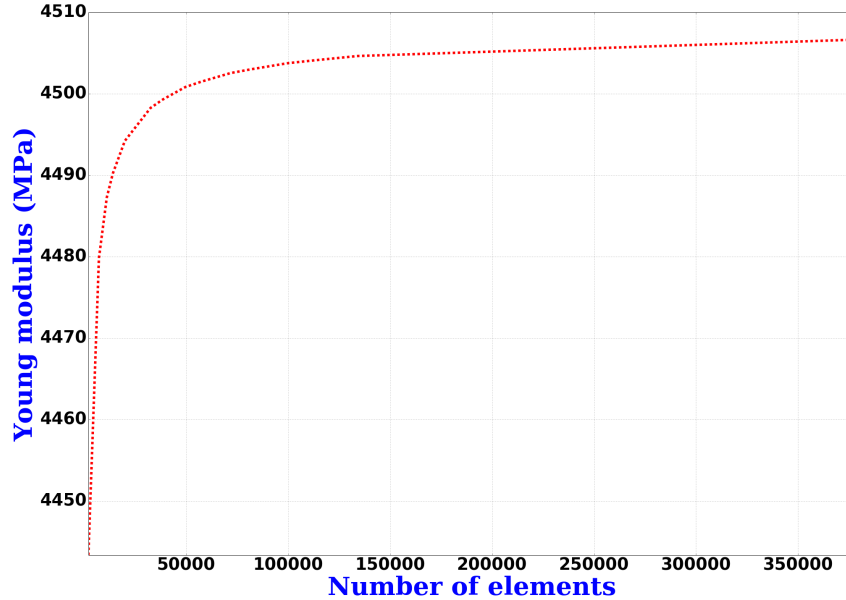


Figure II.10 – Mesh density convergence study.

Figure II.10 presents Young's modulus evolution in terms of mesh density in the heterogeneous patch volume. The curve converges from 49528 finite elements. Therefore, this mesh configuration is kept for all homogenization procedure in this work. Homogenization quantities results are summarized in Table II.3. These properties

Table II.3 – Effective properties computation through KUBC homogenization.

| | Bulk modulus | shear modulus | Young's modulus | Poisson's ratio |
|------|--------------|---------------|-----------------|-----------------|
| KUBC | 3387 MPa | 1760 MPa | 4501 MPa | 0.28 |

(Table II.3) are reinjected into the macroscopic calculation in order to compute the macro mechanical fields.

2. The macroscale embedded result

Figure II.11 shows the actual step of the multi-scale strategy and is explained in the following.

Effective modulus obtained in Table II.3 is used to enrich the macro patch according to Figure II.4. The same model configuration as described in Figure II.2 is used. The heterogeneous patch containing the spherical inclusion is replaced by a homogeneous patch of the same volume. The complete model is meshed with 134971 hexahedrons

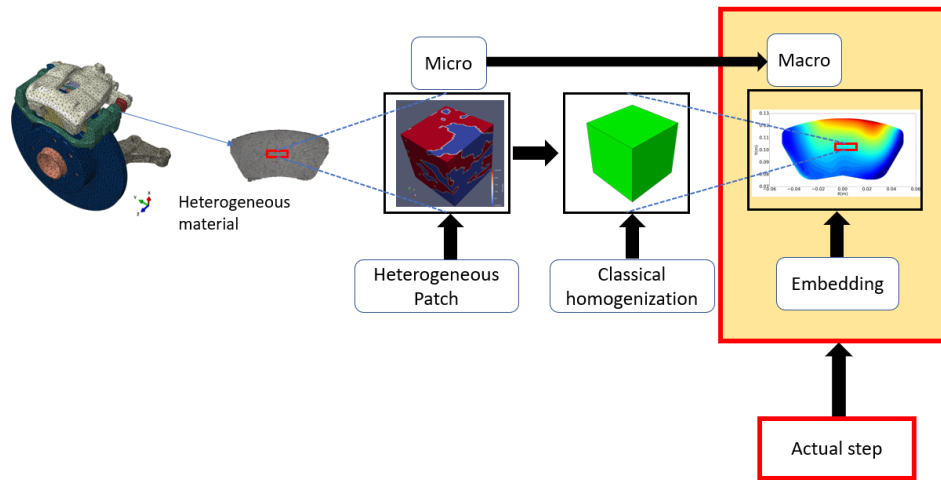


Figure II.11 – Multiscale strategy: micro to macro embedding.

elements and 154092 nodes (the embedded macro patch is the more refined: 900 hexahedrons elements and 961 nodes). Results are presented in Figure II.12.

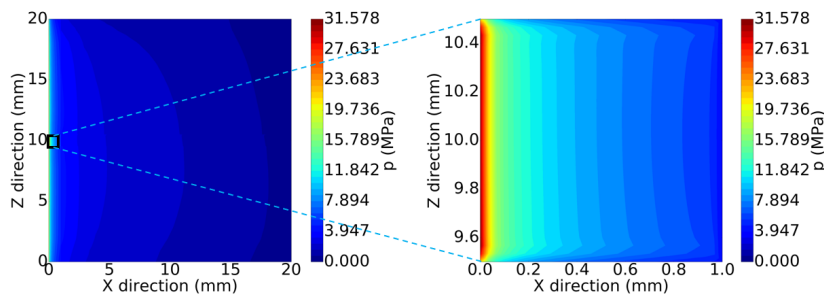


Figure II.12 – Contact pressure distribution of the macro embedded model.

Contact pressure distribution is conventional, the maximum contact pressure is reached at the leading edge of the contact surface and decreases with the sliding direction. However, the maximum contact pressure in the patch area is higher due to its higher rigidity in comparison to the rest of the material.

KUBC embedding result is compared to explicit model one in Figure II.13.

Contact pressure evolution, in the patch area, of both enriched and explicit models does not have the same evolution because the inclusion is not physically present. Moreover, in the enriched patch area, maximum contact pressure is higher than explicit pressure. However, the average contact pressure in the patch area of the explicit and enriched models is very close, 6.930 MPa and 7.06 MPa respectively, as shown by the relative error which is 1.87%

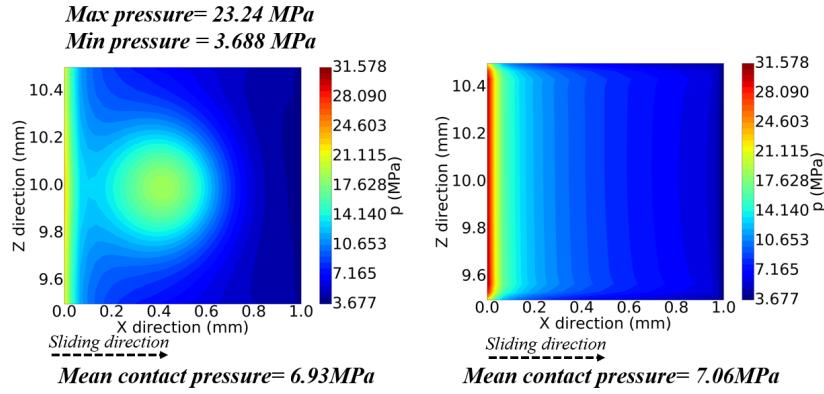


Figure II.13 – Contact pressure distribution: explicit (left) and embedded (right) models.

In this subsection, multi-scale approach based on KUBC homogenization method is presented and compared to the explicit results. The contact pressure distribution in the patch area is not well estimated. The problem is associated to KUBC homogenization method which does not consider the presence of contact constraints in the model. Since contact induces some localizations due to the presence of material heterogeneity, it is necessary to consider contact non linearities in KUBC homogenization method. Therefore, a relocalization of contact stresses can be possible and then better estimations can be expected.

II.1.4 New approach, the homogenization with contact: KUBC-Contact

A multi-scale strategy for contact modelling of heterogeneous material was proposed through a classical homogenization method. It has been shown that, although average mechanical quantities are well estimated, the multi-scale approach based on classical KUBC method cannot estimate mechanical field evolution in the presence of contact constraints. However, in this part, a modified multi-scale approach, inspired from [Feyel and Chaboche, 2000; Peillex et al., 2008; Mbodj et al., 2010; Nhu, 2013], based on new homogenization method (presence of contact interface in each heterogeneous patch) considering contact in the scale of heterogeneities is proposed in Figure II.14:

This multi-scale approach is based on 4 steps: Firstly, a discretization of the whole heterogeneous material into a set of cubical patches is done.

Secondly, an overall behaviour of each patch is obtained by means of a new homogenization method later called **KUBC-Contact**. In this work, an interface of the heterogeneous material is in contact with another material, so one of the faces of each heterogeneous patch is supposed to be in contact with a flat disc in order to consider the non-linearities effects of contact, giving birth to the KUBC-Contact method.

Thirdly, the effective property, of each heterogeneous patch, obtained by KUBC-Contact method is enriched at the macroscale level in terms of behaviour. Then a computation is performed to determine the macroscopic mechanical fields.

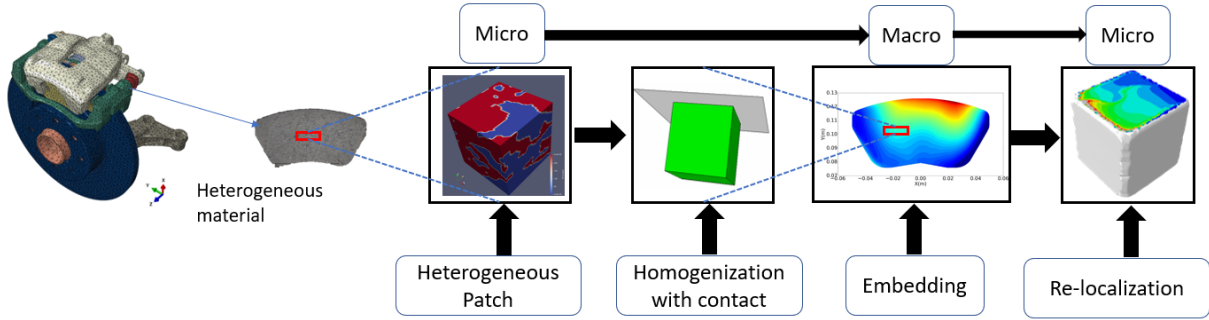


Figure II.14 – Multi-scale strategy for contact modelling of heterogeneous material based on contact homogenization.

Finally, after the macroscopic mechanical fields computation, a macro to micro computation of the mechanical fields is performed using macro contact forces and displacements at the heterogeneous micro patch level.

Compared to [Feyel and Chaboche, 2000; Peillex et al., 2008; Mbodj et al., 2010; Nhu, 2013], the KUBC-Contact homogenization method takes into consideration local contact conditions in the effective properties computation.

II.1.4.1 Contact homogenization: KUBC-Contact

Earlier, three boundary conditions (KUBC, SUBC, PBC), which have largely been used in the literature, were described in the context of heterogeneous material effective properties computation. Nevertheless, these boundary conditions have very different apparent properties, which raise the question of the representativeness of the samples, particularly when an interface of this sample is in contact with another material. Especially if we take the conditions at the known limits, the relocalization of the stresses does not allow us to take into account the engagement effect of the contact, the presence of the friction coefficient, etc. Thus, we propose to take the KUBC boundary conditions on 5 sides of the heterogeneous patch and to introduce on the 6th side a boundary condition with contact. In other words, contact constraints will be imposed on the contact side of the heterogeneous patch. This method will later be called KUBC-Contact. We denote V the domain, ∂V the free boundary, ∂V_c the constraint boundary and $|V|$ the volume of the patch. The KUBC-Contact problem is presented in Figure II.15.

The equations governing the KUBC-Contact method are presented in (II.21):

$$\left\{ \begin{array}{l} \operatorname{div} \sigma(x) = 0 \text{ in } V, \\ u(x) - \bar{\epsilon} \cdot x = 0 \text{ in } \partial V, \\ u_1(x) - \bar{\epsilon} \cdot x = 0 \text{ in } \partial V_c, \\ u_3(x) - \bar{\epsilon} \cdot x = 0 \text{ in } \partial V_c, \\ u_2(x) = U_c(x) \text{ in } \partial V_c, \\ \bar{\epsilon} = \bar{\epsilon}^d. \end{array} \right. , \quad (\text{II.21})$$

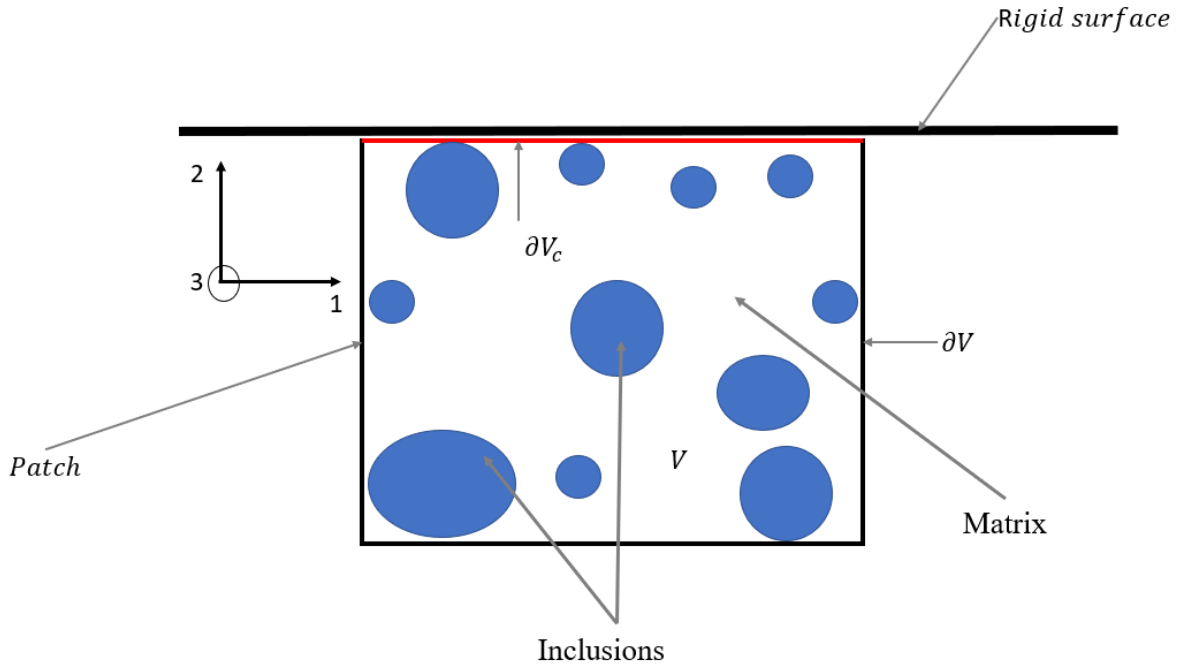


Figure II.15 – KUBC-Contact problem.

where x is a point of the volume of the patch, $\bar{\epsilon}^d$ is the imposed mean strain, and U_c is determined by the contact conditions. In fact, the flat rigid surface displacements are fixed. The subscript 1 and 3 represent the transverse direction and the subscript 2 represents the normal direction. Once the exact micro fields in the patch, σ_{ij} and ϵ_{ij} , under the applied boundary conditions, are obtained, the average stresses and strains are computed from (II.15) and (II.16).

In the context of linear elasticity, bulk and shear modulus are obtained from (II.17) and (II.18) respectively; subsequently leading to Young's modulus (\bar{E}) and Poisson's ratio ($\bar{\nu}$) computation from (II.19) and (II.20) respectively.

These properties will be reinjected into the macroscopic calculation. Once the latter is performed, it will be possible to relocate from macro to micro in order to have a state of local mechanical fields.

In the following, effective properties are estimated using KUBC-Contact and compared to KUBC method.

II.1.4.2 KUBC-Contact versus KUBC

Figure II.16 shows the actual step of the multi-scale strategy implemented in this subsection.

1. KUBC-Contact FEM model description

A flat rigid surface is rubbing on an elastic isotropic cubic patch of 1 mm^3 with a centred inclusion of radius 0.35 mm at 0.15 mm from the contact surface. The constitutive law of the two phases is elastic isotropic. Same material properties, as in

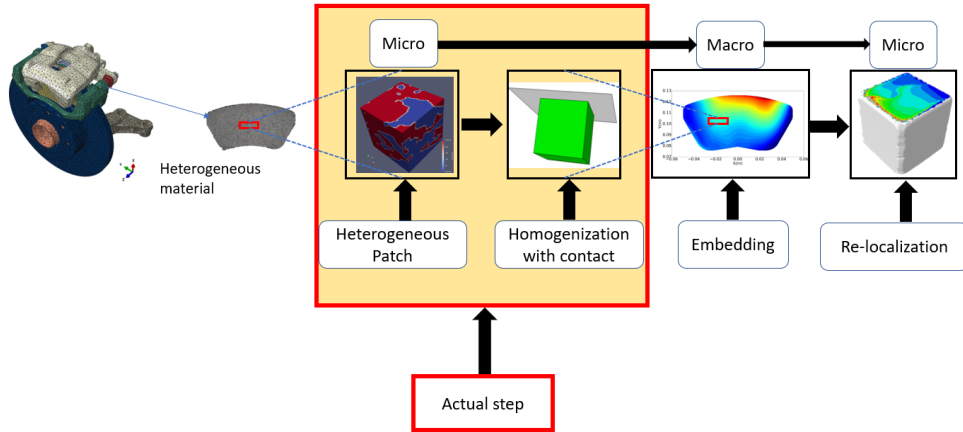


Figure II.16 – Multiscale strategy: homogenization step based on KUBC-Contact.

Table III.12, are considered. The matrix and the inclusion are meshed with 8-node linear brick elements. The disc is meshed with 4-node 3-D bilinear rigid quadrilateral elements. The complete model is meshed with 54090 hexahedrons elements and 59405 nodes. Contact is frictional and penalty contact is used for contact constraints resolution with a friction coefficient of 0.3. The KUBC and KUBC-Contact models are presented in Figure II.17.

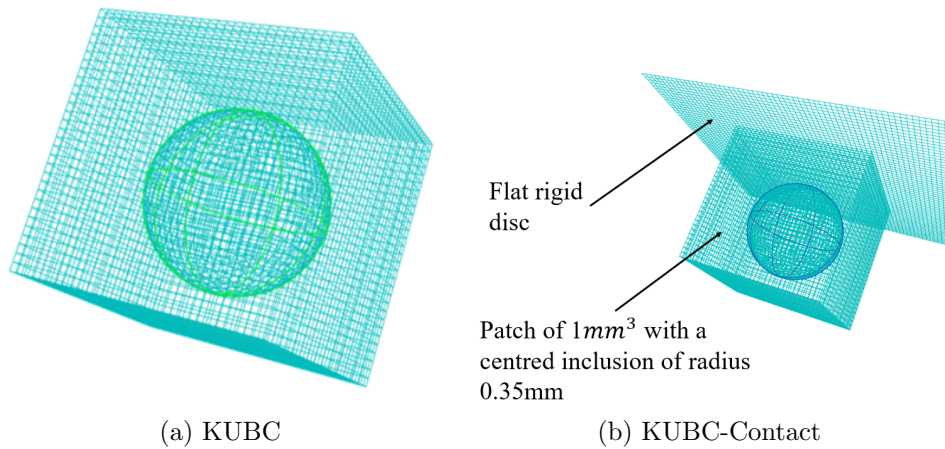


Figure II.17 – KUBC and KUBC-Contact numerical models.

In the following, KUBC-Contact and KUBC results are compared each other.

2. Results

Firstly bulk computation results for both KUBC and KUBC-Contact are illustrated in Figure II.18.

Figure II.18 shows displacements and Von Mises stresses field distribution, compared between KUBC and KUBC-Contact models.

A linear evolution of displacements field for both KUBC and KUBC-Contact models is observed. The applied boundary conditions of (II.13) justifies this evolution.

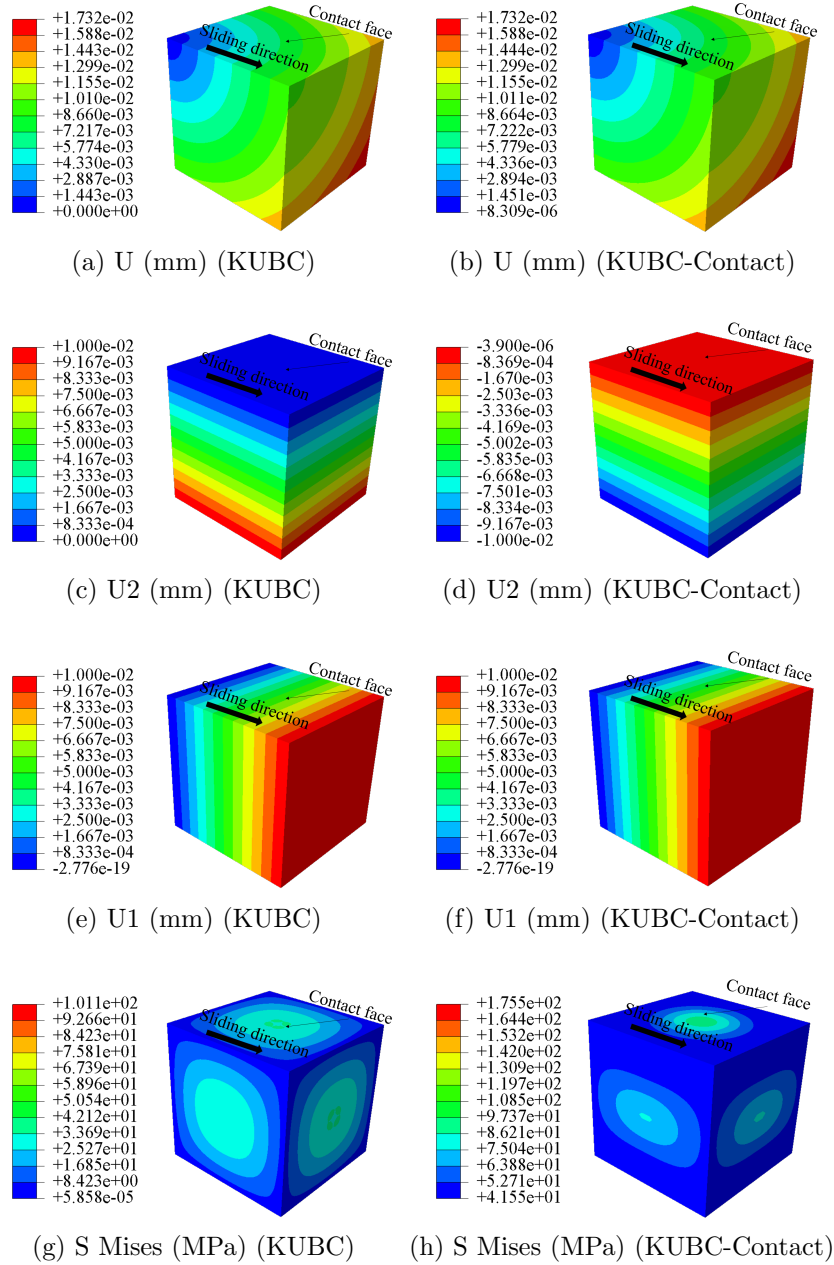


Figure II.18 – Bulk modulus computation: comparison of magnitude of displacements U (mm), normal direction displacements U_2 (mm), sliding direction displacements U_1 (mm) and Von Mises stresses S Mises (MPa) fields between KUBC and KUBC-Contact models.

Figures II.18 (a) and (b) represent a magnitude of displacements field. Between the two models, a similar distribution is obtained. Indeed, the displacements in all faces are prescribed except the normal direction displacement (U_2) at the contact face. This justifies the small difference of the magnitude of displacement obtained in that face, between both KUBC and KUBC-Contact models. However, even if the magnitude of displacements is similar, the normal direction displacements (U_2) field for both models are not equivalent. In that direction, a traction is applied for KUBC

($U_2 > 0$) while a compression is applied for KUBC-Contact ($U_2 < 0$) as seen in Figures II.18 (c) and (d).

For Von Mises stresses, a symmetrical distribution is obtained for KUBC while results are asymmetrical for KUBC-Contact. This is a consequence of the contact interface which disrupts stresses distribution. In fact, as the normal displacements in the contact interface is not prescribed for KUBC-Contact and due to the compression in that direction, the normal strain distribution will be different between the two configurations as shown in Figures II.19 (a) and (b). Consequently, the stresses computation will be different. This justifies the differences obtained in Von Mises stresses distribution. Furthermore, one can notice that, the Von Mises stresses intensity for KUBC-Contact model is higher than KUBC. This is the consequence of the compressive normal direction strain applied for KUBC-Contact. Then, the KUBC-Contact normal direction stresses will be smaller than KUBC. As a result, using the Von Mises criterion, the KUBC-Contact Von Mises stresses will be higher than the KUBC ones.

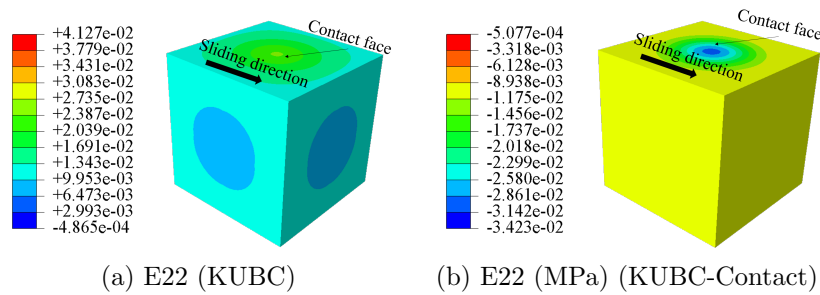


Figure II.19 – Bulk modulus computation: strain in the normal direction (E22) comparison between KUBC and KUBC-Contact models.

Maximum stresses are observed at the matrix-inclusion interface and at the inclusion volume for KUBC-Contact. While, for KUBC model, the stress localization is observed at the matrix-inclusion interface only. In fact, the stresses in the inclusion volume are few (see Figure II.20). The compressive stresses of the KUBC-Contact model justify the obtained differences.

Secondly, shear computation results for both KUBC and KUBC-Contact are illustrated in Figure II.21.

Figure II.21 shows stresses field distribution for shear modulus computation. KUBC-Contact and KUBC results are compared to each other and the same scale is used. Maximum and minimum Von Mises stresses, for KUBC-Contact model, are 670.3 MPa and 18.16 MPa respectively. Figure II.21 (a) shows simple shear stresses involving symmetrical distribution while Figure II.21 (b) is a general shear exhibiting asymmetrical evolution. Moreover, in Figure II.21 (b), stresses are localized near contact interface due to shear displacements at this face.

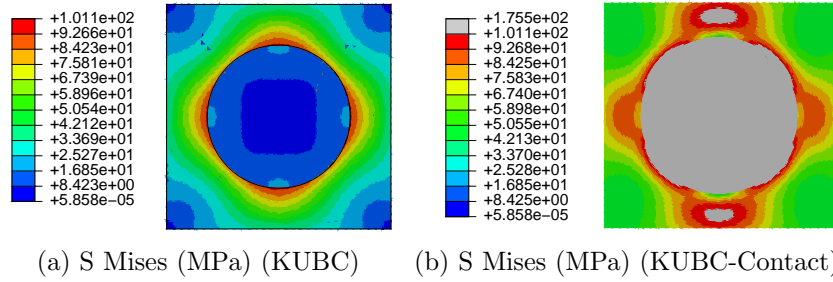


Figure II.20 – Bulk modulus computation: In plane Von Mises stresses (S Mises) field comparison between KUBC and KUBC-Contact models.

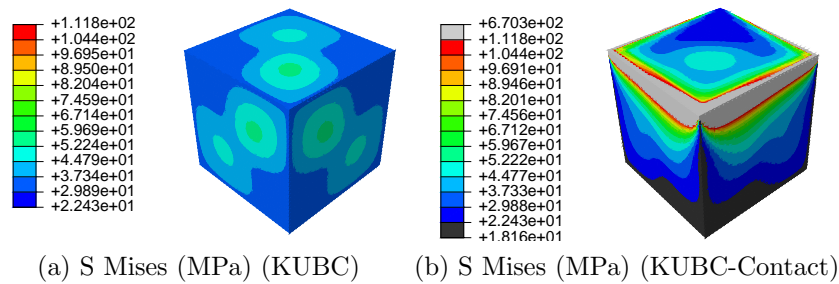


Figure II.21 – Shear modulus computation: Von Mises stresses (S Mises) field comparison between KUBC and KUBC-Contact models.

Once bulk and shear modulus obtained, Effective properties are computed. Results are presented in Table II.4. KUBC-Contact results are in a good agreement with the classical KUBC method. Equivalent Young's modulus obtained from KUBC-Contact is higher than KUBC one. The difference comes from the contact constraints added to the patch surface. Therefore, the new homogenization method has the advantage to account for contact localizations induced by heterogeneities.

Table II.4 – Effective properties computation: KUBC-Contact compared to KUBC homogenization models

| | Bulk modulus | Shear modulus | Young's modulus | Poisson's ratio |
|--------------|--------------|---------------|-----------------|-----------------|
| KUBC | 3387 MPa | 1760 MPa | 4501 MPa | 0.28 |
| KUBC-Contact | 3387 MPa | 1932 MPa | 4870 MPa | 0.26 |

In this part, a new homogenization method having the advantage of considering contact localizations induced by heterogeneities is presented and compared to the classical KUBC method. It allows for the consideration of the engagement effect of contact in the presence of heterogeneities, using the multi-scale approach described in Figure II.14.

In the next subsection, KUBC-Contact is compared to explicit case presented earlier which was the reference results of the numerical complete system considering heterogeneous material (refer to Figure II.2)

II.1.4.3 KUBC-contact versus explicit method

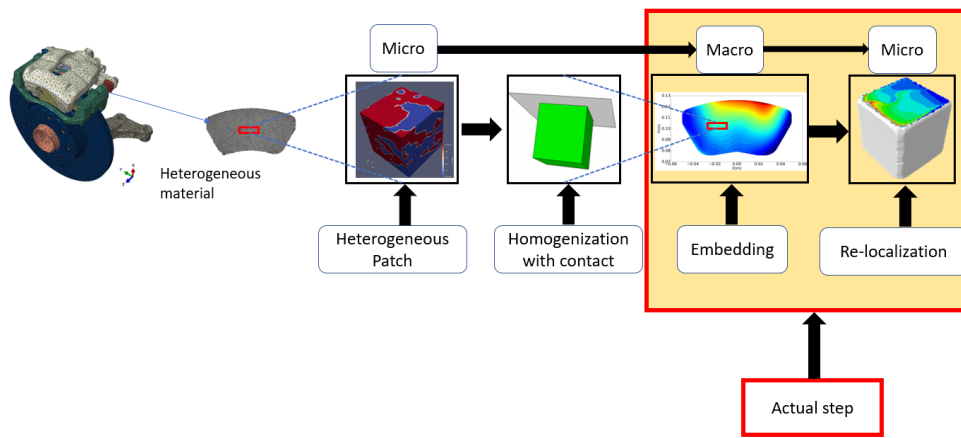


Figure II.22 – Multiscale strategy: micro to macro and macro to micro (thanks to KUBC-Contact) steps where mechanicals field relocalization are performed.

Figure II.22 shows the last steps of the multi-scale strategy, based on KUBC-Contact method, implemented in this subsection.

The 3D FEM model inspired from the experimental pin-on disc system is still considered in this subsection. The same model configuration, as in Figure II.3, is considered. Same material properties (see Table III.13) and boundary conditions are kept. Two models configuration are compared here:

- The reference solution based on the conventional method where the inclusion is explicitly meshed. Contact is frictional and the penalty method is used for contact constraints resolution. Friction coefficient is set to 0.3. The complete model is meshed with 155447 hexahedrons and 175859 nodes.
- The second model is based on the multi-scale strategy presented in Figure II.14. The heterogeneous patch, in the complete model, is replaced by a homogeneous cubic part of the same volume. The effective behaviour of the cubic part is obtained using the KUBC-Contact method (see Figure II.23). The pin-on-disc model is meshed with 134971 hexahedrons and 154092 nodes. Penalty contact with a friction coefficient

of 0.3 is still used for contact constraints resolution. Effective modulus is obtained from Table II.4 and enriched at the macro patch, followed by a macro computation in order to get mechanical fields (refer to Figure II.23).

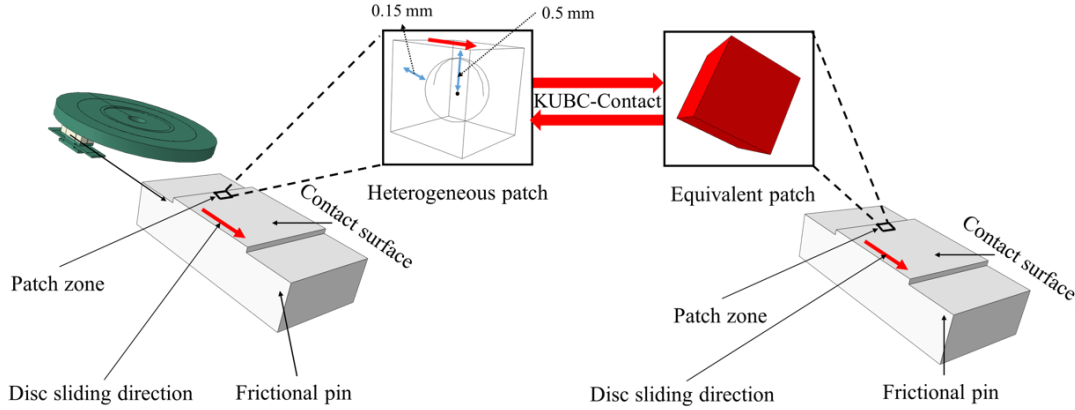


Figure II.23 – Macroscale embedding strategy based on KUBC-Contact.

As previously seen in Figure II.13, contact pressure distribution between explicit and integrated results is different. In all homogenization-based works, this relocalization step (macro to micro) is almost forgotten. However, contact pressure distribution is not well estimated considering just the micro to macro embedding in contact problem. Although the average pressure is the same, a macro to micro strategy, based on the KUBC-Contact model and boundary conditions previously explained, is proposed here in order to obtain a good approximation of the mechanical fields.

After the macroscopic calculation, a relocalization of the mechanical fields is performed. In this relocalization step, macro contact pressure and displacements are reapplied at the microscopic scale. In other words, the macroscopically determined contact pressure and displacements (from macro embedded cubic part) are reinjected at the patch scale where heterogeneity is explicitly represented. This specific boundary conditions and its loadings are shown in Figure II.24.

This relocalization step is very important and makes a big difference between the previous multi-scale approach based on KUBC and the actual strategy based on KUBC-Contact.

Macro to micro strategy, based on macro embedding model boundary conditions and its contact pressure, will refer to the following as micro model.

In the following, two results are illustrated: displacements field and contact pressure evolution in the micro patch area.

Firstly, normal displacements, of the heterogeneous patch boundary, are plotted in Figure II.25.

As seen in Figure II.25, the normal displacement field are negative due to compression between the frictional pin and the disc. In fact, there are prescribed boundary conditions

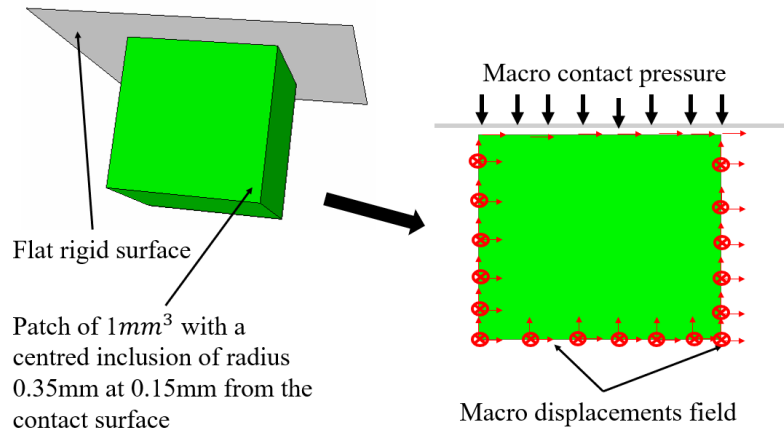


Figure II.24 – 2D representation of the macro to micro boundary conditions: the boundary conditions are obtained from macro embedded model.

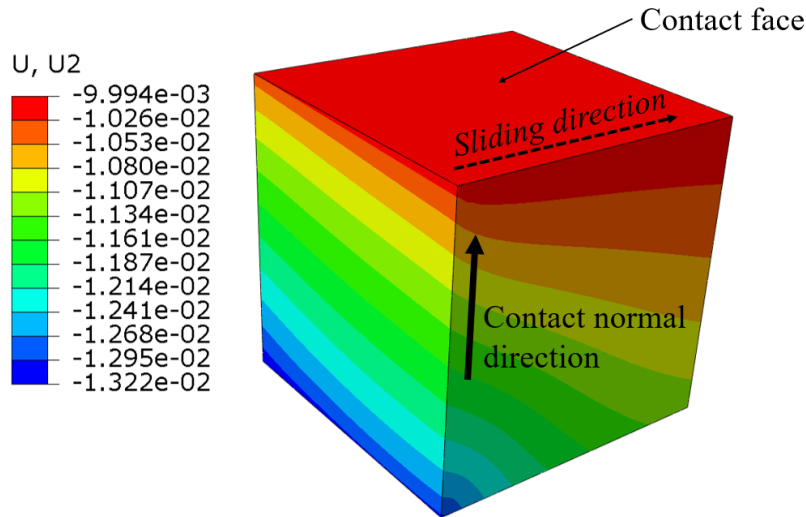


Figure II.25 – Displacement field illustration in the contact normal direction: micro model.

applied at the thin plate extremities in order to enforce contact between the rotating disc and the frictional pin (refer to Figure II.3). Therefore a quite similar distribution of the normal displacement, at the contact face, is obtained.

Secondly, micro model contact pressure result is compared to the explicit contact pressure distribution of the Figure II.6. This result is shown in Figure II.26.

Figure II.26 (a) and Figure II.26 (b) represent contact pressure evolution of explicit and micro models respectively. Figure II.26 (c) shows the relative error between results. Relative error is obtained by computing the ratio between pressure fields difference over explicit pressure. In the central part of the patch and especially at the point where the heterogeneity is located, good approximations are obtained. However, some important errors are found on the edges.

The errors obtained at edges are related to boundary and edges effects which are illustrated in Figure II.27.

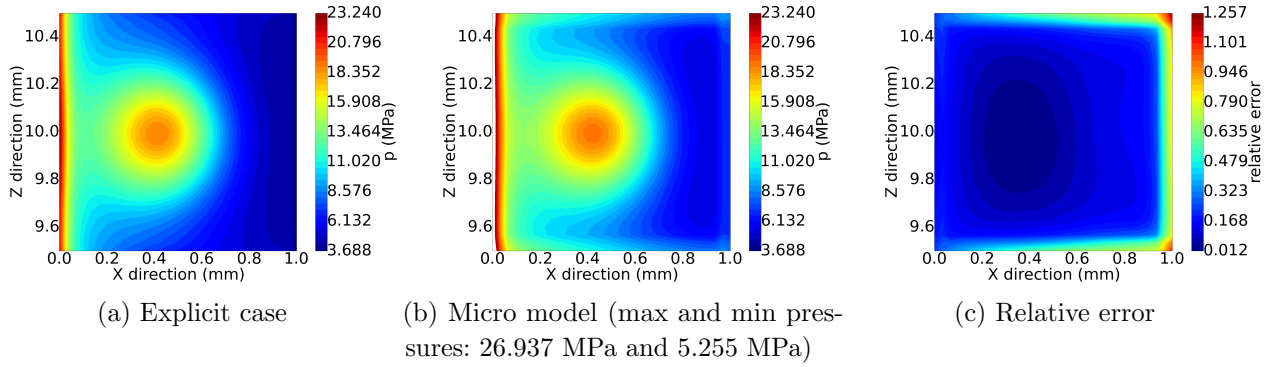


Figure II.26 – Explicit versus macro to micro model contact pressure distribution over the contact surface of the patch: macro to micro model is a part of the multi-scale strategy based on KUBC-Contact.

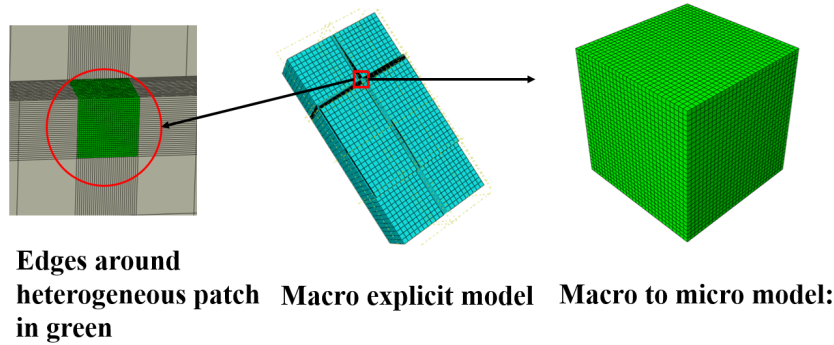


Figure II.27 – Edges effects illustration between the two model configuration: explicit versus multi-scale models.

In the explicit model, the heterogeneous patch is a part of an entire domain. In other words, the heterogeneous patch is surrounded by neighbouring structures as shown in Figure II.27. However, at the micro model level, these surrounded elements, which are present in macro model, do not exist. Moreover, at micro scale, contact is enforced using macro contact force and displacements from macro embedded patch. The problem is that, these macro displacements, may be, do not respect KUBC boundary conditions (five sides of the heterogeneous patch are submitted to KUBC boundary conditions as explained in section II.1.4.1). Hence, the important errors obtained at the edges, in Figure II.26.

In the following, it is proposed to verify the KUBC boundary conditions (II.5), at the boundaries of the micro patch.

Let denote $\mathbf{K} = u(x) - \bar{\epsilon}.x$. After computation of \mathbf{K} , if KUBC boundary conditions are verified, $\mathbf{K} = 0$. Else, \mathbf{K} should be different to 0. Results have been presented, in Figure II.28. Figures II.28 (b) and II.28 (c) show \mathbf{K} distribution over the face 1 and face 2 of the micro heterogeneous patch (Figure II.26 (a)). According to the KUBC hypothesis, this condition should be reduced to zero. However, this hypothesis is not verified. Then, KUBC boundary conditions of the fives sides of the micro patch level, is not verified. The maximum errors are found at contact edges (Figures II.28 (b) and II.28 (c)). This can be

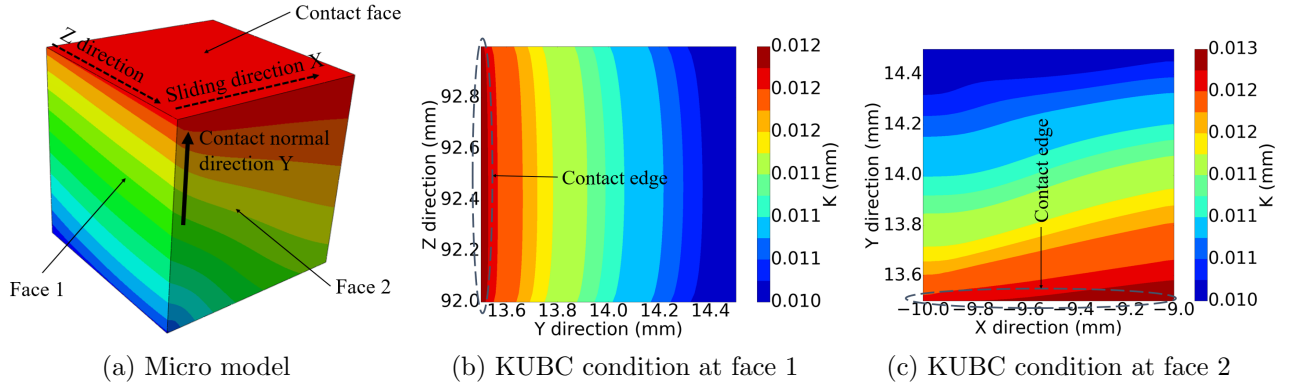


Figure II.28 – KUBC boundary conditions verification in the micro model level.

justified by the errors obtained at the edges, in Figure II.26 (c). Therefore, it is necessary to include boundary effects in the micro model proposed in Figure II.24, in order to have good approximations.

To overcome boundary effects issues, a new micro model boundary is proposed in Figure II.29).

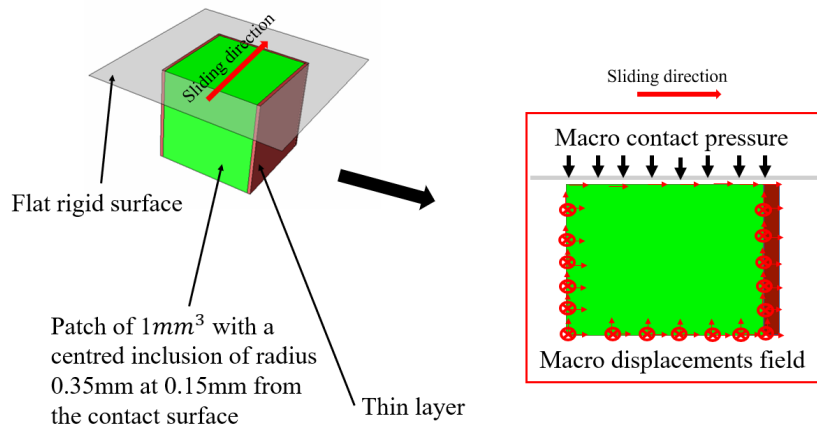


Figure II.29 – New relocation model and its 2D boundary conditions representation: multi-scale strategy based on KUBC-Contact

The idea is to replace the macro neighbouring elements surrounding the heterogeneous explicit patch by a thin layer at the micro model. The boundary conditions of this model are still the same as the ones previously presented in Figure II.24. The thin layer has the same material properties as the homogeneous structure surrounding the explicit heterogeneous patch highlighted in Figure II.27. In this example, the layer size equals to the element mesh size.

Pressure field evolution between explicit and new micro model, incorporating boundary effects, is shown in Figure II.30.

Figures II.30 (a) and (b) show contact pressure distribution for both explicit and new micro model. Figure II.30 (c) shows relative error between the results. As the first micro model, contact pressure obtained via the proposed strategy is in good agreement with

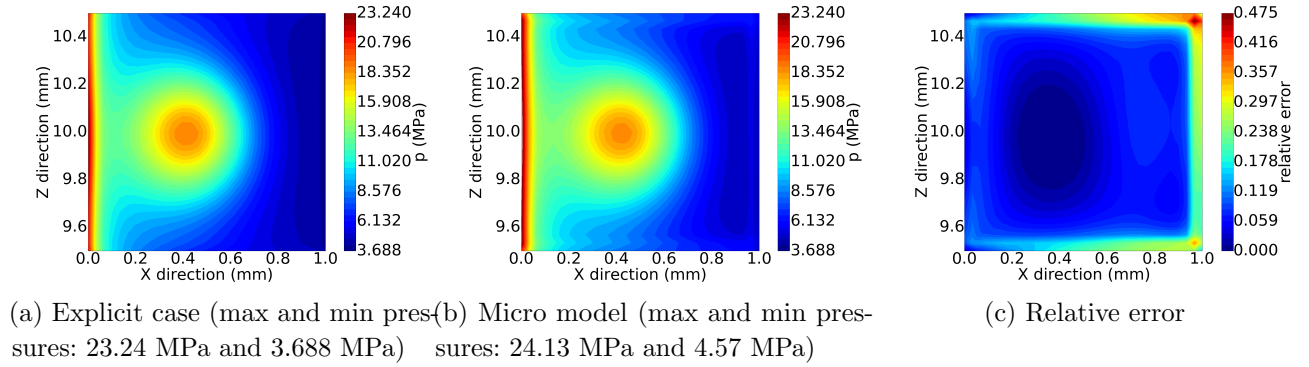


Figure II.30 – Explicit versus multi-scale contact pressure distribution over the patch contact area: micro model with layer incorporating boundaries effects.

the explicit pressure distribution in the central part of the patch (errors are less than 4% in the central part). The most significant errors are located on the edges of the patch. However, compared to the first micro model where edge effects are not considered (Figure II.26), results obtained by the present micro model are better. Errors are very reduced. An illustration is presented, at the leading edge in the Figure II.31:

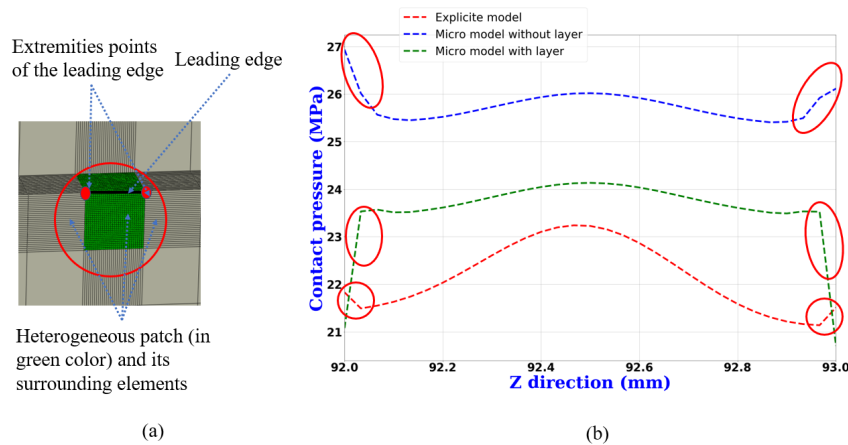


Figure II.31 – Contact pressure distribution between explicit and micro models at the leading edge ($X=0.0$): micro layer with one element mesh size.

Figure II.31 (b) shows contact pressure distribution over the patch contact area, at different nodes of the leading edge, for explicit, micro without layer and micro with layer models. At the leading edges extremities, some jumps in pressure (highlighted in red) are observed for all models. In fact this is due to surrounding macro elements near the heterogeneous patch (Figure II.31 (a)). Results are clear enough: the new micro model with layer, considering boundary effects, shows a good approximation compared to the first micro model where boundary effects are not considered. Compared to the explicit model, results are very satisfying. Edge errors are less than the first micro model.

Using the micro model with a layer, it is possible to improve edges results accuracy by increasing the layer size. Another simulation has been conducted with a layer size higher

than 1 element mesh size. After computation, the contact pressure distribution at different nodes of the leading edge is compared to the explicit results in Figure II.32:

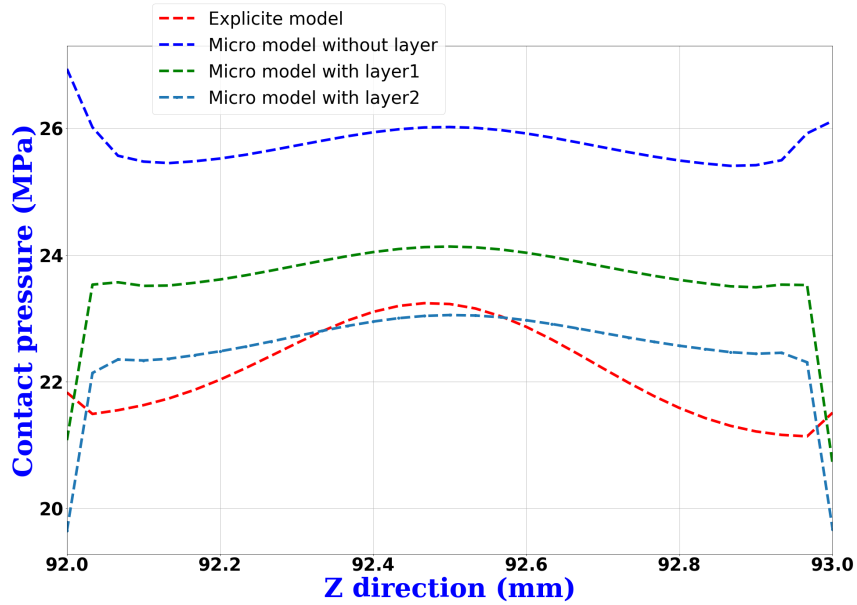
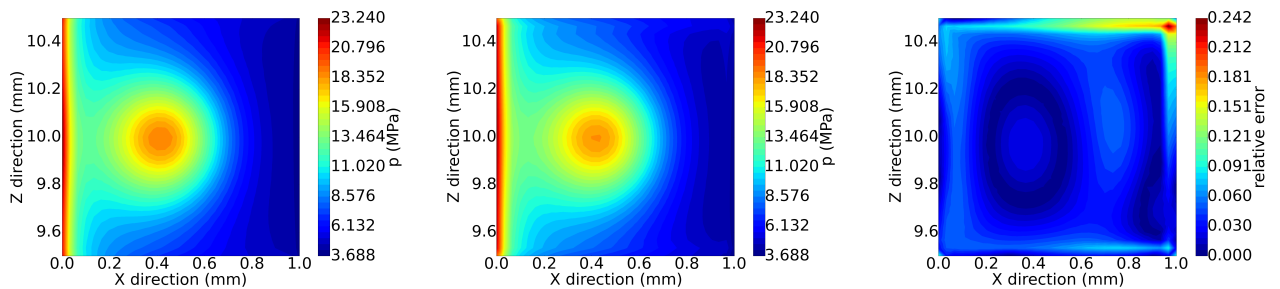


Figure II.32 – Contact pressure distribution between explicit and micro models at the leading edge: micro layer model with one and two elements mesh size.

In Figure II.32, micro models denoted layer 1 and 2 represent respectively the micro model with one element mesh size and two elements mesh size. The micro model with layer 2 reduces enormously edges effects. At the extremities nodes ($Z=92.0$ mm and $Z=93.0$ mm), contact pressure decreases significantly compared to the explicit results because of the increase of the layer area. However, this result is better than the first micro model one. A full 3D illustration is given in the Figure II.33.



(a) Explicit case (max and min pressures: 23.24 and 3.688 MPa) (b) Micro model (max and min pressures: 23.05 and 3.670 MPa)

Figure II.33 – Explicit versus micro model contact pressure distribution over the patch contact surface: micro layer model with two elements mesh size.

Figure II.33 shows a contact pressure comparison between the micro model (size equals to 2 element mesh size) and the explicit model. Good agreement in results is obtained as

illustrated in Figure II.30 (c). Edge errors are very reduced. However, in any case, the important thing is that in the central part, estimations are good, irrespective of layer presence.

The proposed strategy therefore seems relevant to address contact problems in the presence of heterogeneities.

Conclusion of the section

In this section, a multi-scale approach based on the homogenization method having the advantage of considering contact localizations induced by heterogeneities is presented and validated to reference results where inclusion is explicitly meshed. Thanks to the new homogenization boundary conditions, macro to micro contact stresses relocalization is then possible. Two micro models have been presented: the first micro model does not consider macro boundary effects and therefore leads to some important errors at the edges. The second micro model with a layer, contributes in edge errors reduction then allowing for good approximations between micro model and reference. Therefore, considering a layer in the micro model, helps in reducing edge errors. However, the common point between the two micro models is that solution in the central part are well estimated: the relative error is less than 4% in the contact surface of the patch except patch edges.

In the next section, the robustness of KUBC-Contact method through the micro model with a layer, previously introduced, is investigated through a parametrical study where various friction coefficients are considered.

II.1.5 Parametric study on the friction coefficient

In this subsection, in order to show the robustness of the KUBC-Contact method (Figure II.14) proposed in this work, a parametric study on the friction coefficient, μ , is conducted. Micro model with a layer (1 element mesh size) which is employed to obtain results presented in Figure II.30, where friction coefficient is set to 0.3, is used in this section to perform parametric studies. The above results are established for a friction coefficient set at 0.3. Here, μ is varied from 0.1 to 0.8 and results between explicit method and multi-scale strategy are compared. Micro model, allowing micro mechanical field computation, is based on boundary conditions illustrated in Figure II.29). Results are shown in Figure II.34.

For each friction coefficient, results are presented on the same scale. Maximum pressure distribution is achieved on the leading edge of the pin. As the coefficient of friction increases, the maximum pressure also increases due to the greater tilting of the pad. This can be seen in particular by the increasing extent of the area where the pressure is zero. In fact, when the friction coefficient is small, 0.1 for example, the resistance to the disc motion is not high, leading then to a single instability regime (pure sliding). However, when the friction coefficient is higher, 0.8 for example, the resistance to the disc motion is very high then leading to different instabilities regimes: sliding and contact separation. For friction coefficient 0.8, in Figure II.34 (j), the contact pressure tends to zero (0.136 MPa) at the trailing edge of the heterogeneous patch (contact separation).

Between explicit and multi-scale methods, it appears that there is a good agreement of the results, particularly on the central part of the patch, whatever the friction coefficient. The most significant errors (in the order of a few %) are found on the edge of the patch and especially on the leading edge (Figure II.34). In Figure II.34 (l), near the trailing edge of the heterogeneous patch, there is a significant relative error. The latter is numerical. In fact, at this zone (Figure II.34 (j)), contact pressure is almost zero (0.136 MPa). This induces a numerical error in the relative error calculation. Moreover, as contact pressure is very low at this zone, there is no significant impact on the global solution. The important thing relies on the fact that the high-pressure zone is well estimated.

With regard to the results obtained here, it is shown that not only small but high friction coefficients can be considered with the proposed multi-scale strategy and therefore represent an improvement compared to few contact homogenization-based works which exist in the literature like in [Alart and Lebon, 1998].

This parametric study then makes it possible to consolidate the strategy implemented.

II.1 Multi-scale approach for contact modelling considering material heterogeneity

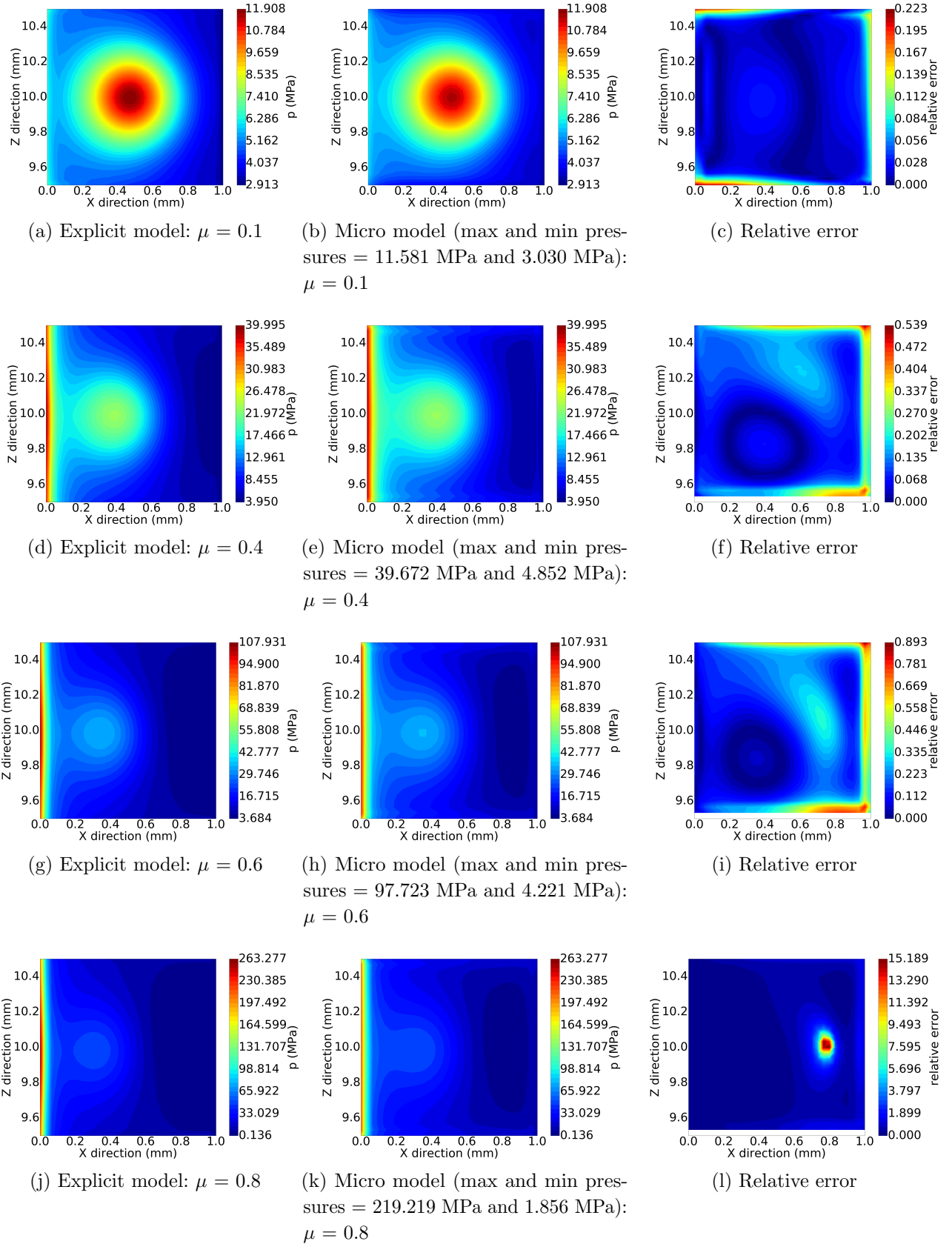


Figure II.34 – Parametric study of friction coefficient: Explicit versus micro model contact pressure distribution and relative error.

II.2 Extension of the proposed strategy to other cases

In the precedent sections, a multi-scale homogenization strategy has been proposed for contact modelling of heterogeneous material, especially for braking applications. Previously, the strategy has been validated with a simple case considering only one heterogeneous patch located at the leading edge of a frictional pin. The inclusion is centred within the patch. The aim of this subsection is to validate the strategy through extreme cases. For example, when the heterogeneity is directly located at the contact surface. Can this strategy still be working for this extreme case? This section will give an answer to this question through several examples.

In this subsection, a cubical heterogeneity is used. The position of the heterogeneity is varied around the contact surface of the patch.

The numerical model, shown in Figure II.2, is still used here for validation purpose. The heterogeneous patch containing a spherical inclusion is replaced by a patch containing a cubical heterogeneity, 0.4 mm of size, located directly on the contact surface. Material properties of cubical inclusion and matrix are presented in Table III.14. 27000 hexa elements have been used to mesh the heterogeneous patch. Penalty method has been used for contact constraint resolution with a friction coefficient of 0.3. 4 cases are presented in Figure II.35 and a simulation is conducted for each case. In the following, results are presented and discussed.

Table II.5 – Elastic properties for heterogeneous patch

| | Young's modulus(MPa) | Poisson's ratio |
|-----------|----------------------|-----------------|
| Inclusion | 2000 | 0.3 |
| Matrix | 3000 | 0.3 |

II.2.1 Homogenization results

Effective behaviour (Young's modulus and Poisson's ratio) obtained from KUBC-Contact homogenization are presented, in Table II.6 and II.7, for the different configurations shown in Figure II.35. KUBC-Contact results are compared to the classical KUBC Method.

Table II.6 – Equivalent modulus computed from KUBC-Contact and compared to KUBC homogenization models: cubical inclusion varied at different positions from the contact surface.

| Young's modulus (MPa) | Case 1 | Case 2 | Case 3 | Case 4 |
|-----------------------|--------|--------|--------|--------|
| KUBC | 2925 | 2931 | 2931 | 2931 |
| KUBC-Contact | 2925 | 2936 | 2931 | 2925 |

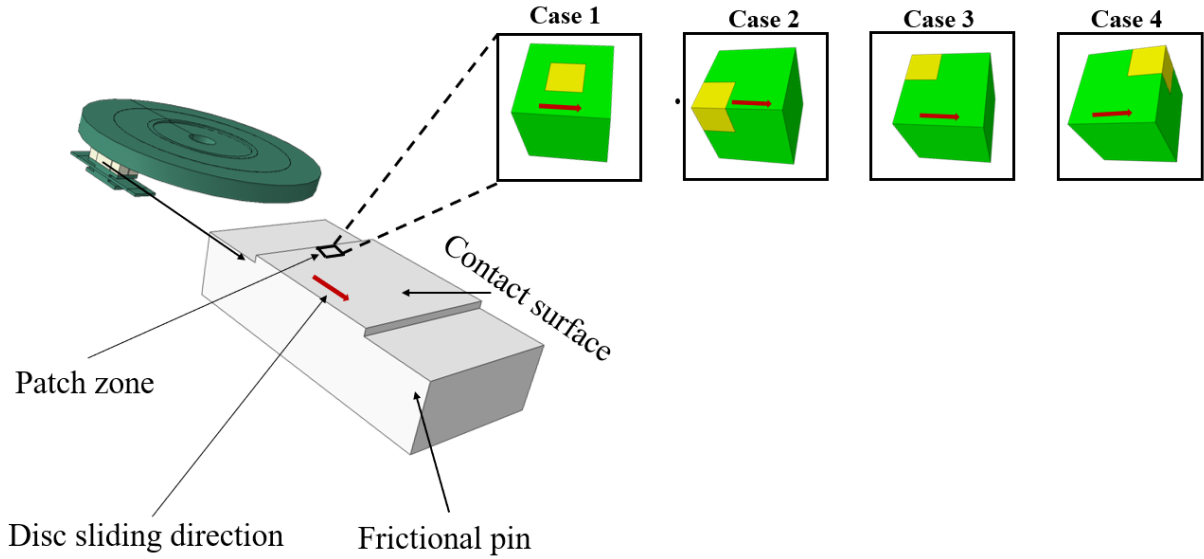


Figure II.35 – Large scale numerical model with cubical heterogeneity at the leading edge: different positions of the cubical heterogeneity, in the contact surface of the heterogeneous patch which belongs to the frictional pin.

Table II.7 – Poisson’s ratio computed from KUBC-Contact and compared to KUBC homogenization models: cubical inclusion varied at different positions from the contact surface.

| Poisson’s ratio | Case 1 | Case 2 | Case 3 | Case 4 |
|-----------------|--------|--------|--------|--------|
| KUBC | 0.299 | 0.299 | 0.299 | 0.299 |
| KUBC-Contact | 0.299 | 0.299 | 0.299 | 0.300 |

Table II.6 shows Young’s modulus obtained from KUBC-Contact and KUBC homogenization models for each inclusion position presented in Figure II.35. KUBC-Contact results are in good agreement with those of KUBC. Case 1 is the case where cubical inclusion is centred at the middle of the patch directly in the contact surface. Case 2, case 3 and case 4 correspond respectively to the cases where the cubical inclusion is placed at the extremities of the patch. KUBC results show a constant behaviour when inclusion is at the patch extremities. The linearity of the boundary conditions in equations II.13 and II.14 explained these results. KUBC-Contact method results are close enough to the KUBC one. The small difference come from the fact that contact is added, making differences in stresses evolution. However, differences are not significant because the inclusion is less rigid and its volume fraction is smaller than the matrix.

Table II.7 shows Poisson’s ratio for each studied case for the two models. Whatever the inclusion position, results are not affected. Results obtained from KUBC-Contact is in a good agreement with KUBC results for each case.

II.2.2 KUBC-contact versus explicit method results

A simulation with friction contact is performed considering the multi-scale strategy presented in Figure II.14. The pin-on-disc model is considered (Figure II.35) for computation. In the context of multi-scale strategy, micro model with a layer (1 element mesh size) is still used for simulation in this subsection.

Multi-scale results are then compared to the explicit method (where inclusion is meshed). Results are presented in Figure II.36.

Figure II.36 presents contact pressure evolution, in the patch area, between explicit and multi-scale strategy. Except cases where inclusion is located at the leading edge, there is an overpressure which decreases with the sliding direction because the matrix is more rigid than inclusion. For each simulation, at the zones where inclusion is located, contact pressure is very low and decreases also with sliding direction.

The multi-scale strategy shows a good agreement with explicit results regarding pressure evolution. The difference between contact pressure is almost null everywhere in the contact area, except some minor localization at the edges of the patch. The multi-scale strategy gives good approximations irrespective of the inclusion location. However, to confirm the robustness of the multi-scale strategy adopted, in order to extend it to complex microstructure, a parametric study is still needed. This is performed in the next subsection.

II.2 Extension of the proposed strategy to other cases

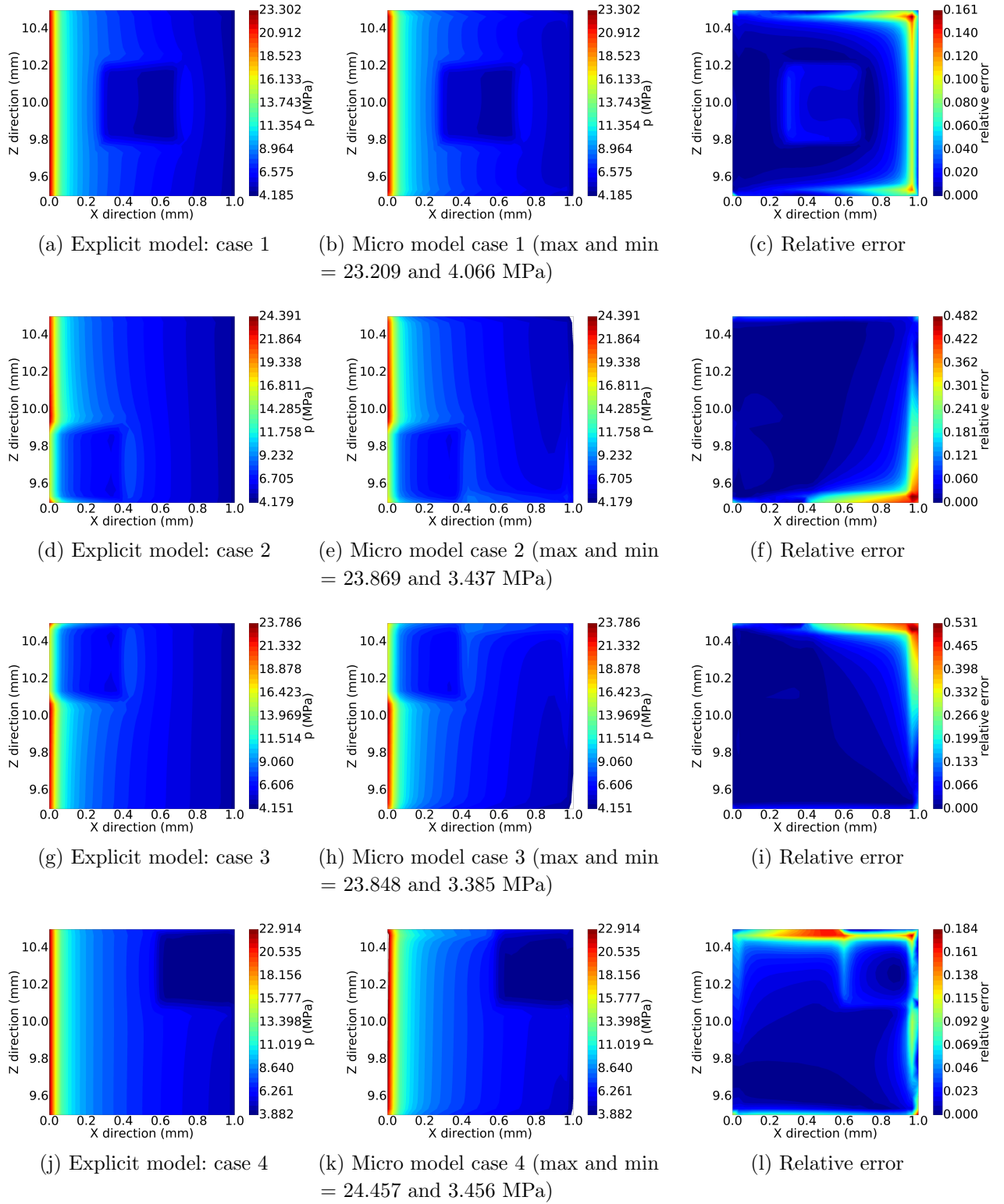


Figure II.36 – Explicit versus multi-scale contact pressure distribution: cubical inclusion located at different positions of the heterogeneous patch.

II.2.3 Parametric study on Young's modulus evolution

In the previous subsection, we consolidate the multi-scale strategy developed in this work using a cubical inclusion placed directly in the contact surface. Four different extreme cases have been presented and validated. Is our model still valid if the inclusion is harder than the matrix? How far can our model go in the context of contact modelling of heterogeneous material? Through a parametric study, an answer is given to this question. Young's modulus of the inclusion is varied from 2000 MPa to 100000 MPa and compared to the explicit method. Case 1 (where cubical inclusion is centred at the contact interface) of the numerical model used in the precedent subsection is considered for this study. Two results are shown: homogenization results and contact pressure distribution which is compared to explicit method where inclusion is explicitly meshed.

Multi-scale model results, varying inclusion rigidity is presented in the following: Table II.8 shows homogenized effective properties evolution in function of inclusion rigidity. As expected, in Table II.8, the equivalent Young's modulus is increasing when the local Table II.8 – Effective properties computation in the context of cubical inclusion centred at middle of the patch (case1): KUBC-Contact compared to KUBC homogenization results for different inclusion rigidity.

| Case 1 | 2000 MPa | 20000 MPa | 50000 MPa | 100000 MPa |
|-------------------------------------|----------|-----------|-----------|------------|
| Young's modulus: KUBC (MPa) | 2931 | 3773 | 4931 | 6794 |
| Young's modulus: KUBC-Contact (MPa) | 2937 | 3730 | 4828 | 6588 |
| Poisson's ratio: KUBC | 0.3 | 0.293 | 0.286 | 0.282 |
| Poisson's ratio: KUBC-Contact | 0.3 | 0.293 | 0.287 | 0.284 |

inclusion rigidity becomes higher than the matrix. However, the equivalent Poisson's ratio is decreasing while the local inclusion Poisson's ratio increases. This could be explained by the fact that, when the inclusion rigidity is increasing, the strain in the transverse direction decreases; subsequently leading to a decrease of Poisson's ratio.

Next, contact pressure distribution is investigated for case 1 numerical model. Recall that case 1 stands for numerical model where cubical inclusion is located at the contact interface. Contact pressure distribution of the latter model is compared to the explicit results and illustrated in Figure II.37

Two cases have to be distinguished: Firstly, when the inclusion is softer than matrix, the contact pressure approximation is very good as shown by the relative error in Figure II.37 (c). Secondly, when the inclusion is stiffer than the matrix, the contact pressure approximation is not well estimated at the inclusion area, especially at the interface between the inclusion and the matrix, which corresponds to discontinuity zones. This discontinuity is particularly observed in Figure II.37 (f). When the inclusion Young's modulus belongs to the interval 2000 MPa to 20000 MPa included, good approximations are obtained. Above 20000 MPa, the relative error is increased almost throughout the inclusion contact area. Such errors are related to KUBC-Contact boundary

II.2 Extension of the proposed strategy to other cases

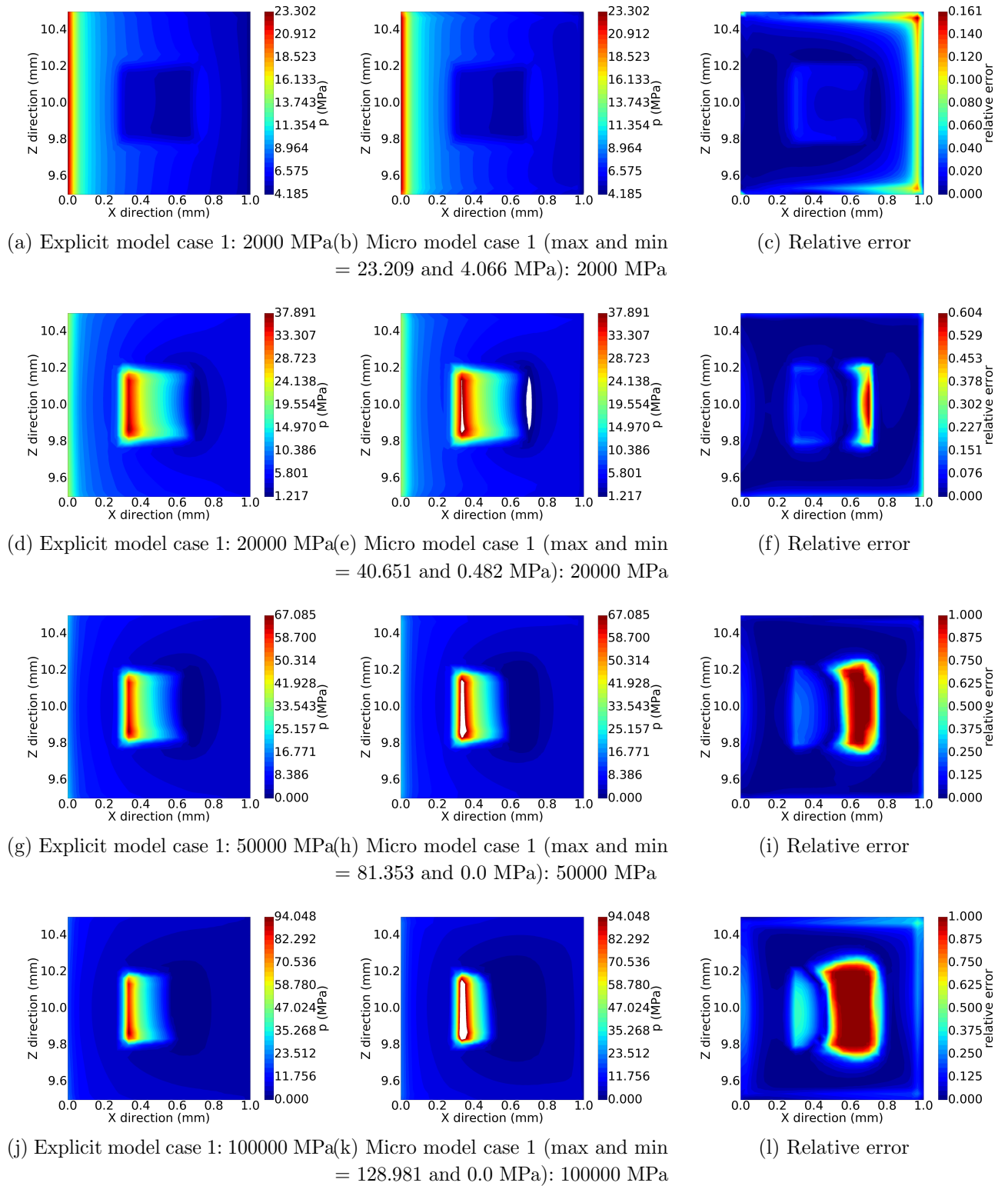


Figure II.37 – Explicit versus multi-scale contact pressure distribution: parametric studies, where inclusion rigidity is varied from 2000 MPa to 100000 MPa: .

conditions shown in Figure II.29. In fact, as macro displacements are applied at each node of the patch, especially at contact interface where the cubical inclusion is located, contact constraints resolution become very difficult for high inclusion stiffness. Therefore, it is essential to apply other boundary conditions, in the relocation model, in order to have better approximations for high inclusion rigidity.

To improve results, new macro to micro boundary conditions, of the multi-scale strategy, are proposed in the following subsection.

II.2.4 Mesh dependence from embedding to relocation

Since the macro to micro strategy proposed in Figures II.24 and II.29 gives satisfying results when the inclusion is located at the contact interface for low rigidity, it has been shown in the previous subsection that it causes difficulties in contact resolution when the inclusion is very stiff and located at the surface. In this subsection a new boundary condition is proposed not only to improve mechanical fields approximation when the inclusion is located at the contact interface, but also to overcome mesh dependence between macro and micro mesh.

The mesh dependence problem is explained in the following: in order to apply macro displacements at the level of the heterogeneous patch, the same mesh is required at the contact face of the homogenized macro patch and heterogeneous patch. This increases computation time in the macro model. Moreover, the micro heterogeneous patch is limited in terms of mesh elements. In other words, a mesh refinement at the micro-scale is not possible without increasing the number of macro-scale elements. The mesh dependence problem is summarized in Figure II.38:

The new boundary condition proposed in this subsection can allow more computation time saving because it is mesh dependent from macro to micro. The use of one element at the level of each homogenized macro patch is sufficient for relocation through average data from macro patch.

The new boundary condition allowing macro to micro mechanical fields computation at the level of heterogeneities, through average macro data, is illustrated in Figure II.39.

This new strategy is based on two ingredients:

- First, a uniform pressure is computed at the contact surface of the embedded patch and is used to enforce contact constraints between the flat disc and the heterogeneous patch.
- Secondly, mean displacements obtained, from embedded homogenized patch, at the contact face and bottom face are computed. Therefore, displacements computed at the bottom face of the macro patch are applied to the bottom face of the micro model with a layer. Three displacements are distinguished at the bottom face: U_{moyN} , U_{moyG} and U_{moyT} . These are displacements applied respectively in the normal, sliding

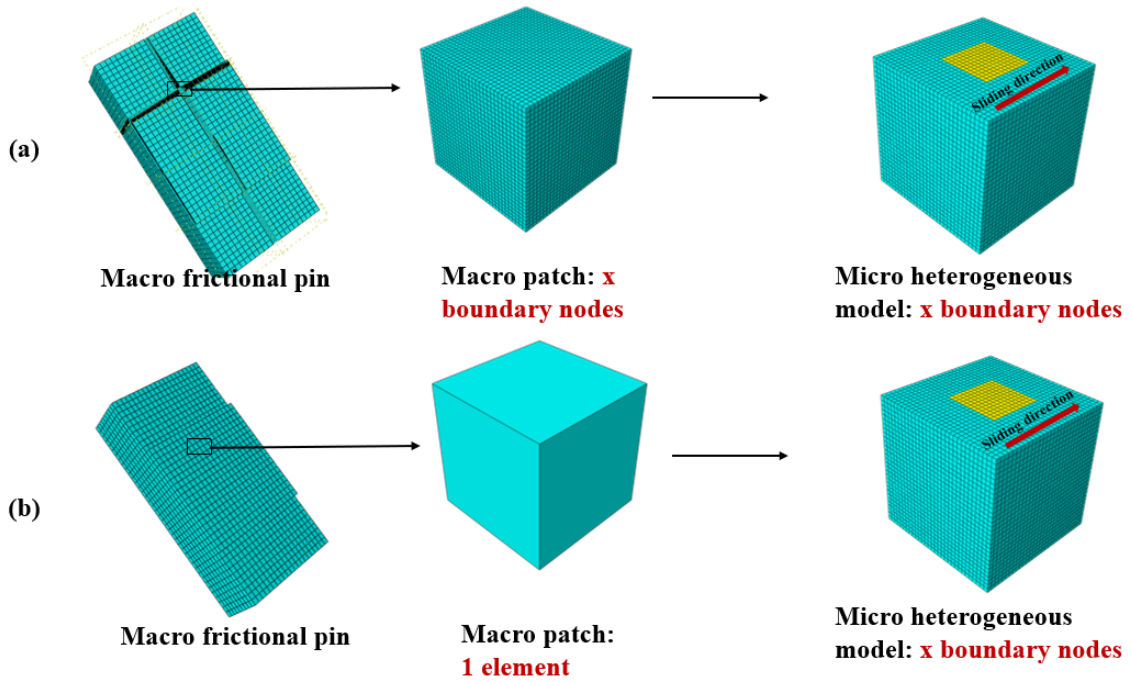


Figure II.38 – (a) fine mesh: macro embedded model is very refined. (b) coarse mesh: macro embedded model is meshed with 1 element, however the macro to micro relocalization is possible.

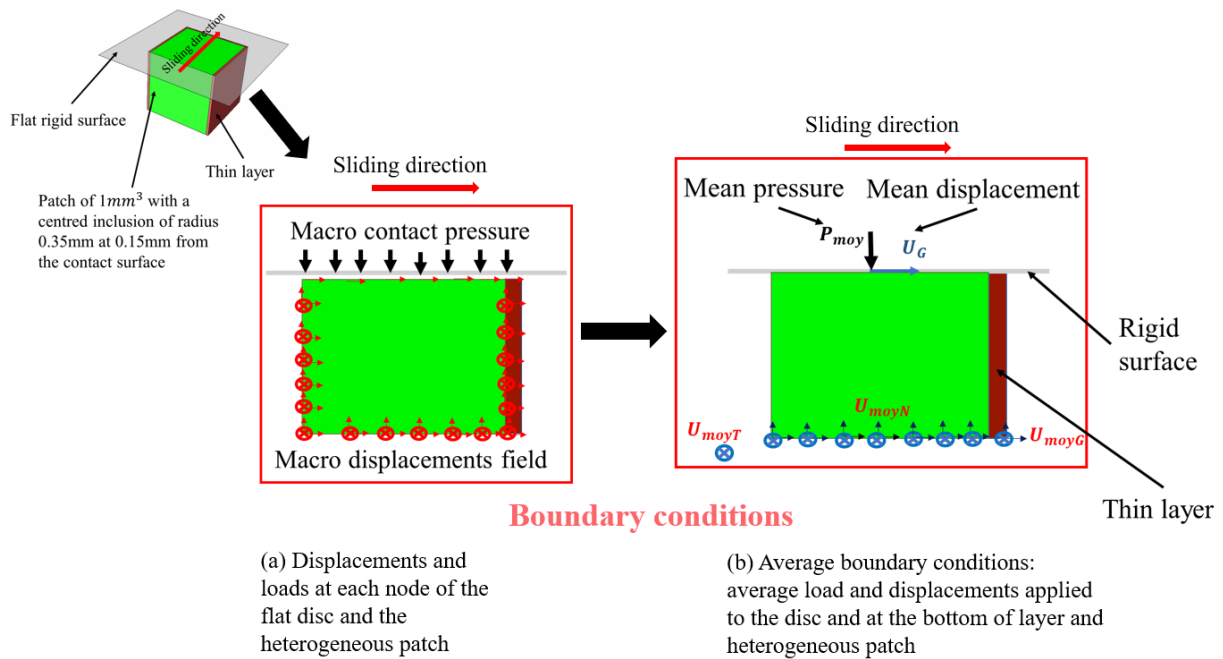


Figure II.39 – Evolution of the boundary conditions from each node, of the heterogeneous patch and disc, to average boundary conditions applied to the disc and at the bottom of micro patch.

and tangential directions. Next, in order to reproduce total sliding of the macro disc in rotation, another displacement U_G is applied to the rigid surface, in the sliding direction. In fact as the contact problem considered in this work is in total sliding, U_G has to be chosen in such a way to obtain total sliding condition at the micro-scale. To do so, in this work, U_G is computed from equation (II.22):

$$U_G = aU_{moycs}, \quad (\text{II.22})$$

where U_{moycs} is the average displacement computed at the contact surface of the macro embedded patch. U_{moycs} represents the displacement necessary to reach sliding limit. Then, U_{moycs} is multiplied by an arbitrary factor a necessary to reach the full sliding condition. In this work, $a = 2$. This value is sufficient to achieve full sliding condition. If our problem were not under full sliding condition, a should be equal to 1. One could choose a factor of 3 or 4 or high factor, and however, will still achieve the same results which will remain unchanged under full sliding conditions.

The parametric study presented in Figure II.37, where the cubical inclusion, located at contact interface, rigidity has been varied from 2000 MPa to 100000 MPa, is performed again using new boundary conditions illustrated in Figure II.39. At the macro embedded model only 1 element is used for the patch. Same mesh is conserved for the heterogeneous micro patch, like in the previous subsections. Let's recall that, the macro to micro boundary conditions, proposed in Figure II.29, needs same elements in the embedded and micro patch level and therefore is time consuming.

Results are presented in Figure II.40:

Figure II.40 shows the contact pressure distribution in the patch area for different inclusion Young's modulus. Results obtained from micro model through this new boundary condition fit very well explicit ones whatever the inclusion rigidity. Relative error, for each simulation, is almost zero everywhere in the patch area except at the zones where pressure is very low, therefore, the quality of results are not impacted. The results obtained in Figure II.40 are better than those obtained in Figure II.37.

Furthermore, micro model, based on average boundary conditions (Figure II.39), has the advantage to reduce computation time over the micro model based on distributed boundary conditions at each node of the patch boundary (Figure II.29). Let's recall that the latter boundary conditions necessitate a refined mesh while the average ones require only 1 element mesh in the macro embedded patch. Although computation time has been reduced more through the average boundary conditions, the precision in results is also improved. Table II.9 shows computation time comparison between the three models configuration (explicit model, multi-scale model with distributed boundary conditions and multi-scale model with average boundary conditions). 10 CPU cores have been used to run calculation.

II.2 Extension of the proposed strategy to other cases

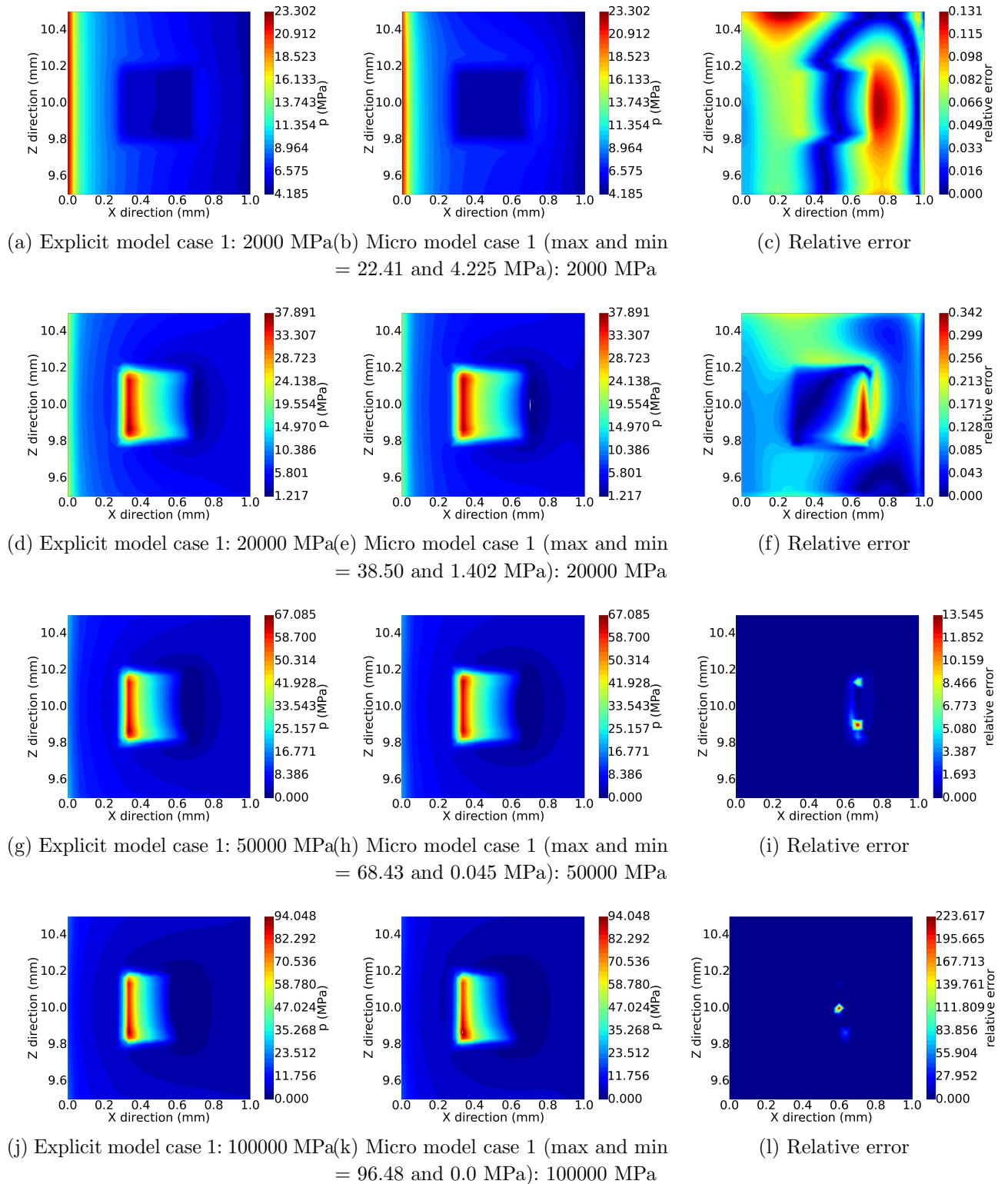


Figure II.40 – Explicit versus multi-scale contact pressure distribution over the patch contact surface: micro model based on average boundary conditions and load.

Table II.9 – CPU time comparison between both explicit and multi-scale models: distributed (fine mesh) and average (coarse mesh) boundary conditions.

| | CPU time |
|---|----------|
| Explicit model | 124 min |
| Multi-scale macro model (fine mesh) | 136 min |
| Multi-scale micro model (distributed boundary conditions) | 8 min |
| Multi-scale macro model (coarse mesh) | 21 min |
| Multi-scale micro model (average boundary conditions) | 16 min |

Conclusion of the section

In this section, the multi-scale strategy illustrated in Figure II.14, has been extended to other cases: a cubical inclusion located at contact interface has been investigated for 4 different cases. Mainly, two boundaries conditions have been proposed and compared to explicit results. The first one needs a refined mesh at macro-scale and the second one, which is based on average boundary conditions, necessitates a coarse mesh. For the latter, only one element is necessary at macro-scale in order to perform mechanical fields relocalization. Consequently, leading to computation time reduction.

Through parametric studies, the robustness of the average boundary conditions has been shown. The results obtained fit very well with explicit ones.

Therefore, in the following sections and chapters, these average boundary conditions and load, presented in Figure II.39, are considered.

II.3 Extension to complex material behaviour laws

In the bibliographical review, it has been shown that friction material exhibits a complex behaviour. Previously, a multi-scale strategy has been developed for contact modelling considering material heterogeneity under the assumption of linear elasticity. Is this multi-scale strategy transposable for complex behaviour laws?

In this section, the multi-scale strategy previously introduced is extended for a complex material behaviour: an isotropic transverse material behaviour is implemented through a simple numerical example. KUBC-Contact formulation is modified to fit this class of material. Other complex material behaviour (elastic-plastic, elastovisco-plastic, etc) can also be introduced in the multi-scale strategy but will not be studied in this work. Next section focuses on a transversely isotropic material behaviour law.

II.3.1 Transversely isotropic material

A material having a plane in which its properties are identical is transversely isotropic (see Figure II.41). The plane is the so called isotropic plane. This material is characterized by 5 independents elastic constants (E_x , E_y , ν_{xz} , ν_{xy} and G_{xy}). y is considered as the revolution axis.

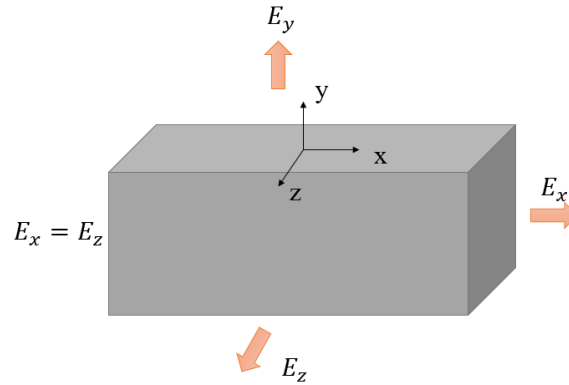


Figure II.41 – Transversely isotropic material: 3D representation.

The Hooke's law expressed in terms of compliance matrix is obtained from II.23:

$$\hat{\epsilon} = \hat{S}\hat{\sigma}. \quad (\text{II.23})$$

Equation II.23 is expressed in terms of matrix as in II.24:

$$\begin{bmatrix} \epsilon_{xx} \\ \epsilon_{yy} \\ \epsilon_{zz} \\ \sqrt{2}\epsilon_{yx} \\ \sqrt{2}\epsilon_{xz} \\ \sqrt{2}\epsilon_{yz} \end{bmatrix} = \begin{bmatrix} 1/E_x & -\nu_{xy}/E_x & -\nu_{xz}/E_x & 0 & 0 & 0 \\ -\nu_{yx}/E_y & 1/E_y & -\nu_{yz}/E_y & 0 & 0 & 0 \\ -\nu_{xz}/E_x & -\nu_{xy}/E_x & 1/E_x & 0 & 0 & 0 \\ 0 & 0 & 0 & 1/G_{xy} & 0 & 0 \\ 0 & 0 & 0 & 0 & 1/G_{xz} & 0 \\ 0 & 0 & 0 & 0 & 0 & 1/G_{xy} \end{bmatrix} \begin{bmatrix} \sigma_{xx} \\ \sigma_{yy} \\ \sigma_{zz} \\ \sqrt{2}\sigma_{yx} \\ \sqrt{2}\sigma_{xz} \\ \sqrt{2}\sigma_{yz} \end{bmatrix}, \quad (\text{II.24})$$

where G_{xz} is obtained from [II.25](#):

$$G_{xz} = E_x/2(1 + \nu_{xz}). \quad (\text{II.25})$$

The quantities ν_{xy} and ν_{yx} are not equal and are obtained from [II.26](#):

$$\nu_{xy}/E_x = \nu_{yx}/E_y. \quad (\text{II.26})$$

The next section is dedicated to the strategy leading to contact modelling of transversely isotropic material.

II.3.2 Transversely elastic isotropic: strategy and effective quantities computation

Previously, the components of heterogeneous material were supposed to be elastic isotropic. In reality, components can have a different behaviour. In this subsection, a strategy is set up for effective properties computation.

The main question is about the overall behaviour computation. If inclusions and the matrix are supposed to have transversely isotropic elastic behaviour, what will be the behaviour of the equivalent media? it is probable that the homogenized behaviour will be transversely isotropic, but we can not be certain one hundred percent. It depends on the geometry of the particles, their orientations, etc. Moreover, what happens if the components of a heterogeneous material are assumed to have different material behaviour? For example the inclusions being elastic isotropic and the matrix being transversely isotropic? That raises many questions, in particular if the homogenized behaviour will be elastic isotropic, transversely isotropic or another behaviour?

In this work, it is assumed, as in [[Peillex et al., 2008](#)], that the overall behaviour, of a heterogeneous media containing elastic isotropic and transversely isotropic particles, is transversely isotropic.

The proposed strategy is illustrated in [Figure II.42](#).

Once this assumption is made, the effective quantities computation of transversely isotropic material should be discussed because boundary conditions applied in the case of isotropic elasticity are no longer valid in this case. In the context of isotropic elasticity, only two independent elastic constants are needed. Therefore, bulk and shear modulus

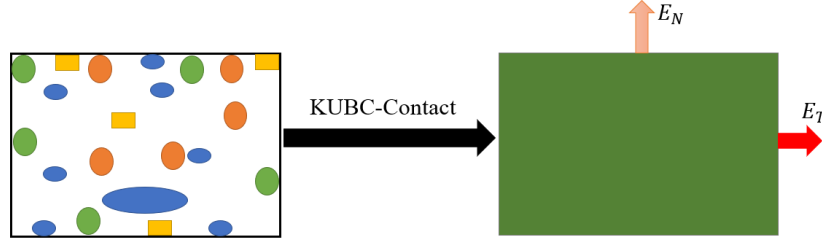


Figure II.42 – Multi-scale approach: embedding of the transversely isotropic material via KUBC-Contact homogenization model.

were necessary to calculate these two coefficients. To do so, boundary conditions were applied in the three directions. In the context of transversely isotropy, it has been said that 5 independent elastic constants are required. Therefore, the boundary conditions applied in equations (II.13) and (II.14) are no longer sufficient for the 5 equivalent coefficients determination.

Another boundary condition is, therefore, required.

For Young's modulus and Poisson's ratio (E_x , E_y , ν_{xz} , ν_{xy}) determination, the following boundary conditions, in each directions (X , Y and Z), are proposed in equations (II.27), (II.28) and (II.29):

$$\begin{bmatrix} U_X \\ U_Y \\ U_Z \end{bmatrix} = \begin{bmatrix} E_{XX} & 0 & 0 \\ 0 & 0 & 0 \\ 0 & 0 & 0 \end{bmatrix} \begin{bmatrix} X \\ Y \\ Z \end{bmatrix}, \quad (\text{II.27})$$

$$\begin{bmatrix} U_X \\ U_Y \\ U_Z \end{bmatrix} = \begin{bmatrix} 0 & 0 & 0 \\ 0 & E_{YY} & 0 \\ 0 & 0 & 0 \end{bmatrix} \begin{bmatrix} X \\ Y \\ Z \end{bmatrix}, \quad (\text{II.28})$$

$$\begin{bmatrix} U_X \\ U_Y \\ U_Z \end{bmatrix} = \begin{bmatrix} 0 & 0 & 0 \\ 0 & 0 & 0 \\ 0 & 0 & E_{ZZ} \end{bmatrix} \begin{bmatrix} X \\ Y \\ Z \end{bmatrix}, \quad (\text{II.29})$$

with $\begin{bmatrix} X \\ Y \\ Z \end{bmatrix}$ a vector of nodal coordinates.

(U_X, U_Y, U_Z) and (E_{XX}, E_{YY}, E_{ZZ}) are respectively displacement field and macro strains. The displacements are then uniform in each direction. Given a direction, the displacements, normal to this direction, are reduced to zero.

For shear modulus (G_{xy} , G_{xz} and G_{yz}) determination, the following boundary conditions are proposed in equations (II.30), (II.31) and (II.32):

$$\begin{bmatrix} U_X \\ U_Y \\ U_Z \end{bmatrix} = \begin{bmatrix} 0 & E_{XY} & E_{XZ} \\ 0 & 0 & 0 \\ 0 & 0 & 0 \end{bmatrix} \begin{bmatrix} X \\ Y \\ Z \end{bmatrix}, \quad (\text{II.30})$$

$$\begin{bmatrix} U_X \\ U_Y \\ U_Z \end{bmatrix} = \begin{bmatrix} 0 & 0 & 0 \\ E_{XY} & 0 & E_{YZ} \\ 0 & 0 & 0 \end{bmatrix} \begin{bmatrix} X \\ Y \\ Z \end{bmatrix}, \quad (\text{II.31})$$

$$\begin{bmatrix} U_X \\ U_Y \\ U_Z \end{bmatrix} = \begin{bmatrix} 0 & 0 & 0 \\ 0 & 0 & 0 \\ E_{XZ} & E_{YZ} & 0 \end{bmatrix} \begin{bmatrix} X \\ Y \\ Z \end{bmatrix}. \quad (\text{II.32})$$

Once the micro fields in the patch, σ_{ij} and ϵ_{ij} , under the applied boundary conditions, are obtained, the averaged stresses and strains are computed over the patch from (II.15) and (II.16).

Young's modulus and Poisson's ratio (E_x , ν_{xy} and ν_{xz}) are obtained resolving the system of equation presented in (II.33):

$$\begin{cases} \frac{\bar{\sigma}_{xx}^x}{E_x} - \frac{\bar{\sigma}_{yy}^x \cdot \nu_{xy}}{E_x} - \frac{\bar{\sigma}_{zz}^x \cdot \nu_{xz}}{E_x} = \bar{\epsilon}_{xx}^x \\ \frac{\bar{\sigma}_{xx}^y}{E_x} - \frac{\bar{\sigma}_{yy}^y \cdot \nu_{xy}}{E_x} - \frac{\bar{\sigma}_{zz}^y \cdot \nu_{xz}}{E_x} = \bar{\epsilon}_{xx}^y, \\ \frac{\bar{\sigma}_{xx}^z}{E_x} - \frac{\bar{\sigma}_{yy}^z \cdot \nu_{xy}}{E_x} - \frac{\bar{\sigma}_{zz}^z \cdot \nu_{xz}}{E_x} = \bar{\epsilon}_{xx}^z \end{cases} \quad (\text{II.33})$$

where $\bar{\epsilon}_{xx}^x$, $\bar{\epsilon}_{xx}^y$, and $\bar{\epsilon}_{xx}^z$ represent average strains obtained from boundary conditions II.27, II.28 and II.29 respectively.

$(\bar{\sigma}_{xx}^x, \bar{\sigma}_{xx}^y, \bar{\sigma}_{xx}^z)$, $(\bar{\sigma}_{yy}^x, \bar{\sigma}_{yy}^y, \bar{\sigma}_{yy}^z)$ and $(\bar{\sigma}_{zz}^x, \bar{\sigma}_{zz}^y, \bar{\sigma}_{zz}^z)$ represent average stresses computed from boundary conditions II.27, II.28 and II.29 respectively.

Once E_x , ν_{xy} and ν_{xz} are obtained, E_y and E_z are deduced from equations (II.34) and (II.35)

$$\frac{\bar{\sigma}_{yy}^y}{E_y} - \frac{\bar{\sigma}_{xx}^y \cdot \nu_{yx}}{E_y} - \frac{\bar{\sigma}_{zz}^y \cdot \nu_{yz}}{E_y} = \bar{\epsilon}_{yy}^y, \quad (\text{II.34})$$

$$\frac{\bar{\sigma}_{zz}^z}{E_z} - \frac{\bar{\sigma}_{xx}^z \cdot \nu_{xz}}{E_z} - \frac{\bar{\sigma}_{yy}^z \cdot \nu_{yz}}{E_z} = \bar{\epsilon}_{zz}^z, \quad (\text{II.35})$$

where $\bar{\epsilon}_{yy}^y$ and $\bar{\epsilon}_{zz}^z$ represent average strains obtained from boundary conditions II.28 and II.29 respectively.

The determination of the shear modulus is very easy. G_{xy} , G_{xz} and G_{yz} are obtained using average stresses and strains from shear boundary conditions (II.30), (II.31) and (II.32) respectively. G_{xy} , G_{xz} and G_{yz} then read equations (II.36), (II.37) and (II.38) respectively:

$$G_{xy} = (\bar{\sigma}_{xy})/(\bar{\epsilon}_{xy}), \quad (\text{II.36})$$

$$G_{xz} = (\bar{\sigma}_{xz})/(\bar{\epsilon}_{xz}), \quad (\text{II.37})$$

$$G_{yz} = (\bar{\sigma}_{yz})/(\bar{\epsilon}_{yz}). \quad (\text{II.38})$$

In the following, a simple numerical example of a transversely isotropic problem is illustrated and results are discussed.

II.3.3 Numerical example:

II.3.3.1 Model description

In this subsection, the 3D numerical FEM pin-on-disc model, shown in Figure II.2, is considered. A heterogeneous patch is placed at the leading edge of the frictional material. The patch contains a cubical inclusion of size 0.4 mm and is centred at the contact surface. The inclusion is considered to be elastic isotropic and the frictional material is transversely elastic isotropic. Material properties of a heterogeneous frictional material, inspired from laboratory experimental works, are shown in Table II.10.

Table II.10 – Mechanical properties of the heterogeneous patch: Young’s modulus (MPa), shear modulus (MPa) and Poisson’s ratio

| | E1 | E2 | E3 | ν_{12} | ν_{13} | ν_{23} | G_{12} | G_{13} | G_{23} |
|---------------------------|-------|------|-------|------------|------------|------------|----------|----------|----------|
| inclusion | 2000 | 2000 | 2000 | 0.3 | 0.3 | 0.3 | 769 | 769 | 769 |
| frictional pin and matrix | 10000 | 3000 | 10000 | 0.1 | 0.3 | 0.03 | 1456 | 3846 | 1456 |

Two models are distinguished here: the explicit model where the inclusion is meshed and the multi-scale model where the inclusion is not physically present. The whole explicit friction heterogeneous pin is meshed with 104550 hexaedric elements. Multi-scale model is meshed with 7980 hexaedric elements. Because the inclusion is not present in the multi-scale model, there is no need to refine mesh for accuracy of results. The load and boundary conditions, of the whole numerical model, are kept the same as in chapter II. 10 CPU cores are used, for computation, for both models. The numerical model, with transversely elastic isotropic behaviour, is presented in Figure II.43:

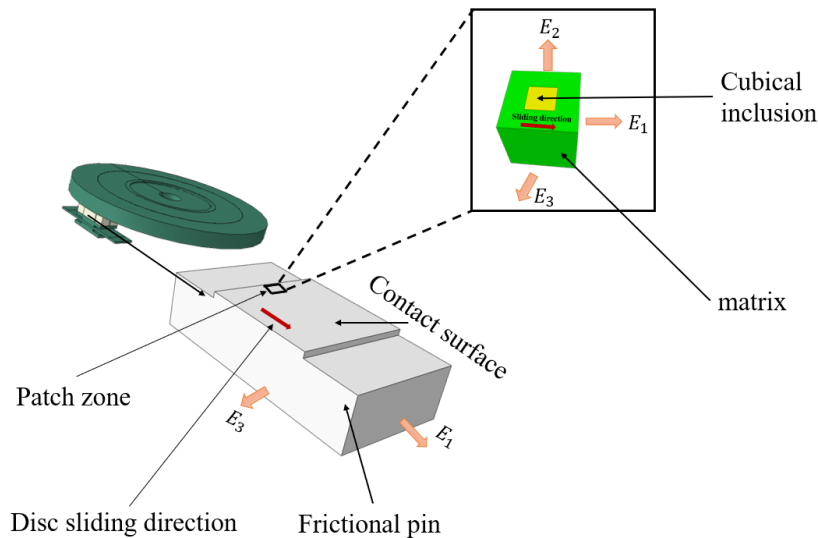


Figure II.43 – Large scale numerical model under the assumption of transversely isotropic material: heterogeneous patch is located at the leading edge, where inclusion is placed at the contact surface.

Results, between the reference model and the multi-scale model, are compared in the next subsection.

II.3.3.2 Results

Multi-scale results are presented in the following:

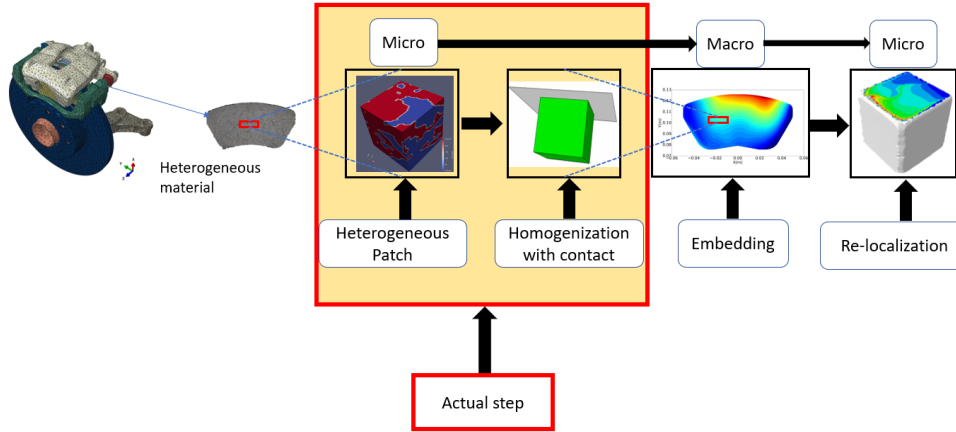


Figure II.44 – Multiscale strategy for contact modelling in the context of transversely isotropic material: KUBC-Contact homogenization step.

Figure II.44 shows the first steps of the multi-scale strategy leading to effective properties computation by the means of KUBC-Contact homogenization method. Homogenized quantities are obtained from equations II.33 to II.38. Results, based on KUBC-Contact, are presented in Table II.11.

Table II.11 – Homogenization results: Effective elastic constants (Young's modulus (MPa), shear modulus (MPa) and Poisson's ratio)

| | E1 | E2 | E3 | ν_{12} | ν_{13} | ν_{23} | G_{12} | G_{13} | G_{23} |
|--------------|-------|------|-------|------------|------------|------------|----------|----------|----------|
| inclusion | 2000 | 2000 | 2000 | 0.3 | 0.3 | 0.3 | 769 | 769 | 769 |
| matrix | 10000 | 3000 | 10000 | 0.1 | 0.3 | 0.03 | 1456 | 3846 | 1456 |
| KUBC-Contact | 9211 | 2960 | 9211 | 0.119 | 0.293 | 0.038 | 1379 | 3579 | 1402 |

With regards to the results obtained in Table III.14, the homogenized media is transversely isotropic according to the assumption made in Section II.4.2. In the isotropic plane (1-3), Young's modulus (9211 MPa) is the same and is less than the matrix one (10000 MPa). In the normal direction (2) the equivalent rigidity (2960 MPa) is also inferior to the matrix rigidity (3000 MPa). This is justified by the small rigidity of the inclusion (2000 MPa) compared to the matrix. Furthermore, Poisson's ratio in the isotropic plane decreases slightly, possibly due to the decrease of rigidity in this plane. It can be noticed also that Poisson's ratio in other directions increases. The reason may be the increase in

rigidity of the equivalent material, in the revolution axis direction.

The volume fraction of the inclusion and the matrix is 0.064 and 0.936 respectively. With respect to Table III.14 results, and considering the law of mixture, homogenized quantities obtained by the means of KUBC-Contact seems to be reasonable in regard of inclusion and matrix material properties and volume fraction.

The second step of the multi-scale strategy consists in the macro-scale embedding followed by a macro to micro relocalization as illustrated in Figure II.45:

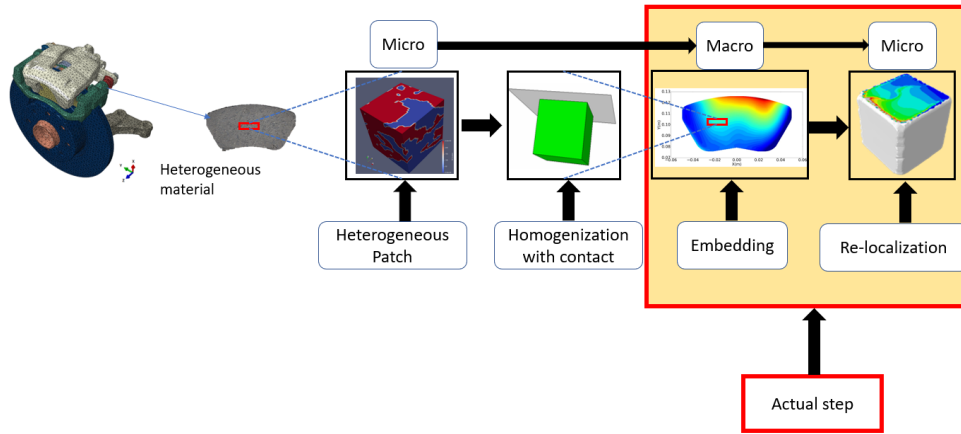


Figure II.45 – Multiscale strategy for contact modeling in the context of transversely isotropic material: embedding and relocalization steps.

Thereby, the quantities computed in Table II.11 are used to enrich macro-scale numerical model in terms of behaviour in the patch zone. After computation, contact forces and displacements are obtained and reinforced in the micro model. Then a local mechanical field is obtained and compared to the explicit results later.

Mean contact force of the multi-scale model compared to explicit contact force, in the patch area, is shown in Table II.12.

Table II.12 – Contact force from embedded homogenized patch

| | contact force |
|---------------------------|---------------|
| contact force (Strategy) | 18.598 N |
| contact force (Explicit) | 18.428 N |

The contact force is in good agreement between the two models. The contact forces are equivalent. In order to confirm our approach, contact pressure evolution between explicit and multi-scale models is illustrated in Figure II.46.

In Figures II.46 (a) and (b), there is an overpressure at the leading edge of the contact surface, which decreases with sliding direction. Moreover, contact pressure intensity is smaller at the zone where inclusion is located because it is less stiff than matrix. At first sight, contact pressure fields between the two models are in a good agreement. However, a look at the Figure II.46 (c) shows some errors at the one interface between inclusion and

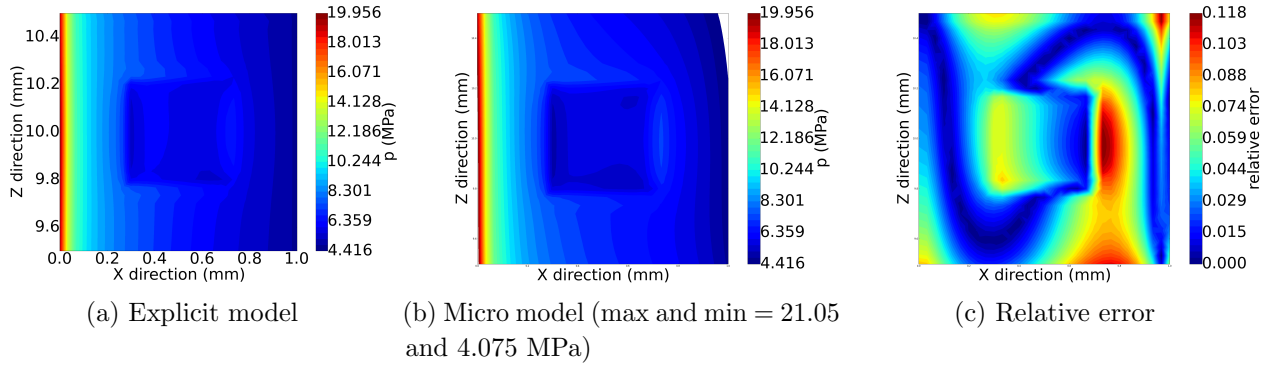


Figure II.46 – Explicit versus multi-scale model contact pressure distribution over the heterogeneous patch contact surface: transversely elastic isotropic assumptions.

matrix. In most of the patch contact area, errors are few. The assumption made for effective properties computation is then relevant to address contact modelling of transversely elastic isotropic material containing elastic particles.

In this section, a multi-scale approach based on KUBC-Contact is extended for transversely isotropic material. The strategy has been validated with reference results where the inclusion is explicitly meshed. Good approximations are obtained. It is then possible to extend this multi-scale approach through other complex material behaviour laws.

Until now, the multi-scale strategy has been validated through a simple microstructure. However, friction material microstructure is more complex unlike all the cases previously presented. The next section will consider a complex microstructure and the computation is performed through KUBC-Contact multi-scale method.

II.4 Application considering complex microstructure

Considering the scale of heterogeneity in a complete brake model is not obvious. In this section, the robustness of the multi-scale strategy through a complex microstructure from tomography is investigated.

II.4.1 Numerical model

The numerical model presented in Figure II.2 is used for implementation. For this application, frictional pad is considered as highly heterogeneous and is discretised into a set of cubical patches of 1 mm^3 of volume. Each set of patches, at the microscale, is constituted of a complex microstructure. Then, a 3D cubical microstructure of 1 mm^3 of volume is extracted from a tomographic image of $20 * 20 * 20 \text{ mm}^3$ of volume. The latter is

obtained from LaMcube laboratory braking applications. The 3D cubical micro-structure is illustrated in Figure II.47:

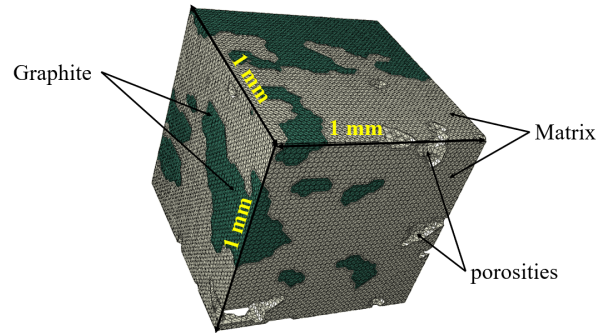


Figure II.47 – Microstructure extracted from tomographic image.

The cubical microstructure of the Figure II.47 is composed of graphite particles, a matrix and some porosities. The volume fraction of matrix, graphite and porosities is 63%, 36% and 1% respectively. However, this cubical microstructure is not representative of the whole tomographic sample ($20*20*20 \text{ mm}^3$ of volume). In fact, the cubical microstructure is extracted near contact interface of the tomographic sample. In order to give an example of application of the proposed multi-scale strategy considering complex microstructure in the numerical model, it is considered that the frictional pad is periodical. Therefore, numerically, the cubical 3D micro-structure extracted from tomography is embedded on the whole frictional material. In other words, each patch (1 mesh element) of the frictional material, of the numerical model presented in Figure II.2, is embedded with the cubical microstructure. The consequence of this choice results in the material continuity: at microscale, the frictional pin is no longer continuous when considering the 3D microstructure at the whole material. The contact surface of the frictional material is $20*20 \text{ mm}^2$ of area, meaning that 400 patches are directly in contact with the rotational disc, is illustrated in Figure II.48:

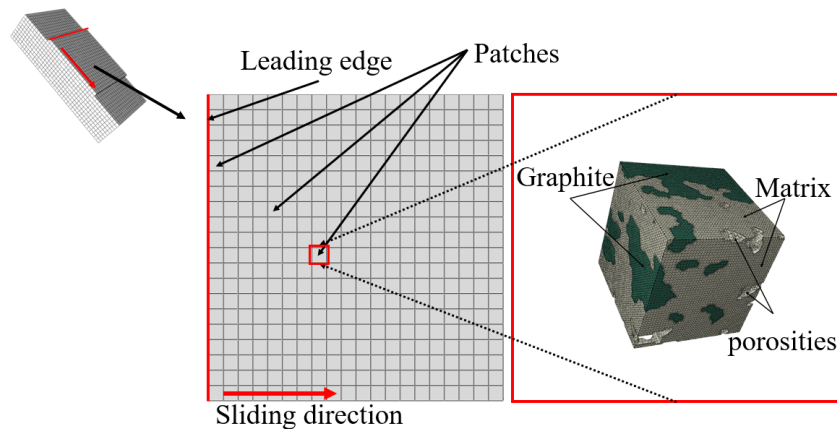


Figure II.48 – Discretized contact surface of the frictional pin: each macro element, is represented, at finer scale, by the biphasic microstructure.

The characteristic mesh size of the 3D cubical microstructure is $22.676e - 3 \text{ mm}$ and its material properties are presented in Table II.13.

Table II.13 – Elastic properties for the materials: biphasic microstructure.

| Real microstructure | Matrix | Graphite |
|-----------------------|--------|----------|
| Young's modulus (MPa) | 10000 | 2000 |
| Poisson's ratio | 0.1 | 0.1 |

After discretization of the whole frictional material into a set of patches, which at microscale is represented by the microstructure presented in Figure II.47, the overall behaviour of the complex microstructure is computed and embedded at each macro patch in terms of behaviour. Finally, a macro to micro computation, based on average boundary conditions presented in Figure II.39, is performed over the microstructure according to its position. One macro element per patch is used.

The whole multi-scale strategy is presented in Figure II.49:

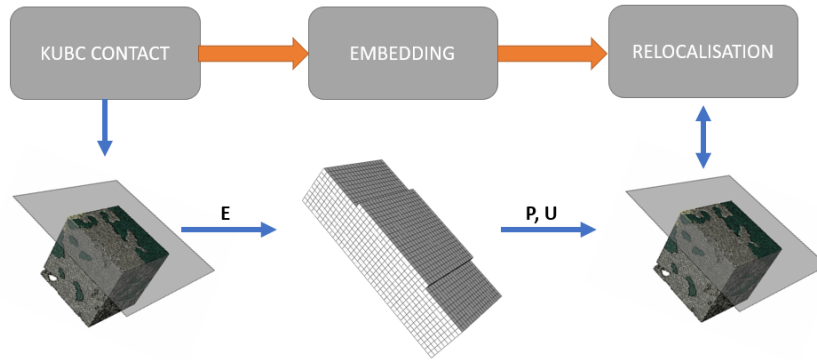


Figure II.49 – Multi-scale method for complex micro-structure application: micro-to-macro and macro-to-micro steps.

Micro model is shown in Figure II.50: All the computation has been done using 10

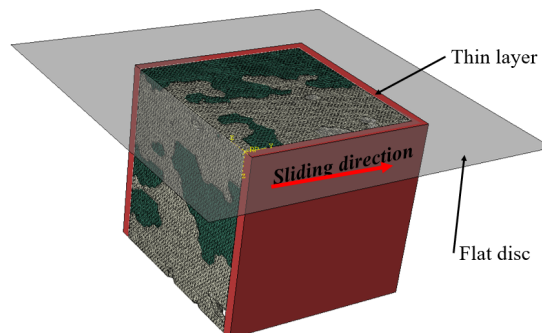


Figure II.50 – Micro model for mechanical field relocalization: complex micro-structure consideration.

CPU cores. Results are presented and discussed in the next subsection.

II.4.2 Results: isotropic elasticity assumption

In this subsection, multi-scale results are presented in the context of linear isotropic elasticity. In other words, homogenized quantities are computed assuming that the homogenized media is linear isotropic.

Two results are presented here:

Firstly, the homogenization results are computed from KUBC-Contact model. Then, equivalent quantities are obtained from equations (II.19) and (II.20) and summarized in Table II.14.

Table II.14 – Equivalent quantities computation under isotropic elasticity hypothesis: biphasic microstructure

| | Matrix | Graphite | KUBC-Contact |
|-----------------------|--------|----------|--------------|
| Young's modulus (MPa) | 10000 | 2000 | 7017 |
| Poisson's ratio | 0.1 | 0.1 | 0.1 |

A simple calculation through the mixture law gives an equivalent modulus of 7020 which is similar to the one obtained by KUBC-Contact homogenization method. Furthermore, experimental results performed in our lab, using different samples from this frictional material, give a similar homogenized quantity.

Secondly, the equivalent modulus obtained is embedded at the macro-scale model, in each patch, and a simulation is performed. After macroscopic computation, mean displacements and pressure in each macro patch are used in the micro model to get mechanical field induced by material heterogeneities. Micro contact pressure distribution of the heterogeneous microstructure, located at different positions (refer to Figure II.51) in frictional material contact surface, is presented in Figure II.52:

From patch 1 to 5, maximum pressure is obtained at the leading edge of the frictional material and decreases with sliding direction. This is confirmed by contact pressure distribution in patch 5 which is mostly reduce to zero. Results are very clear, in fact mean pressure used to enforce contact in the micro model becomes smaller from patch 1 to patch 5 (refer to Table II.15).

Table II.15 – Mean pressure comparison from patches 1 to 5.

| Bi-phasic microstructure | Patch 1 | Patch 2 | Patch 3 | Patch 4 | Patch 5 |
|--------------------------|---------|---------|---------|---------|---------|
| Mean pressure (MPa) | 7.24 | 1.70 | 1.56 | 1.33 | 0.35 |

Moreover, contact pressure repartition is higher in the matrix area than graphite because of matrix high rigidity compared to graphite which is softer. On the other hand, there is no pressure distribution on the zone where porosities are located but some localizations are observed at their boundaries. Furthermore, some contact separation is observed in patch 5

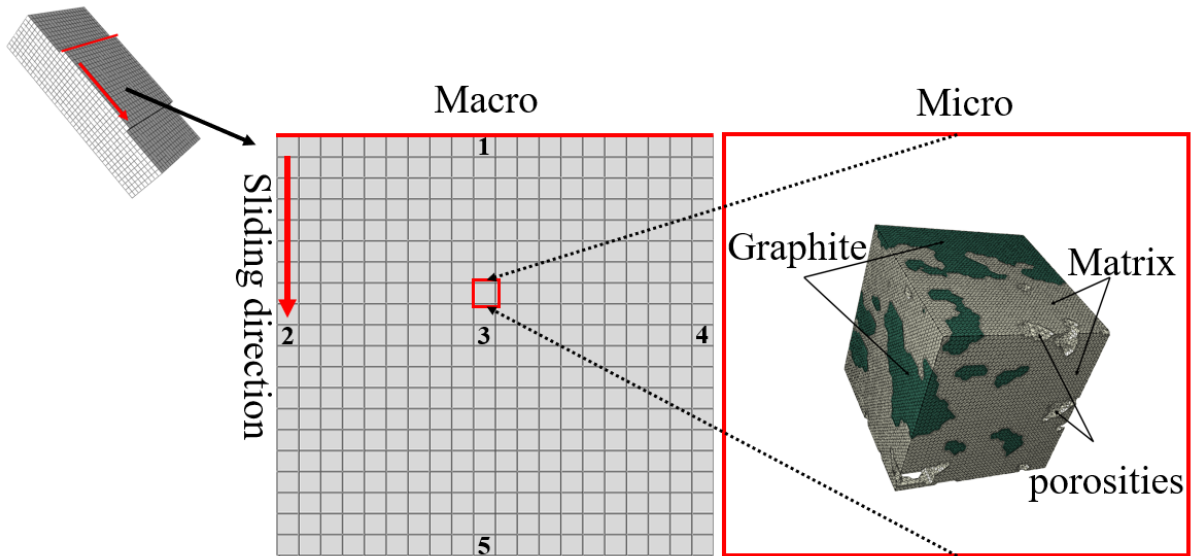


Figure II.51 – Studied macro patches.

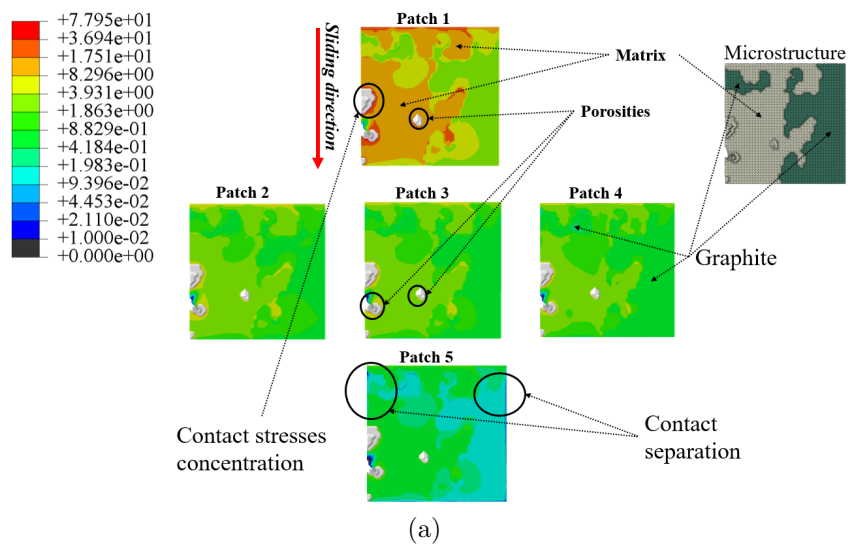


Figure II.52 – Frictional material contact pressure (MPa) distribution in the scale of heterogeneity using relocalization model: gray color refers to zero pressure.

contact area. In fact, contact pressure is almost reduced to zero at this zone, consequently leading to separation at some zones.

These results confirm then the robustness of the multi-scale method, based on KUBC-Contact homogenization method introduced in this work, to address contact problem in the presence of heterogeneities.

II.4.3 Results: transversely isotropic elasticity assumption

Transversely isotropic elasticity assumptions are considered here. The equivalent media, after homogenization of the biphasic microstructure, is supposed to be transversely isotropic. Therefore, equivalent quantities are computed from equations II.33 to II.38.

Firstly, homogenization results are illustrated in Table II.16. KUBC-Contact method is used for computation.

Table II.16 – Homogenization under transversely isotropic elasticity hypothesis by the means of KUBC-Contact: Equivalent constants (Young’s modulus (MPa), shear modulus (MPa) and Poisson’s ratio).

| | E1 | E2 | E3 | ν_{12} | ν_{13} | ν_{23} | G_{12} | G_{13} | G_{23} |
|--------------|-------|-------|-------|------------|------------|------------|----------|----------|----------|
| Graphite | 2000 | 2000 | 2000 | 0.1 | 0.1 | 0.1 | 909 | 909 | 909 |
| Matrix | 10000 | 10000 | 10000 | 0.1 | 0.1 | 0.1 | 4545 | 4545 | 4545 |
| KUBC-Contact | 6217 | 6460 | 5897 | 0.099 | 0.105 | 0.105 | 2910 | 2740 | 2784 |

As first observation, the equivalent quantities obtained in Table II.16 seem to be in good agreement with transversely isotropic hypothesis. In fact Young’s modulus in directions 1 and 2 are in the same order. Moreover, shear modulus G_{13} and G_{23} are approximately equivalents. Therefore, it can be supposed that the equivalent behaviour of the biphasic microstructure is transversely isotropic.

Secondly, it can be observed that Poisson’s ratio are approximately the same. Especially, in the isotropic plan (1-2), ν_{12} tends to 0.1. The latter seems to be well estimated.

As a final observation, Young’s modulus obtained with transversely isotropic assumptions are inferior to the one obtained with linear elastic assumptions (7017 MPa).

Then, equivalent quantities obtained in Table II.16 are enriched at the macro-scale model, in each patch, and a simulation is performed. Here, only patch 1 results are considered and compared to isotropic case. Results are presented in Figure II.53.

Figure II.53 presents contact pressure distribution, between isotropic and transversely isotropic micro models, over the patch 1 contact area. Patch 1 refers to the patch located at the leading edge of the frictional material as shown in Figure II.52. Contact pressure is higher in the matrix area because of its rigidity and decreases with the sliding direction. Same pressure distribution is obtained between the two models. However, maximum pressure is slightly different because, Young’s modulus obtained with the isotropic assumption is greater than the one obtained with transversely isotropic hypothesis. There is no great differences because of the weak anisotropy of this microstructure.

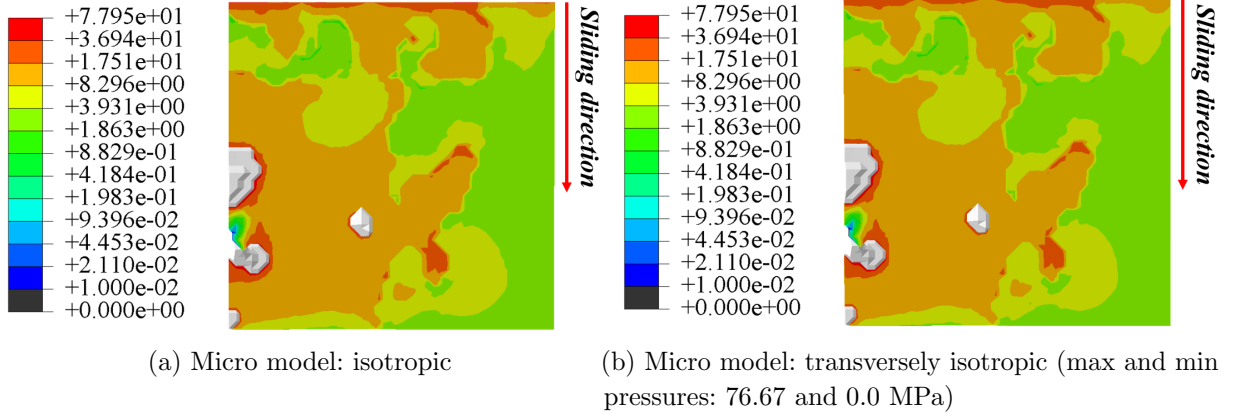


Figure II.53 – Micro contact pressure distribution over patch 1: gray color refers to zero pressure

II.5 Conclusions

In this work, a strategy leading to contact modelling of heterogeneous materials was presented.

Firstly, a simple heterogeneous configuration is considered for the numerical strategy implementation. This numerical strategy is a multi-scale homogenization-based method where contact constraints were added in one face of a heterogeneous patch, allowing then for macro to micro mechanical stresses relocation. The homogenization method including contact constraints, KUBC-Contact, is first validated with the classical KUBC homogenization method. Then, KUBC and KUBC-Contact multi-scale strategies are compared to a reference solution where heterogeneity was explicitly meshed. KUBC multi-scale solution is far from explicit results. Even though the average contact stresses are similar, the prediction in terms of contact stresses distribution is not good for KUBC multi-scale based method. However, the multi-scale strategy, based on KUBC-Contact, not only shows a similar average contact stresses with reference solution but also a similar contact stresses evolution is obtained.

Since the solution at edges is not well estimated, it was proposed a micro model with a layer in order to decrease edge errors. The important thing is the fact that the central part of the micro model, results are very well estimated.

Furthermore, KUBC-Contact multi-scale strategy has the advantage of considering high friction coefficient value from macro to micro scale. Results have been compared to reference solution and good agreements have been found.

Secondly, some complex cases have been investigated through a cubical inclusion located at contact interface. Good agreements in results have been found for small inclusion rigidity (edge errors are about 16% and 6% in patch central part). However, accuracy is lost in inclusion contact surface when its rigidity increases.

In order to improve results, another boundary condition, based on average macro to micro

contact force and displacements relocalization (Figure II.39), is proposed. Compared to the first KUBC-Contact distributed boundary relocalization, at each nodes of the heterogeneous patch boundaries, results were improved. In the case of cubical inclusion located at contact interface, the micro model gives satisfying results even for high inclusion rigidity. Therefore, average boundary conditions of Figure II.39 are used later in the following chapter.

Moreover, not only the average boundary conditions improve results, but they also allow computation time reduction. This is because these boundary conditions are not mesh dependent. The first boundary condition allows 50% computation time reduction. The average one allows 80% of computation saving. The strategy proposed here can be parallelized. Then, it is possible to generalize for highly heterogeneous materials and to save a lot of computation time.

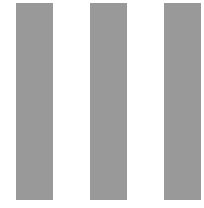
For instance, it was possible to consider a complex microstructure from tomography image which was embedded at the large scale through the KUBC-Contact homogenization method. Good results have been obtained and discussed.

Finally, the proposed multi-scale strategy is updated in the case of transversely elastic isotropic material.

This strategy was first implemented and validated through a simple heterogeneous example. Satisfying results are obtained compared to reference model.

Then, the transversely elastic isotropic hypotheses have been considered in the case of a complex microstructure, from tomography, previously enumerated. Results were compared to the elastic isotropic model and were not so different in terms of contact pressure distribution because of the weak anisotropy of this microstructure.

The main advantage of the macro to micro strategy is a computation time reduction compared to the brute method where all heterogeneities are explicitly meshed. Another advantage of the proposed strategy is a better estimation of the contact pressure evolution compared to the classical KUBC multi-scale based homogenization; thus allowing precision in tribological phenomena consideration, such as wear. Since wear depends on the distribution of contact pressure [Archard, 1953], the location of heterogeneities due to contact forces is important in computing the loss of wear volume. Our strategy allows not only to consider wear modelling, but also other mechanisms can be introduced (decohesion, cracking, etc). Another chapter is dedicated later to address wear modelling at the heterogeneities scale.



Modelling of non-smooth surface and evolution through wear by multi-scale approach with contact

The literature review exhibits the importance of surface scale consideration in the performances of braking systems. From the experimental point of view, it is well known that real surfaces are non-smooth and under contact solicitations present a complex evolution through wear. Therefore, a particular attention is devoted to surface irregularities and their evolution. Then this chapter is divided into two important parts: non-smooth surface modelling and surface evolution through wear.

Firstly, in the context of non-smooth surface modelling, only surface plateaux are considered through the multi-scale strategy. Two academic examples are investigated and validated with a reference solution. This strategy can deal with surface asperities, however, these aspects are not developed in this work and are restricted to surface plateaux (refer to [Waddad et al., 2016] for surfaces asperities consideration in a global brake system). The multi-scale strategy is based on KUBC-Contact homogenization method and a gap introduction in the contact law. The strategy is described in details later.

Secondly, a strategy leading to surface evolution (wear source flow) is introduced by temporal updating of contact gap. Results obtained have been compared with wear modelling strategies available in the literature. The wear modelling strategy based on contact gap is adopted and transposed to a large scale model. At the large scale, a simple heterogeneous case, where the matrix contains a spherical inclusion, is considered and results are compared to a reference solution.

Finally, a biphasic microstructure from tomography image is embedded at the large scale and wear is introduced at micro-scale through the multi-scale strategy. At the level of the biphasic heterogeneous material, different wear rate can be considered. Therefore, different wear evolution is observed and discussed. The introduction of local wear within the homogenization technique shows a variation of the macroscopic properties (Young's modulus and Poisson's ratio).

KUBC-Contact is still the main ingredient of the whole wear modelling strategy.

Mini-Contents

| | | |
|---------|--|------------|
| III.1 | Surface defects | 109 |
| III.1.1 | Strategy | 109 |
| III.1.2 | Global brake system with one surface plateau | 113 |
| III.1.3 | Global brake system with three surface plateaux | 116 |
| III.2 | Wear source flow modelling strategies | 122 |
| III.2.1 | Nodes displacement method | 122 |
| III.2.2 | Wear modelling using the subroutine Umeshmotion | 123 |
| III.2.3 | Strategy of gap : introduction of gap into the contact law in terms of wear depth | 126 |
| III.3 | Numerical example illustrating different wear strategies modelling . | 128 |
| III.3.1 | Results : Contact pressure evolution without wear | 128 |
| III.3.2 | Results : contact pressure distribution considering surface evolution | 129 |
| III.3.3 | Choice of best wear strategy method | 131 |
| III.4 | Wear modelling considering a large scale model: homogeneous material | 134 |
| III.4.1 | Numerical model | 134 |
| III.4.2 | Results | 135 |
| III.5 | Multi-scale strategy for wear modelling of the heterogeneous material | 138 |
| III.5.1 | Numerical example considering heterogeneous patch into the large scale model | 139 |
| III.5.2 | Numerical example considering microstructure from tomography image | 143 |
| III.6 | Application of the multi-scale strategy into a complete brake system considering real microstructure | 151 |
| III.6.1 | Numerical model and the global strategy | 151 |
| III.6.2 | Results and discussion | 152 |
| III.7 | Chapter synthesis | 161 |

III.1 Surface defects

Previously, material heterogeneity has been considered through a multi-scale approach considering linear isotropic elasticity. Moreover, this strategy was extended to a transversely elastic isotropic case. However, the contacted material surfaces are still perfect. In reality, material surfaces are not regular. In fact, at various scales, roughness is present on the surfaces. Under mechanical loading, for example braking applications, surfaces tend to worn and every wear particles trapped in the contact tend to form plateaux as noticed by [Eriksson and Jacobson, 2000]. Therefore, the consideration of this surface heterogeneity is important to estimate contact stresses evolution. In the context of numerical simulation, surface defects (roughness) modelling have been considered in complete brake system by the means of multi-scale methods for example in [Dufrenoy et al., 2016]. However, material heterogeneity is not considered in these works. Furthermore, roughness has been considered through a semi-analytical approach and therefore has many limitations in terms of defect geometry and their behaviour.

In this part, a multi-scale approach based on KUBC-Contact is proposed for surface defect incorporation in the presence of material heterogeneity. This strategy aims to be more general in the context of surface defect modelling. An example of surface plateaux is presented and validated with reference results.

The following subsection presents the strategy in which the surface defects modelling is based.

III.1.1 Strategy

A multi-scale strategy based on KUBC-Contact, previously introduced in Figure II.14, is adopted. The difference comes from the fact that the surface of the heterogeneous patch, obtained after the discretization of the whole friction material, is no longer smooth. Effective properties computation, material heterogeneity and surface defects, are still obtained by the KUBC-Contact homogenization method. However, the micro to macro embedding is modified to take into consideration surface defects. The whole strategy is summarized in Figure III.2:

Figure III.2 illustrates the strategy leading to contact modelling of heterogeneous material in the presence of surface defects and is based on 3 ingredients:

1. Computing the overall behaviour

As said before, this strategy is an extension of the multi-scale method presented in chapter II.

Firstly, a discretization of the entire surface of the heterogeneous material is done into a set of cubical patches containing material heterogeneity and surface defects. Secondly each patch, incorporating surface defects and material heterogeneities, is homogenized using KUBC-contact method; allowing then to obtain a behaviour which will be used in the following step.

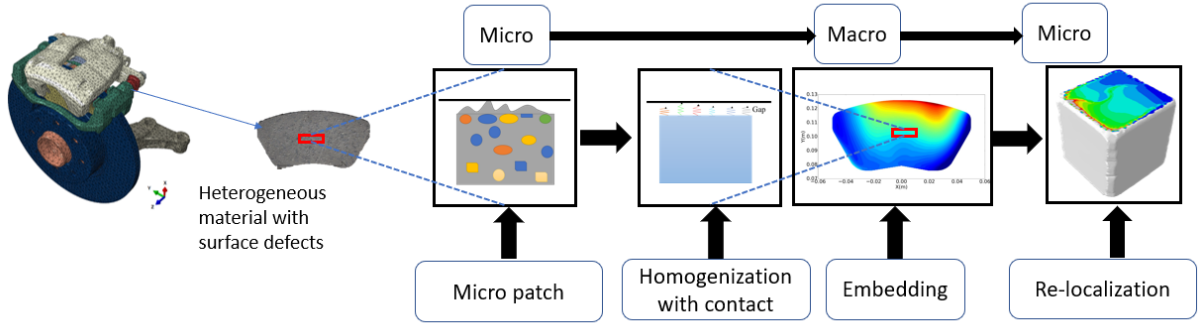


Figure III.1 – Material heterogeneity and surface defects: modelling strategy based on KUBC-Contact homogenization method.

2. Macro scale embedding

The macro-scale embedding problem is illustrated in the Figure III.2:

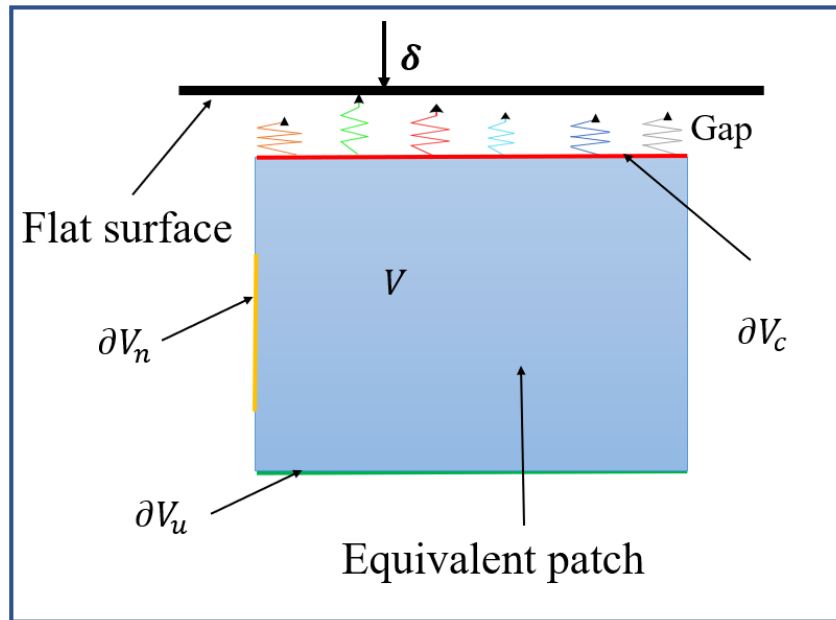


Figure III.2 – Macro-scale embedding problem: surface defect illustration

Figure III.2 shows an equivalent patch with surface defects represented by contact gap. Three boundary conditions have been identified: Neumann and Dirichlet boundary conditions (∂V_n and ∂V_u) and contact boundary condition represented by ∂V_c .

At the macro-scale, each patch is enriched with the behaviour obtained in the previous step and therefore becomes an equivalent patch. Let denote by E the Young's modulus computed from KUBC-Contact method. The stiffness k_{patch} of the overall patch can be deduced from equation (III.1):

$$k_{patch} = \frac{ES}{L}, \quad (III.1)$$

where S is the patch contact area and L the patch height.

Surface defects are represented, at the macro-scale, by a normal gap and a stiffness according to its location. In other words, at the zone where each surface defect is located, a normal gap g_n , which corresponds to the maximal defect height, is introduced. g_n is computed from equation (III.2):

$$g_n = \delta - U(x,y), \quad (\text{III.2})$$

where δ is the rigid body displacement and U the displacement of each surface defects due to the rigid body displacement.

The local stiffness of the defect, at the macro-scale, is obtained through equation (III.3):

$$k_{defect} = \frac{ES}{L_{defect}}, \quad (\text{III.3})$$

where S is the patch contact area and L_{defect} the defect height.

The contact condition is therefore defined by Kuhn–Tucker condition for frictionless contact problems. These constraints lead to the following set of inequation (III.4):

$$g_n \geq 0, p_n \geq 0, p_n g_n = 0, \quad (\text{III.4})$$

where p_n stands for the normal contact force.

Moreover, in the presence of friction forces, two states can be distinguished at the contact interface:

The stick state where the relative tangential velocity is zero according to (III.5):

$$\dot{g}_t = 0 \quad (\text{III.5})$$

The slip state where there is a relative velocity in the contact interface. Classically, sliding is described by Coulomb friction model as in equation (III.6):

$$t_t = -\mu |p_n| \frac{V_t}{\|V_t\|} \text{ if } \|t_t\| > \mu |p_n|, \quad (\text{III.6})$$

where g_t stands for the relative tangential slip, t_t the tangential force, V_t the relative velocity and μ the friction coefficient.

Considering an elastic isotropic media (Figure III.2), embedded with stiffness computed in equation (III.1) and having surface irregularities represented by a normal gap (equation (III.2)), subjected to a rigid body displacement and in the absence of body forces, the static equilibrium of the solid can be written as in equation (III.7):

$$\begin{cases} \text{div} \sigma = 0 \text{ in } V, \\ \sigma n = t_n \text{ in } \partial V_n, \\ u = u_0 \text{ in } \partial V_u \end{cases}, \quad (\text{III.7})$$

where σn and u are the boundary conditions for the stress and the displacement fields; with t_n and u_0 the prescribed quantities. Furthermore contact condition of the equation (III.4) has to be considered. Therefore we define the following condition on the contact boundary ∂V_c from equation (III.8):

$$g_n \geq 0 \text{ in } \partial V_c. \quad (\text{III.8})$$

FEM is used for the numerical resolution of the non-linear boundary value problem summarized above. Thus a weak form of equations (III.7) to (III.8) is needed. The weak form including contact constraints is written in equation (III.9):

$$\int_V \sigma \text{Grad}(\delta u) dV + \int_{\partial V_n} t_n \delta u d\gamma + C = 0, \quad (\text{III.9})$$

where C represents the contact contributions to the weak form equation. Several methods exist for the term C computation. Here we shall focus on a regularization method and more specifically on the penalty method [Kikuchi and Song, 1981]. The term C is expressed as in the following equation (III.10):

$$C = \int_{\partial V_c} (k_n g_n \delta g_n + k_t g_t \delta g_t) d\Gamma, \quad k_n > 0, \quad k_t > 0, \quad (\text{III.10})$$

where k_n and k_t represent the penalty coefficients in the normal and tangential directions respectively.

The penalty method leads to a violation of the contact constraints in equation (III.4). Therefore, a penalty coefficient can be chosen large enough to avoid large penetrations. In the latter case, an ill-conditioning of the global matrix can occur. Finally, in the context of finite element formulation, a Newton–Raphson iteration is often used to solve the global set of equations. For details, refer to [Wriggers, 1995]. After the macro global computation, a relocalization is performed to find macroscopic mechanical fields induced by surface and material heterogeneity.

3. Macro to micro relocalization

After the macro computation is done, macro contact forces and displacements are obtained and a relocalization is performed at the micro model where material and surface heterogeneity are explicitly meshed. This step is largely explained in chapter II. However, in the following, the boundary conditions used for the micro model incorporating surface defects are briefly presented.

These boundary conditions are inspired from Figure II.39 boundary conditions detailed in Figure II.39 (chapter II). Without further discussions, these boundary conditions are presented in Figure III.3.

Compared to the average boundary conditions under perfect contact, where surface defects were not considered, the exterior faces of the layer is submitted to average displacement to prevent excessive patch deformation during contact enforced between surface rigid disc and defects.

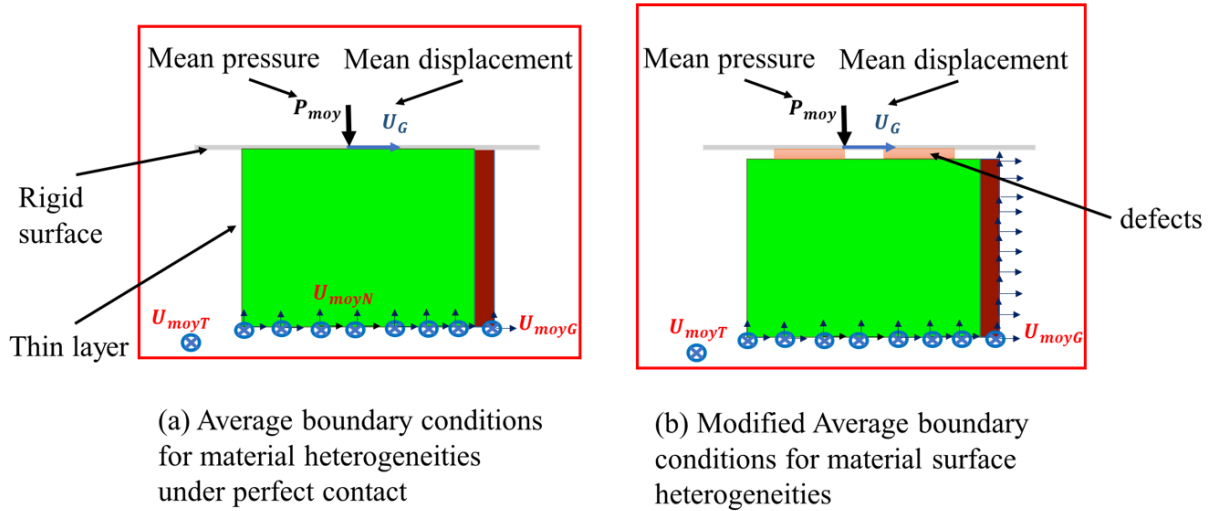


Figure III.3 – Modified average boundary conditions: additionally average displacements are applied to the exterior faces of the layer, in order to prevent excessive deformation of the heterogeneous patch due to contact between rigid surface and defects.

III.1.2 Global brake system with one surface plateau

III.1.2.1 Model description

The 3D numerical FEM model inspired by the experimental pin-on disc system shown in Figure II.2 is still used for our purpose. Figure III.4 shows a heterogeneous patch, containing a centred spherical inclusion, placed at the leading edge of the friction material. Moreover, a defect of height 0.033 mm and surface area 0.16 mm^2 is present in the heterogeneous patch surface. This choice is arbitrary. The total area of the patch is 1 mm^2 . The inclusion of radius 0.35 mm is placed at 0.15 mm from the contact surface and centred within the patch. The constitutive law of the whole material is elastic isotropic. The surface defect has the same material property as the whole patch. Material properties are presented in Table III.1.

Table III.1 – Elastic properties for numerical model different components: presence of the material and surface heterogeneities.

| | Young's modulus (MPa) | Poisson's ratio |
|---------------------------|-----------------------|-----------------|
| Friction pin and defect | 3000 | 0.3 |
| Inclusion | 200000 | 0.3 |
| Disc and other components | 220000 | 0.3 |

Same boundary conditions as in chapter 2 are used: a prescribed displacement of 0.2 mm is applied to enforce contact between the frictional material and the disc at a time period of $t = 1 \text{ s}$. The disc is still rotating with a constant velocity of 0.1 rad/s . Penalty method is used, as previously explained, for contact constraints resolution with a friction

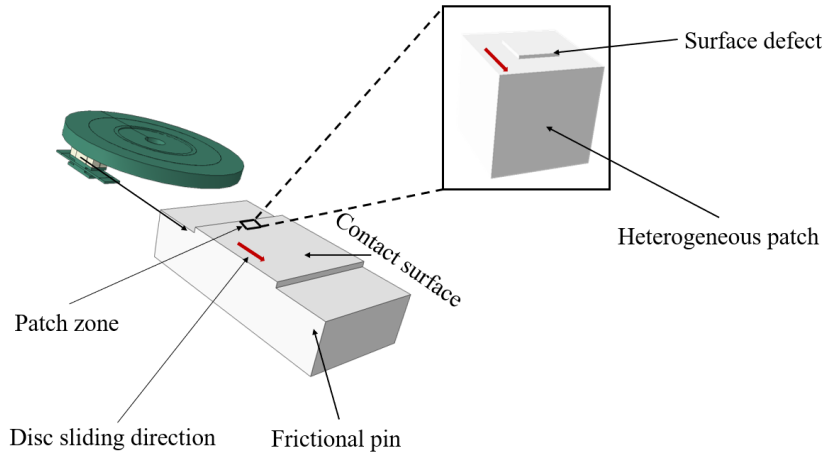


Figure III.4 – Material heterogeneity associated to surface defects strategy: surface defect is located at the heterogeneous patch surface containing a spherical inclusion; the heterogeneous being located at the leading edge of the frictional pin.

coefficient of 0.3. The complete model is meshed with 141065 hexahedrons elements and 162469 nodes.

III.1.2.2 Explicit results

In order to put in evidence, the influence of material heterogeneity, two results are investigated in this subsection: a heterogeneous case where the inclusion is very rigid and a homogeneous case where the inclusion properties are set to be equal to those of the matrix. Results are illustrated in the Figure III.5:

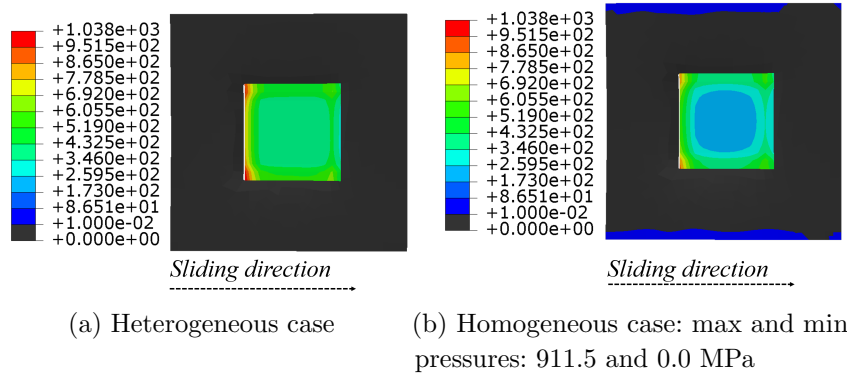


Figure III.5 – Explicit model in the presence of inclusion and surface plateau: heterogeneous versus homogeneous contact pressure distribution

Figure III.5 presents explicit model contact pressure distribution between heterogeneous (in the presence of inclusion and surface plateaux) and homogeneous (in the presence of surface plateaux only) cases. Results have been put on the same scale. An overpressure is observed at the leading edge of the defect and it decreases with sliding

direction. Moreover, the defect carries out mostly the contact constraints. The maximum contact pressure of the heterogeneous case is 1038 MPa whereas the maximum pressure of the homogeneous case is 911.5 MPa. Furthermore, in Figure III.5 (b), the contact area is more extended outside the area of the surface defect while in III.5 (a), there is no contact outside the defect area. Then, material heterogeneity influences contact surface evolution in the presence of the surface plateau.

In the next subsection, a multi-scale strategy is implemented and compared to heterogeneous explicit results.

III.1.2.3 Explicit versus multi-scale results

Firstly, using KUBC-Contact, an equivalent modulus is obtained from the heterogeneous patch composed of a spherical centred inclusion and a surface defect. The whole homogenization model is meshed mostly with 42924 hexahedrons elements and 49552 nodes. Homogenized quantities are presented in Table III.2.

Table III.2 – Equivalent modulus computation through KUBC-Contact homogenization method: presence of both material and surface heterogeneities.

| | Young’s modulus | Poisson’s ratio |
|--------------------|-----------------|-----------------|
| Matrix with defect | 3000 MPa | 0.3 |
| Inclusion | 200000 MPa | 0.3 |
| KUBC-Contact | 4493 MPa | 0.28 |

Secondly, the equivalent modulus, obtained in Table III.2, is enriched at macro-scale model according to the strategy summarized in Figure III.2. The complete model is meshed with 54406 hexahedrons elements and 68154 nodes.

After macro computation, contact forces and displacements are obtained in the patch contact area. Macro mean contact force, from an equivalent model, is compared to the explicit model mean contact force and presented in Table III.3.

Table III.3 – Contact force between explicit and multi-scale models: heterogeneous patch containing spherical inclusion and one surface plateau.

| Contact force | Explicit | Multi-scale model |
|---------------|----------|-------------------|
| Case 1 | 71.8 N | 71.7 N |

As we can see in Table III.3, contact force between explicit and multi-scale model is equivalent. To validate our strategy, a micro computation is still needed. Therefore, contact pressure distribution between explicit and micro models is compared in Figure III.6.

Results have been put on the same scale. At the leading edge, where the defect is located, an overpressure is obtained which decreases with sliding direction. A good agreement, in contact pressure distribution, is observed between the two models. There is no contact

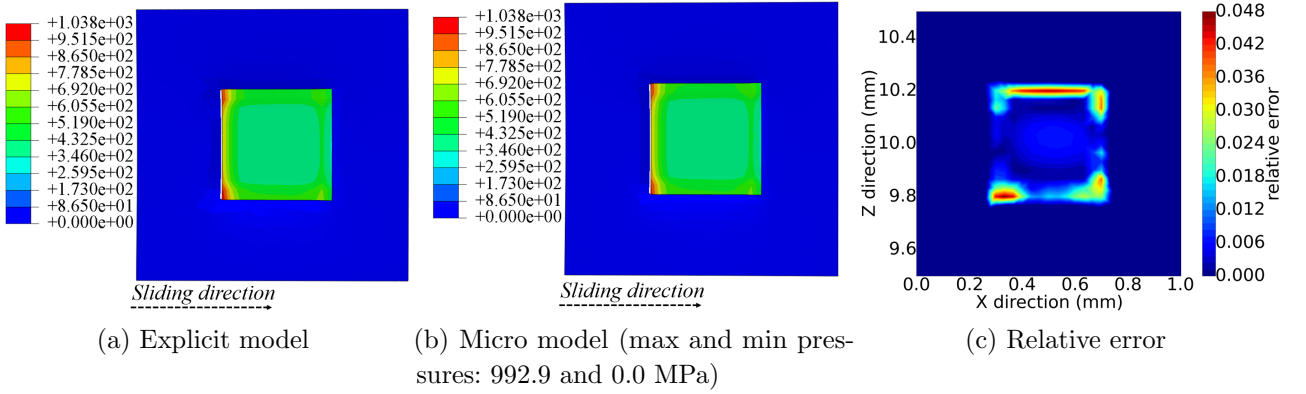


Figure III.6 – Explicit versus relocation contact pressure distribution in the presence of inclusion and surface defect.

pressure outside defect contact area. As mentioned earlier, contact load is carried by the defect which is considered as surface plateau. This aspect is well estimated by the proposed multi-scale model. Relative errors are shown in Figure III.6 (c). Maximum errors are observed at some points and are less than 5%. However, in most of the plateau area, errors tend to zero.

Moreover, overclosure, normal displacement and contact stiffness, between multi-scale and explicit models, are compared to each other and are shown in Table III.4.

Table III.4 – Contact stiffness: multi-scale versus explicit models

| Plateau | Overclosure | Normal displacement | Contact stiffness |
|-------------------|------------------|---------------------|-------------------|
| Multi-scale model | $-3.72e^{-3}$ mm | $-10.40e^{-3}$ mm | 477.719 N/mm |
| Explicit model | $-3.73e^{-3}$ mm | $-9.45e^{-3}$ mm | 477.621 N/mm |

Contact stiffness is obtained by computing the ratio between contact force and gap through the plateau surface. As shown in Table III.4, the contact stiffness, the overclosure and the normal displacement between both explicit and multi-scale models are in a good agreement. From the foregoing, it appears that the proposed multi-scale strategy can then be extended to complex cases.

A more complex case, where more defects are placed directly near the edges of the heterogeneous patch, is investigated in the next section.

III.1.3 Global brake system with three surface plateaux

III.1.3.1 Model description

This section aims to an investigation of a more complex case through the numerical strategy. As seen before, the multi-scale strategy is based on frictional material discretization. So, the complicated situation we can imagine is when defects are located near edges.

This limit case is considered here to show the efficiency or the limits of our multi-scale method to such cases. Therefore, a numerical model is proposed in Figure III.7:

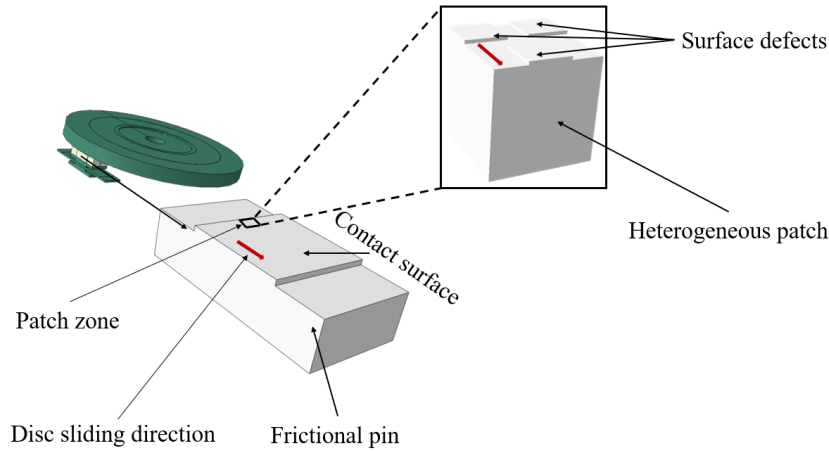


Figure III.7 – Large scale numerical model with three plateaux: plateaux are located at the heterogeneous patch surface containing a spherical inclusion; the heterogeneous being located at the leading edge of the frictional pin.

Figure III.7 shows the numerical model where a heterogeneous patch, with three surfaces defects located at the edges, is placed at the leading edge of the frictional material. The three defects have the same surface and height, 0.16 mm^2 and 0.033 mm respectively. The area of the overall patch, where the defects are located, is 1 mm^2 . The dimensions of the surface plateaux are chosen arbitrary. The three defects have the same material properties as the matrix. Moreover, the inclusion is centred within the matrix. Material properties of this new numerical model are the same as the first model presented in Table III.1. Penalty method is used for contact constraints resolution with a friction coefficient of 0.3. The complete model is meshed with 141616 hexahedron elements and 163333 nodes.

III.1.3.2 Results

Two models configuration are compared here: reference model and multi-scale model results. Firstly, we shall focus on KUBC-Contact homogenization results which is the first step of the multi-scale strategy. KUBC-Contact model is meshed with 43095 hexahedrons elements with 49656 nodes. After computation, results obtained are shown in Table III.5. Then, these homogenized quantities are enriched in the macro-scale embedded model. The complete embedded model is meshed with 122042 hexahedrons elements and 147030 nodes. The heterogeneous patch is, therefore, replaced by a homogeneous macro patch having the behaviour computed by KUBC-Contact. Moreover, appropriate gap is used in the contact law where defects are located. Therefore, a macro computation is performed followed by a macro to micro mechanical field relocalization.

Contact force, between explicit and multi-scale model, is compared in Table III.6.

Before going to the final step where we compare contact pressure distribution between

Table III.5 – Equivalent modulus computation using KUBC-Contact: presence of material heterogeneity and three surface plateaux.

| | Young's modulus | Poisson's ratio |
|--------------|-----------------|-----------------|
| KUBC-Contact | 4476 MPa | 0.28 |

Table III.6 – Contact force between explicit and multi-scale models: heterogeneous patch containing spherical inclusion and three surface plateaux.

| Contact force | Explicit | Multi-scale model |
|---------------|----------|-------------------|
| Case 2 | 126.6 N | 126.4 N |

explicit and micro relocalization model, it is worthy to remark, in Table III.6, that macro mean contact forces is well estimated between explicit and multi-scale models.

Contact pressure evolution between explicit and multi-scale models is illustrated in Figure III.8.

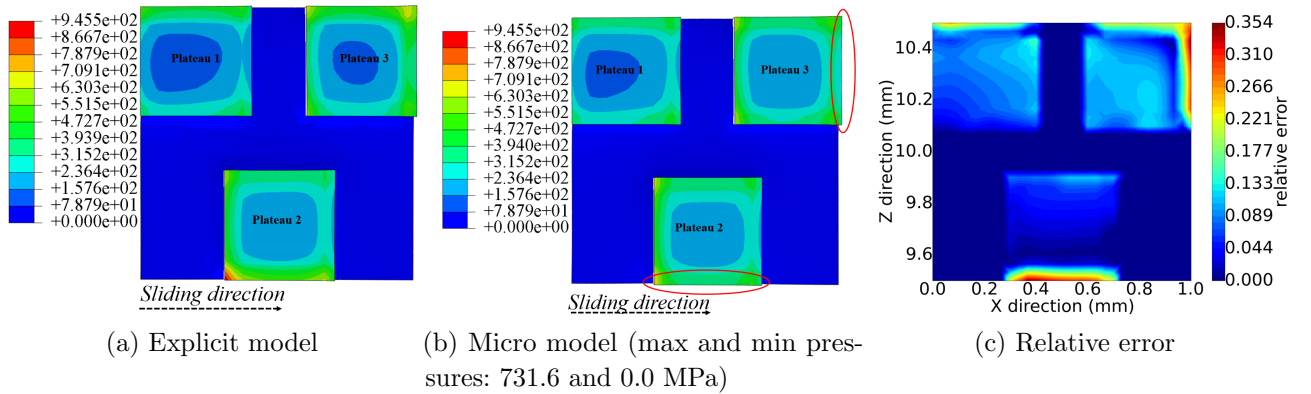


Figure III.8 – Explicit versus relocalization contact pressure distribution: heterogeneous patch containing inclusion and 3 surfaces defects

Results have been put on the same scale. Figure III.8 (a) presents explicit contact pressure evolution in the heterogeneous patch surface composed of three defects located near patch edges. Figure III.8 (b) shows micro model contact pressure distribution. Outside of defects contact surface, the pressure intensity is zero for both models. At each defect contact zone, micro model contact pressure gives good estimations. There is a similar pressure evolution between both micro and explicit models. However, some differences exist and are very highlighted especially at plateaux 2 and 3 edges. This is confirmed by relative errors shown in Figure III.6 (c). The zones which are not well estimated are surrounded in red in Figure III.8 (b). These errors are possibly due to the fact, in the present configuration, surface plateaux are placed near heterogeneous patch edges causing then edges effects. But, the important thing is that, in almost all the area of the 3 surface plateaux, contact pressure is well estimated.

Moreover, displacements, in sliding direction, of both explicit and micro models are

illustrated in Figure III.9.

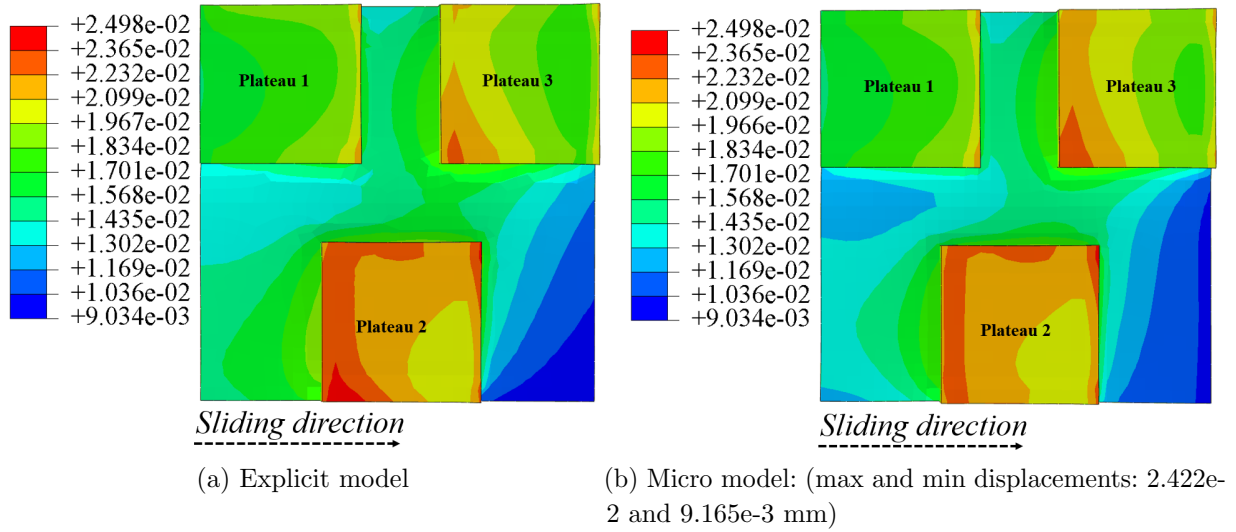


Figure III.9 – Displacements distribution in the sliding direction: micro model composed of heterogeneous patch; containing inclusion and 3 surfaces defects.

These displacements shown in Figure III.9 (b) are very well estimated.

On the other hand, average contact force, overclosure, normal displacements and contact stiffness have been computed at each plateau contact surface. Results have been compared between micro and explicit models and illustrated in Tables III.7, III.8, III.9 and III.10.

Table III.7 – Average force per plateau: multi-scale versus explicit models (three surface plateaux)

| Average force | plateau 1 | plateau 2 | plateau 3 |
|-------------------|-----------|-----------|-----------|
| Multi-scale model | 41.9 N | 49.5 N | 34.9 N |
| Explicit model | 35.3 N | 47.1 N | 44.1 N |

Table III.8 – Overclosure per plateau: multi-scale versus explicit models (three surface plateaux).

| Overclosure | Plateau 1 | Plateau 2 | Plateau 3 |
|-------------------|------------------|------------------|------------------|
| Multi-scale model | $-1.90e^{-3}$ mm | $-2.39e^{-3}$ mm | $-2.27e^{-3}$ mm |
| Explicit model | $-1.83e^{-3}$ mm | $-2.45e^{-3}$ mm | $-2.29e^{-3}$ mm |

As seen in Table III.7, plateau 2 average force is approximately equivalent between the two models. Plateaux 1 and 3 average forces are a little bit different, especially at plateau

Table III.9 – Normal displacement per plateau: multi-scale versus explicit models (three surface plateaux).

| Normal displacement | plateau 1 | plateau 2 | plateau 3 |
|---------------------|------------------|------------------|------------------|
| Multi-scale model | $-9.01e^{-3}$ mm | $-9.15e^{-3}$ mm | $-9.12e^{-3}$ mm |
| Explicit model | $-9.05e^{-3}$ mm | $-9.10e^{-3}$ mm | $-9.19e^{-3}$ mm |

Table III.10 – Contact stiffness per plateau: multi-scale versus explicit models (three surface plateaux).

| Contact stiffness | Plateau 1 | Plateau 2 | Plateau 3 |
|-------------------|------------|------------|------------|
| Multi-scale model | 474.5 N/mm | 472.1 N/mm | 470.8 N/mm |
| Explicit model | 474.2 N/mm | 471.5 N/mm | 469.4 N/mm |

3. This can be justified by the errors observed at the edge of this plateau in Figure III.6 (c). However, the sum of average forces of the three plateaux are equivalent between both multi-scale and explicit models.

Next, overclosures and normal displacements of the 3 surface plateaux are compared to explicit ones. Results are illustrated in Tables III.8 and III.9. Good agreements are obtained.

Finally, as seen in Table III.10, the contact stiffness between the two models configuration is approximately the same.

Regarding all the quantities compared, efficiency of the numerical strategy proposed for surface defects modelling is proven and can be used for all cases.

III.1.3.3 Computation time

One of the advantages of the multi-scale strategy we propose in this work is the computation time reduction for large scale models. In fact, as the heterogeneity and surface defects in each patch are not physically present in the large-scale model, this leads to a gain of computation time.

Presented in Table III.11, is the computation time between explicit and multi-scale surface defects models. The simulation is conducted using 10 CPU cores.

Table III.11 – CPU time comparison between both explicit and multi-scale models: surface defects modelling

| time | Model with one plateau | Model with three plateaux |
|-------------------------|------------------------|---------------------------|
| Explicit model | 242 min | 296 min |
| Multi-scale macro model | 43 min | 122 min |
| Multi-scale micro model | 17 min | 17 min |

There is a significant reduction in computation time with the proposed multi-scale strategy. However, it is possible to gain more computation time in the multi-scale macro model by

working more on its development.

Moreover, if material heterogeneity and surface defects are considered over the whole frictional material, there will be a tremendous gain in computation time. Because, in that configuration, only explicit model will be very expensive.

Conclusion of the section

In this section, a strategy leading to material and surface heterogeneities modelling, is implemented and compared to a reference solution where heterogeneity and defects are meshed explicitly. Surface plateaux are considered for our purpose and good agreements in results are obtained. In this work, even if only surface plateaux cases are investigated, other types of surface defects, for example surface asperities, can be considered also.

The strategy implemented is mainly based on contact gap introduction at the defects location. In the next section, this strategy is extended to surface evolution through wear source flow. In the following sections, the new proposed strategy for wear source flow modelling is explained in details and is compared to some concurrent wear modelling strategies available in the literature.

III.2 Wear source flow modelling strategies

III.2.1 Nodes displacement method

In many works in literature [Podra and Andersson, 1999; Hegadekatte et al., 2004; de Saracibar and Chiumenti, 1999], wear modelling is based on nodes displacement method. The strategy is quite simple and consists in shifting contact surface nodes in the contact forces direction. Wear volume is computed through specific wear law which will be described in next subsection. Nodes displacement strategy is presented in Figure III.10.

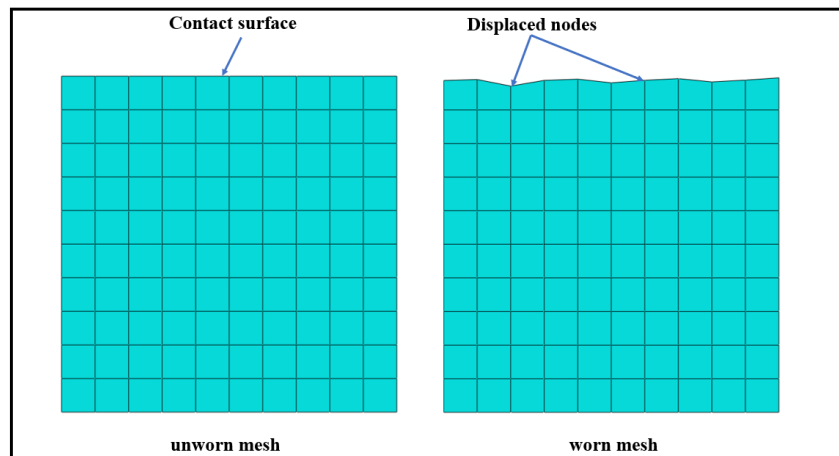


Figure III.10 – Wear modelling based on contact surface nodes displacement.

This method has some limitations. In fact, obtaining good results depends on mesh size in the contact zone. Also, as the nodes are displaced, elements can be submitted to excessive distortions causing convergence difficulties. Additionally, when wear depth is greater than element size, surface elements become excessively distorted and computation is no longer possible. To overcome these issues, it is possible to move not only surface nodes but also sub-surface nodes through a linear law for example. In other words, all displaced nodes will follow a linear distribution. An example of the latter configuration is shown in Figure III.11:

In Figure III.11, a case where only surface nodes are displaced is compared to a case where all nodes follow a linear distribution. It is then possible to reduce elements distortion by doing so. However, this method is also limited. Mesh distortions due to the nodes displacements constitute a principal limitation of the present strategy. Another limitation which is attributed to the nodes displacement strategy is the wear introduction at the end of each calculation. Then it is not possible to introduce wear effects directly in the analysis. In the next subsection, a subroutine, dealing with wear modelling, developed in the calculation code ABAQUS, is introduced.

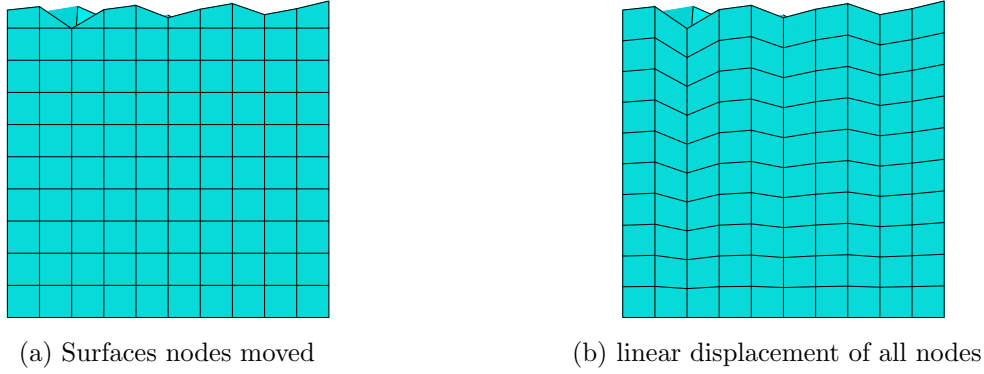


Figure III.11 – Contact surface nodes displacements versus linear distribution of all nodes.

III.2.2 Wear modelling using the subroutine Umeshmotion

III.2.2.1 Adaptive Meshing

In finite element analysis, when deformation takes place, some elements become distorted and may not produce good results. Adaptive meshing consists in, principally, two tasks: new mesh creation through a process called mesh sweeping, and a remapping solution variables from old to new mesh through a process called advection (refer to **ABAQUS 6.13** [LeVeque et al., 2002]).

1. Mesh sweeping

After convergence of the structural equilibrium equations, adaptive meshing will require wear displacement at each node of the contact surface, computed through Fortran subroutine umeshmotion. Then, mesh sweeping is performed over adaptive mesh domain, where nodes have to be relocated. Relocalization of each node in the domain is based on the positions of neighboring nodes. The new position, x_{k+1} , of a node is obtained through equation (III.11):

$$x_{k+1} = X + u_{k+1} = N^n x_k^n \quad (\text{III.11})$$

Where X is the original position of the node, u_{k+1} the nodal displacement, x_k^n are the neighboring nodal positions, N^n are weight functions obtained from least square minimization method which minimizes node displacement in a projection to the original mesh configuration. Also, weight functions can be obtained from volume smoothing by computing volume-weighted average of the element centre positions surrounding a node. Mesh sweeping allows for a smooth mesh and also reduces element distortion.

2. Advection

In [LeVeque et al., 2002], advection process refers to a substance being carried along with fluid motion. In adaptive meshing, advection is the process in which the solution variables are re-mapped from the old mesh to the new mesh by integrating the

advection equation (refer to [LeVeque et al., 2002]) by the means of the Lax-Wendroff numerical method which is second-order accurate in both space and time (refer to [Lax and Wendroff, 1960]).

Let's consider a linear advection equation from (III.12):

$$\frac{\partial q}{\partial t} + a \frac{\partial q}{\partial x} = 0. \quad (\text{III.12})$$

Equation III.12, when we apply Lax-Wendroff numerical method, gives birth to III.13.

$$q_j^{n+1} = q_j^n - \frac{a\Delta t}{2\Delta x}(q_{j+1}^n - q_{j-1}^n) + \frac{(a\Delta t)^2}{2\Delta x^2}(q_{j+1}^n - 2q_j^n + q_{j-1}^n), \quad (\text{III.13})$$

where n is the time increment, j the node number in the adaptive mesh domain, q is the solution variable being advected (contact pressure, stresses, displacement etc.), a is advection velocity, Δt and Δx are increments in time and space respectively.

In the next subsection, a wear modelling methodology based on adaptive meshing is described.

III.2.2.2 Wear source flow modelling strategy based on adaptive meshing

Here, adaptive meshing is used in conjunction with a **FORTRAN** subroutine called **UMESHMOTION** in which a wear model is developed. In this work, the wear model adopted is derived from Archard's wear law:

$$\frac{V}{s} = \frac{k}{H} * F_N, \quad (\text{III.14})$$

where V is the volume of the removed material, k is the dimensionless wear coefficient, s is the sliding distance, H is the hardness of the softer material and F_N is the applied normal load.

By dividing both sides of equation (III.14) by the real area of contact, we get the wear depth expression in (III.15):

$$\frac{h}{s} = \frac{k}{H} * p, \quad (\text{III.15})$$

where p is the contact pressure. The discretized form of equation (III.15) with respect to s is obtained from (III.16):

$$\frac{dh}{ds} = \frac{k}{H} * p. \quad (\text{III.16})$$

By integrating equation (III.16) over the sliding distance, the total wear depth is computed as in (III.17):

$$h_{i+1} = h_i + kp_i ds, \quad (\text{III.17})$$

where h_{i+1} is the total wear depth up to the $(i + 1)th$ wear increment, h_i is total wear depth up to the ith wear increment, p_i is the contact pressure during ith wear increment and $kp_i ds$ is the wear depth for the current wear increment.

The modified form of Archard law is then embedded into **ABAQUS/Standard** with **FORTRAN** subroutine **UMESHMOTION**. The link between **ABAQUS** and **UMESHMOTION** is summarized in Figure III.12:

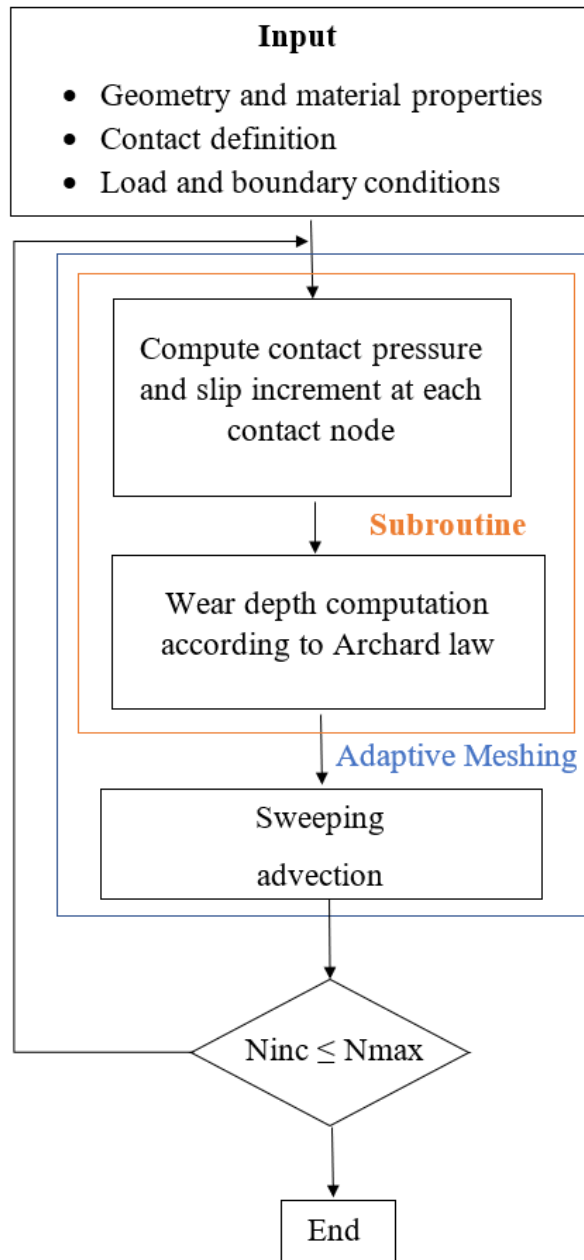


Figure III.12 – Flowchart of the link between ABAQUS and UMESHMOTION.

Where N_{inc} is the current increment number and N_{max} is the maximum increment number. After the equilibrium equations, have converged, **ABAQUS** makes request to the **adaptive meshing** algorithm, previously explained, which in turn call the user defined subroutine **UMESHMOTION**. Then, nodal coordinates, nodal displacements

and respective contact pressures are accessed. Wear depth in this time increment is computed, using equation (III.16), for all surface nodes in the subroutine. Thereby, wear depth for all surface nodes are returned to the adaptive meshing algorithm. The surface nodes are then swept in two steps. First, the surface nodes are swept in the inward normal direction using Eulerian analysis and then the geometry is updated. In the last step, material quantities are re-mapped to the new mesh positions by advection using a Lax-Wendroff method (second order numerical method explained before). The contact pressure and all other material quantities are then updated.

In the next subsection, another wear modelling strategy, which is a continuation of the defects modelling strategy introduced previously, is investigated.

III.2.3 Strategy of gap : introduction of gap into the contact law in terms of wear depth

This strategy is very simple and consists in contact law modification in a way to account for wear. Penalty contact algorithm is still used in this chapter to enforce contact constraints.

The strategy introduced here is a wise use of penalty contact to simulate wear. Contact constraint is imposed at the level of each element of the contact surface followed by an initial gap introduction in the contact law which in return is updated temporally. The initial gap corresponds to wear depth computed from equation (III.15) and introduced in the penalty contact law at each element. Thus, the modified contact law, accounting for wear in terms of gap, is illustrated in Figure III.13:

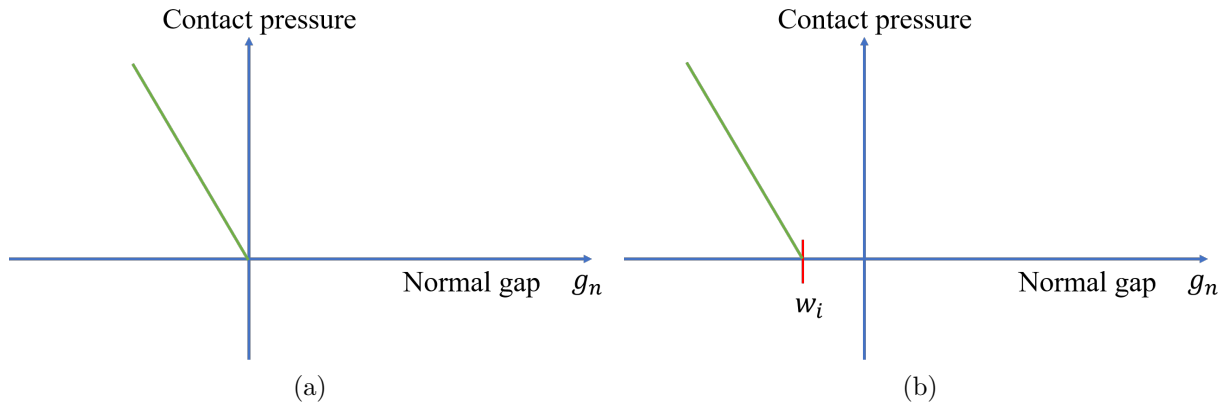


Figure III.13 – Graphical representation of contact laws: In penalty method, the initial gap is reduced to zero (a). In order to consider wear, initial gap corresponds to wear depth in the penalty method (b)

g_n is the normal gap distance of the interface, P_n is the normal contact pressure and w_i is the initial normal gap corresponding to wear depth of element i .

Moreover, a flowchart of the complete strategy is presented in Figure III.14:

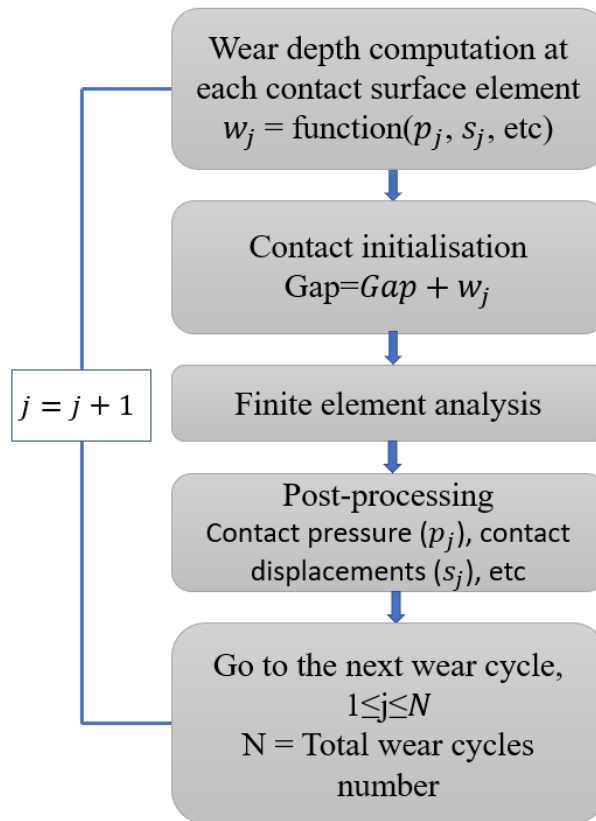


Figure III.14 – Wear modelling strategy: gap updating in the contact law after each wear cycle (transient process).

The strategy presented in Figure III.14 is very simple: at the beginning of the simulation, the surface is not subjected to wear, therefore the initial gap is reduced to zero. At the end of each simulation, the gap is updated in the contact law in terms of the wear depth computed from Archard’s wear model until the total wear cycle is reached.

In this subsection, three wear modelling strategies were presented. The robustness of these strategies is investigated in the next subsection through a simple numerical simulation.

III.3 Numerical example illustrating different wear strategies modelling

The different wear strategies of the previous section are confronted here. Therefore, we shall present a numerical model for the investigation.

A flat rigid surface in contact with an elastic isotropic cubical material of 1 mm^3 , under sliding conditions, is considered. No rigid surface rotation is allowed. Moreover, the cubical part is homogeneous. The material properties of the cubical part are summarized in Table III.12:

Table III.12 – Material properties of the numerical model.

| | |
|-----------------|--------------|
| | Cubical part |
| Young's modulus | 3000 MPa |
| Poisson's ratio | 0.3 |

A normal and tangential displacements of 0.01 mm and 0.2 mm respectively have been applied to the flat rigid surface. The bottom face of the cubical part has been fixed. 27000 and 900 hexahedrons elements have been used to mesh the cubical part and the flat surface respectively. The mesh size of each contacted element is 0.033 mm . Moreover, penalty contact is used to enforce contact constraints with a constant friction coefficient set to 0.3. The whole model, its boundary conditions and its mesh, is shown in Figure III.15.

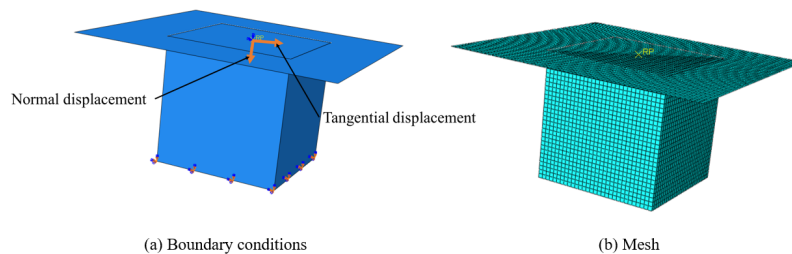


Figure III.15 – Numerical model: a rigid flat surface rubbing on a cubical part.

A simulation is performed with the above statements and results are presented in the next subsection

III.3.1 Results : Contact pressure evolution without wear

With the model described in Figure III.15, a simulation is performed under the consideration of perfect surface. Results are shown in Figure III.16.

Figure III.16 shows contact pressure evolution through the contact surface of the homogeneous patch. Pressure distribution is conventional, there is an overpressure at the

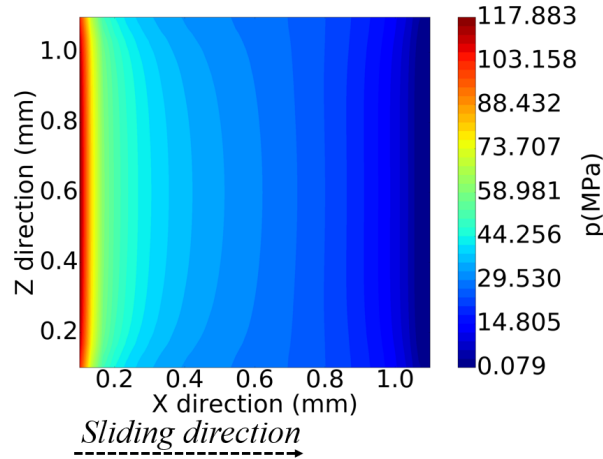


Figure III.16 – Numerical model: contact pressure evolution without wear.

leading edge which decreases with sliding direction (direction X). As expected, the pressure is uniformly distributed through the whole surface.

III.3.2 Results : contact pressure distribution considering surface evolution

The model illustrated in Figure III.15 is extended to wear (source flow) modelling considering the three wear strategies previously described. Therefore, three simulations are performed. These correspond to wear source flow modelling from nodes displacement, subroutine `umeshmotion` with adaptive meshing, and gap methods respectively. Archard's wear model (III.15) is considered. The term $\frac{k}{H}$, the wear rate, has been chosen arbitrarily and equals to $1e - 6 \text{ mm}^2/N$. 100 wear cycles, which is represented by 100 contact updates, are considered. However, for subroutine `Umeshmotion`, the computation is performed iteratively. Results are shown in Figure III.17:

Figure III.17 (a) shows contact pressure evolution under the assumption of perfect contact during the whole analysis. Pressure distribution is conventional, there is overpressure at the leading edge which decreases with sliding direction. Figures III.17 (b), (c) and (d) show contact pressure distribution for 100 wear cycles obtained from nodes displacements, subroutine `umeshmotion` and gap techniques respectively.

In Figure III.17 (b), the leading edge contact pressure is overestimated. In fact, the maximum pressure is about 130 MPa greater than the contact pressure of the perfect contact case (117 MPa). This is not logical since a decrease of contact pressure with wear is expected. This overestimation can be attributed to mesh distortion especially at the leading edge where contact pressure is higher initially. Hence contact constraints resolution become very difficult at the leading edge. Moreover, contact pressure is not uniformly distributed; confirmed by the zone surrounded in red (see the blue band of the Figure III.17 (b)). In the latter, there is a surprising decrease of pressure. This may be the consequence

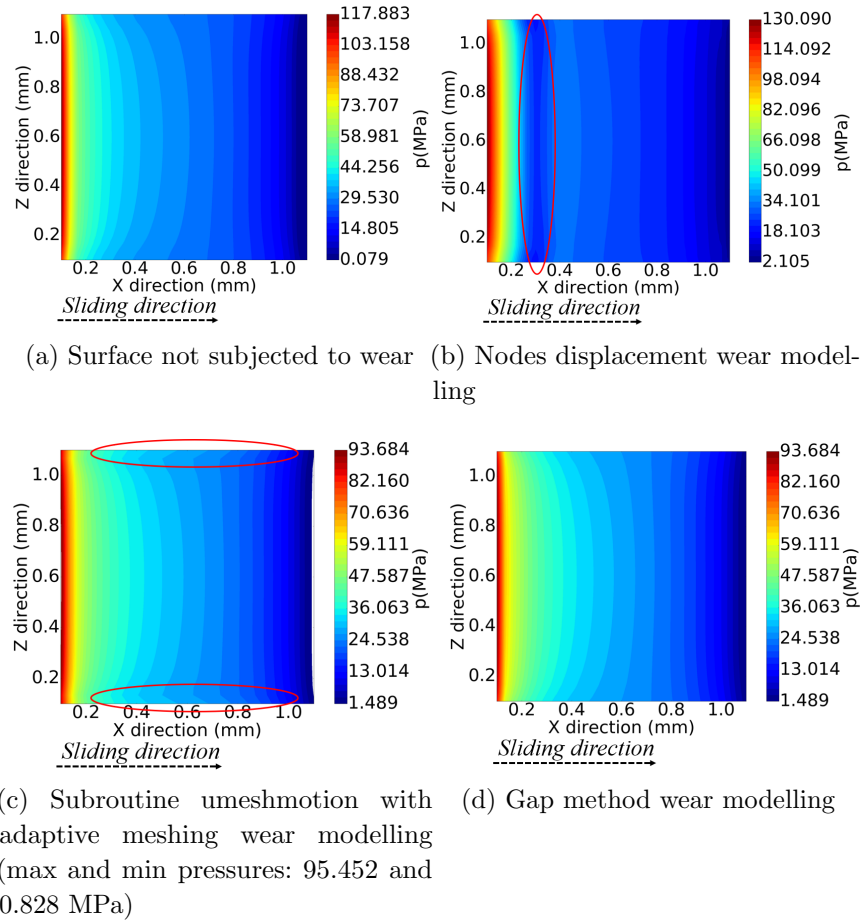


Figure III.17 – Contact pressure evolution with wear through different strategies.

of mesh distortion at the leading edge. It is well known that wear decreases the maximum of contact pressure and tends to uniform it. As a linear wear law is used, this behaviour was expected here. Therefore wear simulation based on nodes displacement method illustrated in Figure III.17 (b) is not consistent for our purpose, because of the inaccurate results obtained.

Next, wear modelling based on umeshmotion and gap method is discussed. As there is a new mesh creation, through adaptive meshing at each iteration, in the umeshmotion wear modelling strategy, the contact stiffness is fixed in order to compare results between the gap strategy. Figure III.17 (c) and (d) shows a decreasing contact pressure with wear. Contact pressure is well distributed and tends to be uniform through all the contacted face. Mostly, the pressure evolution obtained is the same between the gap and umeshmotion strategies. However, in Figure III.17 (c), at the zones surrounded in red, non-physical evolution is obtained. Surprisingly enough, this inconsistency is at the edges. In fact, umeshmotion technique use adaptive meshing to obtain a good mesh during analysis. However, it is not guaranteed that at the edges, mesh is well rearranged. This is possibly the cause of the inconsistency evolution observed in the surrounded zones of the Figure III.17 (c). But, umeshmotion and gap method results seem mostly consistent.

For the purpose of our work, we shall discuss on the best wear strategy for future investigations. This is discussed in the following.

III.3.3 Choice of best wear strategy method

Firstly, due to the inconsistency in contact pressure distribution of the nodes displacements method, we must eliminate this technique without further discussion.

Secondly, as seen in the previous section, wear strategy based on Fortran subroutine `umeshmotion` and gap strategy give mostly similar pressure distribution. However, how can we choose the best strategy? As we know, wear simulation based on subroutine `umeshmotion` is based on adaptive meshing aiming to mesh rearrangement and is widely used in the literature: [Molinari et al., 2001; Hegadekatte et al., 2008; Martinez et al., 2012]. Therefore, this technique can be used as reference of the wear modelling method based on temporal gap updating technique. In regards to the results obtained in Figure III.17 (c) and (d), there is a similar evolution of contact pressure except at edges. Physically, results obtained by `umeshmotion` at edges are not possible. Then the choice of `umeshmotion` as reference is no longer possible. The choice of wear modelling strategy seems then evident: gap strategy. Furthermore, the latter is chosen for three main reasons:

The first reason relies on the fact that with regards to results previously presented, gap strategy is the most convenient.

The second reason is the question of coherence with regards to the strategy adopted in this work. In fact, our strategy is mostly based on gap technique and therefore seems consistent for future investigations.

The third reason is also important: although mesh modelling based on `Umeshmotion` avoids high mesh distortions, this technique is not guaranteed for more wear cycles. However, gap strategy can be very useful in the investigation of more wear cycles. To prove this, other simulations have been conducted for 1000 wear cycles by the means of gap technique. The numerical model, illustrated in Figure III.15, is used. Then contact pressure evolution, for 1000 wear cycles, is presented in the Figure III.18. Results are quite predictive. In fact, a uniformity of contact pressure through the whole surface is observed with time. The maximum pressure goes from 117.883 MPa to 29.747 MPa . Furthermore, contact area is increasing with wear. At the beginning of the simulation, contact pressure is almost zero at the trailing edge; but with wear and due to the increasing of contact area, contact pressure is increased from 0.079 MPa to 5.626 MPa . In fact, the leading edge is submitted to high pressure due to the sliding friction and consequently is highly worn than the trailing edge. Therefore, the latter is more loaded with wear. Then with wear, the contact load is better distributed around the contact surface.

To illustrate better the decreasing effect of contact pressure with wear, contact pressure evolution along the X axis (sliding direction) in the middle of the Z axis (transverse direction) is plotted on Figure III.19:

According to the Figure III.19, the decreasing aspect of contact pressure when the surface is submitted to wear is well highlighted. With time, the pressure tends to increase

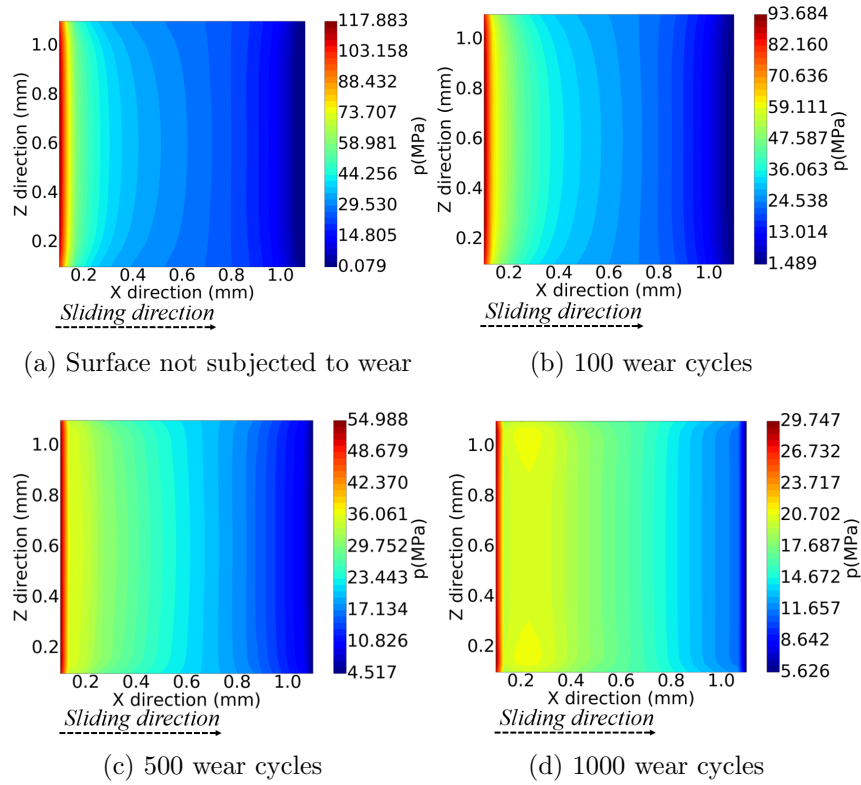


Figure III.18 – Contact pressure evolution for 1000 wear cycles using gap technique: model of disc rubbing on a cubical part.

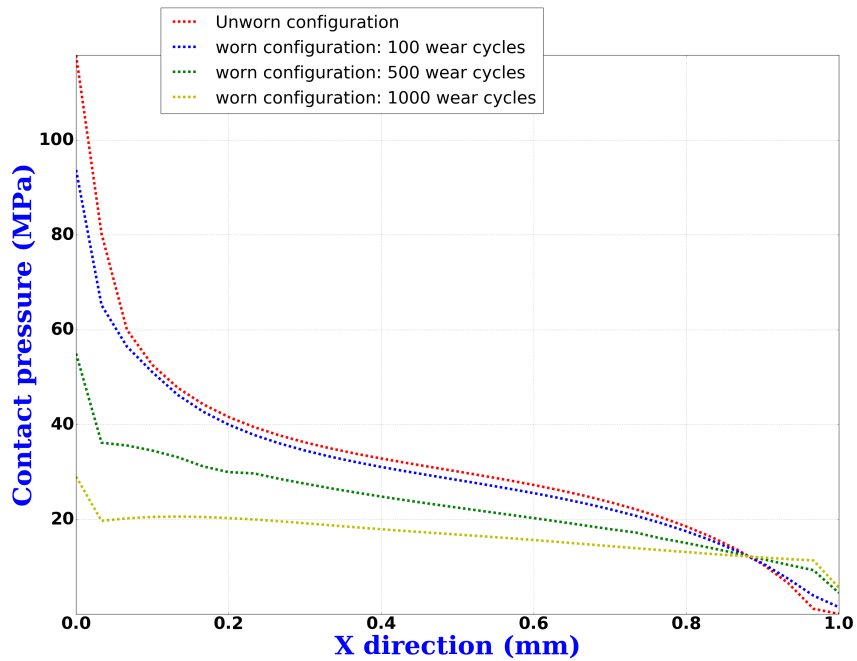


Figure III.19 – Contact pressure evolution with wear along X axis at $Z = 0$; 4 cases considered: from the initial state to 100, 500 and 1000 wear cycles.

at the zones where pressure was small initially due to the increase of contact load. In fact, at these zones, wear is very low as confirmed in the following.

These results are confirmed by the evolution of the cumulative wear depth on the contact surface in Figure III.20. With time, the contact surface is increasingly submitted to wear. A uniform distribution of wear depth is observed through the whole surface because of the contact pressure evolution. As the contact surface undergoes wear, the trailing edge of the cubical part is more and more loaded, then allowing a pressure uniformity through the whole surface.

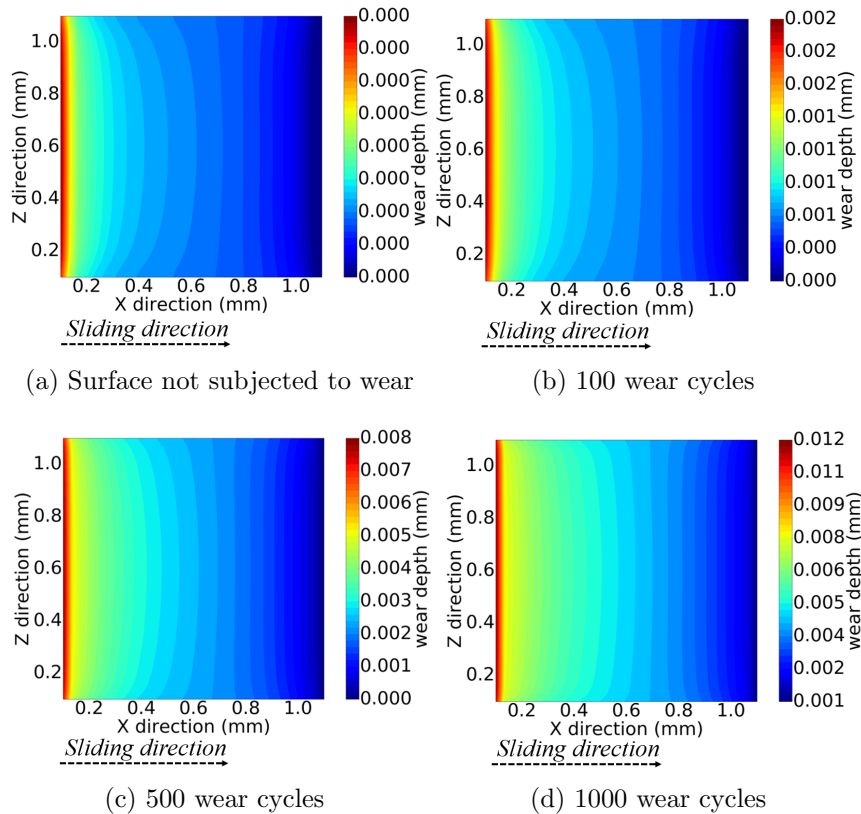


Figure III.20 – Cumulative wear depth evolution through the gap technique: model of disc rubbing on a cubical part.

Furthermore, to obtain a better view of the wear depth increasing with time and its uniformization through the whole contact surface, the total cumulative wear depth along the X axis, in the middle of the Z axis, for 100, 500 and 1000 wear cycles is illustrated in Figure III.21:

As shown in Figure III.21, the wear depth is uniformly increasing, with time, through the whole surface. The zones where wear depth is small enough correspond to the zones where contact pressure is small initially. At these zones, contact pressure will increase with time as wear increases from $X = 0$ to $X = 1$

With these reasons mentioned above, gap technique seems very relevant to address wear source flow modelling for either homogeneous or heterogeneous material investigated later.

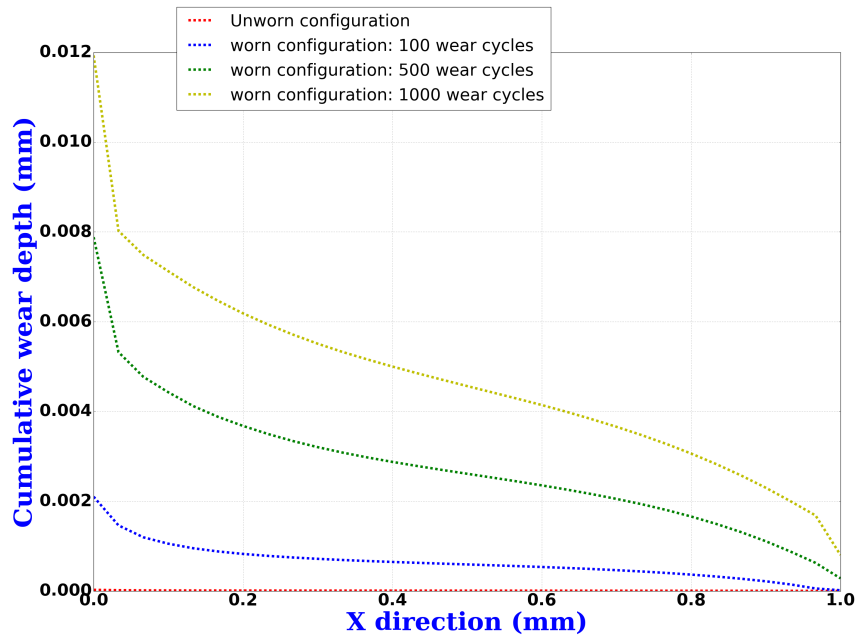


Figure III.21 – Cumulative wear depth evolution along X axis at position $Z = 0$, from initial state to 100, 500 and 1000 wear cycles.

This technique is used to conduct simulations in the following sections of this chapter.

III.4 Wear modelling considering a large scale model: homogeneous material

III.4.1 Numerical model

Three strategies were detailed in the last sections and one of them was chosen for wear modelling. This strategy is based on initial gap introduction in contact law at the level of each element of the contact surface of the part subjected to wear. The strategy was validated through a simple case, where a disc is rubbing on a cubical elastic part.

In this section, a large-scale model is considered. Gap strategy is used for wear modelling of a large-scale model under real braking conditions. The 3D FEM model inspired by the experimental pin-on disc system is used for implementation. As mentioned before, the disc is rotating with a constant velocity of 0.1 rad/s and a prescribed displacement of 0.2 mm is applied at the extremities of the thin plate which enforces contact between frictional material and the disc. The complete model is meshed with 34630 hexahedrons elements and 46472 nodes. Contact is frictional and contact constraints have been solved by the penalty method with a friction coefficient set to 0.3. Archard law (III.15) is used for wear depth computation where the wear rate is set to $1e - 6 \text{ mm}^2/N$. Furthermore, the frictional material is considered to be homogeneous in this section. The complete numerical model is illustrated in Figure III.22:

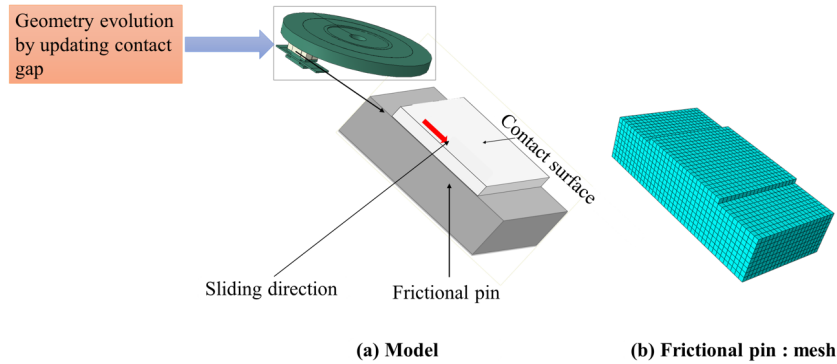


Figure III.22 – Large scale numerical model: Homogeneous frictional material under wear which is introduced through the gap strategy (400 elements in the pad surface).

Results of this simulation are discussed in the following subsection.

III.4.2 Results

In this subsection, Friction material is submitted to adhesive wear using Archard law. Several wear cycles are considered: 100, 200, 400, 700 and 1000 wear cycles. Two results are presented: contact pressure evolution with wear, and cumulative wear depth associated at different wear cycles.

III.4.2.1 Contact pressure evolution with wear

Contact pressure evolution is illustrated in Figure III.23:

Figure III.23 shows contact pressure evolution as a function of wear depth for several wear cycles. Step zero corresponds to the initial braking where the geometry is not subjected to wear. As a function of time, the contact area increases until it reaches the trailing edge of the friction material. Consequently, contact pressure decreases uniformly through the whole surface of the friction material and is progressively increasing at the back of the pad. This is due to the increasing of wear depth at each wear cycle. Moreover, at the bottom left corner, the pressure intensity is higher than the top left corner of the pad. This behaviour can be associated to the high tilting of the pad. In fact, initially, even when the contact surface is not subjected to wear, the pressure intensity is higher at the bottom left corner because of the tilting of the friction pad from inner to outer radius. The left bottom corner is in the side of the disc inner radius and the top left corner is in the outer radius side.

Globally, with wear, a uniform pressure is observed through the whole contact surface. As pressure tends to uniformize through the whole contact surface, some pressure discontinuities are observed at the back of the pin highlighted especially from wear cycles 700 to 1000. These discontinuities are the consequences of the wear strategy adopted. As it

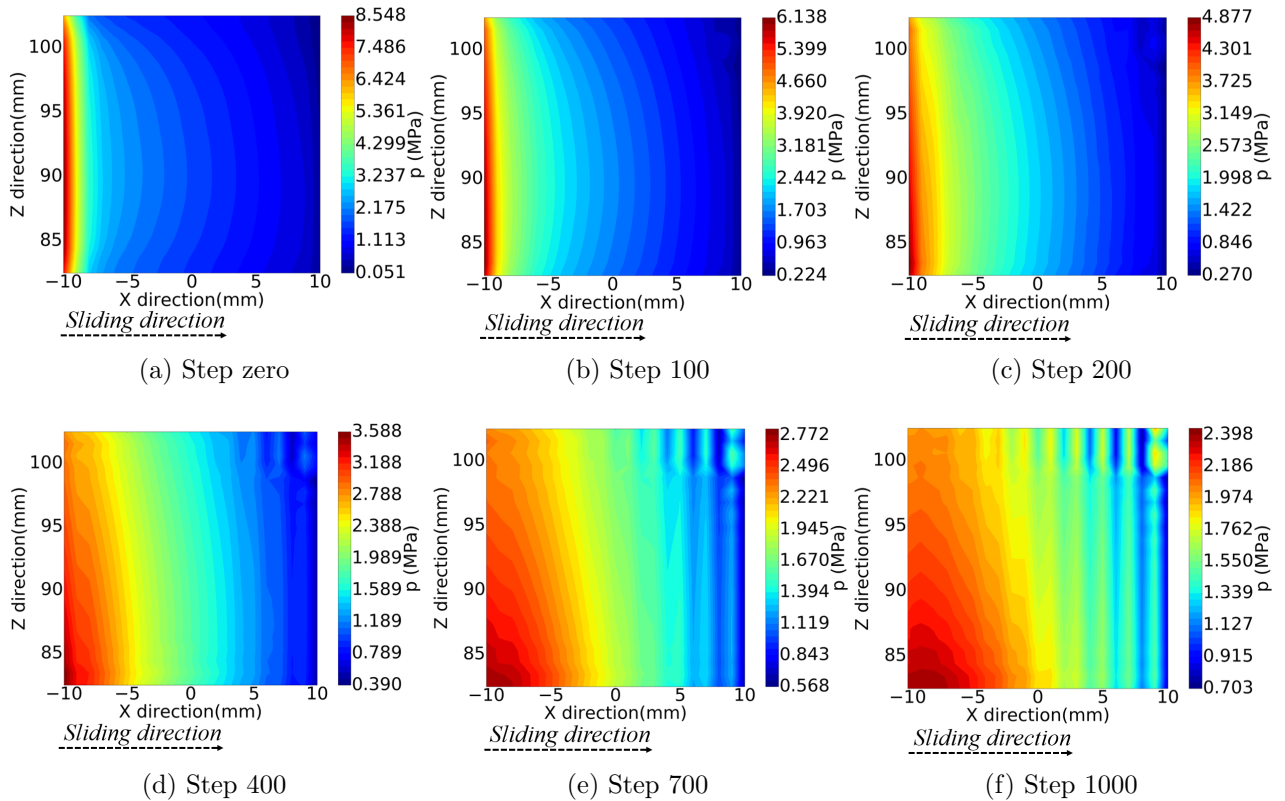


Figure III.23 – Contact pressure evolution with wear in a large scale model: gap strategy

is explained before, contact is done element by element at the level of the frictional pin. Then, a gap is inserted into the contact law at each element of the pad and is updated at each wear cycle. In fact, as the maximum pressure is initially located at the leading edge which decreases to the trailing edge, the leading edge is submitted to wear more than the trailing edge. As wear increases progressively at the leading edge and becomes higher and higher, the contact pressure tends to get more and more higher from the trailing to the leading edge elements. This then leads to discontinuities between each element especially at the elements located at the back of the frictional pin. In fact, the wear depth is small at these zones. It is obvious to notice that this behaviour is observed only when the pressure tends to be uniform through the whole surface.

Next, the cumulative wear through all simulations is illustrated.

III.4.2.2 Total cumulative wear depth

The total cumulative wear depth is shown in Figure III.24:

Figure III.24 shows the cumulative wear depth evolution as a function of time. At step zero, the wear depth is null through the whole contact surface because wear was not considered initially. With time, a progression of wear depth is observed. Most of the contact surface, especially the leading edge is very much worn. The back of the pad, especially the trailing edge is not too much worn. When the surface is subjected increasingly to wear,

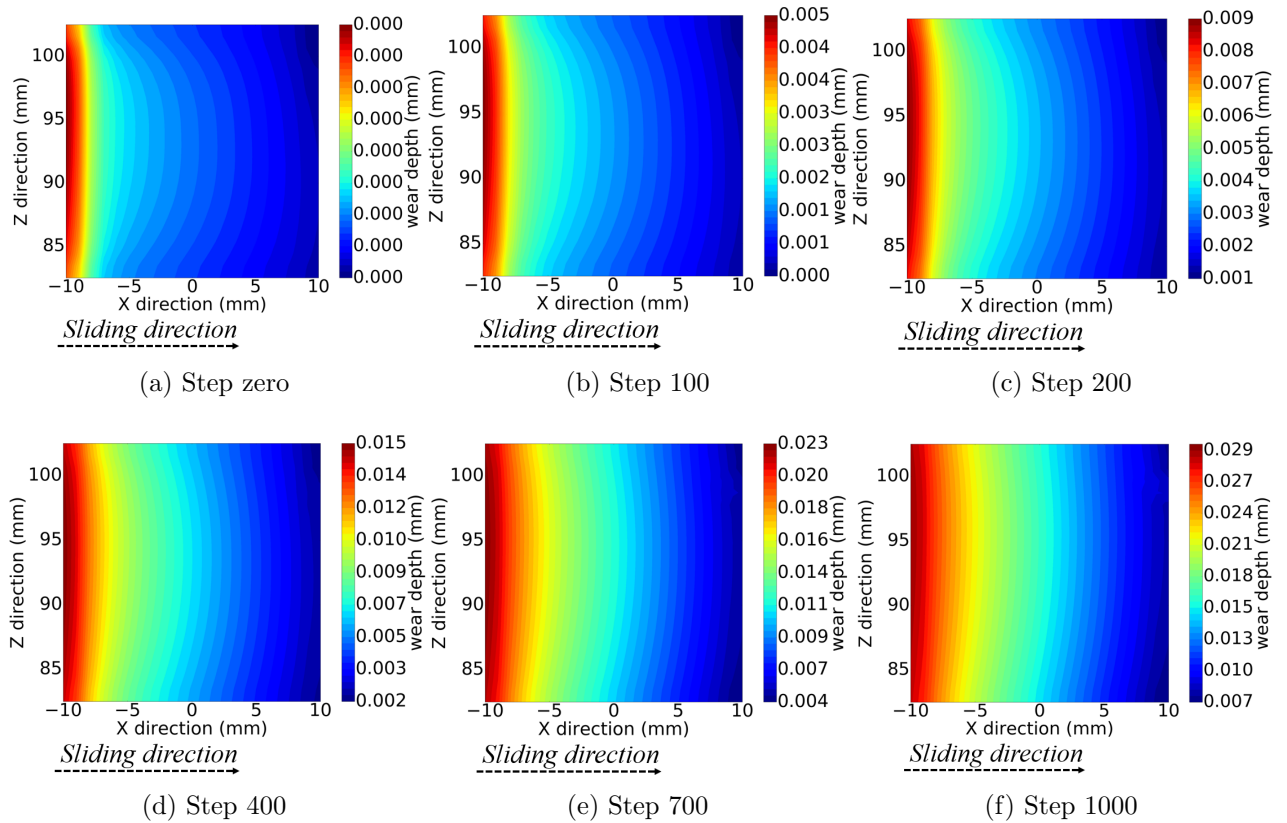


Figure III.24 – Cumulative wear depth as a function of time: gap strategy

contact pressure decreases and contact area increases (Figure III.23). The evolution of the wear depth is uniform through the whole simulation because it is cumulative wear depth. That's why the discontinuities especially highlighted at the back of the pin, from step 700 to 1000, do not effect the wear depth evolution.

In this section, wear modelling of a large-scale model, reproducing braking conditions, has been investigated through the introduction of initial gap into the contact law at each contact surface elements. However, material is considered as homogeneous; which is not true for friction material. In the following section, a strategy leading to wear modelling at the local scale will be implemented.

III.5 Multi-scale strategy for wear modelling of the heterogeneous material

Friction material is highly heterogeneous. Direct computation cannot be possible without a multi-scale method because of excessive computation time it will induce; a fine mesh is necessary in order to capture finely heterogeneities. In the following a strategy based on the KUBC-Contact homogenization method is proposed.

As previously seen, KUBC-Contact allows a macro to micro contact pressure computation. In other words, it is possible, from a macroscopic variable, to obtain an associated microscopic one. It is proposed a wear modelling at local scale knowing the macro mechanical field at a given macro patch. The whole wear modelling strategy is illustrated in Figure III.25:

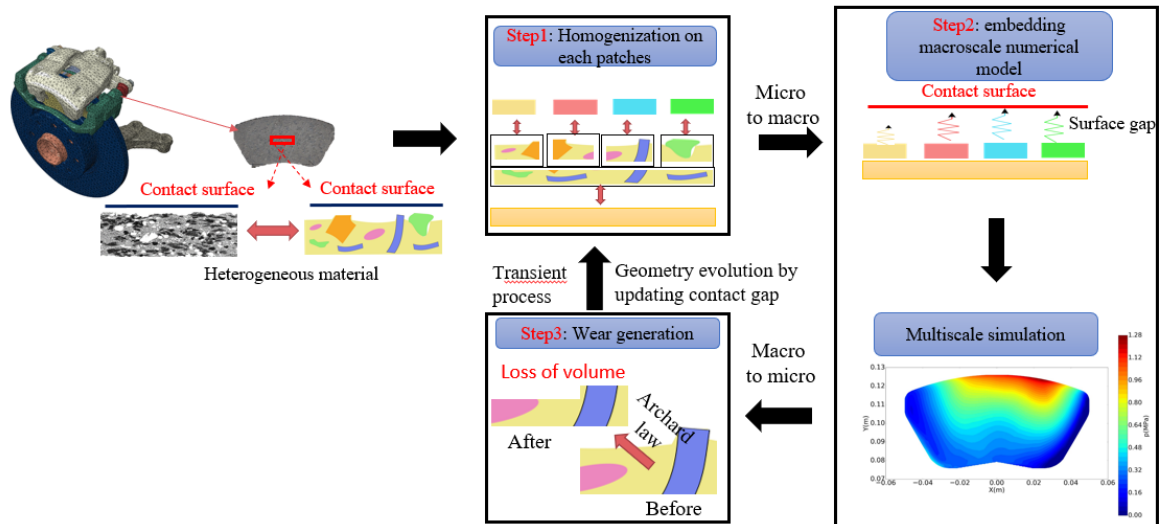


Figure III.25 – Global strategy showing wear modelling considering heterogeneous friction material for large scale models.

In Figure III.25, step 1 corresponds to the homogenization with contact named KUBC-Contact from which equivalent behaviour is obtained at the level of each patch. In step 2, the equivalent behaviour obtained from step 1 is replaced at the macro scale and a computation is performed to obtain contact information which will be serve in step 3. In step 3, contact pressure at the heterogeneities scale is obtained and wear modelling is performed at this scale. Therefore, at the local scale, wear modelling is introduced using the gap technique previously described. At every wear cycle, the cumulative wear depth is introduced in step 1 and new equivalent behaviour induced by heterogeneities is computed using KUBC-Contact homogenization method. In fact, the role of KUBC-Contact resides there. Without this homogenization technique, a computation of equivalent behaviour induced by wear evolution is not possible. Then at each wear cycle, the equivalent behaviour obtained through KUBC-Contact, is embedded at the macro-scale to account for material

properties evolution with wear.

In the next subsection, the strategy proposed in Figure III.25 is validated through a simple heterogeneous case.

III.5.1 Numerical example considering heterogeneous patch into the large scale model

III.5.1.1 Numerical model

The 3D FEM model inspired by the experimental pin-on disc system, introduced in chapter 2, where a heterogeneous patch, composed of a rigid spherical inclusion centred within the matrix, is placed at the leading edge of the frictional material is used here for wear modelling in large scale. The model is reproduced in Figure III.26:

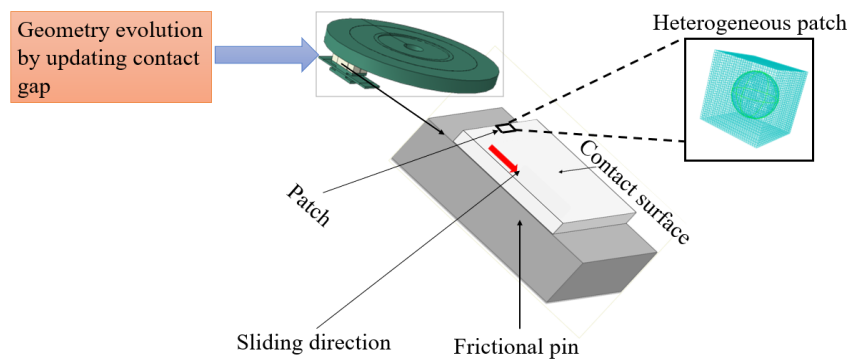


Figure III.26 – Large scale numerical model with heterogeneous patch, containing a spherical inclusion, placed at the leading edge: wear is introduced directly at this scale through the gap strategy described before.

Material properties, loads, boundary conditions are the same as in chapter 2. Contact is frictional and the penalty method is used for contact constraints solving. Friction coefficient is set to 0.3. The step 3 of the strategy introduced in Figure III.25 is implemented for validation purpose. Two models have to be distinguished:

1. Explicit method where inclusion is explicitly meshed.
Inclusion is explicitly meshed and wear is introduced directly at the macro-scale via initial gap introduction in the contact law. The complete model is meshed with 411962 hexahedrons elements and 474256 nodes.
2. Multi-scale model.
The multi-scale model is composed of three models interacting together: the KUBC-Contact model aiming at the computation of the equivalent modulus. These results have been presented in chapter 2 (Table II.4).
The embedded model which is a macro model where the heterogeneous patch is not

physically present and is replaced by a homogeneous patch enriched with KUBC-Contact homogenized properties. Complete embedded model is meshed with 34630 hexahedrons elements and 46472 nodes. To observe what happens at fine scale, one has to use the micro relocalization model.

Micro relocalization model based on average boundary conditions illustrated in Figure II.39 is used for wear modelling at local scale. The complete micro model is meshed with 76577 hexahedrons elements and 91292 nodes. Cumulative initial gap is introduced in the contact law, at each contact surface elements, to simulate wear. All the wear cycles are performed at local scale.

Therefore, two simulations have been conducted in order to validate our local wear strategy. 10 CPU cores are used for simulations under the computation code Abaqus through a python script. Results are presented in the following.

III.5.1.2 Results

Archard wear law (III.15) is used for wear depth computation. The wear rate, in wear depth equation, is set to $1e - 6 \text{ mm}^2/N$. The rotation speed of the disc is 0.1 rad/s . After 20 wear cycle, micro model contact pressure distribution is compared to the explicit model in Figure III.27.

Figure III.27 shows contact pressure evolution with wear in the heterogeneity scale, where the spherical inclusion is centred within the cubical patch, for both explicit and micro models:

Figure III.27 (a) shows an overpressure at the leading edge and at the zone where the inclusion is located due to its rigidity. Moreover, contact pressure is decreasing with sliding direction. Globally, an increasing contact area and decreasing contact pressure, with time, are observed. For large wear cycles, the inclusion effect diminishes with wear as shown in Figure III.27 (g). Furthermore, micro model results are in a good agreement with explicit results. This then confirms our approach for wear modelling, in the presence of heterogeneities, at local scale. Moreover, our micro model has the advantage to reduce enormously computation time in the context of wear simulation. For one simulation, computation time between both explicit and multi-scale models is shown in Table III.13.

Table III.13 – Average CPU time per simulation comparison between explicit and micro models

| | Explicit model | Multi-scale macro model | Multi-scale micro model |
|------|----------------|-------------------------|-------------------------|
| time | 2j 8h | 31 min | 1h 50 min |

A gain of computation time is obtained through the multi-scale model. However, by working more on the micro model mesh and other aspects, the computation time could be reduced even further.

III.5 Multi-scale strategy for wear modelling of the heterogeneous material

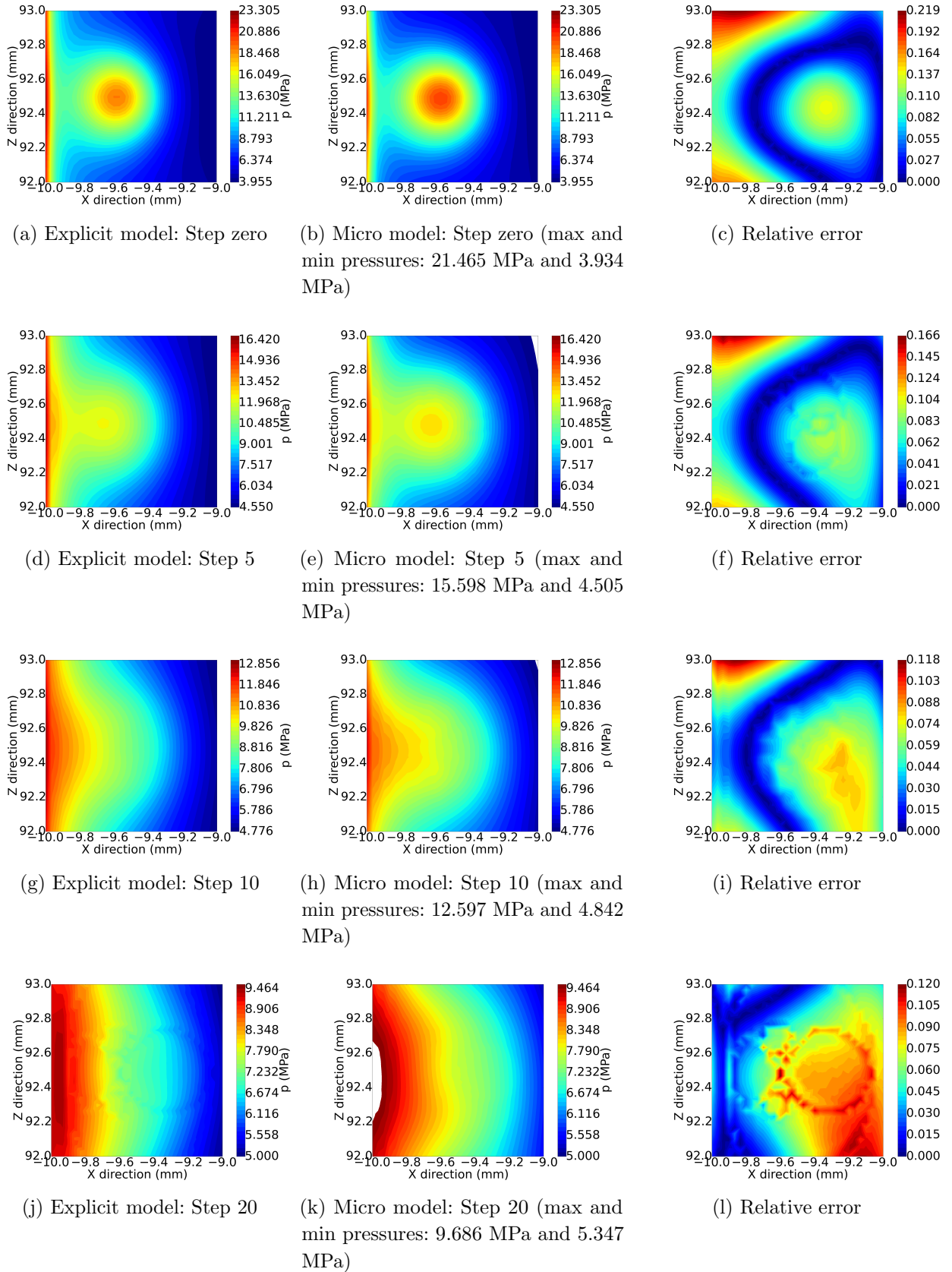


Figure III.27 – Heterogeneous contact pressure evolution, with wear, at local scale through the gap strategy. Both explicit and multi-scale models contact pressure distribution are compared each other (explicit heterogeneous patch compared to micro model contact pressure distribution).

The aim of this section was the validation of the proposed wear modelling strategy, through a simple heterogeneous case, with explicit results. Satisfying results are obtained. Therefore, in the next section, the wear modelling strategy is extended to complex microstructure.

III.5.2 Numerical example considering microstructure from tomography image

III.5.2.1 Numerical model

In this section, microstructure from tomography image, described in chapter 2, is considered in the large scale model described previously in Figure III.26.

The biphasic heterogeneous material is composed of matrix, graphite and porosity. As discussed before, the friction material is supposed to have a periodical microstructure. Therefore, the whole friction material is embedded with the biphasic microstructure homogenized properties obtained from KUBC-Contact method. Wear modelling strategy is introduced at the large-scale model previously used. All the patches (represented by each macro element) in the friction material are heterogeneous at micro-scale. The heterogeneities are represented by the biphasic microstructure.

In this section, a patch located at the leading edge is considered and studied as in Figure III.26.

As said in chapter 2, the volume fraction of matrix and graphite is 63% and 36% respectively. Only the linear elasticity is considered. Then, elastic material properties of the two phases are presented in Table III.14.

Table III.14 – Elastic properties for the materials: biphasic microstructure

| Real microstructure | Matrix | Graphite |
|---------------------|-----------|----------|
| Young's modulus | 10000 MPa | 2000 MPa |
| Poisson's ratio | 0.1 | 0.1 |

The penalty method is used for contact constraints resolution with a constant friction coefficient of 0.3. Adhesive wear is considered and introduced at local scale to count for heterogeneities influence. Moreover, Archard's wear law is considered. The whole numerical model is shown in Figure III.28.

III.5.2.2 Wear modelling considering same wear rate at the heterogeneous material phases

The heterogeneous patch, placed at the leading edge of the frictional material and represented by the biphasic microstructure is considered here, as stated previously in Figure III.28. All the results will be presented in the local scale directly.

As mentioned before, the heterogeneous microstructure is composed of two phases: matrix, and graphite. The matrix is more rigid than graphite. Do the graphite and matrix phases have the same likelihood of wear? Here we suppose that these two phases have the same probability to wear. Therefore, in Archard wear law (III.15), the wear rate, in wear depth equation, is set to $1e - 6 \text{ mm}^2/N$ for both phases. 100 wear cycles have been

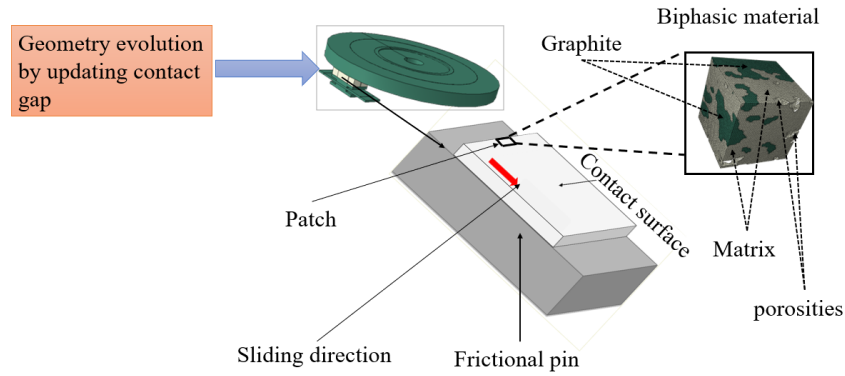


Figure III.28 – Large scale numerical model considering complex microstructure at the leading edge near contact interface: wear is introduced at local scale, where all the complexity of this microstructure is highlighted.

performed at local scale. In the following, the cumulative wear depth evolution resulting from the wear simulations is presented in Figure III.29:

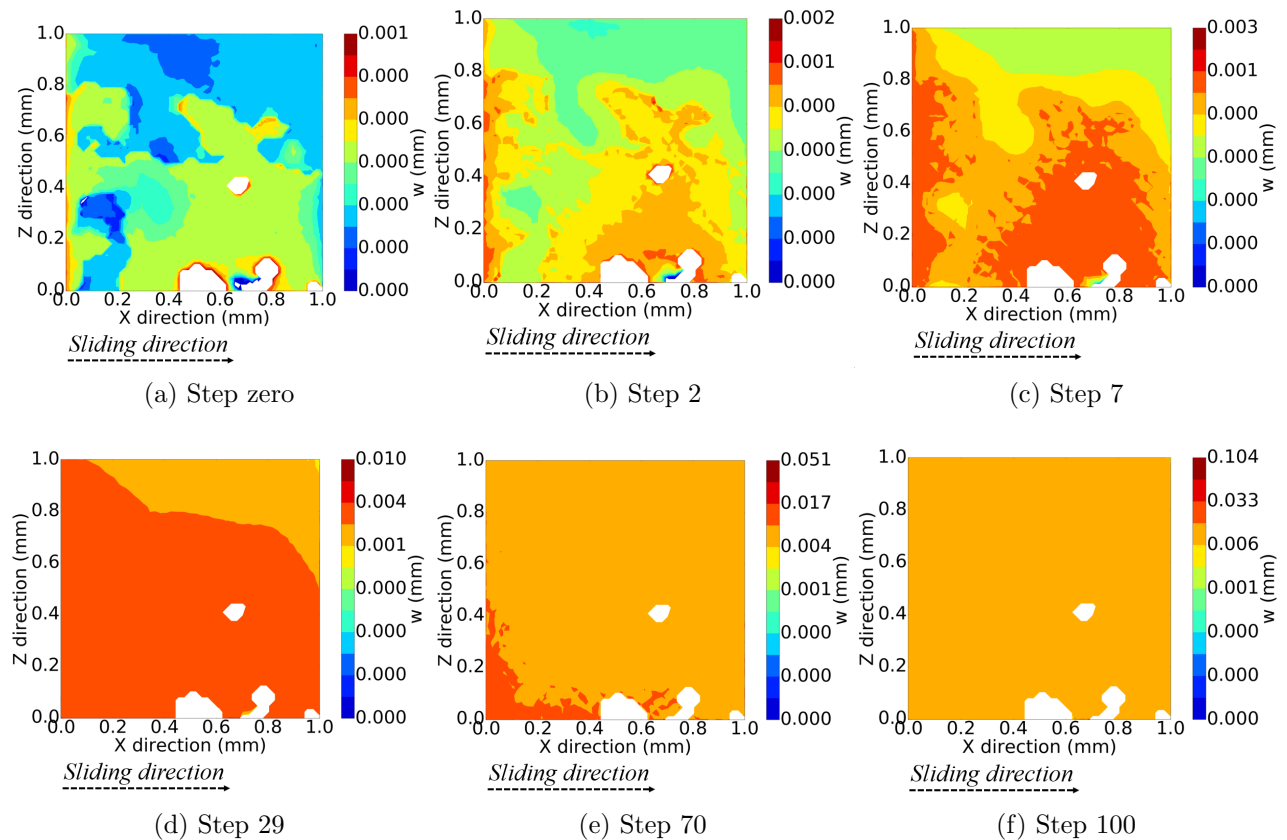


Figure III.29 – Cumulative wear depth evolution as a function of time at local scale: complex microstructure considered.

Figure III.29 presents wear depth evolution, as a function of time, in the heterogeneous biphasic material located at the leading edge of the frictional material. Wear modelling

is performed at local scale. Figure III.29 (a) shows the wear depth corresponding to the first braking. At first braking, the matrix is worn more than graphite because of its higher rigidity (refer to Figure III.30).

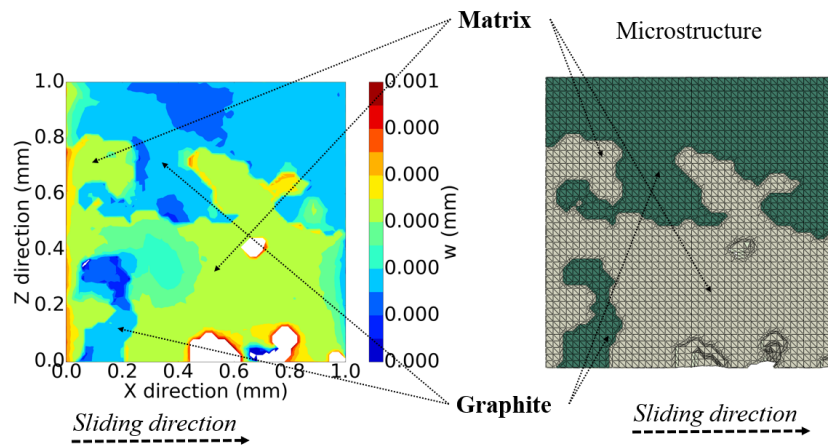


Figure III.30 – Initial braking wear depth evolution.

From step 2 to step 29 which correspond respectively to the second and 29 braking, cumulative wear depth is increasing progressively not only at the matrix but also at the graphite contact areas. From step 29 to step 100, wear in the contact area of the two phases is increasing and tends to be uniform. Maximum cumulative wear depth is observed near porosities. In fact, edges near porosities induce some contact pressure localizations, consequently leading to high wear depth near porosities. Globally, considering the fact that the two phases have the same likelihood of wear, leads to uniform wear distribution with time.

Contact pressure, under the assumption of uniform wear modelling through the two phases, is investigated in the following:

Figure III.31 shows contact pressure evolution with different wear cycles. Results have been put on the same scale in order to obtain a better view of contact pressure evolution in the two phases. At initial braking (Step zero), contact pressure intensity in matrix area is higher because of its rigidity compared to graphite. Moreover, maximum contact pressure is observed at the leading edge and decreases in the sliding direction, except for some localizations near porosities edges. When the material started to wear, contact pressure decreases at the leading edge while increasing at the trailing edge. With time, contact pressure is increasing in the graphite contact area while decreasing in the matrix contact area. In fact, the matrix is rubbing faster than graphite, leading therefore, to an increase in the contact area of the graphite phase. This is quite well observed from step 29 to step 100.

Furthermore, there is some localization bands growing with time and leading to non-uniform pressure distribution in the contact area of the matrix. This can be explained by the fact that contact is done element by element. As the pressure distribution is not uniform from one element to another, this leads to a non-uniform pressure distribution,

when wear depth increases.

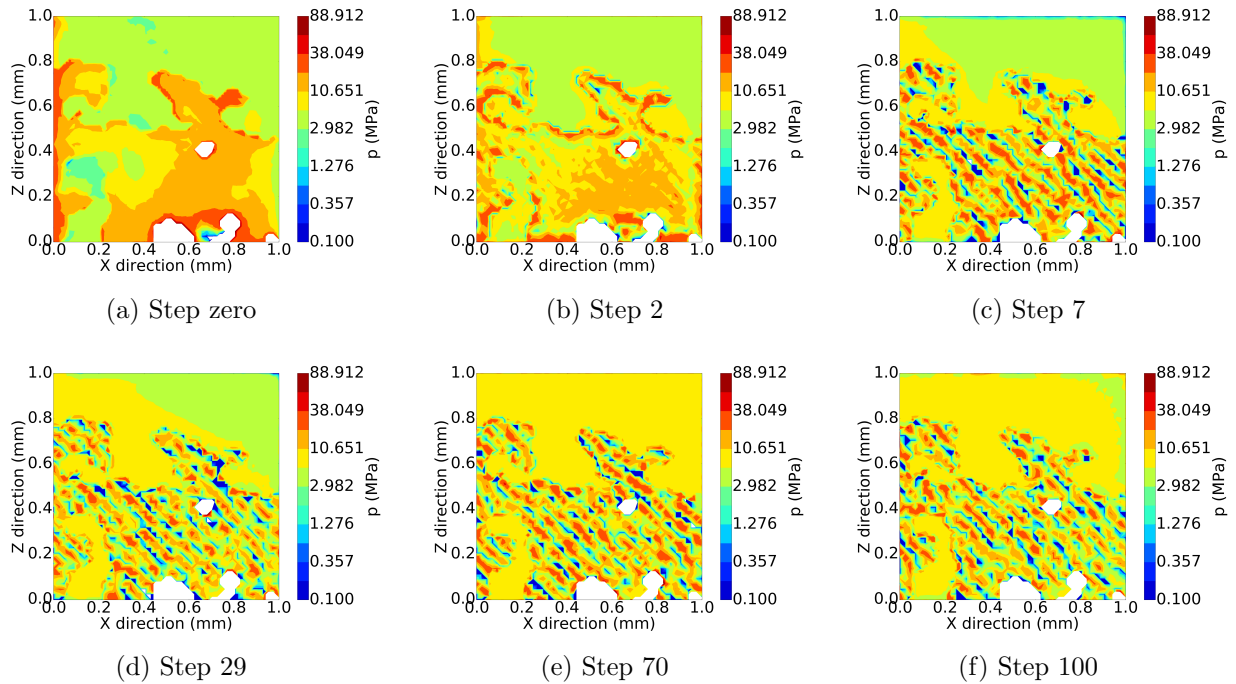


Figure III.31 – Contact pressure evolution with wear under considering that the two phases are submitted to same wear rate: wear is introduced at local scale using the complex microstructure

In reality, as the matrix is stiffer than the graphite, the latter contact surface is not much subjected to wear according to the wear mechanism considered here (adhesive wear). The latter assumption is dealt in the next subsection.

III.5.2.3 Wear modelling considering different wear rate at the heterogeneous material phases

Previously, same wear rate has been considered, in the wear modelling process, for the two material phases. Here a new assumption is made about the two phases degradation probability: the graphite contact surface is supposed to wear just a little. Therefore, the wear rate is reduced to zero for this phase. In reality, graphite is used as a dry lubricant during contact process. However, according to the wear mechanisms taken into consideration, in this case adhesive wear, therefore it seems reasonable to reduce the wear rate at zero in graphite contact area. In reality, under other wear mechanisms, for example cracking or decohesion, there can be graphite particles fragmentation and ejection. Same wear rate, previously used, is kept for the matrix phase. Based on this new assumption, new simulations are run and results are presented in the following.

The cumulative wear depth of 100 wear cycles simulations is computed. Results are plotted on the Figure III.32:

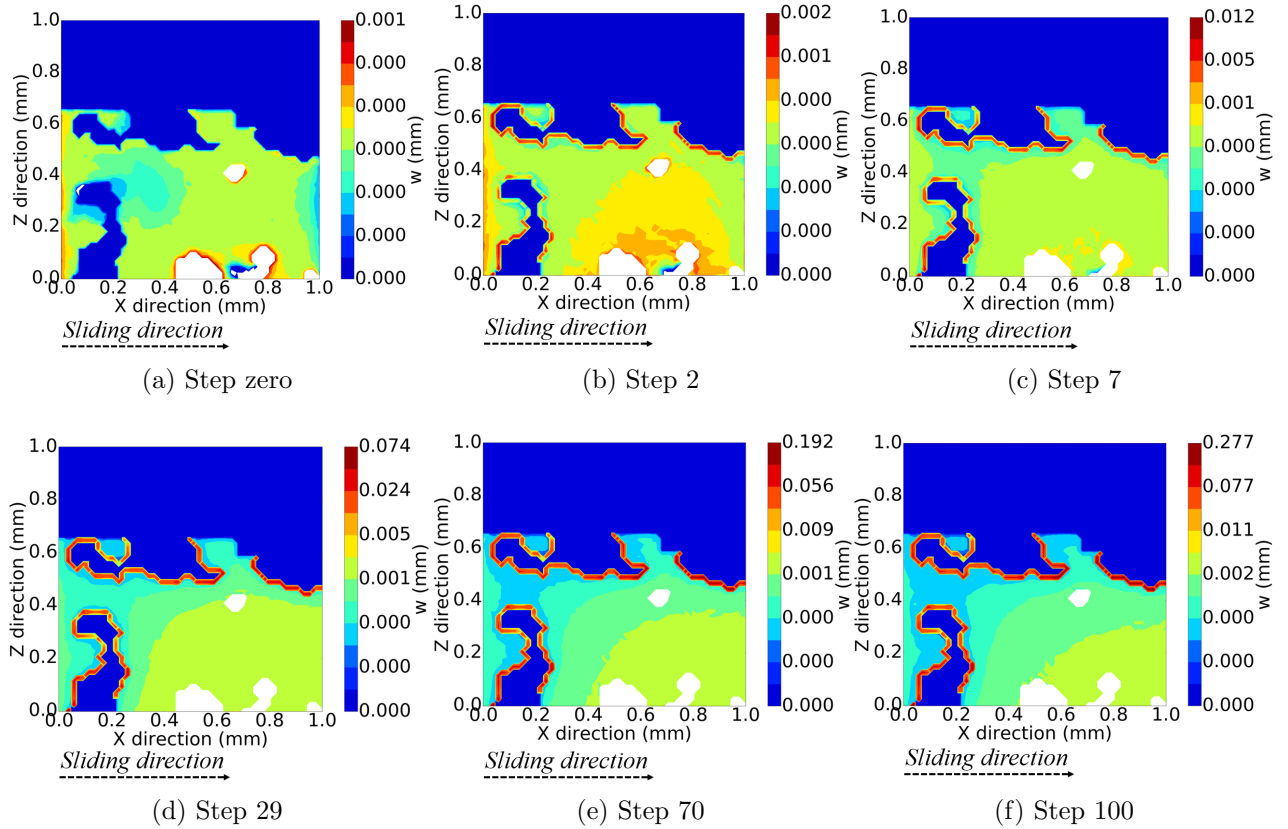


Figure III.32 – Cumulative wear depth as a function of time: non uniform wear distribution

Firstly, the graphite contact area is not subjected to wear. Therefore, wear depth for all wear cycles is reduced to zero on the graphite contact surface. Secondly, at the start of the simulation, wear depth is distributed on whole matrix contact area and localizations are found near porosities edges. From step 1 to step 100, two observations are made: firstly, the cumulative wear depth is increasing in the whole matrix contact surface; secondly it is principally concentrated at the interface between matrix and graphite. In fact, the second observation is very interesting. The interface between matrix and graphite undergoes a lot of wear because of shear stresses which are very discontinuous, consequently, leading to the graphite particle decohesion. These particles can contribute in the tribological phenomenon of the whole system.

In the same vein, contact pressure evolution with wear, is investigated in order to consolidate wear evolution previously obtained: Figure III.33 presents contact pressure evolution over the contact area of the biphasic material with wear. At the first braking, contact pressure is more concentrated on the matrix contact area than graphite because of its high rigidity compared to graphite phase. When wear increases, contact pressure decreases and tends to zero pressure at the whole contact area of the matrix. In fact, the latter is decreasing with time. Meanwhile, contact pressure increases in the graphite contact area and tends to stabilize when matrix contact pressure is disappearing. Especially, in the interface matrix-graphite, the pressure intensity is very high. As the matrix is submitted to

wear, with time, these localizations in the matrix-graphite interface are expected. Therefore, mechanisms such as particles decohesion and/or cracking can be expected around these zones.

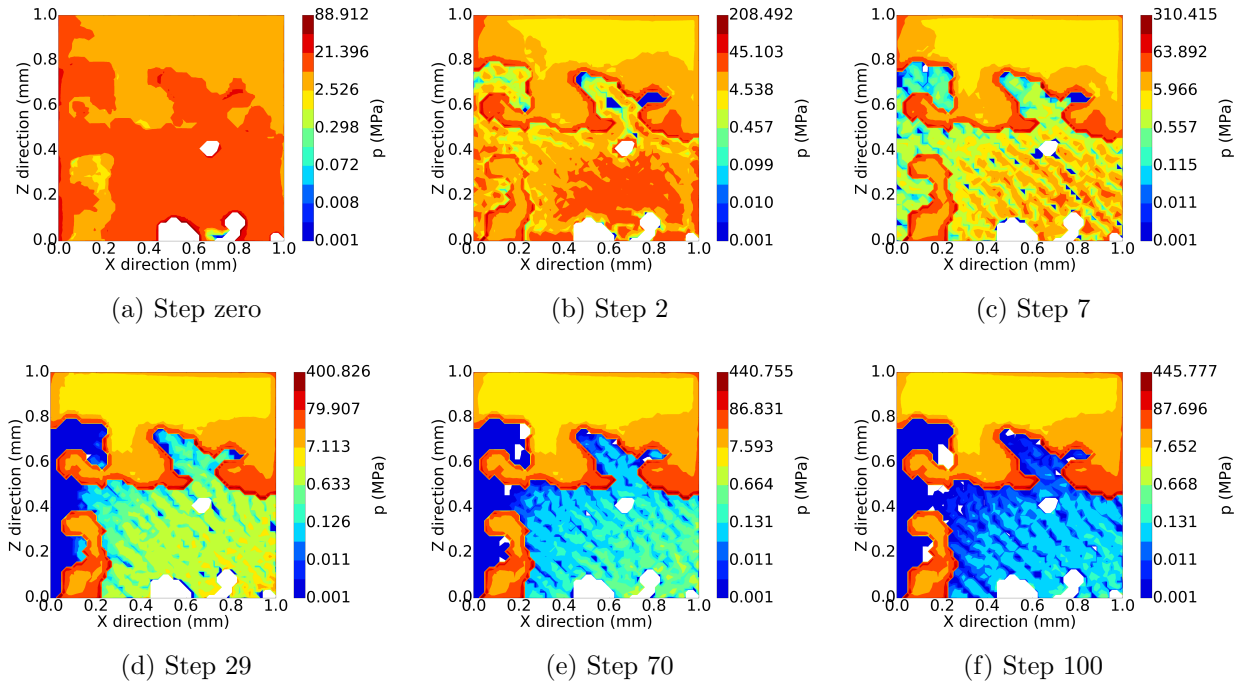


Figure III.33 – Contact pressure evolution with wear: non uniform wear distribution

III.5.2.4 Evolution of the homogenized microstructure elastic properties with wear

Previously, wear modelling has been performed at local scale considering heterogeneous biphasic material. Wear and contact pressure evolution have been computed with time by the means of the multi-scale micro model. In this subsection, an evolution of the elastic constants, through wear, is performed through KUBC-Contact homogenization method. This step is necessary for the simple reason that, when wear is computed at the macro-scale, considering material heterogeneity, the elastic properties will no longer be linear. We shall believe that wear influences material behaviour law. This is presented and discussed next. To illustrate our purpose, wear evolution over the microstructure considering the same probability of the two phases to wear, obtained in Figure III.29, is considered. Using the latter configuration, wear is introduced in the KUBC-Contact model through the gap technique and then computation has been done.

The procedure, allowing elastic properties computation under wear, is highlighted in orange color in the multi-scale strategy summarized in Figure III.34.

Regarding the Figure III.34, results obtained in Figure III.29 represent the actual step 3. Step 3 represents the wear generation box at local scale. From step 3 to step 1, which

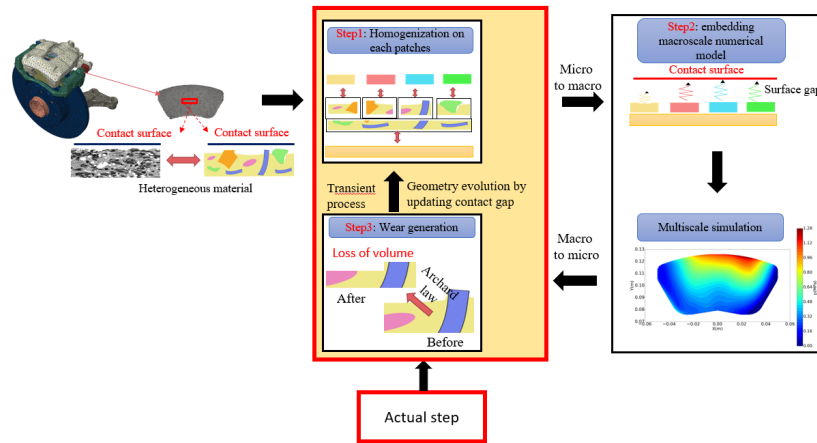


Figure III.34 – Strategy of computing the elastic properties of the heterogeneous microstructure under wear evolution: wear depth obtained at local scale (step 3) is updated in the homogenization box for microstructure elastic properties computation over different wear cycles performed.

represents the homogenization box by the means of the KUBC-Contact.

Then at each wear cycle, the resulting wear depth computed, in Figure III.29, is updated in the KUBC-Contact model in order to compute the associated microstructure elastic properties evolution through wear. Computation is performed for 100 wear cycles and results are illustrated in Figure III.35:

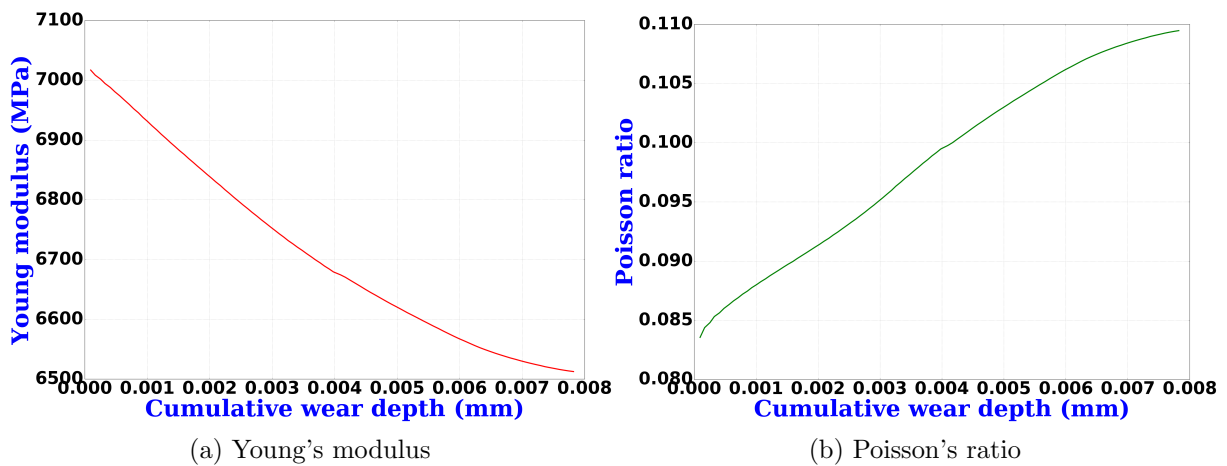


Figure III.35 – Young's modulus and Poisson's ratio evolution with wear: 100 wear cycles performed.

Figure III.35 (a) presents Young's modulus evolution as a function of the cumulative wear depth computed at each wear cycle. For Young's modulus evolution, non-linear behaviour is observed. At each wear cycle, equivalent Young's modulus of the heterogeneous biphasic material is decreasing. This is due to the loss of volume of the heterogeneous material, consequently leading to a loss of material rigidity. Moreover, a non-linear behaviour evolution is also observed for Poisson's ratio in Figure III.35 (b). Poisson's ratio is increasing

with wear. That means, the transverse deformation of the heterogeneous patch is increasing with material degradation.

III.5.2.5 Macro contact pressure evolution with wear

Before presenting and discussing results of this subsection, it is necessary to recall the different steps of our multi-scale strategy proposed, in Figure III.25, for wear modelling of heterogeneous material. Step 1 allows through homogenization method to embed macro model with an equivalent quantity obtained from micro computation. This approach allows only to obtain macro mechanical quantities which is not really what happens at a local scale. However, mean mechanical quantities are very well estimated. In step 2 of our strategy we propose a macro to micro computation which is important for tribological phenomena computation like wear. This step has been computed in the previous section with a realistic microstructure. Based on step 2, elastic constants evolution with wear has been computed through KUBC-Contact homogenization methods (step 3). In this subsection, we proposed to introduce at the macro-scale wear modelling, the equivalent behaviour evolution obtained in Figure III.35. This behaviour is only introduced at the zone where the macro contact patch is located. Two different results are compared here:

1. Homogeneous wear modelling

The equivalent behaviour obtained by KUBC-Contact homogenization method is supposed to be constant through the whole macro wear process.

2. Heterogeneous wear modelling

Here, the equivalent modulus obtained from the KUBC-Contact homogenization method changes at every wear cycle. Then, the behaviour obtained in Figure III.35 is enriched at the macro contact patch level.

Two wear simulations are computed according to the above statements. Results are presented in Figure III.36:

Figure III.36 presents mean contact pressure evolution as a function of wear between the heterogeneous (red dashed curve) and homogeneous (green dashed curve) configurations describe above. At first observation, mean contact pressure between the two configurations decreases with wear. However, when micro behaviour evolution is considered, it impacts mean contact pressure which decreases more than the homogeneous configuration (constant equivalent behaviour). This difference can be more significant with time; even more, when mechanisms as decohesion and/or cracking are considered at the local scale.

In the next section, the behaviour obtained, in Figure III.35, is used in the process of the wear modelling considering a complete braking model.

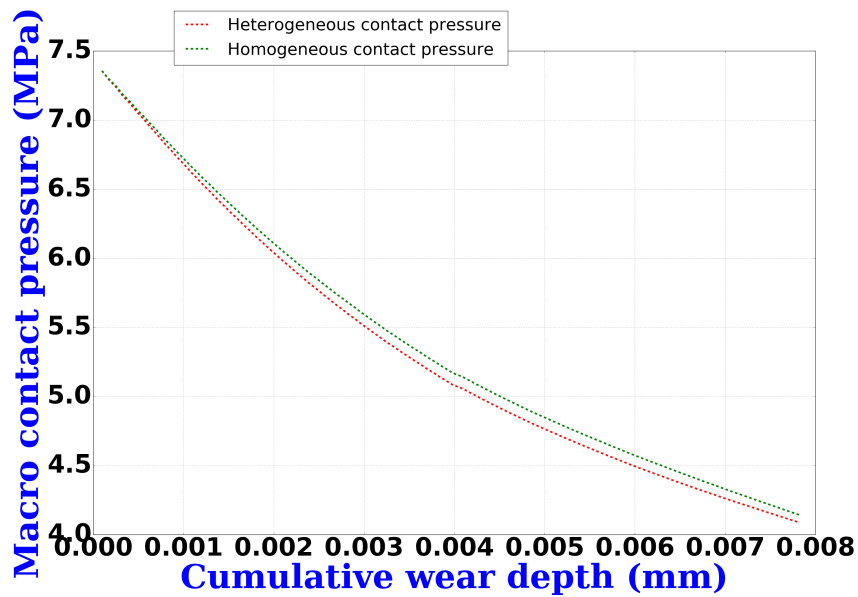


Figure III.36 – Macro mean contact pressure evolution with wear.

III.6 Application of the multi-scale strategy into a complete brake system considering real microstructure

Until now, the experimental pin on disc system has been used for implementation. The purpose of this section is to conduct a numerical investigation of the influence of wear modelling on the dynamic behaviour of a complete disc brake system. To do so, a 3D finite element analysis has been implemented taking into account wear and material behaviour through the multi-scale approach presented in section 4. In the following, the numerical model and the results are presented and discussed.

III.6.1 Numerical model and the global strategy

Many structural components are part of the brake system. Essentially, there is a calliper, a piston, an anchor, a knuckle, a disc and two brake pads. The disc is rotating with a constant velocity of $\omega = 5rad/s$ which correspond to low velocity braking. In order to brake, a load of $P = 10 bar$ is applied on the piston and calliper. This action allows to maintain contact between the rotating disc and the two pads. Most of the system components are made of steel and cast iron except the two brake pads. They are composite materials.

For boundary conditions, the displacements of the disc inner annular face and the knuckle extremities are fixed. The whole model is meshed with 243573 tetrahedral and hexahedron elements and 401079 nodes. The contact is frictional and penalty contact is

used for contact constraints resolution. The friction coefficient is set at 0.4.

The two pads composite material are embedded with the heterogeneous biphasic microstructure presented in Figure III.28. Thus, the material behaviour is integrated using the multi-scale approach introduced in chapter 2. In the same vein, interface evolution through wear is introduced in the numerical simulation by the means of the wear modelling strategy introduced in Figure III.25. Moreover, material behaviour evolution through wear is incorporated in this simulation, using the material behaviour law obtained in Figure III.35. The latter is integrated at the whole contact elements of the pads. Even if this behaviour does not represent the exact model condition here, therefore, it is used to highlight the influence of material evolution, on brake dynamics, with wear.

The numerical analysis is composed of two steps:

1. The quasi static analysis

It consists in applying progressively the load P , while the disc is in rotation, until a steady state braking is achieved.

2. The complex modal analysis

The second step consists in complex modal analysis under sliding contact conditions. The complex eigenvalues and mode shapes of the entire system are then extracted. Modal coupling theory, due to the contribution of friction, is used. And then, unstable modes are studied.

The whole strategy is summarized in the Figure III.37:

A particular attention is, therefore, devoted to the influence of material and wear evolution on the system's stability. Results are presented and discussed in the following.

III.6.2 Results and discussion

Results issued from quasi-static and complex modal analysis are presented and discussed. For quasi-static analysis, heterogeneous contact pressure evolution with wear, for both inner and outer pad, is compared to a reference homogeneous case where no heterogeneity is considered. Results are illustrated in Figures III.38 and III.39.

At first observation, in the two pads (inner and outer), there is an increase of contact area and a decrease of contact pressure which is a consequence of wear evolution. For the inner pad, the maximum pressure is obtained in the upper central zone, whereas, on the outer pad, the maximum pressure is obtained in the upper right corner. With wear, the intensity of pressure decreases for both inner and outer pads, even for both homogeneous and heterogeneous configurations.

For homogeneous case, the pressure is uniformly distributed for all wear cycles. In terms

III.6 Application of the multi-scale strategy into a complete brake system considering real microstructure

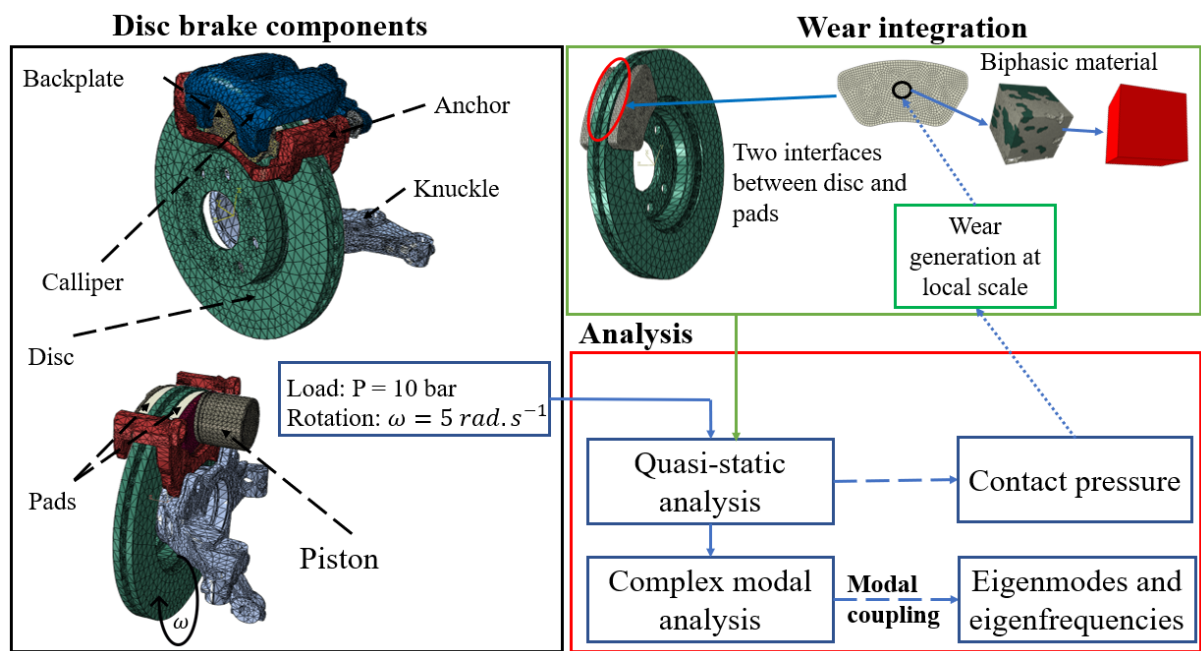


Figure III.37 – Multi-scale modelling strategy of the complete braking system.

of intensity, it is remarked that, homogeneous maximum contact pressure is greater than heterogeneous model for both inner and outer pads. However, in the heterogeneous model, some contact pressure localizations are observed at upper central zone of inner pad and upper right corner of outer pad. These localizations are the consequences of contact stiffness which are non-uniformly distributed over the contact area of the heterogeneous model. In fact, every contacted element has its own stiffness which represents the heterogeneity inside. The heterogeneity comes from biphasic microstructure presented in Figure III.28. As the contacted element does not have the same area and therefore the same volume, the contact stiffness is different per element. Moreover, due to wear, the contact stiffness decreases non-uniformly at each element. This non-uniformity of stiffness evolution is the consequence of some localizations observed for both inner (principally) and outer pads in the heterogeneous model especially at the zones of high gradient of pressure. Also, one can then explain why the maximum pressure of the homogeneous model is greater than the heterogeneous configuration: the decreasing contact stiffness, due to wear, in heterogeneous configuration.

In order to explain better the presence of these localizations, an illustration is done in Figure III.40.

The non-uniform initial gap distribution, influenced by the contact stiffness, leads to discontinuities at the zones of high pressure. However, at the zones where initial gap is uniformly distributed, the pressure distribution is uniform also.

Finally, for outer pad, the lower central zone seems to not be influenced by wear. Moreover, for inner pad, the lower right corner is not subjected to wear. This may be a consequence of pads geometry.

III.6 Application of the multi-scale strategy into a complete brake system considering real microstructure

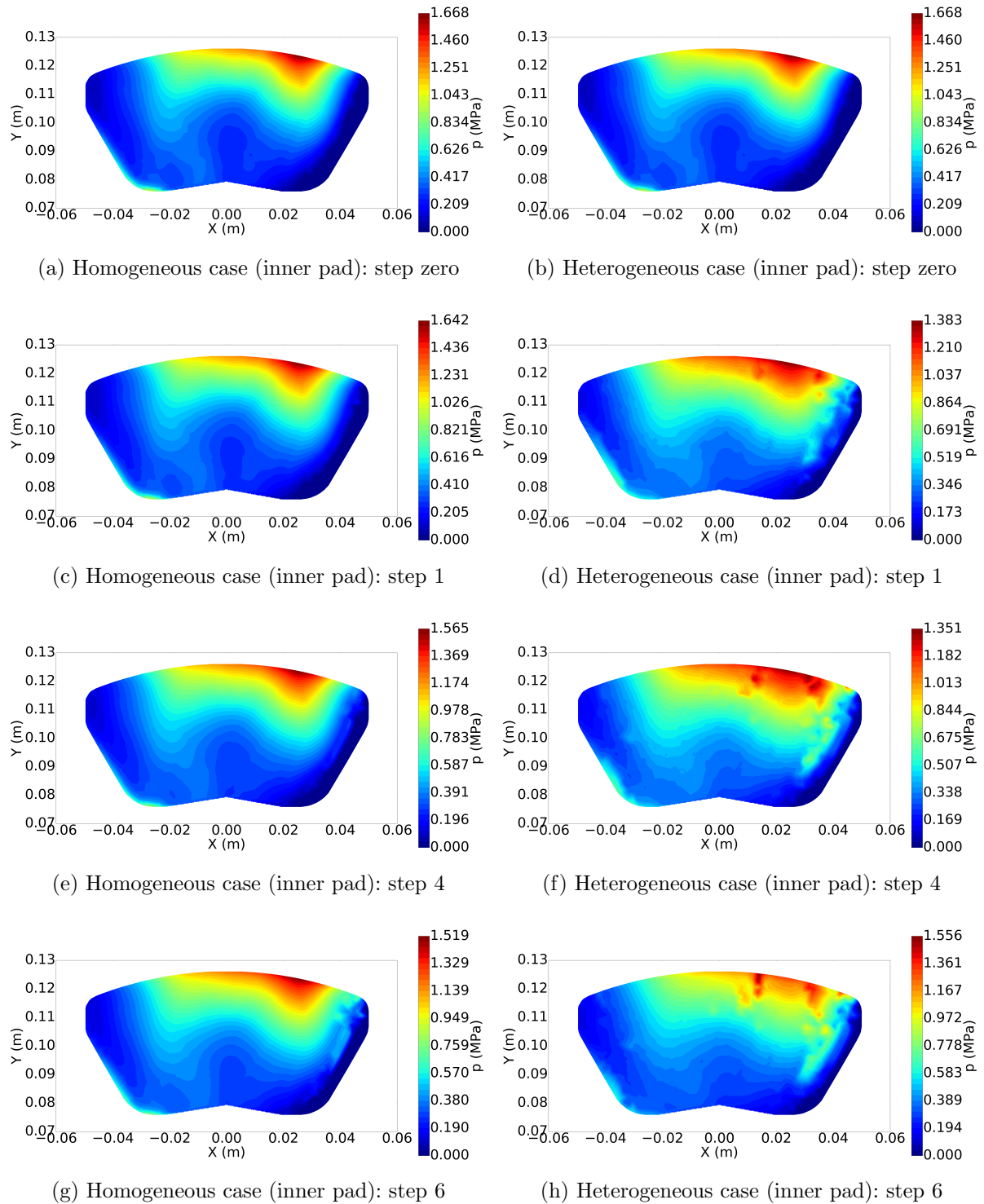


Figure III.38 – Homogeneous versus heterogeneous contact pressure evolution with wear: Braking model

III.6 Application of the multi-scale strategy into a complete brake system considering real microstructure

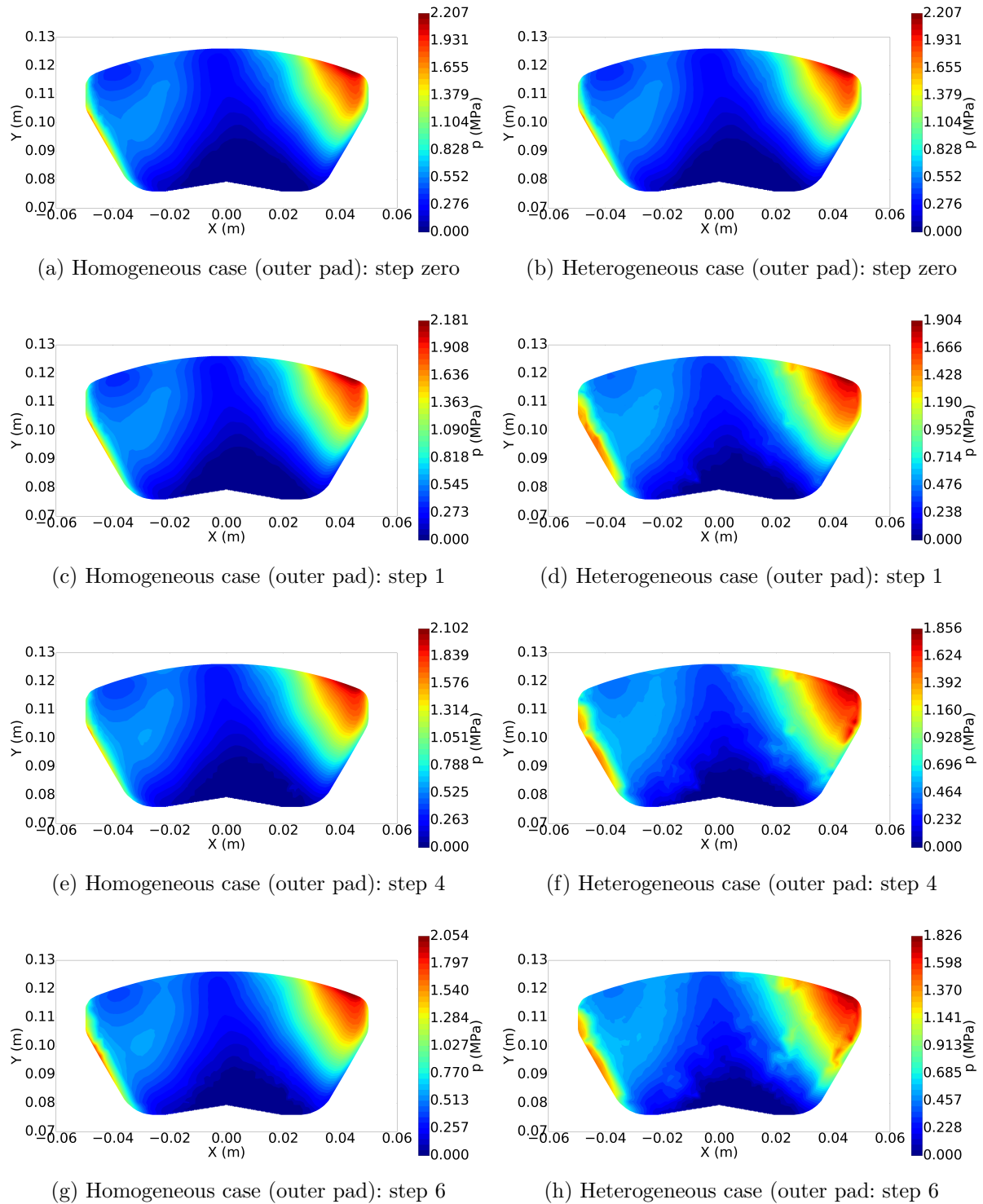


Figure III.39 – Homogeneous versus heterogeneous contact pressure evolution with wear: Braking model

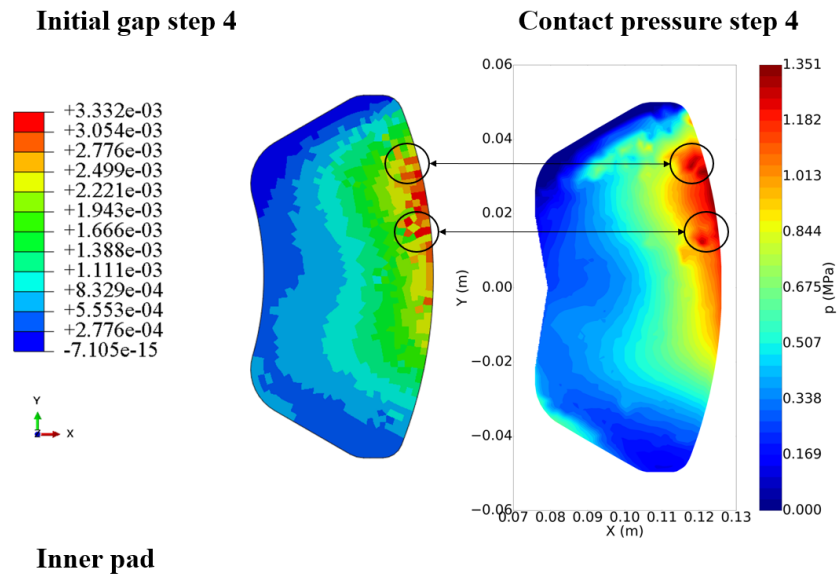


Figure III.40 – Origin of the localizations explained by initial gap illustration: Inner pad.

Next, complex modal analysis results is investigated. Results are illustrated in Figures III.41 and III.42:

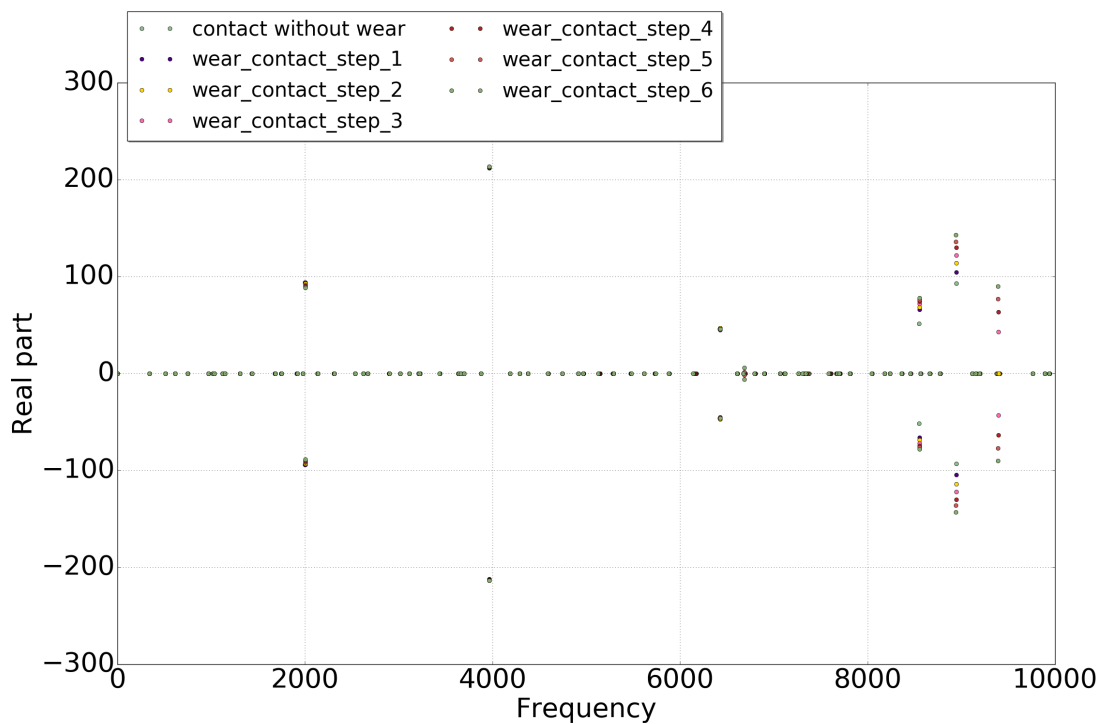


Figure III.41 – Eigenfrequency real part versus imaginary part: homogeneous configuration.

Figures III.41 and III.42 show the real part of complex frequencies against the imaginary part for respectively homogeneous and heterogeneous configurations. All wear cycles are represented. One can observe that eigenfrequencies are affected by the contact interface evolution due to wear.

III.6 Application of the multi-scale strategy into a complete brake system considering real microstructure

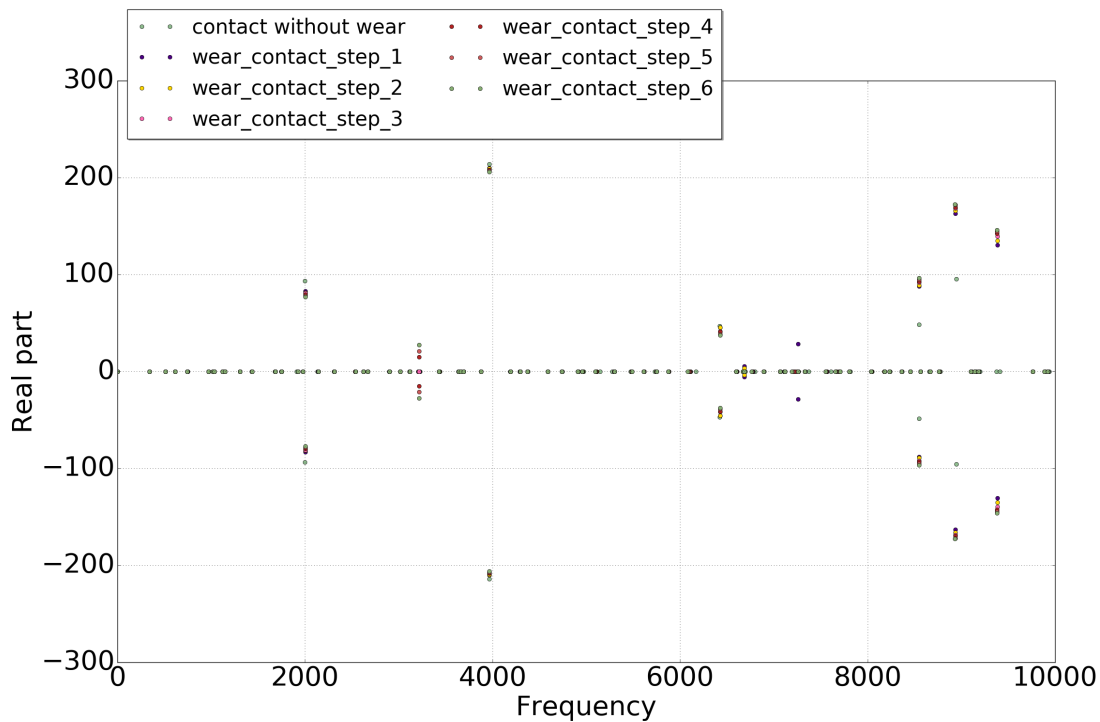


Figure III.42 – Eigenfrequency real part versus imaginary part: heterogeneous configuration.

Moreover, modes characterized by a strictly positive eigenfrequency real part are unstable. Additionally, predicted unstable modes differ at each wear cycles. Compared to homogeneous case, there is some additional eigenfrequencies, with positive real parts, at low and high frequency for heterogeneous model.

The evolution of instability, for each wear cycle and for both models, is shown in Figures III.43 and III.44:

The unstable modes, characterized by positive real parts, are represented by full bars in Figures III.43 and III.44. When the surface is not subjected to wear evolution, there are 5 unstable modes (modes 17, 34, 50, 73 and 78) whether it is homogeneous or heterogeneous model. Furthermore, these unstable modes remain for all wear cycles studied. However, some eigenmodes have the same shape, like mode 73 illustrated in Figure III.45; and some modes differ, like mode 50 illustrated in Figure III.46.

On the other hand, wear evolution influence on system instability can be illustrated by unstable modes 54, 61 and 83. Mode 83, which is obtained at very high frequency close to 9.4 KHz , remains for all wear cycles studied and, therefore, is a characteristic mode related to wear evolution. Mode 83 is shown in Figure III.47. Even if this mode appears different between wear cycles, therefore, its shape is different.

Furthermore, the instability of mode 61, close to 7.3 KHz , is strongly affected by surface evolution due to wear and material heterogeneity.

As seen in Figure III.44, mode 61 is only present in step 1 (see Figure III.48). In step 2, mode 61 disappears and mode 54 remains (see Figure III.49), which in return

III.6 Application of the multi-scale strategy into a complete brake system considering real microstructure

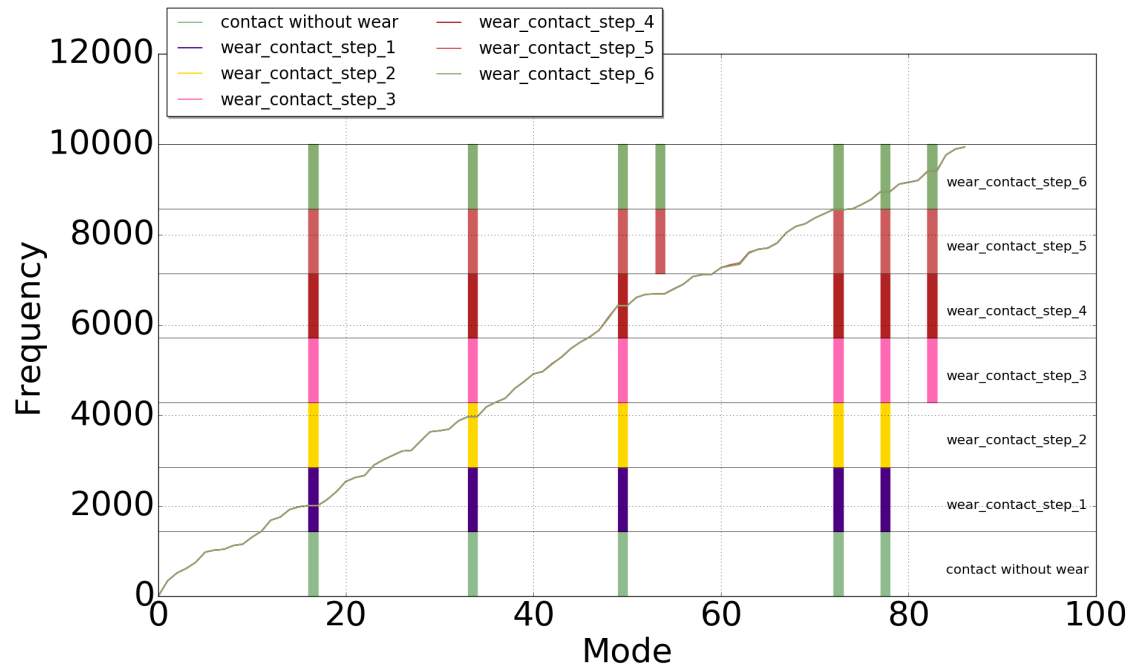


Figure III.43 – Unstable modes evolution versus eigenmodes for different wear cycles: homogeneous configuration.

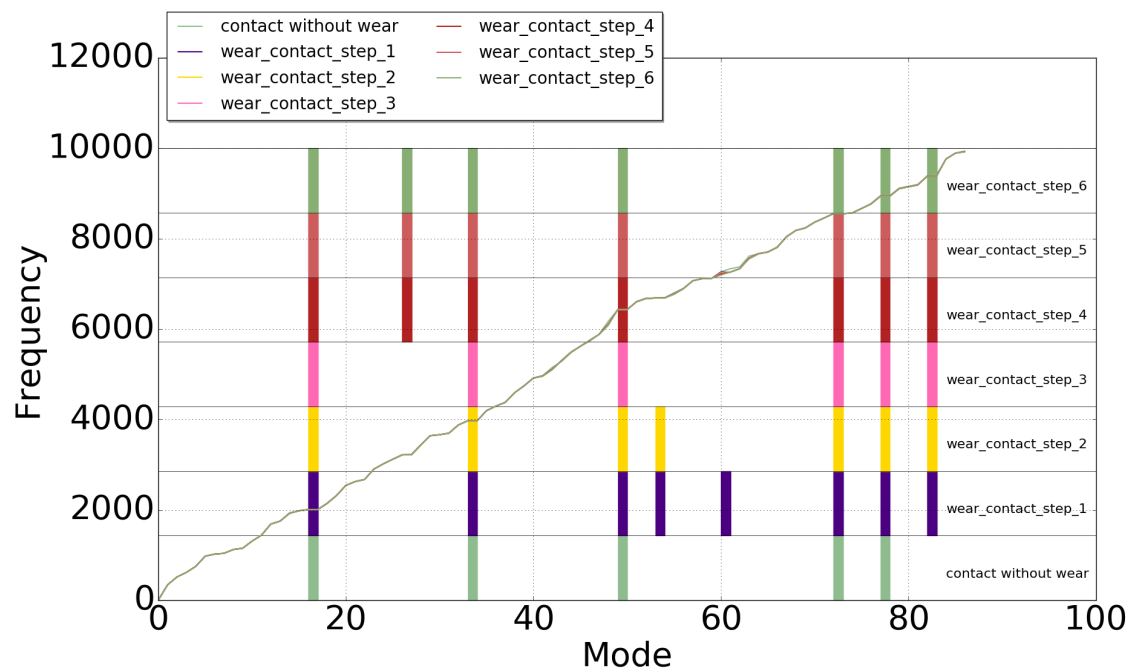


Figure III.44 – Unstable modes evolution versus eigenmodes for different wear cycles: heterogeneous configuration.

will disappear in step 3. However this mode appear later in step 5 and 6 when considering homogeneous configuration (Figure III.43). In the latter case, this mode is a little bit different from heterogeneous configuration. (refer to III.50)

III.6 Application of the multi-scale strategy into a complete brake system considering real microstructure

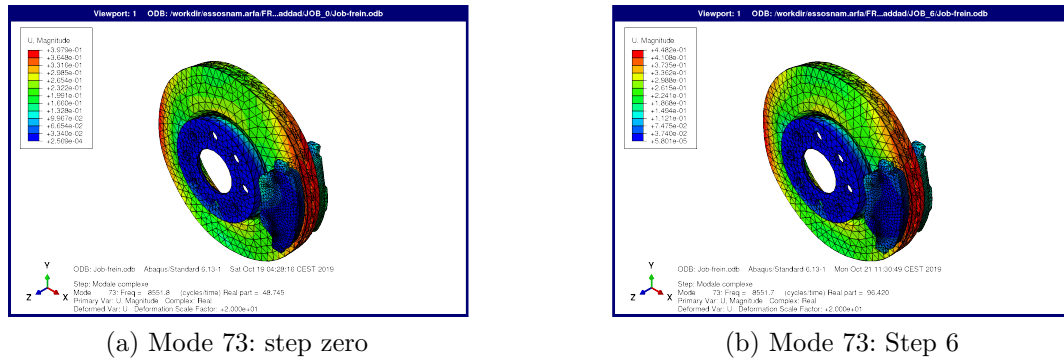


Figure III.45 – Mode 73 comparison between step zero and 6.

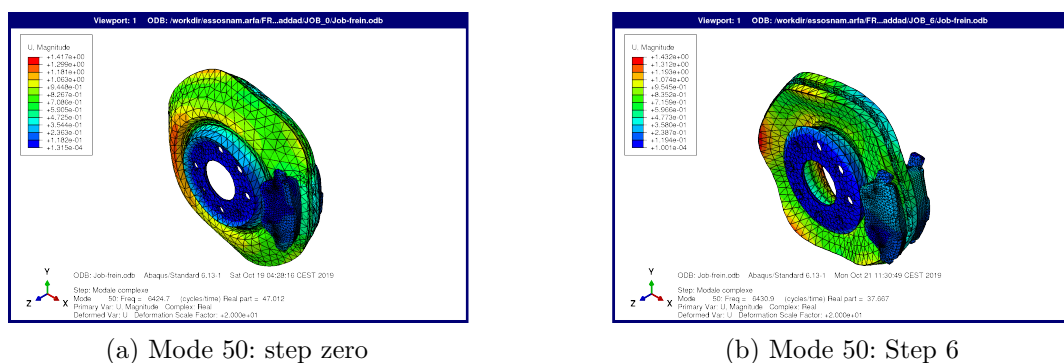


Figure III.46 – Mode 50 comparison between step zero and 6.

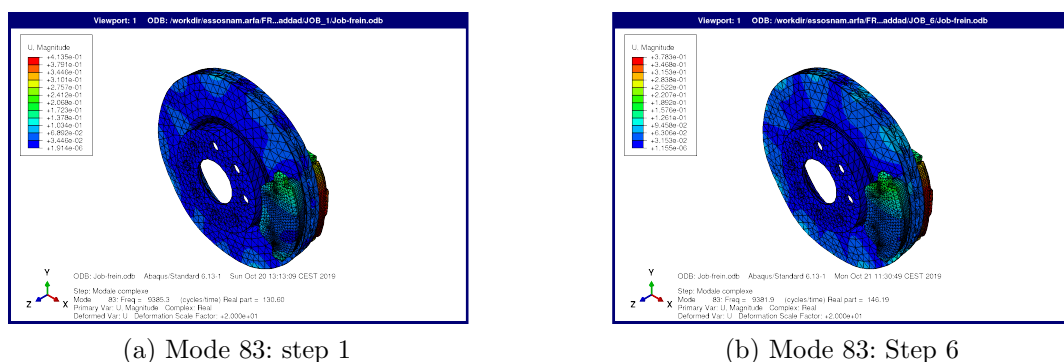
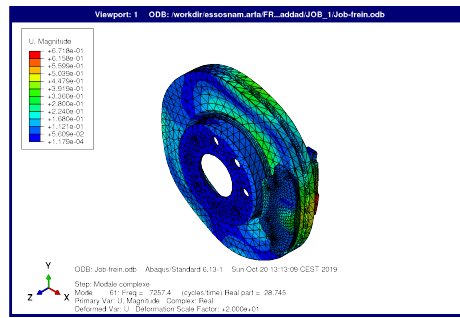


Figure III.47 – Mode 83 comparison between step 1 and 6.

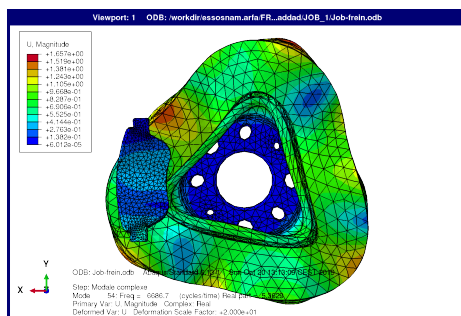
Considering the heterogeneous model, it seems like there is appearance and disappearance of unstable modes, from modes 61 to 54 and modes 54 to mode 27, due to wear. Mode 27, obtained at frequency close to 3.2 KHz , appears at wear cycle 4 and remains from cycle 4 to cycle 6 (see Figure III.51). So, as the wear increases, a disappearance and appearance of unstable modes are observed. However, for the homogeneous model, only an appearance of unstable modes is observed. Moreover, these modes remain for all the wear cycles considered.

III.6 Application of the multi-scale strategy into a complete brake system considering real microstructure

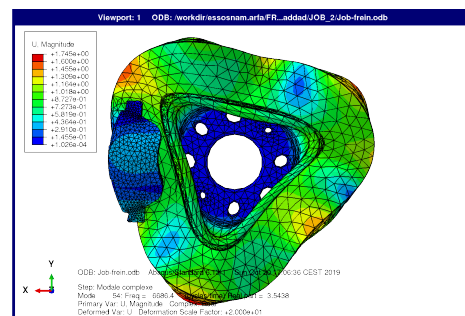


(a) Mode 61: step 1

Figure III.48 – Mode 61 for step 1.

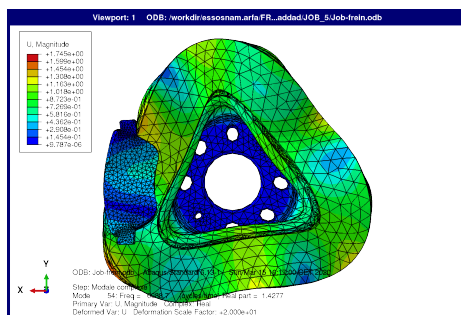


(a) Mode 54: step 1

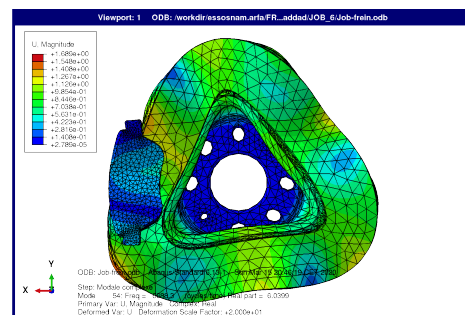


(b) Mode 54: Step 2

Figure III.49 – Mode 54: heterogeneous model.



(a) Mode 54: step 5



(b) Mode 54: Step 6

Figure III.50 – Mode 54: homogeneous model.

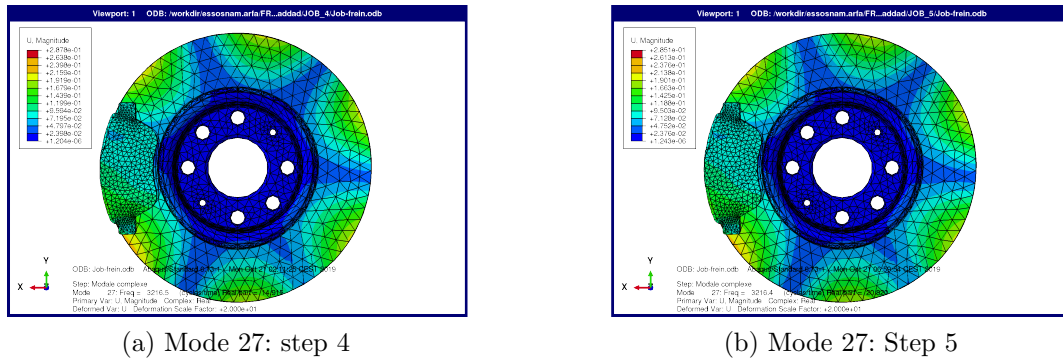


Figure III.51 – Mode 27 comparison between step 4 and 5.

III.7 Chapter synthesis

This chapter was dedicated to a strategy leading to surface defects in the presence of material heterogeneity modelling through a multi-scale method. Two examples have been proposed: case 1 where surface defect was centred in the contact area of the heterogeneous patch and case 2 where three surface defects were placed near patch edges. These examples were validated with explicit results where heterogeneity and surface defects have been meshed. Multi-scale strategy gives satisfying results.

Thereby, the surface defect strategy is extended for surface evolution, for instance wear source flow modelling:

Firstly, three modelling examples have been studied and implemented on a simple model in order to determine their accuracy. From this study, a wear modelling method based on initial gap introduction in the contact law was chosen because of its accuracy and efficiency. Furthermore, wear modelling of a large-scale model has been investigated considering a homogeneous friction material. The numerical pin on disc model has been used for this purpose. Accurate results have been obtained by the means of gap technique. Results for this case were conventional. Contact pressure decreases with wear evolution while the contact area increases. Moreover, for large wear cycles, it was found that contact is localized on the upper right corner and the lower left corner of the pad.

Secondly, in the context of wear modelling of heterogeneous material, a strategy based on KUBC-Contact and gap technique has been proposed and validated through a simple heterogeneous case. A rigid spherical inclusion centred at the leading edge of the frictional material is used for this purpose. Results obtained from our multi-scale method were in a good agreement with explicit method, where inclusion is explicitly meshed. However, our strategy has the advantage to save a lot of computational time. Additionally, the multi-scale strategy proposed, allows wear modelling at local scale. Therefore, complex phenomena as decohesion and cracking can be introduced at this scale.

Thereafter, a generalization of the multi-scale wear modelling strategy has been proposed

considering a realistic biphasic microstructure over the whole friction material. A case where the heterogeneous biphasic microstructure is located at the leading edge of the frictional material has been considered and studied. Wear modelling has been performed at the local scale considering then the influence of this biphasic material constituted of the matrix and the graphite. In fact, good results have been obtained. With our strategy, it is possible to introduce different wear behaviour at this scale. An example, where graphite phase was supposed to wear just a little, shows interesting results. It has been shown that decohesion of graphite particles can occur under the latter assumption. On the other hand, based on KUBC-Contact homogenization method, a non-linear law of elastic constants is obtained and embedded at the large scale, consequently leading to a contact pressure decreasing with wear.

Finally, the biphasic microstructure has been considered in a complete braking system. Wear modelling has been performed in this model by the means of the proposed multi-scale method in order to study system instabilities. After, a quasi-static analysis, complex modal analysis has been investigated using mode coupling theory. Instability study reveals that wear, through material heterogeneity, can exhibit unstable modes appearance and disappearance. Although, unstable modes due to system dynamics remains during wear cycles performed, it has been shown that modes shape are influenced by wear.

BIBLIOGRAPHICAL REFERENCES

- A. Abu Bakar, H. Ouyang, S. James, and L. Li. Finite element analysis of wear and its effect on squeal generation. *Proceedings of the Institution of Mechanical Engineers, Part D: Journal of Automobile Engineering*, 222(7):1153–1165, 2008.
- A. R. AbuBakar and H. Ouyang. A prediction methodology of disk brake squeal using complex eigenvalue analysis. *International Journal of Vehicle Design*, 46(4):416–435, 2008.
- A. Akay. Acoustics of friction. *The Journal of the Acoustical Society of America*, 111(4):1525–1548, 2002.
- P. Alart and F. Lebon. Numerical study of a stratified composite coupling homogenization and frictional contact. *Mathematical and computer modelling*, 28(4-8):273–286, 1998.
- G. Anciaux and J.-F. Molinari. A molecular dynamics and finite elements study of nanoscale thermal contact conductance. *International Journal of Heat and Mass Transfer*, 59:384–392, 2013.
- J. Archard. Contact and rubbing of flat surfaces. *Journal of applied physics*, 24(8):981–988, 1953.
- J. Archard. The temperature of rubbing surfaces. *wear*, 2(6):438–455, 1959.
- H. Baba, T. Wada, and T. Takagi. Study on reduction of brake squeal caused by in-plane vibration on rotor. Technical report, SAE Technical Paper, 2001.
- J.-C. Bae and J. Wickert. Free vibration of coupled disk–hat structures. *Journal of sound and vibration*, 235(1):117–132, 2000.
- A. Bajer, V. Belsky, and L. J. Zeng. Combining a nonlinear static analysis and complex eigenvalue extraction in brake squeal simulation. Technical report, SAE Technical Paper, 2003.
- A. Bajer, V. Belsky, and S.-W. Kung. The influence of friction-induced damping and nonlinear effects on brake squeal analysis. Technical report, SAE Technical Paper, 2004.
- A. R. A. Bakar, H. Ouyang, L. Li, and J. E. Siegel. Brake pad surface topography part ii: Squeal generation and prevention. Technical report, SAE Technical Paper, 2005.
- A. A. Bandeira, P. Wriggers, and P. de Mattos Pimenta. Numerical derivation of contact mechanics interface laws using a finite element approach for large 3d deformation. *International Journal for numerical methods in Engineering*, 59(2):173–195, 2004.
- J. Barber. Thermoelastic instabilities in the sliding of conforming solids. *Proceedings of the Royal Society of London. A. Mathematical and Physical Sciences*, 312(1510):381–394, 1969.

- J. Barber. Bounds on the electrical resistance between contacting elastic rough bodies. *Proceedings of the royal society of London. Series A: mathematical, physical and engineering sciences*, 459(2029):53–66, 2003.
- S. Basseville, E. Héripré, and G. Cailletaud. Numerical simulation of the third body in fretting problems. *Wear*, 270(11-12):876–887, 2011.
- Y. Berthier. Maurice godet’s third body. In D. Dowson, C. Taylor, T. Childs, G. Dalmaz, Y. Berthier, L. Flamand, J.-M. Georges, and A. Lubrecht, editors, *The Third Body Concept Interpretation of Tribological Phenomena*, volume 31 of *Tribology Series*, pages 21 – 30. Elsevier, 1996. doi: [https://doi.org/10.1016/S0167-8922\(08\)70766-1](https://doi.org/10.1016/S0167-8922(08)70766-1). URL <http://www.sciencedirect.com/science/article/pii/S0167892208707661>.
- P. Blaschke, M. Tan, and A. Wang. On the analysis of brake squeal propensity using finite element method. Technical report, SAE Technical Paper, 2000.
- M. Bornert, T. Bretheau, and P. Gilormini. *Homogénéisation en mécanique des matériaux, Tome 1: Matériaux aléatoires élastiques et milieux périodiques*. Hermes science, 2001.
- J. Bos and H. Moes. Frictional heating of tribological contacts. *Journal of tribology*, 117(1):171–177, 1995.
- A. Bousselham, V. Magnier, F. Roudet, A.-L. Cristol, D. Yuhas, P. Dufrenoy, and J. Hosdez. Mechanical characterization and modeling of heterogeneous friction pad material under multiaxial loading. Technical report, Eurobrake technical paper EB2020-STP-055, 2020.
- F. P. Bowden, F. P. Bowden, and D. Tabor. *The friction and lubrication of solids*, volume 1. Oxford university press, 2001.
- A. Bush, R. Gibson, and T. Thomas. The elastic contact of a rough surface. *Wear*, 35(1): 87–111, 1975.
- M. Champagne, M. Renouf, and Y. Berthier. Modeling wear for heterogeneous bi-phasic materials using discrete elements approach. *Journal of Tribology*, 136(2):021603, 2014.
- D. Chan and G. Stachowiak. Review of automotive brake friction materials. *Proceedings of the Institution of Mechanical Engineers, Part D: Journal of Automobile Engineering*, 218(9):953–966, 2004.
- A. B. Chaudhary and K.-J. Bathe. A solution method for static and dynamic analysis of three-dimensional contact problems with friction. *Computers & Structures*, 24(6): 855–873, 1986.
- G. Chen. Ballistic-diffusive equations for transient heat conduction from nano to macro-scales. *Journal of Heat transfer*, 124(2):320–328, 2002.
- A. Chmiel. Finite element simulation methods for dry sliding wear. Technical report, AIR FORCE INST OF TECH WRIGHT-PATTERSON AFB OH SCHOOL OF ENGINEERING, 2008.

- C.-H. J. Chung and M. Donley. Mode coupling phenomenon of brake squeal dynamics. Technical report, SAE Technical Paper, 2003.
- M. Ciavarella, V. Delfino, and G. Demelio. A “re-vitalized” greenwood and williamson model of elastic contact between fractal surfaces. *Journal of the Mechanics and Physics of Solids*, 54(12):2569–2591, 2006.
- C. Collettini, C. Viti, T. Tesei, and S. Mollo. Thermal decomposition along natural carbonate faults during earthquakes. *Geology*, 41(8):927–930, 2013.
- M. Cooper, B. Mikic, and M. Yovanovich. Thermal contact conductance. *International Journal of heat and mass transfer*, 12(3):279–300, 1969.
- A.-L. Cristol-Bulthé, Y. Desplanques, G. Degallaix, and Y. Berthier. Mechanical and chemical investigation of the temperature influence on the tribological mechanisms occurring in omc/cast iron friction contact. *Wear*, 264(9-10):815–825, 2008.
- P. A. Cundall. A computer model for simulating progressive, large-scale movement in blocky rock system. In *Proceedings of the International Symposium on Rock Mechanics, 1971*, 1971.
- P. A. Cundall and O. D. Strack. A discrete numerical model for granular assemblies. *geotechnique*, 29(1):47–65, 1979.
- L. De Lorenzis and P. Wriggers. Computational homogenization of rubber friction on rough rigid surfaces. *Computational Materials Science*, 77:264–280, 2013.
- C. A. de Saracibar and M. Chiumenti. On the numerical modeling of frictional wear phenomena. *Computer methods in applied mechanics and engineering*, 177(3-4):401–426, 1999.
- G. De Saxcé and Z.-Q. Feng. The bipotential method: a constructive approach to design the complete contact law with friction and improved numerical algorithms. *Mathematical and computer modelling*, 28(4-8):225–245, 1998.
- R. Deltombe, K. Kubiak, and M. Bigerelle. How to select the most relevant 3d roughness parameters of a surface. *Scanning: The Journal of Scanning Microscopies*, 36(1):150–160, 2014.
- G. V. Des Roches. *Frequency and time simulation of squeal instabilities. Application to the design of industrial automotive brakes*. PhD thesis, Ecole Centrale Paris, 2011.
- H. B. Dhia. Problèmes mécaniques multi-échelles: la méthode arlequin. *Comptes Rendus de l’Académie des Sciences-Series IIB-Mechanics-Physics-Astronomy*, 326(12):899–904, 1998.
- J. H. Dieterich. Time-dependent friction in rocks. *Journal of Geophysical Research*, 77(20):3690–3697, 1972.

- A. Dmitriev, M. Schargott, and V. Popov. Direct modelling of surface topography development in a micro-contact with the movable cellular automata method. *Wear*, 268 (7-8):877–885, 2010.
- M. Duboc. *Etude multi-échelle du crissement: dispositif expérimental et éléments de compréhension*. PhD thesis, Lille 1, 2013.
- P. Dufrenoy, V. Magnier, Y. Waddad, J.-F. Brunel, and G. De Saxce. A multiscale model of a disc brake including material and surface heterogeneities. *SAE International Journal of Passenger Cars-Mechanical Systems*, 9(2016-01-1911):1136–1143, 2016.
- G. J. Dvorak. Transformation field analysis of inelastic composite materials. *Proceedings of the Royal Society of London. Series A: Mathematical and Physical Sciences*, 437(1900): 311–327, 1992.
- H. G. Elrod and D. E. Brewe. Paper v (iv) numerical experiments with flows of elongated granules. In *Tribology Series*, volume 21, pages 219–226. Elsevier, 1992.
- M. Eriksson and S. Jacobson. Tribological surfaces of organic brake pads. *Tribology international*, 33(12):817–827, 2000.
- J. D. Eshelby. The determination of the elastic field of an ellipsoidal inclusion, and related problems. *Proceedings of the Royal Society of London. Series A. Mathematical and Physical Sciences*, 241(1226):376–396, 1957.
- J. D. Eshelby. The elastic field outside an ellipsoidal inclusion. *Proceedings of the Royal Society of London. Series A. Mathematical and Physical Sciences*, 252(1271):561–569, 1959.
- C. Farhat and F.-X. Roux. A method of finite element tearing and interconnecting and its parallel solution algorithm. *International Journal for Numerical Methods in Engineering*, 32(6):1205–1227, 1991.
- A. Felske, G. Hoppe, and H. Matthäi. Oscillations in squealing disk brakes-analysis of vibration modes by holographic Interferometry. Technical report, SAE Technical Paper, 1978.
- F. Feyel and J.-L. Chaboche. Fe2 multiscale approach for modelling the elastoviscoplastic behaviour of long fibre sic/ti composite materials. *Computer methods in applied mechanics and engineering*, 183(3-4):309–330, 2000.
- J. D. Fieldhouse and P. Newcomb. The application of holographic interferometry to the study of disc brake noise. Technical report, SAE Technical Paper, 1993.
- N. Fillot, I. Iordanoff, and Y. Berthier. A granular dynamic model for the degradation of material. *J. Trib.*, 126(3):606–614, 2004.
- J. Fortin. *Simulation numérique de la dynamique des systèmes multicorps appliquée aux milieux granulaires*. PhD thesis, 2000.

- M. Furey. Surface temperatures in sliding contact. *ASLE TRANSACTIONS*, 7(2):133–146, 1964.
- A. Ghaouti, M. Chaze, P. Dubujet, and F. Sidoroff. Particulate and granular simulation of the third body behaviour. In *Tribology series*, volume 31, pages 355–365. Elsevier, 1996.
- A. Ghosh, W. Wang, and F. Sadeghi. An elastic–plastic investigation of third body effects on fretting contact in partial slip. *International Journal of Solids and Structures*, 81: 95–109, 2016.
- M. Godet. The third-body approach: a mechanical view of wear. *Wear*, 100(1-3):437–452, 1984.
- D. L. Goldsby and T. E. Tullis. Flash heating leads to low frictional strength of crustal rocks at earthquake slip rates. *Science*, 334(6053):216–218, 2011.
- J. Greenwood and J. P. Williamson. Contact of nominally flat surfaces. *Proceedings of the royal society of London. Series A. Mathematical and physical sciences*, 295(1442): 300–319, 1966.
- P. Gurunath and J. Bijwe. Friction and wear studies on brake-pad materials based on newly developed resin. *Wear*, 263(7-12):1212–1219, 2007.
- Z. Hashin and S. Shtrikman. A variational approach to the theory of the elastic behaviour of multiphase materials. *Journal of the Mechanics and Physics of Solids*, 11(2):127–140, 1963.
- V. Hegadekatte, S. Kurzenhäuser, N. Huber, and O. Kraft. A predictive modeling scheme for wear in tribometers. *Tribology international*, 41(11):1020–1031, 2008.
- V. Hegadekatte, N. Huber, and O. Kraft. Finite element based simulation of dry sliding wear. *Modelling and Simulation in Materials Science and Engineering*, 13(1):57, 2004.
- H. Hertz. Über die berührung fester elastischer körper und über die härte-verhandlungen des vereins zur beförderung des gewerbefleißes. 1882.
- M. R. Hestenes. Multiplier and gradient methods. *Journal of optimization theory and applications*, 4(5):303–320, 1969.
- R. Hill. Elastic properties of reinforced solids: some theoretical principles. *Journal of the Mechanics and Physics of Solids*, 11(5):357–372, 1963.
- N. Hoffmann, M. Fischer, R. Allgaier, and L. Gaul. A minimal model for studying properties of the mode-coupling type instability in friction induced oscillations. *Mechanics Research Communications*, 29(4):197–205, 2002.
- C. Hohmann, K. Schiffner, and J. Brecht. Pad wear simulation model. *SAE transactions*, pages 3389–3397, 1999.

- Y.-K. Hu and L. I. Nagy. Brake squeal analysis by using nonlinear transient finite element method. *SAE transactions*, pages 2219–2226, 1997.
- R. A. Ibrahim. Friction-induced vibration, chatter, squeal, and chaos—part i: mechanics of contact and friction. *Applied mechanics reviews*, 47(7):209–226, 1994.
- R. Jarvis and B. Mills. Vibrations induced by dry friction. *proceedings of the Institution of mechanical Engineers*, 178(1):847–857, 1963.
- M. Jean. The non-smooth contact dynamics method. 1999.
- K. L. Johnson and K. L. Johnson. *Contact mechanics*. Cambridge university press, 1987.
- S. Kamat, J. Hirth, and R. Mehrabian. Mechanical properties of particulate-reinforced aluminum-matrix composites. *Acta Metallurgica*, 37(9):2395–2402, 1989.
- P. Kapsa and M. Cartier. Usure des contacts mécaniques-manifestations de l’usure. 2001.
- K. Kato. Classification of wear mechanisms/models. *Proceedings of the Institution of Mechanical Engineers, Part J: Journal of Engineering Tribology*, 216(6):349–355, 2002.
- F. E. Kennedy Jr. Thermal and thermomechanical effects in dry sliding. *Wear*, 100(1-3):453–476, 1984.
- N. Kikuchi and Y. J. Song. Penalty/finite-element approximations of a class of unilateral problems in linear elasticity. *Quarterly of Applied Mathematics*, 39(1):1–22, 1981.
- N. Kinkaid, O. M. O’Reilly, and P. Papadopoulos. Automotive disc brake squeal. *Journal of sound and vibration*, 267(1):105–166, 2003.
- M. Kok. Production and mechanical properties of al₂o₃ particle-reinforced 2024 aluminium alloy composites. *Journal of Materials Processing Technology*, 161(3):381–387, 2005.
- P. Lax and B. Wendroff. Systems of conservation laws. *Communications on Pure and Applied mathematics*, 13(2):217–237, 1960.
- S. Lejeunes and S. Bourgeois. Une toolbox abaqus pour le calcul de propriétés effectives de milieux hétérogènes. In *10e colloque national en calcul des structures*, pages Clé–USB, 2011.
- B. D. Leonard, A. Ghosh, F. Sadeghi, S. Shinde, and M. Mittelbach. Third body modeling in fretting using the combined finite-discrete element method. *International Journal of Solids and Structures*, 51(6):1375–1389, 2014.
- J. Leroux, B. Fulleringer, and D. Nelias. Contact analysis in presence of spherical inhomogeneities within a half-space. *International Journal of Solids and Structures*, 47(22-23):3034–3049, 2010.
- R. J. LeVeque et al. *Finite volume methods for hyperbolic problems*, volume 31. Cambridge university press, 2002.

- Liberation. Jusqu'à dix fois plus de particules fines dans le métro et le RER qu'à l'extérieur. <https://frama.link/8Nz012V5>, 2019.
- G. D. Liles. Analysis of disc brake squeal using finite element methods. Technical report, SAE technical paper, 1989.
- C. V. Madhusudana and C. Madhusudana. *Thermal contact conductance*. Springer, 1996.
- V. Magnier, J.-F. Brunel, and P. Dufrénoy. Impact of contact stiffness heterogeneities on friction-induced vibration. *International Journal of Solids and Structures*, 51(9):1662–1669, 2014.
- V. Magnier, D. N. Ramasami, J.-F. Brunel, P. Dufrénoy, and T. Chancelier. History effect on squeal with a mesoscopic approach to friction materials. *Tribology International*, 115:600–607, 2017.
- A. Majumdar and B. Bhushan. Fractal model of elastic-plastic contact between rough surfaces. *Journal of Tribology*, 113(1):1–11, 1991.
- J. Mandel. Balancing domain decomposition. *Communications in numerical methods in engineering*, 9(3):233–241, 1993.
- R. Mann. *Experiments and thermomechanical modelling of braking application & friction material characterization with loading history effect*. PhD thesis, Lille 1, 2017.
- R. Mann, V. Magnier, J.-F. Brunel, F. Brunel, P. Dufrénoy, and M. Henrion. Relation between mechanical behavior and microstructure of a sintered material for braking application. *Wear*, 386:1–16, 2017.
- F. Martinez, M. Canales, S. Izquierdo, M. Jimenez, and M. Martinez. Finite element implementation and validation of wear modelling in sliding polymer–metal contacts. *Wear*, 284:52–64, 2012.
- F. Massi, L. Baillet, O. Giannini, and A. Sestieri. Brake squeal: linear and nonlinear numerical approaches. *Mechanical Systems and Signal Processing*, 21(6):2374–2393, 2007.
- C. Mbodj, G. Peillex, M. Renouf, L. Baillet, Y. Berthier, and P. Jacquemard. Influence du «contraste» des propriétés élastiques des composites carbone/carbone (c/c) sous conditions dynamiques de contact frottant. *Mechanics & Industry*, 11(3-4):289–294, 2010.
- H. Meng and K. Ludema. Wear models and predictive equations: their form and content. *Wear*, 181:443–457, 1995.
- J. Michel, U. Galvanetto, and P. Suquet. Constitutive relations involving internal variables based on a micromechanical analysis. In *Continuum Thermomechanics*, pages 301–312. Springer, 2000.

- J. Ménard. La quatrième voie du RER A, un cauchemar pour les riverains de Courdimanche. <https://frama.link/eWPm86z1>, 2019.
- J. Molinari, M. Ortiz, R. Radovitzky, and E. Repetto. Finite-element modeling of dry sliding wear in metals. *Engineering Computations*, 18(3/4):592–610, 2001.
- J. J. Moreau. Unilateral contact and dry friction in finite freedom dynamics. In *Nonsmooth mechanics and Applications*, pages 1–82. Springer, 1988.
- M. Müller and G. Ostermeyer. A cellular automaton model to describe the three-dimensional friction and wear mechanism of brake systems. *Wear*, 263(7-12):1175–1188, 2007.
- H. Murakami, N. Tsunada, and T. Kitamura. A study concerned with a mechanism of disc-brake squeal. *SAE transactions*, pages 604–616, 1984.
- L. I. Nagy, J. Cheng, and Y.-K. Hu. A new method development to predict brake squeal occurrence. *SAE transactions*, pages 416–423, 1994.
- D. Naidoo Ramasami. *Influence of friction material & test sequence on disc brake squeal*. PhD thesis, Lille 1, 2014.
- P. R. Nayak. Random process model of rough surfaces. *Journal of Lubrication Technology*, 93(3):398–407, 1971.
- V.-H. Nhu. *Dialogues numériques entre échelles tribologiques*. PhD thesis, 2013.
- M. Nishlwakl, H. Harada, H. Okamura, and T. Ikeuchi. Study on disc brake squeal. Technical report, SAE Technical Paper, 1989.
- M. North. *Disc brake squeal-a theoretical model*. MIRA, 1972.
- J. Oden and J. Martins. Models and computational methods for dynamic friction phenomena. *Computer methods in applied mechanics and engineering*, 52(1-3):527–634, 1985.
- H. Okada, Y. Fukui, and N. Kumazawa. Homogenization method for heterogeneous material based on boundary element method. *Computers & Structures*, 79(20-21):1987–2007, 2001.
- B. Paul. Prediction of elastic constants of multi-phase materials. Technical report, BROWN UNIV PROVIDENCE RI, 1959.
- L. Pei, S. Hyun, J. Molinari, and M. O. Robbins. Finite element modeling of elasto-plastic contact between rough surfaces. *Journal of the Mechanics and Physics of Solids*, 53(11):2385–2409, 2005.
- G. Peillex, L. Baillet, and Y. Berthier. Homogenization in non-linear dynamics due to frictional contact. *International Journal of Solids and Structures*, 45(9):2451–2469, 2008.

- B. Persson, O. Albohr, U. Tartaglino, A. Volokitin, and E. Tosatti. On the nature of surface roughness with application to contact mechanics, sealing, rubber friction and adhesion. *Journal of physics: Condensed matter*, 17(1):R1, 2004.
- B. N. Persson. Theory of rubber friction and contact mechanics. *The Journal of Chemical Physics*, 115(8):3840–3861, 2001.
- P. Podra and S. Andersson. Simulating sliding wear with finite element method. *Tribology international*, 32(2):71–81, 1999.
- K. Popp and P. Stelter. Stick-slip vibrations and chaos. *Philosophical Transactions: Physical Sciences and Engineering*, pages 89–105, 1990.
- K. Popp, M. Rudolph, M. Kroger, and M. Lindner. Mechanisms to generate and to avoid friction induced vibrations. *VDI BERICHTE*, 1736:1–16, 2002.
- M. J. Powell. Algorithms for nonlinear constraints that use lagrangian functions. *Mathematical programming*, 14(1):224–248, 1978.
- Q.-H. Qin and Q.-S. Yang. *Macro-micro theory on multi-field coupling behavior of heterogeneous materials*. Springer,, 2008.
- T. Quinn. Oxidational wear. *Wear*, 18(5):413–419, 1971.
- A. Ramesh and S. N. Melkote. Modeling of white layer formation under thermally dominant conditions in orthogonal machining of hardened aisi 52100 steel. *International Journal of Machine Tools and Manufacture*, 48(3-4):402–414, 2008.
- F. Renaud, G. Chevallier, J.-L. Dion, and G. Taudière. Motion capture of a pad measured with accelerometers during squeal noise in a real brake system. *Mechanical Systems and Signal Processing*, 33:155–166, 2012.
- M. Renouf and N. Fillot. Coupling electrical and mechanical effects in discrete element simulations. *International journal for numerical methods in engineering*, 74(2):238–254, 2008.
- M. Renouf, H.-P. Cao, and V.-H. Nhu. Multiphysical modeling of third-body rheology. *Tribology International*, 44(4):417–425, 2011.
- S. Rhee, P. Tsang, and Y. Wang. Friction-induced noise and vibration of disc brakes. *Wear*, 133(1):39–45, 1989.
- A. D. Sarkar. Friction and wear. *Academic Press, xvi+ 423, 23 x 15 cm, illustrated*, 1980.
- R. S. Sayles and T. R. Thomas. Surface topography as a nonstationary random process. *Nature*, 271(5644):431, 1978.
- I. Serrano-Munoz, J. Rapontchombo, V. Magnier, F. Brunel, S. Kossman, and P. Dufrénoy. Evolution in microstructure and compression behaviour of a metallic sintered friction material after braking. *Wear*, 436:202947, 2019.

- K. Shin, M. Brennan, J.-E. Oh, and C. Harris. Analysis of disc brake noise using a two-degree-of-freedom model. *Journal of Sound and Vibration*, 254(5):837–848, 2002.
- J. C. Simo and T. Laursen. An augmented lagrangian treatment of contact problems involving friction. *Computers & Structures*, 42(1):97–116, 1992.
- J.-J. Sinou. Transient non-linear dynamic analysis of automotive disc brake squeal—on the need to consider both stability and non-linear analysis. *Mechanics Research Communications*, 37(1):96–105, 2010.
- S. Solhjoo and A. I. Vakis. Surface roughness of gold substrates at the nanoscale: an atomistic simulation study. *Tribology International*, 115:165–178, 2017.
- R. T. Spurr. A theory of brake squeal. *Proceedings of the Institution of Mechanical Engineers: Automobile Division*, 15(1):33–52, 1961.
- A. Y. Suh, A. A. Polycarpou, and T. F. Conry. Detailed surface roughness characterization of engineering surfaces undergoing tribological testing leading to scuffing. *Wear*, 255(1-6):556–568, 2003.
- N. P. Suh. The delamination theory of wear. *Wear*, 25(1):111–124, 1973.
- I. Temizer and P. Wriggers. On the computation of the macroscopic tangent for multiscale volumetric homogenization problems. *Computer Methods in Applied Mechanics and Engineering*, 198(3-4):495–510, 2008.
- D. Tolstoi. Significance of the normal degree of freedom and natural normal vibrations in contact friction. *Wear*, 10(3):199–213, 1967.
- A. Vakis, V. Yastrebov, J. Scheibert, L. Nicola, D. Dini, C. Minfray, A. Almqvist, M. Paggi, S. Lee, G. Limbert, et al. Modeling and simulation in tribology across scales: An overview. *Tribology International*, 125:169–199, 2018.
- U. von Wagner, D. Hochlenert, and P. Hagedorn. Minimal models for disk brake squeal. *Journal of Sound and Vibration*, 302(3):527–539, 2007.
- Y. Waddad. *Multiscale thermomechanical strategies for rough contact modeling: application to braking systems*. PhD thesis, Lille 1, 2017.
- Y. Waddad, V. Magnier, P. Dufrénoy, and G. De Saxcé. A multiscale method for frictionless contact mechanics of rough surfaces. *Tribology International*, 96:109–121, 2016.
- A. Wang, J. Mo, X. Wang, M. Zhu, and Z. Zhou. Effect of surface roughness on friction-induced noise: exploring the generation of squeal at sliding friction interface. *Wear*, 402:80–90, 2018.
- I. Ward and P. Hine. The science and technology of hot compaction. *Polymer*, 45(5):1413–1427, 2004.

- J. Wells. Kinetic boundary friction. *The engineer*, 147:454, 1929.
- P. Wriggers. Finite element algorithms for contact problems. *Archives of Computational Methods in Engineering*, 2(4):1–49, 1995.
- T. Yue and M. Abdel Wahab. A numerical study on the effect of debris layer on fretting wear. *Materials*, 9(7):597, 2016.
- G. Zavarise, P. Wriggers, E. Stein, and B. Schrefler. Real contact mechanisms and finite element formulation—a coupled thermomechanical approach. *International Journal for numerical methods in Engineering*, 35(4):767–785, 1992.